Title

Modeling, Estimation and Control of Distributed Parameter Systems: Application to Transportation Networks

Author

Blandin, Sebastien

Publication Date

2012

Modeling, estimation and control of distributed parameter systems: application to transportation networks

by

Sébastien Blandin

A dissertation submitted in partial satisfaction of the
requirements for the degree of
Doctor of Philosophy

in

Engineering – Civil and Environmental Engineering

in the

Graduate Division
of the
University of California, Berkeley

Committee in charge:
Professor Alexandre M. Bayen, Chair
Professor Laurent El Ghaoui
Professor Lawrence C. Evans
Professor Sanjay Govindjee
Professor Roberto Horowitz
Professor Alexander Skabardonis

Spring 2012

Modeling, estimation and control of distributed parameter systems: application to transportation networks

Abstract

Modeling, estimation and control of distributed parameter systems:
application to transportation networks

by

Sébastien Blandin
Doctor of Philosophy in Engineering – Civil and Environmental Engineering

University of California, Berkeley

Professor Alexandre M. Bayen, Chair

The research presented in this dissertation is motivated by the need for well-posed mathematical models of traffic flow for data assimilation of measurements from heterogeneous sensors and flow control on the road network.

A new 2×2 *partial differential equation* (PDE) model of traffic with phase transitions is proposed. The system of PDEs constitutes an extension to the *Lighthill-Whitham-Richards* model accounting for variability around the empirical *fundamental diagram* in the congestion phase. A Riemann solver is constructed and a variation on the classical Godunov scheme, required due to the non-convexity of the state-space, is implemented. The model is validated against experimental vehicle trajectories recorded at high resolution, and shown to capture complex traffic phenomena such as forward-moving discontinuities in the congestion phase, which is not possible with scalar hyperbolic models of traffic flow. A corresponding mesoscopic interpretation of these phenomena in terms of drivers behavior is proposed.

The structure of the uncertainty distribution resulting from the propagation of initial uncertainty in weak entropy solutions to first order scalar hyperbolic conservation laws is characterized in the case of a Riemann problem. It is shown that at shock waves, the uncertainty is a mixture of the uncertainty on the left and right initial condition, and the consequences of this specific class of uncertainty on estimation accuracy is assessed in the case of the extended Kalman filter and the ensemble Kalman filter. This sets the basis for filtering-based traffic estimation and traffic forecast with appropriate treatment of the specific type of uncertainty arising due to the mathematical structure of the model used, which is of critical importance for road networks with sparse measurements.

As a first step towards controlling general distributed models of traffic, a benchmark problem is investigated, in the form of a first order scalar hyperbolic conservation law. The weak entropy solution to the conservation law is stabilized around a uniform solution using boundary actuation. The control is designed to be compatible with the proper weak boundary conditions, which given specific assumptions guarantees that the corresponding *initial-boundary value problem* is well-posed. A semi-analytic boundary control is proposed and shown to stabilize the solution to the scalar conservation law. The benefits of introducing discontinuities in the solution are discussed. For traffic applications, this method allows us to pose the problem of ramp metering on freeways for congestion control and reduction of the amplitude of the *capacity drop*, as well as the problem of vehicular guidance for *phantom jam* stabilization on road networks, in a proper mathematical framework.

To my family

Contents

List of Figures **v**

List of Tables **vii**

Acknowledgments **viii**

1 Introduction **1**
- 1.1 Motivation 2
- 1.2 Hyperbolic conservation laws 3
  - 1.2.1 A brief history of hyperbolic conservation laws 3
  - 1.2.2 Review of macroscopic traffic models 4
  - 1.2.3 Scalar models of traffic flow 5
  - 1.2.4 Non-scalar models of traffic flow 8
- 1.3 Estimation problem for distributed parameter systems 9
  - 1.3.1 A brief history of estimation 9
  - 1.3.2 A state-space formulation for sequential estimation 10
  - 1.3.3 Normality and nonlinearity 12
- 1.4 Contributions and organization of the dissertation 12
  - 1.4.1 Contributions 12
  - 1.4.2 Additional contributions 14
  - 1.4.3 Organization of the dissertation 15

2 A general phase transition model for vehicular traffic **16**
- 2.1 The Colombo phase transition model 17
- 2.2 Extension of the Colombo phase transition model 19
  - 2.2.1 Analysis of the standard state 20
  - 2.2.2 Analysis of the perturbation 21
  - 2.2.3 Definition of parameters 23
  - 2.2.4 Cauchy problem 24
  - 2.2.5 Model properties 25
  - 2.2.6 Numerics 27
- 2.3 The Newell-Daganzo phase transition model 29

    - 2.3.1 Analysis 29
    - 2.3.2 Solution to the Riemann problem 29
    - 2.3.3 Model properties 31
    - 2.3.4 Benchmark test 32
  - 2.4 The Greenshields phase transition model 33
    - 2.4.1 Analysis 33
    - 2.4.2 Solution to the Riemann problem 35
    - 2.4.3 Model properties 36
    - 2.4.4 Benchmark test 36
  - 2.5 The Li phase transition model 38
    - 2.5.1 Analysis 38
    - 2.5.2 Solution of the Riemann problem 42
    - 2.5.3 Benchmark tests 44

3 Phase transition model analysis: properties and performance 47
  - 3.1 Modeling traffic at a macroscopic scale 47
    - 3.1.1 First order scalar macroscopic models 48
    - 3.1.2 Non-stationary traffic flow 49
  - 3.2 Phase transition model properties 51
    - 3.2.1 Mesoscopic interpretation 51
    - 3.2.2 Set-valued fundamental diagram 52
    - 3.2.3 Forward-moving discontinuity in congestion phase 55
    - 3.2.4 Hysteresis phenomenon 56
    - 3.2.5 Phantom jam 59
  - 3.3 Phase transition model validation 60
    - 3.3.1 Vehicle trajectories datasets 60
    - 3.3.2 Model calibration 61
    - 3.3.3 Model comparison 66

4 Advanced estimation methods for distributed systems 70
  - 4.1 Bayesian networks 70
    - 4.1.1 Mathematical formulation 71
    - 4.1.2 Bayesian network for traffic modeling 72
    - 4.1.3 Bayesian structure learning 73
  - 4.2 Kernel method for state-space identification 78
    - 4.2.1 Regression methods 78
    - 4.2.2 Kernel methods 79
    - 4.2.3 Kernel learning 79

5 Sequential data assimilation for scalar macroscopic traffic flow models 85
  - 5.1 Data assimilation 86
    - 5.1.1 Application to transportation networks 86

5.1.2 Optimal filtering for LWR PDE 87
5.2 Nonlinear estimation 88
5.2.1 Deterministic filters 88
5.2.2 Stochastic filters 91
5.3 Discontinuities and uncertainty 93
5.3.1 Estimation and control 93
5.3.2 Riemann problem 94
5.3.3 Riemann problem with stochastic datum 95
5.4 Model nonlinearity 96
5.4.1 Mixture solution to the Riemann problem 97
5.4.2 Mixture solutions to the Godunov scheme 101
5.4.3 Discussion 104
5.5 Model non-differentiability 109
5.5.1 Characterization of non-differentiability domain 109
5.5.2 Numerical experiments 112
5.5.3 Discussion 113

6 Boundary stabilization of weak solutions to scalar conservation laws 117
6.1 Problem statement 118
6.2 Preliminaries 119
6.2.1 BV functions 119
6.2.2 Weak solutions to the initial-boundary value problem 120
6.2.3 Well-posedness of the initial-boundary value problem 123
6.3 Approximation of solution 124
6.4 Lyapunov analysis 125
6.4.1 Lyapunov function candidate 126
6.4.2 Differentiation of the Lyapunov function candidate 126
6.4.3 Internal stability 127
6.5 Well-posed boundary stability 129
6.5.1 Control space 129
6.5.2 Lyapunov stabilization 131
6.6 Maximizing Lyapunov function decrease rate 133
6.6.1 Nature of the waves created by boundary control 133
6.6.2 Greedy boundary control 135
6.7 Numerical examples 136

7 Contributions and open problems 140

Bibliography 143

List of Figures

1.1 Traffic data collection in the Bay area. 2
1.2 Fundamental diagrams. 6

2.1 Colombo phase transition model. 18
2.2 Fundamental diagram in density flux coordinates from a street in Rome. 19
2.3 Newell-Daganzo standard flux function. 22
2.4 Different free-flow phases. 26
2.5 Phase transitions. 27
2.6 Numerical benchmark of Newell-Daganzo phase transition model. 32
2.7 Phase transition model with a Greenshields standard state. 34
2.8 Numerical benchmark of Greenshields phase transition model. 37
2.9 Phase transition model with a Li equilibrium. 40
2.10 Free-flow to congestion benchmark Riemann problem. 44
2.11 Congestion to free-flow benchmark Riemann problem. 45
2.12 Experimental benchmark conditions. 46

3.1 Set-valued congestion phase. 53
3.2 Projection onto PTM diagram. 54
3.3 Forward-moving discontinuity in congestion. 55
3.4 I80 5-5:30 time-space diagrams for NGSIM dataset. 57
3.5 Hysteresis patterns. 58
3.6 Density time-space diagrams. 62
3.7 Sensitivity to congestion wave speed. 65
3.8 Time-space diagrams. 69

4.1 Bayesian network for vehicular traffic. 71
4.2 Stability of the structure learning algorithm. 76
4.3 Dependency to optimal number of parents 77

5.1 Mixture random field. 98
5.2 Distribution of vehicle density at different space-time locations. 99
5.3 Numerical diffusion. 102
5.4 Model noise. 103

5.5 State error log-covariance matrix. 105
5.6 EKF analysis step. 106
5.7 EnKF analysis step. 107
5.8 Locus of non-differentiability of the numerical Godunov flux. 111
5.9 Mean error growth. 113
5.10 Covariance error growth. 114
5.11 Posterior mean error. 115
5.12 Posterior covariance error. 116

6.1 Weak boundary conditions. 122
6.2 Control space. 130
6.3 Representation of the variations of g. 132
6.4 Numerical solution of Burgers equation. 137
6.5 Boundary controls and Lyapunov functions. 138

List of Tables

2.1 Congestion phase. 23
2.2 Numerical error. 33
2.3 Relative error. 38
2.4 L^1 relative error. 46

3.1 Average projection error. 54
3.2 Discretization parameters for NGSIM dataset. 60
3.3 Optimal parameters for I80, 4:00-4:15. 64
3.4 Optimal parameters for I80, 5:00-5:30. 64
3.5 Model accuracy. 67

6.1 Upstream boundary. 134

Acknowledgments

This dissertation constitutes a written account of the research endeavors undertaken as a PhD student at the University of California, Berkeley.

I am greatly indebted to my advisor Professor Alex Bayen, who granted me access to research at UC Berkeley, oriented my research work, kept in mind every single of my deadlines during three years, sent me out to conferences worldwide, and guided me through mathematical creations. I could not have imagined a better role model, and a better start for a research career.

I had the deep honor to work with Professor Benedetto Piccoli, who introduced me to the intricacies of hyperbolic conservation laws. His guidance has been paramount to most of my research, and working with Benedetto has been a constant excitement.

I had the chance to work with Professor Xavier Litrico, who showed me that climbing the hardest mathematical problems in our field, could be as simple as a sunny afternoon in Berkeley, a couple of sheets of paper, and passion.

I would like to express my gratitude to Professors Craig Evans, Laurent El Ghaoui, Sanjay Govindjee, Roberto Horowitz, and Alexander Skabardonis for serving on my dissertation committee. Each half-hour spent on the board with Professor Craig Evans exploring the world of partial differential equations felt like a semester of a typical class. Professor Laurent El Ghaoui introduced me to the wonders of convexity, and the beauty of matrix inequalities. Professor Sanjay Govindjee provided acute comments on my research, which gave me a new perspective on the fascinating world of numerical analysis. I have had the chance to face the scrutiny of Professor Roberto Horowitz, and to enjoy amazing board discussions on traffic control subtleties. The comments of Professor Alexander Skabardonis have been extremely constructive, and his work on traffic modeling and estimation very inspirational.

During my second year of PhD, I had the opportunity to take the class of Professor Hochbaum on integer programming. This class has been one of the most intellectually enjoyable classes of my entire education. Professor Hochbaum presents the smartness of complex algorithms, the intricacy and cleverness of some of the most fundamental concepts in algorithmic and computational science, with incomparable passion.

Upon arrival at UC Berkeley, I met with my academic older brother, who illustrated by example that with work, and with (now Professor) Dan Work in particular, nothing was impossible. The constant excitement, perfectionism, vision, of Dan has been a constant motivation during my PhD, and beyond.

A research effort with my colleague Samitha Samaranayake has been the start of a great research adventure on stochastic routing. I have never ceased to be amazed by Samitha's ability to unravel the apparent complexity of any combinatorial problem. Working together on stochastic routing questions has been extremely fruitful, and a lot of fun.

Multiple research endeavors significantly contributed to my academic education. Professor Paola Goatin helped me tremendously with hyperbolic conservation laws research. I also learned a lot from efforts with Juan Argote, Paul Borokhov, Adrien Couque, Dr. Olivier Goldshmidt, Amir Salam in particular.

I would like to thank Professor Satish Rao for serving on my Qualifying Exam, and for being so inspirational in his constant research approach to daily questions.

I learned a lot from UC Berkeley professors who had their doors open and took the time to answer my questions; Professor Steve Glaser, Professor Kameshwar Poolla, Professor Alexandre Chorin, Professor Pravin Varaiya, Professor Raja Sengupta, Professor Carlos Daganzo, Professor Claire Tomlin, in particular.

The sharpness and fun of the students of Alex's group and the Civil Systems Program have been a constant source of enjoyment and motivation; Dr. Olli-Pekka Tossavainen who taught me that nothing was ground-truth, (now Professor) Chris Claudel who manipulates ideas that standard humans cannot comprehend, (now Professor) Saurabh Amin whose knowledge's frontiers have not yet been explored, Aude Hofleitner who has produced some of the most refreshing recent research in the traffic/learning community, Dr. Ryan Herring whose graph structure is at the basis of a significant part of the Mobile Millennium work, Dr. Andrew Tinka who could probably challenge Mac Gyver and Deep Blue concurrently, Dr. Branko Kerkez whose originality and witted kindness cannot cease to amaze me.

I also had the chance to share office, and coffee breaks, with (now Professor) Florent Di Meglio and Julie Percelay, during my first months and years at UC Berkeley.

During my PhD I have had the luxury of working at and with the California Center for Innovative Transportation (CCIT). I am deeply indebted to Tom West for contributing to the success of my academic career, and to Jean-Damien Margulici, Ali Mortazavi, for their support at CCIT. I have learned tremendously from Joe Butler. In particular I have a great admiration for Joe's incredible talent for managing people, and the art and elegance with which he goes through organizational nightmares. I also had the privilege of interacting with Saneesh Apte, which has been a unique experience.

To go back in time, I must acknowledge the impact that years of Classes Preparatoires, and Professor Frederic Massias and Professor Richard Antetomaso in particular, had on my education, and on my life.

I would also like to acknowledge the spirit of the city of Berkeley. My morning walk on Telegraph Avenue greatly contributed to convince me that new solutions always existed, that different perspectives were possible, and that my mathematical issues could be turned around.

I would like to acknowledge companies, federal and state agencies who funded this dissertation work and raised practical issues for large-scale systems motivating the applicability of theoretical research. The *Mobile Century* experiment was made possible by a joint part-

nership between Nokia, UC Berkeley, and the California DOT. Numerous interactions with NAVTEQ and Telenav on probe data under the umbrella of the *Mobile Millennium* project led to the development of several of the techniques presented in this dissertation.

Several organizations also contributed to sustain this research work via various awards and fellowship, notably the National Science Foundation, the University of California Transportation Center, the IEEE Control Systems Society, the US Department of Transportation, the California Transportation Foundation, and the ITS World Congress.

Finally I would like to acknowledge the support of all my Berkeley and Bay Area friends Karla, Bala, Panna, Nico, Pravin, Indira, Sanjay, John, Brian, roomates, Josh, Jessie, Kristi, Sara, Andre, Gary, and also visitors and worldwide friends Isabelle, Veronique, Vincent, Aurelien, Miguel, Adeline, Jeremy, Guillaume, who helped me build a social structure in this fantastic environment.

I would like to play the last note for my family, who is of course the cause of all of this.

Chapter 1

Introduction

Human activities have historically evolved toward increased spatio-temporal concentration, leading to significant efficiency and economic gains. In 2007, about half of the global GDP was generated by 22 percent of the population living in the largest 600 cities [80]. By 2025, the 600 largest cities are expected to account for 60 percent of the global GDP, and 25 percent of the world population.

Higher density of population and activities requires more efficient infrastructure development. The emergence of recurring traffic congestion in large cities world wide in the recent decades illustrates the growing impact of negative externalities caused by increased demand for scarce resources managed by outdated infrastructure and non adaptive systems. Traffic congestion in the US and in Europe for the year 2009 amounts to about 1 percent of their GDP, in terms of wasted time and fuel [195]. Moreover, about half of the congestion is typically due to non-recurrent events, and not to a systemic lack of capacity.

In the context of individual vehicles operated by human drivers with limited abilities and imperfect information, traffic phenomena exhibit the behavior of a nonlinear system, in which spatio-temporal discontinuities commonly arise, and in which rare events can cause large disruptions to the nominal behavior. Notable examples include the formation of queues in traffic flow, and panic waves in crowds. These properties, among others, make traffic modeling challenging and highlight the need for joint use of information from physical assumptions, statistical analysis, and field measurements.

Traffic monitoring research is concerned with modeling traffic phenomena, estimating real-time and future traffic conditions, and designing preventive and reactive control mechanisms. This dissertation is motivated by the need for novel mathematical techniques for modeling, estimation and control algorithms, able to take advantage of the deluge of new traffic data types and increased adaptivity and robustness requirement of smart infrastructure.

1.1 Motivation

Historically, sensing infrastructure has been dominated by static sensors collecting aggregate information on the traffic state. In particular, availability of counts and occupancy from loop detectors has strongly steered research towards traffic models based on these quantities. In the last decade, the spread, democratization, and rapid increase in the number of *smart phones* with rich communication capabilities and wide sensing abilities has revolutionized the field of traffic sensing, and allowed the consideration of complex problems and systemic issues at unprecedented scales [115].

As illustrated by pilot projects such as the *Mobile Millennium* [19] and the *Mobile Millennium Stockholm* [2], collection of anonymized individual sub-sampled trajectories could be considered a valid substitute to the installment and maintenance of fixed sensing infrastructure in the future. In the Bay Area, the *Mobile Millennium* system receives several millions data points from GPS devices and GPS-enabled smart phones daily. A comparable volume of data is received from loop detectors (see Figure 1.1). Fundamental differences between these two data types are related to their spatial coverage, their noise statistics, and their usability for traffic monitoring.

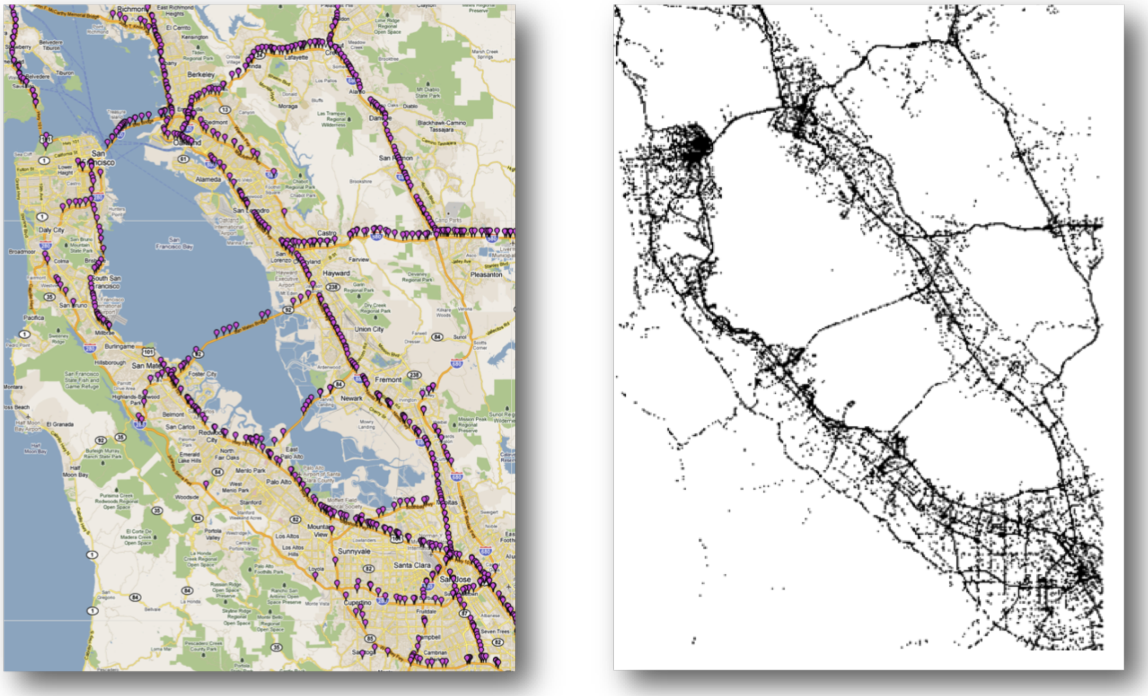

Figure 1.1: Traffic data collection in the Bay area.
Left: loop detector locations at which count and occupancy are measured. Right: one day of GPS point speeds collected by the *Mobile Millennium* system.

Wide availability of traffic measurements collected along individual trajectories, i.e. in Lagrangian coordinates, and from personal multi-purpose sensing devices with specific constraints and error characteristics present new opportunities and challenges for traffic modeling and estimation, among which the design of models able to account for heterogeneous behaviors, the design of transparent estimation methods and robust control algorithms able to perform efficiently in the context of uncertain error propagation in complex systems.

Classical traffic models are based on flow and density information, and consists of modeling the *average driver*, or the *average of drivers*. This paradigm has provided reasonable results, and significant insights on traffic behavior at a macroscopic level. GPS measurements from individual drivers allow the observation of different driving behaviors and require the design of novel traffic models able to account for macroscopic phenomena resulting from the interaction of heterogeneous agents.

The field of estimation is concerned with the construction of estimates that best represent a process of interest. With the multiplication of the number of traffic sensors, the growing complexity of sensors and data processing algorithms, the need for estimation methods able to properly account for error propagation increases. The choice of congestion control algorithms is also driven by the need to provide optimality guarantees in the presence of unknown error given the increasing volume of data used for the computation of the control variables.

This dissertation is centered on hyperbolic partial differential equations methods combined with filtering techniques from estimation theory and stabilization approaches for dynamical systems. Relevant introductory material pertaining to these different fields is presented in the following sections.

1.2 Hyperbolic conservation laws

1.2.1 A brief history of hyperbolic conservation laws

The conservation principle is one of the most fundamental modeling principles for physical systems. Statements of conservation of mass, momentum, energy are at the center of modern classical physics. For distributed dynamical systems, this principle can be written in *conservation law* form with the use of *partial differential equations* (PDE). The problem of *well-posedness* of the partial differential equation is concerned with the existence, uniqueness, and continuous dependence of the solution to the problem data [89].

First existence results for scalar conservation laws in one dimension of space date back to [180]. For hyperbolic systems of conservation laws in one dimension of space, existence results were provided in [101] with the introduction of the *random choice method*. Existence and uniqueness in the scalar case for several spatial dimensions were proven in [141], and to this date constitute the only general results known on well-posedness for several dimensions of space. Uniqueness for $n \times n$ hyperbolic systems of conservation laws in one-dimension of space was shown only recently in [40]. Existence results can also be obtained using the techniques developed in [40]. The global well-posedness of solutions to hyperbolic systems of conservation laws in several dimensions of space is still a largely open problem.

Hyperbolic systems of conservation laws have been extensively applied to the modeling of physical systems. In the following section, we present seminal macroscopic traffic flow models based on hyperbolic systems of conservation laws.

1.2.2 Review of macroscopic traffic models

Macroscopic traffic modeling provides description of traffic phenomena as a continuum of vehicles, instead of modeling individual vehicle dynamics. Macroscopic traffic models are historically inspired from constitutive models for hydrodynamics systems, which share properties with traffic flow.

First order scalar models of traffic.

Hydrodynamic models of traffic go back to the 1950's with the work of Lighthill, Whitham and Richards [159, 189], who proposed the first model of the evolution of vehicle density on the highway using a first order scalar hyperbolic *partial differential equation* (PDE) referred to as the LWR PDE. Their model relies on the knowledge of an empirically measured *flux function*, also called the *fundamental diagram* in transportation engineering, for which measurements go back to 1935 with the pioneering work of Greenshields [107]. Numerous other flux functions have since been proposed in the hope of capturing effects of congestion more accurately, in particular: Greenberg [106], Underwood [216], Newell-Daganzo [71, 177], and Papageorgiou [221]. The existence and uniqueness of an *entropy* solution to the *Cauchy problem* [198] for the class of scalar conservation laws to which the LWR PDE belongs go back to the work of Oleinik [180] and Kruzhkov [141], (see also the seminal article of Glimm [101]), which was extended later to the *initial-boundary value problem* [15], and specifically instantiated for the scalar case with a concave flux function in [153], in particular for traffic in [205]. Numerical solutions of the LWR PDE go back to the seminal *Godunov scheme* [103, 156], which was shown to converge to the entropy solution of the first order hyperbolic PDE (in particular the LWR PDE). In the transportation engineering community, the Godunov scheme in the case of a triangular flux is known under the name of *Cell Transmission Model* (CTM), which was brought to the field of transportation by Daganzo in 1995 [71, 72] (see [150] for the general case), and is one of the most used discrete traffic flow models in the literature today [48, 74, 126, 160, 174, 181, 220].

Set-valued fundamental diagrams.

The assumption of a Greenshields fundamental diagram or a triangular fundamental diagram, which significantly simplifies the analysis of the model algebraically, led to the aforementioned theoretical developments. Yet, experimental data clearly indicates that while the free flow part of a fundamental diagram can be approximated fairly accurately by a straight line, the congested regime is set valued, and can hardly be characterized by a single curve [219]. An approach to model the set-valuedness of the congested part of the fundamental diagram consists in using a second equation coupled with the mass conservation equation (i.e. the LWR PDE model). Such models go back to Payne [183] and Whitham [223] and generated significant research efforts, but led to models with inherent weaknesses pointed out by del Castillo [78] and Daganzo [73]. These weaknesses were ultimately addressed in several responses [13, 181, 230], leading to sustained research in this field.

The following sections are focused on the mathematical theory of scalar and non-scalar traffic flow models.

1.2.3 Scalar models of traffic flow

Classical scalar models of traffic consider the traffic state at a point x at time t to be fully represented by the density $\rho(t, x)$ of vehicles at this point. The evolution of the density of vehicles can be modeled by a combination of physical principles, statistical properties, and empirical findings. All the models considered in this section are single-lane single-class models of traffic.

Continuous models

A classical state equation used to model the evolution of the density $\rho(\cdot,\cdot)$ of vehicles on the road network is the LWR PDE [159, 189], which expresses the conservation of vehicles on road links:

$$\partial_t \rho + \partial_x Q(\rho) = 0 \tag{1.1}$$

where the flux function $Q(\cdot)$, assumed to be space-time invariant on limited space-time domains, denotes the realized flux of vehicles with the density ρ, at the stationary state. The flux function, or *fundamental diagram*, is classically given by an empirical fit of the relation between density and flow. It can be equivalently given by an empirical fit $V(\cdot)$ of the relation between density and space-mean speed, which allows us to define the flux function as:

$$Q(\rho) = q = \rho\, v = \rho\, V(\rho),$$

where the central equality is a definition of the flow q. A variety of parametric flux functions can be found in the literature. One of the earliest flux functions is the *Greenshields flux function* [107] or quadratic flux function (represented in Figure 1.2, left), which expresses a linear relationship between density and speed, or equivalently a quadratic relation between density and flow:

$$Q(\rho) = v_{\max}\, \rho \left(1 - \frac{\rho}{\rho_{\max}}\right) \tag{1.2}$$

where $v_{\max}$ denotes the *free-flow speed* and $\rho_{\max}$ the *jam density.* The *Newell-Daganzo flux function* [72, 177] or triangular flux function, represented in Figure 1.2, center, is a piecewise linear function of the density, with different slopes in free-flow and congestion:

$$Q(\rho) = \begin{cases} \rho\, v_{\max} & \text{if} \quad \rho \in [0, \rho_c] \\ \rho_c\, v_{\max} \frac{\rho_{\max} - \rho}{\rho_{\max} - \rho_c} & \text{if} \quad \rho \in [\rho_c, \rho_{\max}] \end{cases} \tag{1.3}$$

where ρ_c denotes the critical density, which represents the density at which the realized flow is maximal. The speed of backward moving waves in congestion is given by $w = v_{\max}\, \rho_c / (\rho_c - \rho_{\max})$. Variations on a flux function based on an exponential relation between density and flow [158, 182], parameterized by a, such as the one represented in Figure 1.2, right, can be found in the literature:

$$Q(\rho) = \rho\, v_{\max} \exp\left(-\frac{1}{a} \left(\frac{\rho}{\rho_c} \right)^{a} \right). \tag{1.4}$$

The interested reader might also consider the *Greenberg* fundamental diagram [106] or the *Van-Aerde* fundamental diagram [217].

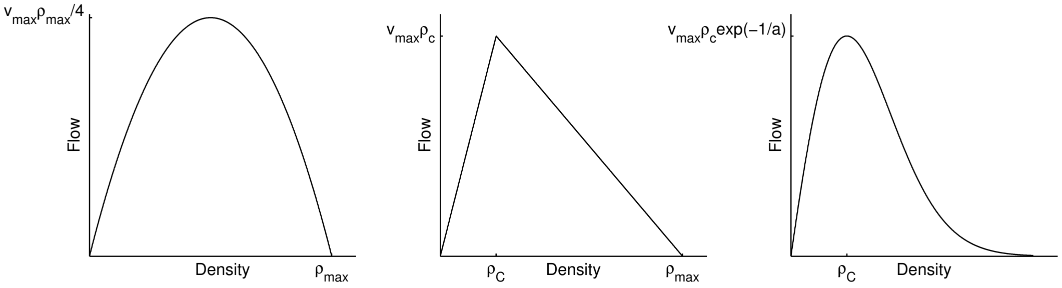

Figure 1.2: Fundamental diagrams.
Greenshields (left), triangular (center), exponential (right).

Remark 1.1. *The LWR PDE models the evolution of traffic flow on a road segment with uniform topology. A junction is defined by a change of topology (crossing, number of lanes, speed limit, curvature, etc) on a road segment, which requires specific efforts for physical consistency and mathematical compatibility with the link model. A junction can be modeled as a vertex of the graph representing the road network. To each vertex is associated an allocation matrix A, where a_{ij} expresses the proportion of the incoming flow from link i going to link j. For uniqueness of the solution of the junction problem, different conditions have been considered in the literature: for instance maximizing the incoming flow through the junction [60, 72] or maximizing a concave function of the incoming flow [116]. A formulation using internal dynamics for the junction [149] has been shown to be equivalent to the vertex models for merge and diverge junction. The interested reader is referred to the book from Garavello and Piccoli [97] for more details on the junction problem.*

For traffic applications, given an initial condition $\rho_0(\cdot)$ defined on a stretch $[0, L]$, using the LWR model requires solving the associated *Cauchy problem*, defined as the problem of existence and uniqueness of a solution to the LWR PDE with initial condition $\rho_0(\cdot)$. If the initial condition is piecewise constant (which is the case for many numerical approximations) and self-similar[1], the Cauchy problem reduces to the Riemann problem (see Section 5.3.2).

For numerical computations, it is in general necessary to discretize the space of independent variables. The corresponding numerical schemes applied to the continuous models described in this section can themselves be understood as discretized link models.

Discretized link models

Given a discretization grid defined by a space-step Δx and a time-step Δt, if we note ρ_i^n the discretized solution at $i\,\Delta x, n\,\Delta t$ and $\mathcal{C}_i^n$ the cell defined by $\mathcal{C}_i^n = [n\,\Delta t, (n+1)\,\Delta t] \times [i\,\Delta x, (i+1)\,\Delta x]$, the discretization of the LWR PDE using the *Godunov scheme* [103] reads:

$$\rho_i^{n+1} = \rho_i^n + \frac{\Delta t}{\Delta x}\left(q_G(\rho_{i-1}^n, \rho_i^n) - q_G(\rho_i^n, \rho_{i+1}^n)\right) \tag{1.5}$$

where the numerical Godunov flux $q_G(\cdot,\cdot)$ is defined as follows for a concave flux function $Q(\cdot)$ with a maximum at ρ_c:

$$q_G(\rho_l, \rho_r) = \begin{cases} Q(\rho_l) & \text{if} \quad \rho_r \leq \rho_l < \rho_c \\ Q(\rho_c) & \text{if} \quad \rho_r \leq \rho_c \leq \rho_l \\ Q(\rho_r) & \text{if} \quad \rho_c < \rho_r \leq \rho_l \\ \min(Q(\rho_l), Q(\rho_r)) & \text{if} \quad \rho_l < \rho_r \end{cases} \tag{1.6}$$

The Godunov scheme is a first order finite volume discretization scheme commonly used for numerical computation of *weak entropy solutions* to one-dimensional conservations laws such as the LWR PDE [156]. The design of the Godunov scheme dynamics (1.5) results from the following steps:

1. At time $n\,\Delta t$, for each couple of neighboring cells $\mathcal{C}_i^n$, $\mathcal{C}_{i+1}^n$, compute the solution to the Riemann problem defined at the intersection of cells $\mathcal{C}_i^n$, $\mathcal{C}_{i+1}^n$, by the left datum ρ_i^n and the right datum ρ_{i+1}^n.
2. At time $(n+1)\,\Delta t$, on each domain $\{(n+1)\,\Delta t\} \times [i\,\Delta x, (i+1)\,\Delta x]$ compute the average of the solution of the Riemann problem. Specifically, integrating the LWR PDE on the domain $\mathcal{C}_i^n$,

$$\iint_{\mathcal{C}_i^n} \left(\frac{\partial \rho}{\partial t} + \frac{\partial Q(\rho)}{\partial x}\right) dxdt = 0 \tag{1.7}$$

---

[1] A function f of n variables $x_1, \ldots, x_n$ is called self-similar if $\forall \alpha > 0 \in \mathbb{R}, f(\alpha\, x_1, \ldots, \alpha\, x_n) = f(x_1, \ldots, x_n)$.

and applying the Stokes theorem on $\mathcal{C}_i^n$ to this equality yields:

$$\Delta x\, \rho_i^{n+1} + \int_{n\,\Delta t}^{(n+1)\,\Delta t} Q(\rho(t, i\,\Delta x))dt - \Delta x\, \rho_i^n - \int_{n\,\Delta t}^{(n+1)\,\Delta t} Q(\rho(t,(i+1)\,\Delta x))dt = 0, \quad (1.8)$$

where we note ρ_i^{n+1} the space average of the solution to the Riemann problems on $\{(n+1)\,\Delta t\} \times [i\,\Delta x, (i+1)\,\Delta x]$. Since the solution to the Riemann problems are self-similar (see footnote 1), hence constant at $i\,\Delta x$ and $(i+1)\,\Delta x$, if we note respectively $Q(\rho_{i-1}^n, \rho_i^n)$, $Q(\rho_i^n, \rho_{i+1}^n)$ the value of the corresponding flow at these locations over the interval $[n\Delta t, (n+1)\,\Delta t]$, we obtain:

$$\Delta x\, \rho_i^{n+1} - \Delta x\, \rho_i^n = \Delta t\, Q(\rho_{i-1}^n, \rho_i^n) - \Delta t\, Q(\rho_i^n, \rho_{i+1}^n),$$

which is the dynamics equation (1.5) of the Godunov scheme.

The first step of the Godunov scheme is exact whereas the second step, through averaging, introduces numerical diffusion (see [156] for more details). The consequence of this diffusion on estimation is further discussed in Section 5.4.

Remark 1.2. *It must be noted that grid-free algorithms allow the computation of numerical solutions of scalar conservation laws without numerical diffusion [39], with a higher complexity in general. In the case of transportation, some algorithms have be shown to be exact for specific fundamental diagrams and particular initial and boundary conditions [58, 59, 167, 225].*

The Godunov scheme has been shown to provide a numerical solution consistent with classical traffic assumptions [150] and to be equivalent to the *supply-demand* formulation for concave flux functions with a single maximum. In the case of a triangular flux function (1.3), the Godunov scheme reduces to the CTM [71, 72]:

$$q_G(\rho_l, \rho_r) = \min\left(\rho_l\, V, \rho_c\, V, \rho_c\, V \frac{\rho_{\max} - \rho_r}{\rho_{\max} - \rho_c}\right).$$

Modeling capabilities of macroscopic traffic flow models can be extended by considering non-scalar models, presented in the following section.

1.2.4 Non-scalar models of traffic flow

Non-scalar models of traffic flow consider additional state variables and additional physical principles to model traffic states. One of the first non-scalar traffic flow models is the *Payne-Whitham* model [183, 223]:

$$\begin{cases} \partial_t \rho + \partial_x q & = 0 \\ \partial_t v + v\, v_x + \frac{c_0^2}{\rho}\, \partial_x \rho & = \frac{V(\rho) - v}{\tau}. \end{cases} \quad (1.9)$$

The first equation expresses the conservation of vehicles, and the second equation models the evolution of speed, which is subject to convection, anticipation, and relaxation (respectively second and third left-hand side terms of second equation, and right-hand side term of the second equation).

The EKF has been applied to networks[2] for state and parameter estimation [221, 222], with the following discretization of the *Payne-Whitham* model (1.9):

$$\begin{cases} \rho_i^{n+1} & = \rho_i^n + \tfrac{\Delta t}{\Delta x}\,\left(q_{i-1}^n - q_i^n\right) \\ v_i^{n+1} & = v_i^n + \tfrac{\Delta t}{\Delta x}\, v_i^n\,\left(v_{i-1}^n - v_i^n\right) + \tfrac{\Delta t}{\tau}\,\left(V(\rho_i^n) - v_i^n\right) - \tfrac{c_0^2\,\Delta t}{\tau \Delta x}\tfrac{\rho_{i+1}^n - \rho_i^n}{\rho_i^n + \kappa} \\ q_i^n & = \rho_i^n\, v_i^n \end{cases} \tag{1.10}$$

where κ is a regularization parameter and the function $V(\cdot)$ is the exponential fundamental diagram (1.4). Other notable models with two state variables (so-called *second order models*) include the *Aw-Rascle* model [13], the *non-equilibrium* model [233], or the *phase transition* model [31, 61]. Traffic models with three state variables have also been proposed [112] by addition of a state equation for the variance. The discrete second order model (1.10) is by definition unable to capture discontinuities exactly, and differentiable, however structural properties of the continuous Payne-Whitham model from which it is derived exhibit similarities with the LWR model [231] and allow the generalization of some of our conclusions. The filtering algorithms used for estimation in general and for traffic flow models in particular, are described in the following section.

1.3 Estimation problem for distributed parameter systems

1.3.1 A brief history of estimation

The theory of *estimation* is concerned with the problem of providing statistics of a process state ψ_t, based on measurements Y_t and a-priori knowledge. The a-priori knowledge of the process often consists of a parametric *model*, which approximately describes the process behavior mathematically. The definition of a *loss function* allows the formulation of the estimation problem as an optimization problem and the identification of certificates of optimality. When the estimated quantities are not directly observed, (so-called *latent variables*) the estimation problem is referred to as an *inverse problem* [131]. For physical systems, the estimation problem, or *data assimilation* problem [36, 152], is solved using a data assimilation algorithm, which combines optimally, in the sense of the loss function, the a-priori knowledge of the system, and the observations from the system. In particular, a *filtering* algorithm provides the solution to an inverse problem which includes the additional constraint that, for all times t, only observations at or before time t can be used to compute estimates at time t.

---

[2] For simplicity we omit the network terms (sources and sinks) in equation (1.10).

The use of the *quadratic loss function* dates back to the estimation problem posed by Gauss in the 18th century for astronomy [203, 204]. The solution proposed by Gauss is the so-called *least-squares method*, justified by the *Gauss-Markov* theorem [124]. The theorem proves that, assuming a linear observation model with additive white noise, the *best linear unbiased estimator* (BLUE) (best in the minimum variance sense), of a random process ψ_t can be computed as the solution to the *ordinary least squares* (OLS) problem.

The role of the quadratic norm for estimation is further emphasized by a result from Sherman [199], which shows that for a large class of loss functions, which includes the quadratic loss function, the mean of the conditional distribution $p(\psi_t|Y_t)$ is optimal.

Formally, given a loss function $L(\cdot)$ such that:

$$\begin{aligned}
&L(0) = 0 \\
&\exists \quad f \quad \text{real-valued convex s.t.} \quad \forall \psi_1, \psi_2 \quad \text{s.t.} \quad f(\psi_1) \geq f(\psi_2) \\
&\text{then} \qquad L(\psi_1) \geq L(\psi_2),
\end{aligned} \tag{1.11}$$

given a random variable ψ, if the probability density function associated with the random variable ψ is symmetric around the mean, and unimodal, then $\mathbb{E}(\psi)$ is the optimal estimator of ψ for the loss function $L(\cdot)$.

When applied to the conditional random variable $\psi_t|Y_t$, this shows that the conditional mean is the optimal estimator in the sense of the loss function $L(\cdot)$ for this particular class of loss functions and probabilities.

For dynamical systems, the estimation problem can be solved online sequentially using this result in a state-space formulation.

1.3.2 A state-space formulation for sequential estimation

Given a system with true state at time t denoted by Ψ_t, and Y_t the vector of all available observations up to time t, the *filtering problem* is concerned with the computation of an *optimal estimate* of Ψ_t for a predefined loss function. Solvability of the estimation problem heavily depends on the loss function used, and on the statistics considered.

The basis for modern filtering theory was set by Kalman in 1960 who introduced a sequential filtering algorithm for linear dynamical systems, the *Kalman filter* (KF) [132]. This algorithm extended the work of Wiener [224] and proposed one of the first results on optimal filtering for linear dynamical systems with non-stationary statistics. The KF *sequentially* computes the best estimate of the *true state* of a system from combined knowledge of a model and observations. The KF has been widely applied by the control community, notably to signal processing, sensor data fusion, navigation and guidance [17, 193].

For transportation applications involving macroscopic variables, the state is typically a set of densities, speeds, or counts, defined on a discretization grid. The true state consists of the true traffic conditions on the road, which are only available to an oracle, or some high fidelity datasets such as the NGSIM dataset [179]. For simulation purposes, it is common practice to use a well-calibrated model, or a Monte Carlo simulation with high number of samples, as a proxy for the true state (to avoid the so-called *inverse crime* [131], the model used for estimation should be different from the model used for computing the true state).

Kalman filter

In his seminal article [132], Kalman provides a *sequential* algorithm to compute the BLUE of the state for *dynamical systems*, under additive white Gaussian noise, with a deterministic linear observation equation (this result was later extended to include additive white Gaussian observation noise). The *Kalman filter* is defined in a *state-space model*, which consists of a state equation and an observation equation.

We consider the following discrete linear model:

$$x_t = A_t\, x_{t-1} + w_t \tag{1.12}$$

where we note A_t the state model or time-varying state transition matrix at time t, and where the random variable $w_t \sim \mathcal{N}(0, W_t)$ is a white noise vector which accounts for modeling errors. In particular in this setting the true state Ψ_t is assumed to follow the dynamics A_t without additional noise. Measurements are modeled by the linear observation equation:

$$y_t = C_t\, \Psi_t + v_t \tag{1.13}$$

where $v_t \sim \mathcal{N}(0, V_t)$ is a white noise vector which accounts for measurement errors assumed uncorrelated with modeling errors, and C_t is the modeled measurement matrix at time t (also time-varying, to integrate the possibility of moving or intermittent sensors). The KF sequentially computes the BLUE estimate at time $t+1$ from the BLUE estimate at time t as follows:

$$\text{Forecast:} \begin{cases} x_{t+1|t} = A_{t+1}\, x_{t|t} \\ \Sigma_{t+1|t} = A_{t+1}\, \Sigma_{t|t}\, A_{t+1}^T + W_{t+1} \end{cases} \tag{1.14}$$

$$\text{Analysis:} \begin{cases} x_{t+1|t+1} = x_{t+1|t} + K_{t+1} \left(y_{t+1} - C_{t+1}\, x_{t+1|t} \right) \\ \Sigma_{t+1|t+1} = \Sigma_{t+1|t} - K_{t+1}\, C_{t+1}\, \Sigma_{t+1|t} \\ \text{where} \quad K_{t+1} = \Sigma_{t+1|t}\, C_{t+1}^T \, \left(C_{t+1}\, \Sigma_{t+1|t}\, C_{t+1}^T + V_{t+1} \right)^{-1} \end{cases} \tag{1.15}$$

The forecast step (1.14) consists in propagating the mean $x_{t|t}$ and covariance $\Sigma_{t|t}$ of the state through the linear model (1.12). The analysis step (1.15) amounts to the computation of the conditional mean of the state given the observations, for the linear observation model (1.13) and jointly Gaussian statistics. The conditional covariance is computed similarly. From a Bayesian perspective, the Kalman filter sequentially computes the posterior distribution of the state, based on the prior distribution given by the state-space model.

When the state model is not linear, there is no general analytical expression for the propagation of the statistics. Suboptimal filters of different types have been derived. In the following section, we present the concepts related to estimation of nonlinear or non-normal processes.

1.3.3 Normality and nonlinearity

The statistical assumptions on the processes ψ_t and Y_t are tied to prior knowledge of the generative distributions. However, a significant computational argument in favor of the use of normal statistics is the optimality guarantee provided by combining the two arguments above. Without any assumption on the statistics, the Gauss-Markov theorem states that the BLUE is given by the solution to the OLS algorithm. Sherman's result for the class of loss functions (1.11) states that the solution of the OLS is the conditional mean. In the Gaussian case the conditional mean is linear, hence it is also the solution of the OLS with constraint that the estimator be linear. Hence the BLUE of the process is optimal, without restriction of linearity on the estimator, if we assume that the statistics are Gaussian.

The need for solving the inverse problem for increasingly complex systems, for which the classical assumptions of linearity of the dynamics and normality of the error terms break, has motivated the development of *suboptimal* sequential estimation algorithms. Suboptimal sequential estimation algorithms can be derived from the Kalman filter using different methods:

1. Deterministic filters: *extended Kalman filter* (EKF) [9], *unscented Kalman filter* (UKF) [129].

2. Stochastic filters: *ensemble Kalman filter* (EnKF) [93], *particle filter* (PF) [163].

Stochastic methods consider propagating the state through the nonlinear model using a sample representation. *Deterministic methods* consist in propagating analytical approximations of low order moments through the model. Stochastic methods in general require sampling schemes and pseudo-random generators for the correct execution of the filters, unlike deterministic methods.

For traffic applications, it is also important to mention the *mixture Kalman filter* (MKF) [51], which provides optimality guarantees for *conditionally linear* systems. In this dissertation, we analyze the error structure resulting from the propagation of uncertainty in the initial condition of a Cauchy problem and assess the performances of the EKF and EnKF for realistic scalar traffic models.

1.4 Contributions and organization of the dissertation

1.4.1 Contributions

The contributions of this dissertation encompass the theory of hyperbolic conservation laws for traffic estimation and control. They include contributions to mathematical modeling, theory of partial differential equations, numerical analysis, control theory, filtering, and data analysis.

Phase transition traffic flow model [31, 32].

- Definition of a phase transition traffic flow model as a perturbation of the classical *Lighthill-Whitham-Richards* scalar traffic flow model.
- Well-posedness constraints on the classical fundamental diagram for instantiations on the well-known Newell-Daganzo, Greenshield, Li fundamental diagrams.
- Construction of a Riemann solver in the case of a Newell-Daganzo, Greenshield, Li fundamental diagram.

Analysis of complex traffic phenomena [30, 23].

- Investigation of the existence of complex macroscopic traffic phenomena in high resolution data.
- Implementation of a modified Godunov scheme able to account for non-convexity of model state space in the phase transition model.
- Comparison of time-space diagram reconstruction performance for phase transition model and scalar traffic models.

Error propagation in filtering algorithms [25].

- Construction of the solution to a Riemann problem with random initial datum.
- Analysis of uncertainty structure arising in the solution to the Riemann problem with random initial datum.
- Quantification of error propagation resulting from non differentiability of Godunov discrete time dynamics at the location of stationary shock waves.

Boundary stabilization of entropic solutions to scalar conservation laws [27, 28].

- Approximation of a solution to a scalar conservation law by a piecewise differentiable solution in the case of a traffic model.
- Differentiation of Lyapunov function candidate for an entropic solution to the initial boundary value problem associated with a scalar conservation law.
- Design of weak boundary conditions that maximize the decrease of the Lyapunov function candidate.

1.4.2 Additional contributions

Along with the main contributions outlined in the previous subsection, several independent and related research endeavors led to significant results, presented in associated dissertation works.

Velocity formulation for scalar hyperbolic conservation laws [227].

- Derivation of a velocity PDE (v-PDE) for scalar conservation laws.
- Proof of equivalence of the weak entropy solution to the v-PDE with the weak entropy solution to the corresponding LWR PDE for the Greenshields flux function.
- Design of a numerical scheme derived from the Godunov scheme, for the velocity formulation.
- Real-time data assimilation with the v-PDE and traffic data on the Bay Area transportation network.

Stochastic routing algorithm for on-time arrival problem [191, 35].

- Design of a routing algorithm based on the Fast Fourier Transform for fast computation of the solution to the on-time arrival problem.
- Definition of an optimal order for computing the policy and experimental results of the order of magnitude computation time gain.
- Extensions to time-varying and correlated link travel-time distributions case.
- iPhone app design and deployment of the routing algorithm on the Bay Area transportation network.

Additional contributions include:

- Numerical analysis results for the LWR equation [24].
- Data analysis of radar measurements and identification of experimental relation between speed variance and traffic flow [29].
- Forecast algorithms for distributed systems based on kernel methods in a convex optimization framework [26] and using Bayesian networks [192].
- Deployment of the *Mobile Millennium Stockholm* [2].

1.4.3 Organization of the dissertation

The dissertation is organized as follows.

Chapter 2 presents a novel 2×2 phase transition model introduced in this dissertation. The original phase transition model is presented, as well as its limitations for traffic modeling. A new perspective on the derivation of the phase transition model as a perturbation of classical macroscopic traffic model resulting from heterogeneous driving behavior is proposed, and constraints required for the well-posedness of the system of partial differential equations are derived. The model is instantiated on several well-known traffic models, and a Riemann solver is constructed in each case.

Chapter 3 presents an analysis of the performance of the phase transition model for the construction of spatio-temporal traffic patterns using high-resolution field data. Physical interpretations of the nature of the waves introduced by the model are proposed, discussed, and critically assessed in the light of experimental observations. An itemized implementation of a modified Godunov scheme is proposed.

Chapter 4 consists of a review of novel estimation methods proposed in this work for distributed parameter systems. The framework of Bayesian networks, which allows the computationally efficient modeling of non-independence structure of joint random variables, is presented and the specific assumptions made for traffic models are described, as well as numerical results for a Bay Area stretch of road. Finally, a novel technique for convex identification of optimal state space representation using kernel methods is described.

Chapter 5 presents an analytical and numerical study of the structure of the true uncertainty associated with the propagation of uncertainty on the initial condition of an initial boundary value problem associated with a scalar hyperbolic conservation law. A solution to the Riemann problem with stochastic datum is proposed in the case of a shock wave, and the mixture nature of the resulting random field is shown. The consequence of the non-linearity of the flow of the PDE is assessed numerically on several benchmark estimation tests using the EKF and the EnKF on scenarios relevant for traffic. The non-differentiability of the Godunov scheme at the location of stationary shock waves is shown, and the consequence on the accuracy of the estimates produced by the EKF is assessed on a test case.

Chapter 6 proposes the approximation of BV solutions to scalar conservation laws by piecewise differentiable solutions, and presents a differentiation of an associated Lyapunov function candidate. A greedy controller is derived semi-analytically at each boundary. The controller accounts for weak boundary conditions while maximizing the decrease rate of the Lyapunov function candidate.

Section 7 summarizes the contributions of this dissertation work, and describes novel research tracks opened by the results obtained.

Chapter 2

A general phase transition model for vehicular traffic

In this chapter, we present a novel 2×2 hyperbolic system of conservation laws for macroscopic traffic modeling. The use of non-scalar macroscopic models of traffic flow has been motivated by experimental data suggesting the existence of complex traffic phenomena that could not be modeled using a scalar represention. The model introduced in this chapter is shown to not exhibit most of the issues existing in most of the so-called *higher-order* models of traffic flow available today, such as vanishing velocities below jam density, which is not a classical assumption in traffic theory [98].

The *phase transition model* introduced in this chapter extends the work of Colombo [62]. In agreement with the remarks from Kerner [134, 135] affirming that traffic flow presents three different behaviors, *free-flow*, *wide moving jams*, and *synchronized flow*, Colombo proposed a 2×2 phase transition model [61, 62] which considers *congestion* and *free-flow* in traffic as two different phases, governed by distinct evolutionary laws (see also [102] for a phase transition version of the Aw-Rascle model). The well-posedness of this model was proved in [63] using *wavefront tracking* techniques [39, 117]. In the phase transition model, the evolution of the parameters is governed by two distinct dynamics; in *free-flow*, the Colombo phase transition model is a classical first order model (LWR PDE), whereas in *congestion* a similar equation governs the evolution of an additional state variable, the *linearized momentum* q. The motivation for an extension of the 2×2 phase transition model comes from the following items, which are addressed by the class of models presented in this chapter:

i *Phases gap.* The phase transition model introduced by Colombo in [61] uses a Greenshields flux function to describe *free-flow*, which despite its simple analytical expression yields a fundamental diagram which is not connected and thus a complex definition of the solution to the Riemann problem between two different phases. We solve this problem by introducing a Newell-Daganzo flux function for *free-flow*, which creates a non-empty intersection between the congested phase and the *free-flow* phase, called *metastable phase.* It alleviates the inconvenience of having to use a shock-like phase transition in many cases of the Riemann problem between two different phases.

ii *Definition of a general class of set-valued fundamental diagrams.* The work presented in [62] enables the definition of a set-valued fundamental diagram for the expression of the velocity function introduced. However, experimental data shows that several types of fundamental diagrams exist, with different congested domain shapes. Here, we provide a method to build an arbitrary set-valued fundamental diagram which in a special case corresponds to the fundamental diagram introduced in [61]. This enables us to define a custom-made set-valued fundamental diagram.

This chapter is organized as follows. Section 2.1 presents the fundamental features of the Colombo phase transition model [62], which serves as the basis for the present work. In Section 2.2, we introduce the modifications to the Colombo phase transition model, and introduce the notion of *standard state* which provides the basis for the construction of a class of 2×2 traffic models. We also assess general conditions which enable us to extend the results obtained for the original Colombo phase transition model to these new models. Finally, this section presents a modified *Godunov scheme* which can be used to solve the equations numerically. The two following sections instantiate the constructed class of models for two specific flux functions, which are the Newell-Daganzo (affine) flux function (Section 2.3) and the Greenshields (parabolic concave) flux function (Section 2.4). Each of these sections includes a discussion of the choice of parameters needed for each of the models, the solution to the Riemann problem, a description of the specific properties of the model, and a validation of the numerical results using a benchmark test.

2.1 The Colombo phase transition model

The original Colombo phase transition model [61, 62] is a set of two coupled PDEs respectively valid in a *free-flow* regime and *congested* regime:

$$\begin{cases} \partial_t \rho + \partial_x(\rho\, v_f(\rho)) = 0 & \text{in free-flow } (\Omega_f) \\ \begin{cases} \partial_t \rho + \partial_x(\rho\, v_c(\rho, q)) = 0 \\ \partial_t q + \partial_x((q - q^*)\, v_c(\rho, q)) = 0 \end{cases} & \text{in congestion } (\Omega_c) \end{cases} \tag{2.1}$$

where the state variables ρ and q denote respectively the density and the *linearized momentum* [62]. Ω_f and Ω_c are the respective domains of validity of the free-flow and congested equations of the model and are explicited below. The term q^* is a characteristic parameter of the road under consideration. An empirical relation expresses the velocity v as a function of density in free-flow: $v := v_f(\rho)$, and as a function of density and linearized momentum in congestion: $v := v_c(\rho, q)$. Following usual choices for traffic applications [97], the functions below are used:

$$v_f(\rho) = \left(1 - \frac{\rho}{R}\right) V \quad \text{and} \quad v_c(\rho, q) = \left(1 - \frac{\rho}{R}\right) \frac{q}{\rho}$$

where R is the maximal density or *jam density* and V is the maximal *free-flow speed*. The relation for free-flow is the *Greenshields* model [107] mentioned earlier while the second relation has been introduced in [61]. Since Ω_c has to be an invariant domain [198] for the congested dynamics from system (2.1), and according to the definition of v, the free-flow and congested domains are defined as follows:

$$\begin{cases} \Omega_f = \{(\rho, q) \in [0, R] \times [0, +\infty[\ , v_f(\rho) \geq V_{f-} \ , \ q = \rho V\} \\ \Omega_c = \left\{(\rho, q) \in [0, R] \times [0, +\infty[\ , v_c(\rho, q) \leq V_{c+} \ , \ \frac{Q^- - q^*}{R} \leq \frac{q - q^*}{\rho} \leq \frac{Q^+ - q^*}{R}\right\} \end{cases}$$

where V_{f-} is the minimal velocity in free-flow and V_{c+} is the maximal velocity in congestion such that $V_{c+} < V_{f-} < V$. R is the maximal density and Q^- and Q^+ are respectively the minimal and maximal values for q. The fundamental diagram in (ρ, q) coordinates and in $(\rho, \rho v)$ coordinates is presented in Figure 2.1.

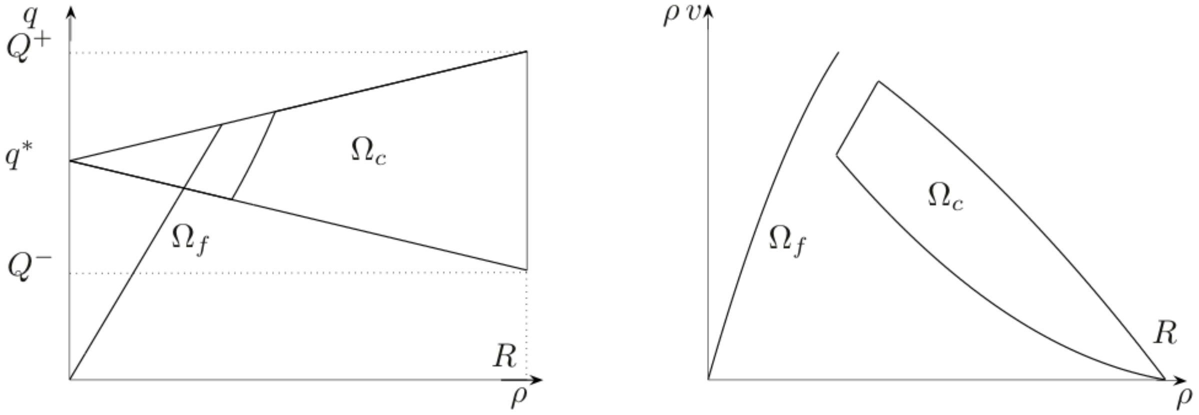

Figure 2.1: Colombo phase transition model.
Left: Fundamental diagram in state space coordinates (ρ, q). Right: Fundamental diagram in density flux coordinates $(\rho, \rho v)$.

Remark 2.1. The congested part of system (2.1) is strictly hyperbolic if and only if the two eigenvalues of its Jacobian are real and distinct for all states $(\rho, q) \in \Omega_c$.

Remark 2.2. The 1-Lax curves are straight lines going through $(0, q^*)$ in (ρ, q) coordinates which means that along these curves shocks and rarefactions exist and coincide [210]. One must note that the 1-Lax field is not *genuinely non-linear* (GNL). Indeed the 1-Lax curves are *linearly degenerate* (LD) for $q = q^*$ and GNL otherwise with rarefaction waves propagating in different directions relatively to the eigenvectors depending on the sign of $q - q^*$. The 2-Lax curves, which are straight lines going through the origin in $(\rho, \rho v)$ coordinates, are always LD.

2.2 Extension of the Colombo phase transition model

The approach developed by Colombo provides a fundamental diagram which is thick in congestion (Figure 2.1), and thus can model clouds of points observed experimentally (Figure 2.2). We propose to extend this approach by considering the second equation in congestion as modeling a perturbation [230, 233]. The *standard state* (Definition 2.1) would be the usual one-dimensional fundamental diagram, with dynamics described by the conservation of mass. Perturbations can move the system off standard state, leading the diagram to span a two-dimensional area in congestion. A single-valued map is able to describe the free-flow mode, which is therefore completely described by the free-flow standard state.

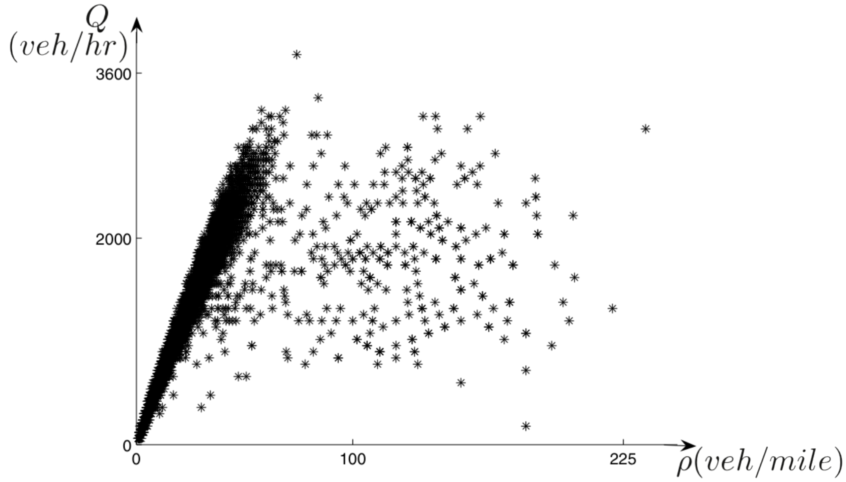

Figure 2.2: Fundamental diagram in density flux coordinates from a street in Rome.
In congestion (high densities) the flux is multi-valued. Count C and velocity v were recorded every minute during one week. Flux Q was computed from the count. Density ρ was computed from flux and velocity according to the expression $Q = \rho v$ (see [24] for an extensive analysis of this dataset).

Definition 2.1. *We call standard state the set of states described by a one dimensional fundamental diagram and the classical LWR PDE. In the following we respectively refer to the standard velocity and standard flux as the velocity and flux at the standard state.*

In this section we present analytical requirements on the velocity function in congestion which, given the work done in [62], enable us to construct a 2×2 phase transition model. These models provide support for a physically correct, mathematically well-posed initial-boundary value problem which can model traffic phenomena where the density and the flow are independent quantities in congestion, allowing for multiple values of the flow for a given value of the density. Our framework allows the definition of the two dimensional zone span by the congestion phase according to the reality of the local traffic nature, which is not always possible with the original Colombo phase transition model.

2.2.1 Analysis of the standard state

We consider the density variable ρ to belong to the interval $[0, R]$ where R is the maximal density. Given the *critical density*[1] σ in $(0, R]$, we define the standard velocity $v^s(\cdot)$ on $[0, R]$ by:

$$v^s(\rho) := \begin{cases} V & \text{for } \rho \in [0, \sigma] \\ v^s_c(\rho) & \text{for } \rho \in [\sigma, R] \end{cases}$$

where V is the free-flow speed and $v^s_c(\cdot)$ is in $C^\infty((\sigma, R), \mathbb{R}^+)$. It is important to note that $v^s_c(\cdot)$ is a function of ρ only, as it is the case for the classical fundamental diagram. The standard flux $Q^s(\cdot)$ is thus defined on $[0, R]$ by:

$$Q^s(\rho) := \rho\, v^s(\rho) = \begin{cases} Q_f(\rho) := \rho\, V & \text{for } \rho \in [0, \sigma] \\ Q^s_c(\rho) := \rho\, v^s_c(\rho) & \text{for } \rho \in [\sigma, R]. \end{cases}$$

In agreement with traffic flow features, the congested standard flux $Q^s_c(\rho)$ must satisfy the following requirements (which are consistent with the ones given in [77]).

i *Flux vanishes at the maximal density*: $Q^s_c(R) = 0$.
This condition encodes the physical situation in which the jam density has been reached. The corresponding velocity and flux of vehicles on the highway is zero.

ii *Flux is a decreasing function of density in congestion*: $dQ^s_c(\rho)/d\rho \leq 0$.
This is required as a defining property of congestion. It implies that $dv^s_c(\rho)/d\rho \leq 0$.

iii *Continuity of the flux at the critical density*: $Q^s_c(\sigma) = Q_f(\sigma)$.
Even if some models account for a discontinuous flux at capacity, the *capacity drop* phenomenon [135], we assume, following most of the transportation community, that the flux at the standard state is a continuous function of density.

iv *Concavity of the flux in congestion*: $Q^s_c(\cdot)$.
The flux function at the standard state $Q^s_c(\cdot)$ must be concave on $[\sigma, \sigma_i]$ and convex on $[\sigma_i, R]$ where σ_i is in $(\sigma, R]$. Given the experimental datasets obtained for congestion (Figure 2.2), it is not clear in practice if the standard flux is concave or convex in congestion. The assumption made here is motivated in Remark 2.8.

Remark 2.3. In this chapter we instantiate the general model proposed on the most common standard flux functions, i.e. linear or concave, but the framework developed here applies to flux functions with changing concavity such as the Li flux function [158], although it yields a significantly more complex analysis.

---

[1] Density for which the flux is maximal at the standard state. At this density the system switches between free-flow and congestion.

2.2.2 Analysis of the perturbation

Model outline

In this section we introduce a perturbation q to the standard velocity in congestion.

Definition 2.2. *The perturbed velocity function $v_c(\cdot,\cdot)$ is defined on Ω_c by:*

$$v_c(\rho,q) = v_c^s(\rho)\,(1+q) \tag{2.2}$$

where $v_c^s(\cdot) \in C^\infty((\sigma_-,R),\mathbb{R}^+)$ is the congested standard velocity function.

The standard state corresponds to $q=0$, and the evolution of (ρ,q) is described similarly to the classical Colombo phase transition model [62] by:

$$\begin{cases} \partial_t\rho + \partial_x(\rho\, v) = 0 & \text{in free-flow} \\ \begin{cases} \partial_t\rho + \partial_x(\rho\, v) = 0 \\ \partial_t q + \partial_x(q\, v) = 0 \end{cases} & \text{in congestion} \end{cases} \tag{2.3}$$

with the following expression of the velocity:

$$v = \begin{cases} v_f(\rho) := V & \text{in free-flow} \\ v_c(\rho,q) & \text{in congestion.} \end{cases} \tag{2.4}$$

The perturbed velocity function defines the velocity in congestion whereas a Newell-Daganzo function describes the velocity in free-flow. The analytical expression of the free-flow and congested domains as explicited in (2.5) is motivated by the analysis conducted in Table 2.1 and the necessity for these domains to be invariants [198] for the dynamics (2.3) in order to have a well-defined Riemann solver [212].

$$\begin{cases} \Omega_f = \{(\rho,q)\mid(\rho,q)\in[0,R]\times[0,+\infty[\ \ ,v_c(\rho,q)=V\ \ ,\ 0\le\rho\le\sigma_+\} \\ \Omega_c = \left\{(\rho,q)\mid(\rho,q)\in[0,R]\times[0,+\infty[\ \ ,v_c(\rho,q)<V\ \ ,\ \frac{q_-}{R}\le\frac{q}{\rho}\le\frac{q_+}{R}\right\} \end{cases} \tag{2.5}$$

$\sigma_\pm$ is defined by $v_c(\sigma_\pm,\sigma_\pm\, q_\pm/R)=V$ and we assume that $V>0$ and $q_-\le 0\le q_+$. A definition of the complete set of parameters can be found in Section 2.2.3 (See also Figure 2.3 for an illustration in the Newell-Daganzo case.).

Definition 2.3. *The set $\{(\rho,q)\mid v_c(\rho,q)=V,\ \ \sigma_-\le\rho\le\sigma_+\}$ defines the meta- -stable phase. This phase defines transition states between the congestion phase and the free-flow phase.*

Remark 2.4. The left boundary of the congested domain is a convex curve in (ρ,q) coordinates (in Figure 2.1 for the Colombo phase transition model as in Figure 2.3 for the new model derived). Thus Ω_c is not convex in (ρ,q) coordinates.

The analysis of the congestion phase of the model (2.3) is outlined in Table 2.1.

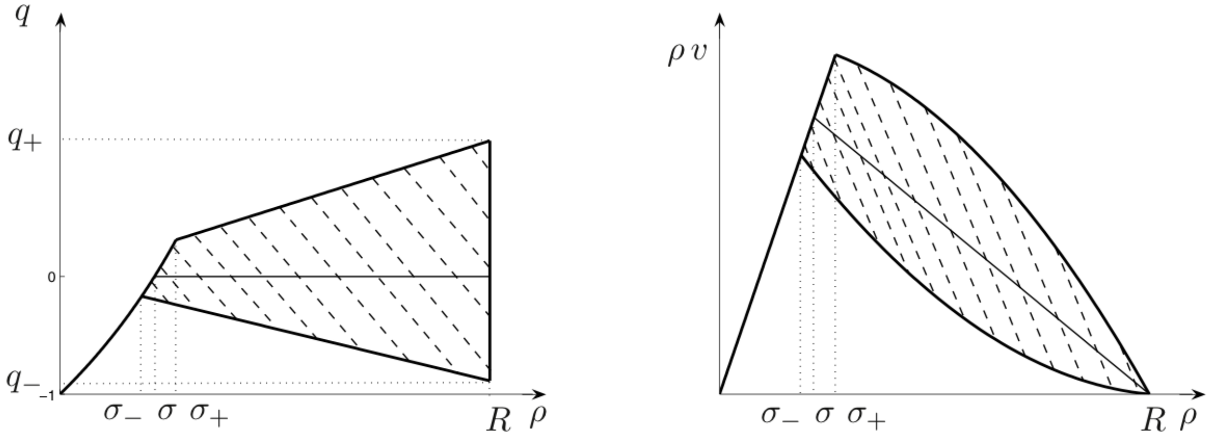

Figure 2.3: Newell-Daganzo standard flux function.
Left: Fundamental diagram in state space coordinates. Right: Fundamental diagram in flux-density coordinates. The standard state is the usual triangular diagram. The congestion phase is two-dimensional (striped domain).

Physical and mathematical considerations

Physical interpretation and mathematical conditions translate into the following conditions:

Condition 2.1. ***Positivity of speed.*** *In order to maintain positivity of $v_c(\cdot,\cdot)$ on the congested domain, one must have:*

$$\forall\, q \in [q_-, q_+] \quad 1 + q > 0 \tag{2.6}$$

which is satisfied if and only if $q_- > -1$.

Condition 2.2. ***Strict hyperbolicity of the congested system.*** *In order for the congested part of (2.3) to be strictly hyperbolic, one must have:*

$$\forall\, (\rho, q) \in \Omega_c \quad \lambda_1(\rho, q), \lambda_2(\rho, q) \in \mathbb{R} \;\; \text{and} \;\; \lambda_1(\rho, q) \neq \lambda_2(\rho, q).$$

Given the expression of the eigenvalues outlined in Table 2.1, and modulo a rearrangement, this yields:

$$\forall\, (\rho, q) \in \Omega_c \quad \rho\, \partial_\rho v_c^s(\rho) + q\, (v_c^s(\rho) + \rho\, \partial_\rho v_c^s(\rho)) \neq 0. \tag{2.7}$$

Since $v_c^s(\cdot)$ is positive and $\rho\, v_c^s(\cdot)$ is a decreasing function of ρ, this can always be satisfied for small enough values of q, and when instantiated for specific expressions of $v_c^s(\cdot)$, will result in a bound on the perturbation q.

Eigenvalues	$\lambda_1(\rho, q) = \rho\,(1+q)\partial_\rho v_c^s(\rho) + v_c^s(\rho)\,(1+2\,q)$	$\lambda_2(\rho, q) = v_c^s(\rho)\,(1+q)$
Eigenvectors	$r_1 = \begin{pmatrix} \rho \\ q \end{pmatrix}$	$r_2 = \begin{pmatrix} v_c^s(\rho) \\ -(1+q)\,\partial_\rho v_c^s(\rho) \end{pmatrix}$
Nature of the Lax curves	$\nabla\lambda_1.r_1 = \rho^2\,(1+q)\partial^2_{\rho\rho} v_c^s(\rho) + 2\,\rho\,(1+2\,q)\,\partial_\rho v_c^s(\rho) + 2\,q\,v_c^s(\rho)$	$\nabla\lambda_2.r_2 = 0$
Riemann-invariants	q/ρ	$v_c^s(\rho)\,(1+q)$

Table 2.1: Congestion phase.
Algebraic properties of the general phase transition model.

Condition 2.3. ***Shape of Lax curves***. *For modeling consistency, we require the* 1*-Lax curves to be LD or to have no more than one inflexion point* (σ_i, q_i)*. In the latter case they should be concave for* $\rho \leq \sigma_i$ *and convex for* $\rho \geq \sigma_i$*. Since* $\nabla\lambda_1.r_1$ *is the second derivative of the* 1*-Lax curve with respect to* ρ*, this condition can be enforced, for any* (ρ, q) *in the congested domain, by checking the sign of the expression:*

$$\nabla\lambda_1.r_1 = \rho\,(2\,\partial_\rho v_c^s(\rho) + \rho\,\partial^2_{\rho\rho} v_c^s(\rho)) + q\,(2\,v_c^s + 4\,\rho\,\partial_\rho v_c^s(\rho) + \rho^2\,\partial^2_{\rho\rho} v_c^s(\rho)) \tag{2.8}$$

which has the sign of the first term for q *small enough. So if* $2\,\partial_\rho v_c^s(\rho) + \rho\,\partial^2_{\rho\rho} v_c^s(\rho) > 0$ *the rarefaction waves go right in the* (ρ, q) *or* $(\rho, \rho\,v)$ *plane. When* $v_c^s(\cdot)$ *is such that* $2\,\partial_\rho v_c^s(\rho) + \rho\,\partial^2_{\rho\rho} v_c^s(\rho) = 0$ *the heading of rarefaction waves changes with the sign of* q *(it is the case for the original phase transition model), and in this case the* 1*-curves are LD for* $q = 0$*.*
This condition consists in ensuring that expression (2.8) *is either identically zero (LD curve), or has no more than one zero and is an increasing function of the density.*

Remark 2.5. One may note that condition 2.2 on the strict hyperbolicity of the system is satisfied whenever condition 2.1 on the positivity of speed is satisfied. Indeed equation (2.7) can be re-written as $\forall(\rho, q) \in \Omega_c \quad \rho\,\partial_\rho v_c^s(\rho) + q\partial_\rho Q_c^s(\rho) \neq 0$, which since the first term is negative, is equivalent to $\forall(\rho, q) \in \Omega_c \quad \rho\,\partial_\rho v_c^s(\rho) + q\partial_\rho Q_c^s(\rho) < 0$. For non-zero values of $\partial_\rho Q_c^s(\rho)$, it yields $q > -\rho\,\partial_\rho v_c^s(\rho)/\partial_\rho Q_c^s(\rho) = -1 + v_c^s(\rho)/\partial_\rho Q_c^s(\rho)$ which is always satisfied when $q_- > -1$, because the second term of the right hand side is negative.

Remark 2.6. In this model, traffic is anisotropic in the sense that no wave travels faster than vehicles ($\lambda_1(\rho, q) < \lambda_2(\rho, q) = v_c(\rho, q)$). The speed of vehicles is always positive and they stop only at maximal density.

2.2.3 Definition of parameters

Several parameters are used in the proposed model, which we summarize below:

i The free-flow speed V.

ii The maximal density R.

iii The critical density σ at standard state.

iv The critical density for the lower bound of the diagram σ_-.

v The critical density for the upper bound of the diagram σ_+.

These parameters can be identified from experimental data, and enable the definition of the parameters q_- and q_+. Figure 2.3 graphically summarizes the definition of the parameters chosen. One must note that the constraints on q_-, q_+ detailed in (2.6)-(2.7)-(2.8) translate into constraints on σ_-, σ_+, which cannot be freely chosen.

2.2.4 Cauchy problem

In this section we define a solution to the Cauchy problem for the system (2.3). Following [62], we use a definition derived from [39].

Definition 2.4. *Given T in $\mathbb{R}_+$, u_0 in $L^1(\mathbb{R};\Omega_f \cup \Omega_c) \cap BV(\mathbb{R};\Omega_f \cup \Omega_c)$, an admissible solution to the corresponding Cauchy problem for (2.3) is a function $u(\cdot,\cdot)$ in $L^1([0,T] \times \mathbb{R};\Omega_f \cup \Omega_c) \cap BV([0,T] \times \mathbb{R};\Omega_f \cup \Omega_c)$ such that the following holds.*

i For all t in $[0,T]$, $t \mapsto u(t,.)$ is Lipshitz continuous with respect to the L^1 norm.

ii For all functions φ in $C_c^1([0,T] \times \mathbb{R} \mapsto \mathbb{R})$ with compact support contained in $u^{-1}(\Omega_f)$:

$$\int_0^T \int_{\mathbb{R}} (u(t,x)\,\partial_t\varphi(t,x) + Q_f(u(t,x))\partial_x\varphi(t,x))\,dxdt + \int_{\mathbb{R}} u_0(x)\,\varphi(0,x)dx = 0.$$

iii For all functions φ in $C_c^1([0,T] \times \mathbb{R} \mapsto \mathbb{R}^2)$ with compact support contained in $u^{-1}(\Omega_c)$:

$$\int_0^T \int_{\mathbb{R}} (u(t,x)\,\partial_t\varphi(t,x) + Q_c(u(t,x))\partial_x\varphi(t,x))\,dxdt + \int_{\mathbb{R}} u_0(x)\,\varphi(0,x)dx = 0.$$

iv The set of points (t,x) for which there is a change of phase is the union of a finite number of Lipschitz curves $p_i : [0,T) \mapsto \mathbb{R}$ such that if $\exists i \neq j$ and $\exists \tau \in [0,T]$ such that $p_i(\tau) = p_j(\tau)$ then $\forall t \in [\tau,T]$ we have $p_i(t) = p_j(t)$.

v For all points (t,x) where there is a change of phase, let $\Lambda = \dot{p}_i(t^+)$, and introducing the left and right flow at (t,x):

$$F^l = \begin{cases} \rho(t,x^-)\,V & \text{if } \rho(t,x^-) \in \Omega_f \\ \rho(t,x^-)\,v_c(\rho(t,x^-),q(t,x^-)) & \text{if } \rho(t,x^-) \in \Omega_c \end{cases}$$

$$F^r = \begin{cases} \rho(t,x^+)\, V & \text{if } \rho(t,x^+) \in \Omega_f \\ \rho(t,x^+)\, v_c(\rho(t,x^+), q(t,x^+)) & \text{if } \rho(t,x^+) \in \Omega_c \end{cases}$$

the following relation must be satisfied:

$$\Lambda \cdot (\rho(t,x_+) - \rho(t,x_-)) = F_r - F_l. \tag{2.9}$$

Remark 2.7. This definition matches the standard Lax entropy solution for an initial condition with values in Ω_f or Ω_c. Equation (2.9) is a Rankine-Hugoniot relation needed to ensure mass conservation at the phase transition.

Theorem 2.1. *Let Ω_f and Ω_c be defined by* (2.5)*, $v_c(\cdot,\cdot)$ be defined by* (2.2)*. If condition 2.2 is satisfied, then for all $u_0 \in L^1(\mathbb{R};\Omega_f \cup \Omega_c) \cap BV(\mathbb{R};\Omega_f \cup \Omega_c)$ the corresponding Cauchy problem for* (2.3) *has an admissible solution, (see definition 2.4) $u(\cdot,\cdot)$ such that $u(t,\cdot) \in BV(\mathbb{R};\Omega_f \cup \Omega_c)$ for all $t \in [0,T]$.*

Proof. A solution is constructed through a standard wavefront tracking procedure by iteratively gluing together the solution to Riemann problems corresponding to piecewise constant approximations of the solution. Measuring total variation along the trajectories of these solutions leads to a conclusion on the convergence of the sequence of successive approximations. The interested reader is referred to [39] for more details on wavefront tracking techniques and to [62, 63] for more insights on proofs of existence for systems of conservation laws with phase transition. □

2.2.5 Model properties

The main differences between the original Colombo model [62] and the class of models introduced in this chapter result from the following design choices:

Choice of $q^* = 0$.

This is a change of variable which has several consequences. Related computations are more readable. The congested standard state is $q = 0$. According to (2.2), the meaning of the perturbation q is also more intuitive. Positive values of q correspond to elements of flow moving at a greater speed than the standard speed for this density, and negative values of q correspond to slower elements of flow. In the traffic context, this can be understood as groups of driver characterized by their degree of agressivity, q, which leads them to drive faster or slower than the standard driver.

Newell-Daganzo flux function in free-flow.

This feature leads to connected free-flow and congested domains for the fundamental diagram proposed in the present work, and the definition of a metastable phase, as illustrated in Figure 2.4. This yields a well-posed Riemann problem which can be solved in a simple way (see Remark 2 of [62]). Moreover, the derived models need less parameters and thus are easier to calibrate. Finally, it is consistent with the fact that a gap between phases is not observed in experimental data, see Figure 2.2.

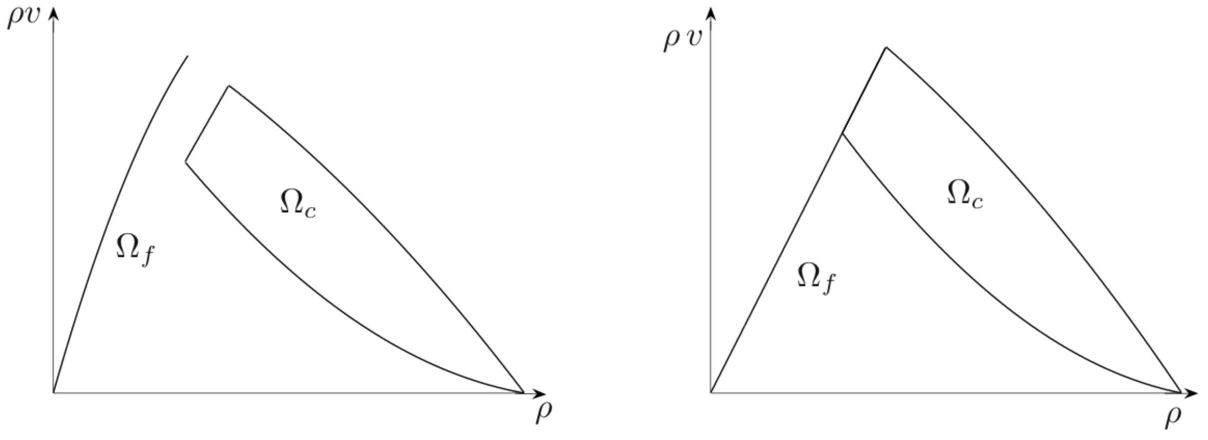

Figure 2.4: Different free-flow phases.
Left: Fundamental diagram from the original Colombo phase transition model. Right: Fundamental diagram of the model derived in this chapter in the particular case of a Newell-Daganzo standard state flux in the congestion phase.

The expression of the function v_c is not fully specified.
This allows us to customize the model depending on the features observed in practice. As explained in Remark 2.8 below, the concavity of the 1-Lax curves is related to driving behavior. In the class of models we introduce, since $v_c(\cdot,\cdot)$ is not fully specified, in the limit of conditions 2.1-2.2-2.3, it is possible to define the perturbed phase transition model which corresponds to the observed driver agressivity.

Remark 2.8. A physical interpretation can be given to the concavity of the flux function. In congestion, when the density increases toward the maximal density, the velocity decreases toward zero. This yields a decreasing slope of the flux function in congestion. The way in which drivers velocity decreases impacts the concavity of the flux, as per the expression of the second derivative of the standard flux function, $d^2Q_c^s(\rho)/d\rho^2 = \rho\, d^2v_c^s(\rho)/d\rho^2 + 2\, dv_c^s(\rho)/d\rho$.

i If for a given density increase, the drivers reduce their speeds more at high densities than at low densities (modeling aggressive drivers who wait until high density to reduce speed), then the velocity function is concave and the flux function is concave.

ii If the drivers reduce their speeds less at high densities than at low densities (modeling careful drivers who anticipate and reduce their speed early), then the velocity function is convex, and the flux function may be convex.

iii An affine flux is given by a velocity function which satisfies $\rho\, d^2v_c^s(\rho)/d\rho^2 + 2\, dv_c^s(\rho)/d\rho = 0$.

2.2.6 Numerics

Because of the non-convexity of the domain $\Omega_f \cup \Omega_c$ (illustrated in Figure 2.3), using the classical Godunov scheme [156] is not feasible due to the projection step of the scheme. We propose to use a modified version of the scheme (see [49]) which mimics the two steps of the classical Godunov scheme and adds a final sampling step.

i The Riemann problems are solved on a regular time space mesh. When two space-consecutive cells do not belong to the same phase, the position of the phase transition at the next time step is computed.

ii The solutions are averaged on the domains defined by the position of the phase transitions arising from Riemann problems at neighboring cells (Figure 2.5).

iii A sampling method is used to determine the value of the solution in each cell of the regular mesh.

This process answers the issues of the classical Godunov scheme with non-convex domains. Numerical results have shown that it gives accurate results on benchmark tests (we refer to [49] for more details on the test cases used).

Let us note Δt the time discretization and Δx the space discretization satisfying the *Courant-Friedrichs-Lewy* (CFL) condition [156]. We call $x_j = j\,\Delta x$ for $j \in \mathbb{Z}$ and $t_n = n\,\Delta t$ for $n \in \mathbb{N}$. We call $x_{j-1/2} = x_j - \Delta x/2$ and we define a cell $C_j^n = \{t_n\} \times [x_{j-1/2}, x_{j+1/2}[$ which has a length Δx. We call u_j^n the value of $u := (\rho, q)$ at (t_n, x_j), and, by extension, in C_j^n. The speed of the phase transition between each pair of cells (C_j^n, C_{j+1}^n) is noted $\nu_{j+1/2}^n$ ($\nu_{j+1/2}^n$ equals zero if u_j^n and u_{j+1}^n belongs to the same phase). If we call $\overline{x}_{j-1/2}^{n+1} = x_{j-1/2} + \nu_{j-1/2}^n \Delta t$ we can define cell $\overline{C}_j^{n+1}$ as $\overline{C}_j^{n+1} = \{t^{n+1}\} \times [\overline{x}_{j-1/2}^{n+1}, \overline{x}_{j+1/2}^{n+1}[$ which has a length $\Delta \overline{x}_j^n = \overline{x}_{j+1/2}^{n+1} - \overline{x}_{j-1/2}^{n+1}$, as shown in Figure 2.5. The solution to the Riemann problem between cells C_j^n is averaged on cells $\overline{C}_j^{n+1}$, which by construction enclose states which are either free-flowing or congested, according to the modified Godunov scheme. We define:

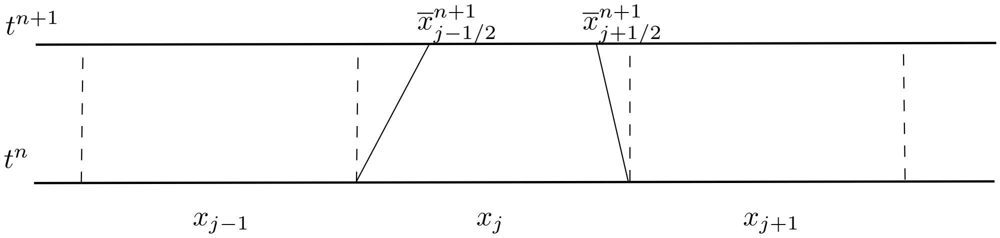

Figure 2.5: Phase transitions.
The phase transitions enter cell C_j^n from both sides.

i $u_R(\nu^{n,+}_{j-1/2}, u^n_{j-1}, u^n_j)$ as the solution to the Riemann problem between u^n_{j-1} and u^n_j, at $\frac{x-x_{j-1/2}}{t-t^n} = \nu^n_{j-1/2}$, and calculated at the right of the cell boundary.

ii $g\left(\nu^{n,-}_{j+1/2}, u^n_j, u^n_{j+1}\right) := f(u_R(\nu^{n,-}_{j+1/2}, u^n_j, u^n_{j+1}))$ with $f(\rho, q) = (\rho\, v, q\, v)$ and the definition of v from (2.4), as the numerical flux between cells C^n_j and C^n_{j+1}, at $\frac{x-x_{j+1/2}}{t-t^n} = \nu^n_{j+1/2}$, and calculated at the left of the cell boundary.

The averaging step of the modified Godunov scheme reads:

$$\begin{aligned}\Delta\overline{x}^n_j\, \overline{u}^{n+1}_j = \Delta x\, u^n_j - \Delta t\, &\left(g\left(\nu^{n,-}_{j+1/2}, u^n_j, u^n_{j+1}\right) - \nu^n_{j+1/2}\, u_R\left(\nu^{n,-}_{j+1/2}, u^n_j, u^n_{j+1}\right)\right)\\ +\Delta t\, &\left(g\left(\nu^{n,+}_{j-1/2}, u^n_{j-1}, u^n_j\right) - \nu^n_{j-1/2}\, u_R\left(\nu^{n,+}_{j-1/2}, u^n_{j-1}, u^n_j\right)\right).\end{aligned}$$

One can notice that when there is no phase transition, $\nu^n_{j-1/2} = \nu^n_{j+1/2} = 0$, $\Delta x = \Delta\overline{x}^n_j$ and we obtain the classical Godunov scheme. The last step is the sampling phase to define the solutions on the cells C^{n+1}_j. Following [49], for cell C^{n+1}_j we randomly pick a value between $\overline{u}^{n+1}_{j-1}$, $\overline{u}^{n+1}_j$ and $\overline{u}^{n+1}_{j+1}$ according to their rate of presence in cell C^{n+1}_j. This is done using the Van der Corput sequence $(a_n)_{n\in\mathbb{N}}$ (2.10) which is a low-discrepancy sequence in the interval $[0, 1]$:

$$u^{n+1}_j = \begin{cases}\overline{u}^{n+1}_{j-1} & \text{if } a_n \in]0, \max(\frac{\Delta t}{\Delta\overline{x}^n_j}\, \nu^n_{j-1/2}, 0)]\\ \overline{u}^{n+1}_j & \text{if } a_n \in]\max(\frac{\Delta t}{\Delta\overline{x}^n_j}\, \nu^n_{j-1/2}, 0), 1 + \min(\frac{\Delta t}{\Delta\overline{x}^n_j}\, \nu^n_{j+1/2}, 0)[\\ \overline{u}^{n+1}_{j+1} & \text{if } a_n \in [1 + \min(\frac{\Delta t}{\Delta\overline{x}^n_j}\, \nu^n_{j+1/2}, 0), 1[\end{cases} \tag{2.10}$$

Remark 2.9. In the general case the congested domain Ω_c is not convex in (ρ, q) coordinates due to the convexity of the metastable border of the domain as illustrated on Figure 2.3. It is therefore needed to add a projection step as a fourth step to the modified Godunov scheme. The projection (ρ_p, q_p) of state (ρ, q) is defined as the solution in the metastable phase of the system:

$$\begin{cases}\frac{q_p}{\rho_p} = \frac{q}{\rho}\\ v_c(\rho_p, q_p) = V\end{cases}$$

The error metric chosen to assess the numerical accuracy of the scheme is the $C^0(\mathbb{R}, L^1(\mathbb{R}, \mathbb{R}^2))$ relative error between the computed solution and the analytical solution. We call u and u_c the exact and computed solutions respectively. For the computational domain $[x_0, x_1]$, the error at T is computed as follows:

$$E(T) = \frac{\sup_{t\in[0,T]} \int_{x_0}^{x_1} \|u(t, x) - u_c(t, x)\|_1 dx}{\sup_{t\in[0,T]} \int_{x_0}^{x_1} \|u(t, x)\|_1 dx}.$$

2.3 The Newell-Daganzo phase transition model

In this section, we use a Newell-Daganzo velocity function for congestion, i.e. a velocity function for which the flux is affine with respect to the density. We instantiate the corresponding phase transition model for this flux function and derive a corresponding Riemann solver, which we implement and test on a benchmark case.

2.3.1 Analysis

We propose to use the following standard velocity function:

$$v_c^s(\rho) = \frac{V\,\sigma}{R-\sigma}\left(\frac{R}{\rho}-1\right),$$

which is clearly the unique function yielding an affine flux, and satisfying the requirements from Section 2.2.1, on the vanishing point, trend, continuity and concavity property of the standard flux.

For a perturbed state, the velocity function reads:

$$\begin{cases} v_f(\rho) = V & \text{for } (\rho,q)\in\Omega_f \\ v_c(\rho,q) = \frac{V\,\sigma}{R-\sigma}\left(\frac{R}{\rho}-1\right)(1+q) & \text{for } (\rho,q)\in\Omega_c \end{cases} \tag{2.11}$$

where Ω_f and Ω_c are defined by (2.5). The corresponding fundamental diagram is shown in Figure 2.3. The standard flux is affine with the density, but the 1-Lax curves outside the standard state are either convex or concave in $(\rho, \rho\, v)$ coordinates depending on the sign of the perturbation.

Remark 2.10. Note that the expression of the velocity in Figure 2.3 is given by (2.11), depends on the phase, and is therefore set-valued for $\rho > \sigma_-$ which is the lowest density value at which congestion can arise.

The conditions from Section 2.2.2 to have positive speed and strict hyperbolicity of the congested part of the system (2.3) reduce to:

$$q_- > -1.$$

2.3.2 Solution to the Riemann problem

Following [62],we construct the solution to the Riemann problem for the system (2.3) with the velocity function defined by (2.11) and the initial datum:

$$(\rho,q)(0,x) = \begin{cases} (\rho_l, q_l) & \text{if } x<0 \\ (\rho_r, q_r) & \text{if } x>0. \end{cases}$$

We note u the vector (ρ, q). We define u_m by the solution in Ω_c of the system:

$$\begin{cases} \frac{q_m}{\rho_m} = \frac{q_l}{\rho_l} \\ v_c(u_m) = v_c(u_r) \end{cases} \tag{2.12}$$

which yields a quadratic polynomial in ρ_m. We address the general case where the solution u_m of system (2.12) can coincide with u_l or u_r.

- **Case 1:** $u_l \in \Omega_f$ and $u_r \in \Omega_f$

  For all values of (ρ_l, ρ_r) the solution consists of a contact discontinuity from u_l to u_r.

- **Case 2:** $u_l \in \Omega_c$ and $u_r \in \Omega_c$

  i If $q_l > 0$ and $v_c(u_r) \geq v_c(u_l)$ the solution consists of a 1-rarefaction wave from u_l to u_m and a 2-contact discontinuity from u_m to u_r.

  ii If $q_l > 0$ and $v_c(u_l) > v_c(u_r)$ the solution consists of a shock wave from u_l to u_m and a 2-contact discontinuity from u_m to u_r.

  iii If $q_l = 0$ the solution consists of a 1-contact discontinuity from u_l to u_m and a 2-contact discontinuity from u_m to u_r.

  iv If $0 > q_l$ and $v_c(u_r) > v_c(u_l)$ the solution consists of a shock wave from u_l to u_m and a 2-contact discontinuity from u_m to u_r.

  v If $0 > q_l$ and $v_c(u_l) \geq v_c(u_r)$ the solution consists of a 1-rarefaction wave from u_l to u_m and a 2-contact discontinuity from u_m to u_r.

- **Case 3:** $u_l \in \Omega_c$ and $u_r \in \Omega_f$

  i If $0 > q_l$ the solution consists of a shock wave from u_l to u_m and of a contact-discontinuity from u_m to u_r.

  ii If $q_l = 0$ the solution consists of a 1-contact discontinuity from u_l to u_m and of a contact-discontinuity from u_m to u_r.

  iii If $q_l > 0$ the solution consists of a 1-rarefaction wave from u_l to u_m and of a contact-discontinuity from u_m to u_r.

- **Case 4:** $u_l \in \Omega_f$ and $u_r \in \Omega_c$ Let u_{m-} be defined by the solution in Ω_c of the system:

  $$\begin{cases} \frac{q_{m-}}{\rho_{m-}} = \frac{q_-}{R} \\ v_c(u_{m-}) = v_c(u_r) \end{cases}$$

  and let $\Lambda(u_l, u_{m-})$ be the Rankine-Hugoniot phase transition speed between u_l and u_{m-} defined by equation (2.9).

  i If $\Lambda(u_l, u_{m-}) \geq \lambda_1(u_{m-})$ the solution consists of a phase transition from u_l to u_{m-} and of a 2-contact discontinuity from u_{m-} to u_r.

ii If $\Lambda(u_l, u_{m-}) < \lambda_1(u_{m-})$ let u_p be defined by the solution in Ω_c of the system:

$$\begin{cases} \frac{q_p}{\rho_p} = \frac{q_-}{R} \\ \Lambda(u_l, u_p) = \lambda_1(u_p). \end{cases}$$

The solution consists of a phase transition from u_l to u_p, of a 1-rarefaction wave from u_p to u_{m-}, and of a 2-contact discontinuity from u_{m-} to u_r.

2.3.3 Model properties

The properties of the Newell-Daganzo model can be abstracted from the definition of the Riemann solver in previous Section.

The nature of the Lax curves in congestion is the same for the original Colombo model and the Newell-Daganzo phase transition model (see Figure 2.4). Thus the solution for each model differ only when a free-flow state is involved. Three differences appear in that case:

i For a given density corresponding to the free-flow phase, the associated velocity differ in general between the two models.

ii Within the free-flow phase, only contact discontinuity can arise in the Newell Daganzo phase transition model, whereas rarefaction waves and shockwaves can arise in the original Colombo model.

iii A transition from congestion to free-flow always involves a shock-like phase transition in the Colombo model (and thus the solution is composed of three waves in general), whereas the transition occurs through a metastable state in the Newell-Daganzo phase transition model, and involves only a “congestion to metastable” wave and a “metastable to free-flow” wave.

These properties are illustrated in the next Section on a Riemann problem.
As in the original Colombo phase transition model [62], the 1-Lax curves are LD for $q = 0$, and the direction of the rarefaction waves changes according to the sign of q. This yields interesting modeling capabilities, but requires the Riemann solver to be more complex than the one described in the following Section.

Remark 2.11. As illustrated on Figure 2.3 the flux is linear in congestion at the standard state as per the Newell-Daganzo flux function. Remark 2.8 states that this shape models neutral drivers (aggressivity-wise). When the traffic is above the standard state, meaning that the velocity is higher that what it is for the same density at the standard state, the 1-Lax curves are concave in $(\rho, \rho\, v)$ coordinates, meaning that the drivers are more aggressive. So such a fundamental diagram shape seems to be in accordance with the intuition, that for a given density, the most aggressive drivers tend to have a greater speed. This is symmetrically true for less aggressive drivers, also accounted for by this model.

2.3.4 Benchmark test

In this section we compare the numerical solution given by the modified Godunov scheme with the analytical solution to a Riemann problem. We use the phase transition model (2.3) in the Newell-Daganzo case (2.11) with the following choice of parameters: $V = 45$, $R = 1000$, $\sigma_- = 190$, $\sigma = 220$, $\sigma_+ = 270$. The benchmark test is a phase transition from congestion to free-flow with the following left and right states:

i $u_l = (800, -0.1)$ which corresponds to congestion below standard state with $\rho = 800$ and $v = 2.9$.

ii $u_r = (100)$ which corresponds to a free-flow state with $\rho = 100$ and $v = 45$.

This configuration gives rise to a shock wave between u_l and a congested state u_m followed by a contact discontinuity between u_m and u_r (Riemann case 3, first subcase), as shown in Figure 2.6.

We also present the solution given by the original Colombo model with the following parameters: $V_{c+} = 45$, $V_{f-} = 57$, $V = 67$, $q^* = 0$, $Q^- = -0.88$ and $Q^+ = 1.15$. The congested phases in the two models are identical with this choice of parameters. One may note that because the fundamental diagram in free-flow differs between the original Colombo model and the Newell-Daganzo phase transition model (see Figure 2.4), the speed corresponding to the right initial state in the Riemann problem is greater in the Colombo model.

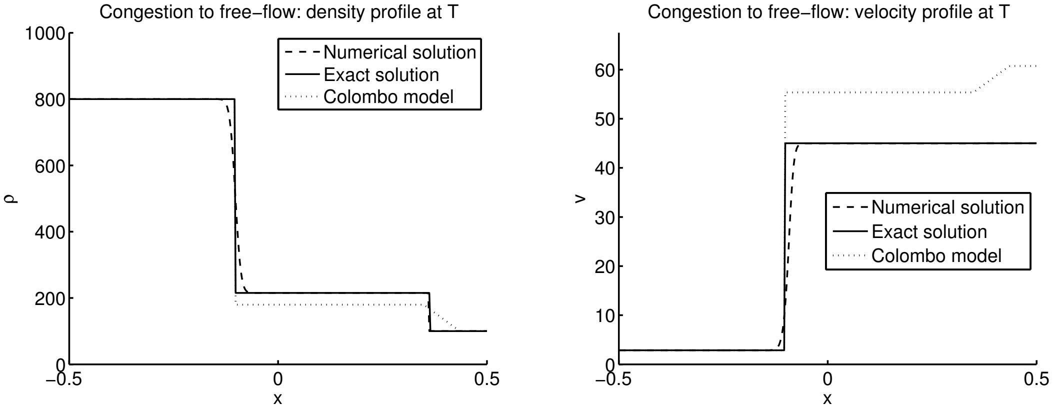

Figure 2.6: Numerical benchmark of Newell-Daganzo phase transition model.
Exact solution (continuous line), computed solution (dashed line), and exact solution for the Colombo model (dotted line) for density (left) and speed (right). Between the two initial states, arises a state $u_m = (215.4, -0.03)$ which corresponds to the intersection of the 1-Lax curve going through u_l with the metastable phase. In this graph $T = 0.4$ and $\Delta x = 0.0013$.

The solutions to the Riemann problem for each model differ on several points. First the intermediary state u_m belongs to the metastable phase in the Newell-Daganzo model whereas it belongs to the free-flow phase for the Colombo model. Second the wave from the intermediary state u_m to the right state u_r is a rarefaction wave in the Colombo model, as illustrated in Figure 2.6, whereas it is a contact discontinuity in the Newell-Daganzo phase transition model.

The values of the error $E(T)$, as described in Section 2.2.6 for $T = 4$, (a typical time for which all interactions have moved out of the computational domain) are outlined in Table 2.2.

Cell ♯	$E(T)$
50	$5.8\ 10^{-04}$
100	$2.0\ 10^{-04}$
200	$6.4\ 10^{-05}$
400	$2.0\ 10^{-05}$

Table 2.2: Numerical error.
Relative error between exact solution and the modified Godunov scheme solution for the benchmark described above, for different discretizations.

2.4 The Greenshields phase transition model

In this section we use a Greenshields model to describe the velocity function in congestion, i.e. we use a concave quadratic flux function. We present the standard and perturbed flux functions, derive the corresponding Riemann solver which we test on a benchmark case, and describe the properties of the Greenshields phase transition model.

2.4.1 Analysis

We use a quadratic relation to describe the congestion standard state, which for physical considerations needs to satisfy the requirements from Section 2.2.1. This leads us to choose the flux as a quadratic function of the form:

$$\rho\, v_c^s(\rho) = (\rho - R)\,(a\,\rho + b)$$

such that the vanishing condition at $\rho = R$ is satisfied. Continuity at the critical density σ yields:

$$b = \frac{\sigma\, V}{\sigma - R} - a\,\sigma$$

so the flux at the standard state reads:

$$\rho\, v_c^s(\rho) = (\rho - R)\,\left(a\,(\rho - \sigma) + \frac{\sigma\, V}{\sigma - R}\right)$$

with a variation interval for a defined by the second and third conditions of Section 2.2.1 as:

$$a \in \left[-\frac{\sigma V}{(\sigma - R)^2}, 0\right[.$$

Note that for the specific case in which $R = 2\sigma$ and a is defined by the fact that the derivative of the flux equals zero at σ (which reads $a = -\sigma V/(\sigma - R)^2$), we obtain the classical Greenshields flux.

Following the general form given in system (2.4), we write the perturbed velocity function as:

$$\begin{cases} v_f(\rho) = V & \text{for } (\rho, q) \in \Omega_f \\ v_c(\rho, q) = \left(1 - \frac{R}{\rho}\right) \left(a\,(\rho - \sigma) + \frac{\sigma V}{\sigma - R}\right) (1 + q) & \text{for } (\rho, q) \in \Omega_c \end{cases} \tag{2.13}$$

with $a \in \left[-\frac{\sigma V}{(\sigma - R)^2}, 0\right[$, and where Ω_f and Ω_c are defined by (2.5). The corresponding fundamental diagram is presented in Figure 2.7.

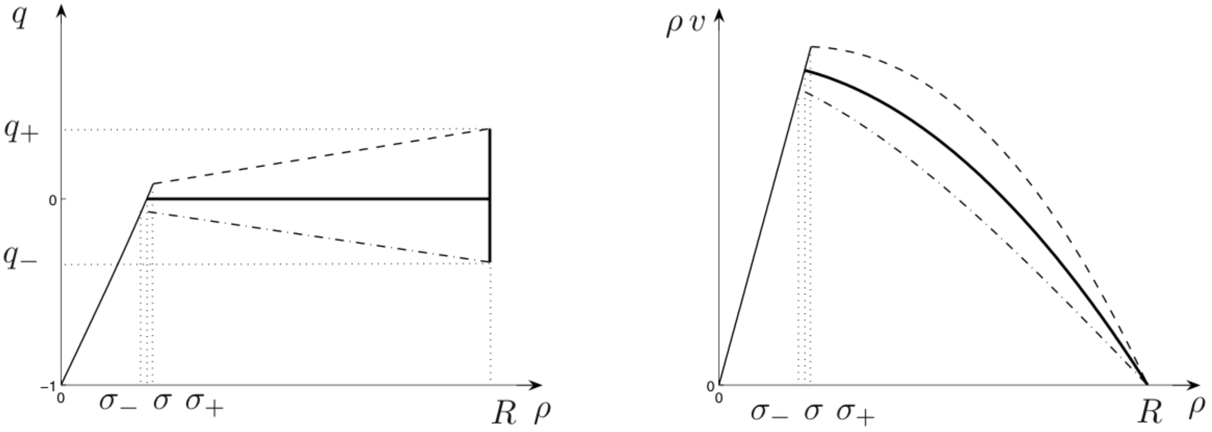

Figure 2.7: Phase transition model with a Greenshields standard state.
Left: State-space coordinates. Right: Flux-density coordinates. Thin solid line: Free-flow. Bold solid line: Congestion standard state. Thin dashed line: Upper bound of congestion. Thin dot-dashed line: Lower bound of congestion. The standard flux is concave, and all the 1-Lax curves are concave in $(\rho, \rho\, v)$ coordinates. In (ρ, q) coordinates the free-flow phase is not a straight line but has a very light convexity.

Remark 2.12. The expression of the velocity function given by system (2.13) enables a set-valued velocity function for $\rho > \sigma_-$. For a given density the variable velocity can take several values. The lower bound of the congestion phase is concave, unlike for the model presented in Section 2.3. This feature may be more appropriate for usual experimental datasets.

The requirements from Section 2.2.2 here reduce to:

$$q_- > -\frac{a\,R}{\frac{\sigma\,V}{\sigma - R} + a\,(2\,R - \sigma)}.$$

While in the Newell-Daganzo phase transition model the bound on the perturbation is given by the fact that the speed had to be positive, here the bound is given by the requirement on the constant concavity of the 1-Lax curves.

Remark 2.13. The lower bound on the perturbation is an increasing function of the parameter a, so this parameter should be chosen as small as possible to guarantee more freedom, namely $a_{\min} = -\sigma\,V/(\sigma - R)^2$ which yields the lowest lower bound bound $q_-^{\min} = R/(2\,\sigma - 3\,R)$.

2.4.2 Solution to the Riemann problem

We consider the Riemann problem for system (2.3) with the velocity function from equation (2.13) and the initial datum:

$$(\rho, q)(0, x) = \begin{cases} (\rho_l, q_l) & \text{if } x < 0 \\ (\rho_r, q_r) & \text{if } x > 0. \end{cases} \tag{2.14}$$

We follow the method used in [62] to construct the solution. We define u_m by the solution in Ω_c of the system:

$$\begin{cases} \frac{q_m}{\rho_m} = \frac{q_l}{\rho_l} \\ v_c(u_m) = v_c(u_r) \end{cases} \tag{2.15}$$

which yields a quadratic polynomial in ρ_m with one root in $[0, R]$. In the general case, the solution u_m of the system (2.15) can be equal to u_l or u_r.

i **Case 1:**

  $u_l \in \Omega_f$ and $u_r \in \Omega_f$ For all values of (ρ_l, ρ_r) the solution consists of a contact discontinuity from u_l to u_r.

ii **Case 2:** $u_l \in \Omega_c$ and $u_r \in \Omega_c$

  i If $v_c(u_r) \geq v_c(u_l)$ the solution consists of a 1-rarefaction wave from u_l to u_m and a 2-contact discontinuity from u_m to u_r.

  ii If $v_c(u_l) > v_c(u_r)$ the solution consists of a shock wave from u_l to u_m and a 2-contact discontinuity from u_m to u_r.

iii **Case 3:** $u_l \in \Omega_c$ and $u_r \in \Omega_f$ The solution consists of a 1-rarefaction wave from u_l to u_m and of a contact-discontinuity from u_m to u_r.

iv **Case 4:** $u_l \in \Omega_f$ and $u_r \in \Omega_c$ Let u_{m-} be defined by the solution in Ω_c of the system:

$$\begin{cases} \frac{q_{m-}}{\rho_{m-}} = \frac{q_-}{R} \\ v_c(u_{m-}) = v_c(u_r). \end{cases}$$

The solution consists of a phase transition from u_l to u_{m-} and of a 2-contact discontinuity from u_{m-} to u_r.

Remark 2.14. The analysis in the case of a convex standard flux function, which we do not address here, is closely related to this case, modulo the sign of the parameter a and the concavity of the 1-Lax curves.

2.4.3 Model properties

The structure of the solution to the Riemann problem presented in previous section explains the distinction with the original phase transition model:

i Since the 1-Lax curves are concave, within the congestion phase, shock waves occur only from a low density on the left to a high density on the right. This is similar to classical traffic models with concave flux.

ii The concavity of the 1-Lax curves yields simple transitions from a free-flow state to a congested state. These phase transitions are composed of a shock-like phase transition followed by a contact discontinuity, whereas a rarefaction wave can appear between the two in the original phase transition model or in the Newell-Daganzo phase transition model.

iii Similarly to the Newell-Daganzo phase transition model, within the free-flow phase, the Greenshield phase transition model exhibits only contact discontinuities.

Another consequence of the fact that the 1-Lax curves are concave is that the Riemann solver is much simpler than in the Newell-Daganzo case, with only five different types of solutions, compared to the Newell-Daganzo case which has eleven different types of solutions.

Remark 2.15. According to Remark 2.8 this flux function models aggressive drivers only, who drive along concave 1-Lax curves. In practice, it is able to model a class of clouds of points observed experimentally where the congested domain has a concave lower border in $(\rho, \rho\, v)$ coordinates.

2.4.4 Benchmark test

In this section we compare the numerical results given by the modified Godunov scheme on a benchmark test with its analytical solution. We use the phase transition model (2.3) in the Greenshields case (2.13) with the following choice of parameters: $V = 45$, $R = 1000$, $\sigma_- = 190$, $\sigma = 200$, $\sigma_+ = 215$. We choose $a = -0.01$. The resulting values for the extrema of the perturbation are $q_- = -0.34$ and $q_+ = 0.44$. The benchmark test is a phase transition from free-flow to congestion, with the following left and right states:

i $u_l = (180)$ which corresponds to a free-flow state with $\rho = 180$ and $v = 45$.

ii $u_r = (900, 0.2)$ which corresponds to a congested situation above standard state with $\rho = 900$ and $v = 2.4$.

This configuration gives rise to a phase transition between u_l and a congested state u_m followed by a 2-contact discontinuity between u_m and u_r (Riemann case 4) which is illustrated in Figure 2.8.

We also present the solution to the Riemann problem for the original Colombo model with parameters: $V_{c+} = 45$, $V_{f-} = 57$, $V = 67$, $q^* = 0$, $Q^- = -0.32$ and $Q^+ = 0.44$. The speed in free-flow differs between the two models. The phase transition speed is negative for both models but is greater in the case of the Greenshields phase transition model which models more aggressive drivers which have a higher flux in congestion for the same density value. The second wave has the same speed in the two models.

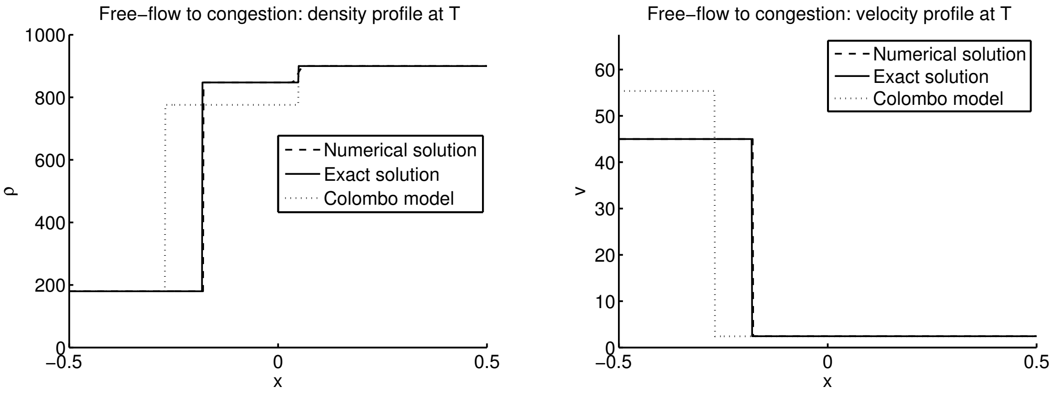

Figure 2.8: Numerical benchmark of Greenshields phase transition model.
Exact solution (continuous line), computed solution (dashed line), and solution to the Colombo model (dotted line) for density (left) and speed (right). Between the two initial states appears a state $u_m = (847.4, -0.24)$ which corresponds to the intersection of the lower bound of the diagram in congestion with the 2-Lax curve going through u_r. In this graph $T = 1$ and $\Delta x = 0.0013$.

Table 2.3 summarizes the values of the error $E(T)$, as defined in Section 2.2.6, for different sizes of the discretization step, at $T = 4$.

Cell ♯	$E(T)$
50	$3.1\ 10^{-04}$
100	$7.8\ 10^{-05}$
200	$2.1\ 10^{-05}$
400	$5.4\ 10^{-06}$

Table 2.3: Relative error.
Relative error between exact solution and numerical solution for the test case explicitly described above, for different numbers of space cells.

2.5 The Li phase transition model

In this section, we use a Li model [158] to describe the velocity function in congestion. The flux function is concave below a density σ_i in $(\sigma, R]$ and is convex for densities above σ_i. According to our interpretation of the concavity of the flux given in remark 2.8, this model accounts for a changing behavior among drivers who drive in a less aggressive way when congestion becomes too high. We present the equilibrium relation for this model, then we analyze the perturbation, and finally we derive a Riemann solver and test it on benchmark cases.

2.5.1 Analysis

The Li model that we use for the congestion phase is concave above critical density σ until a density σ_i and is convex from σ_i to R. Due to the requirements listed in 2.2.1, we propose to write the flux as a cubic function of the density.

Remark 2.16. *In the following we will assume that the density parameters are sorted as $0 < \sigma < \sigma_i \leq R$ and $\sigma_i \approx R$.*

1. The requirement that the flux should vanish at the maximal density R leads to the following expression:
$$\rho\, v_c^s(\rho) = (\rho - R)\,(a\,\rho^2 + b\,\rho + c). \tag{2.16}$$

2. The existence of an inflexion point for the flux at $\rho = \sigma_i$ yields:
$$\frac{d^2(\rho\, v_c^s(\rho))}{d\rho^2}(\sigma_i) = 2\,a\,(3\,\sigma_i - R) + 2\,b = 0. \tag{2.17}$$

   Thus the following relation must be verified:
$$a = \frac{b}{R - 3\,\sigma_i} \tag{2.18}$$

   where we assume in agreement with remark 2.16 that $R - 3\,\sigma_i \neq 0$.

3. According to expression (2.17) of the second derivative of the flux and using relation (2.18) between a and b, we obtain that the concavity of the flux in R is defined by the sign of $6\,b\,\frac{R-\sigma_i}{R-3\,\sigma_i}$ and assuming as per remark 2.16 that $R-3\,\sigma_i<0$ we must have $b<0$ to have a flux convex in R. A similar reasoning shows that the concavity of the flux in the critical density σ is defined by the sign of $6\,b\,\frac{\sigma-\sigma_i}{R-3\,\sigma_i}$, so in order to have a flux concave at the critical density, assuming $\sigma<\sigma_i$ consistently with remark 2.16 we must have $b<0$.

4. The continuity of the flux function at the critical density σ leads to:

$$c=\frac{V\,\sigma}{\sigma-R}-b\left(\frac{\sigma^2}{R-3\,\sigma_i}+\sigma\right).$$

5. The fact that the flux is decreasing in R and in σ, and thus everywhere, comes from:

$$\frac{d(\rho\,v_c^s(\rho))}{d\rho}(\sigma)\leq 0 \;\text{ and }\; \frac{d(\rho\,v_c^s(\rho))}{d\rho}(R)\leq 0$$

which respectively yields:

$$b\geq-\frac{\sigma\,V}{(R-\sigma)^2}\,\frac{R-3\,\sigma_i}{2\,\sigma+R-3\,\sigma_i} \;\text{ and }\; b\leq\frac{\sigma\,V}{(R-\sigma)^2}\,\frac{R-3\,\sigma_i}{2\,R+\sigma-3\,\sigma_i}$$

where we assumed that $2\,\sigma+R-3\,\sigma_i<0$ and $2\,R+\sigma-3\,\sigma_i<0$ consistently with the ordering of the parameters of remark 2.16. The second inequality is less restrictive than $b<0$ required above.

Finally the Li flux reads:

$$\rho\,v_c^s(\rho)=(\rho-R)\left[b\left(\frac{\rho^2}{R-3\,\sigma_i}+\rho-\left(\frac{\sigma^2}{R-3\,\sigma_i}+\sigma\right)\right)+\frac{\sigma\,V}{\sigma-R}\right] \tag{2.19}$$

and under this form satisfies all requirements as long as the following assumptions hold:

$$\begin{cases}2\,\sigma+R-3\,\sigma_i<0\\ b\in\left[-\frac{\sigma\,V}{(R-\sigma)^2}\,\frac{R-3\,\sigma_i}{2\,\sigma+R-3\,\sigma_i},0\right].\end{cases}$$

The perturbed velocity function reads:

$$\begin{cases}v_f(\rho)=V & \text{for } (\rho,q)\in\Omega_f\\ v_c(\rho,q)=\left(1-\frac{R}{\rho}\right)\,[a\,\rho^2+b\,\rho+c]\,(1+q) & \text{for } (\rho,q)\in\Omega_c.\end{cases} \tag{2.20}$$

We note as in 2.2.2:

$$\begin{cases}\Omega_f = \{(\rho, q) \mid (\rho, q) \in [0, R] \times [0, +\infty[\ \ , v_c(\rho, q) = V\ \ ,\ \ 0 \le \rho \le \sigma_+\} \\ \Omega_c = \left\{(\rho, q) \mid (\rho, q) \in [0, R] \times [0, +\infty[\ \ , v_c(\rho, q) < V\ \ ,\ \ \frac{q^-}{R} \le \frac{q}{\rho} \le \frac{q^+}{R}\right\}.\end{cases}$$

Figure 2.9 presents the corresponding fundamental diagram in state-space coordinates and in density-flux coordinates.

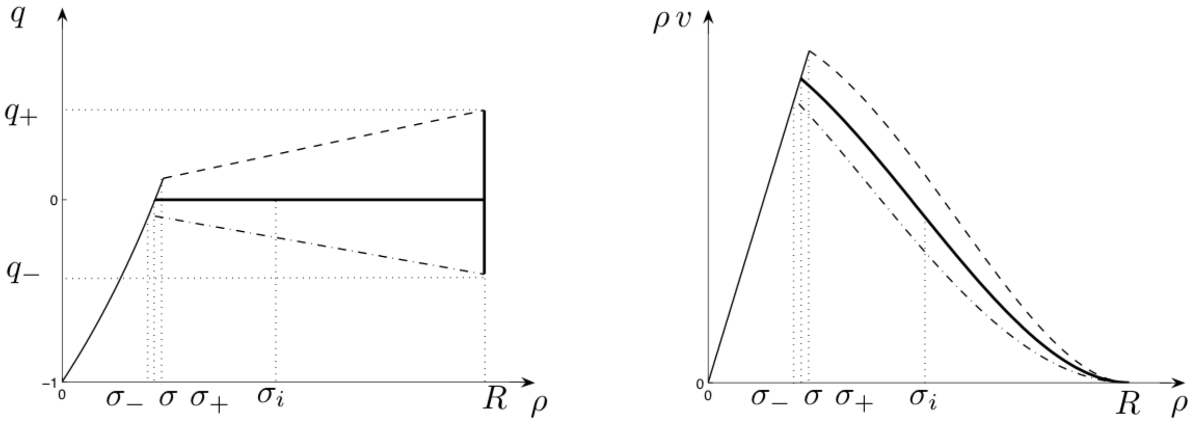

Figure 2.9: Phase transition model with a Li equilibrium.
Left: State-space coordinates. Right: Flux-density coordinates. Thin solid line: Free-flow. Bold solid line: Congestion equilibrium. Thin dashed line: Upper bound of congestion. Thin dot-dashed line: Lower bound of congestion. The 1-Lax curves do not have a constant concavity but have no more than one inflexion point.

The equilibrium flux (2.19) has one and only one inflexion point, located at $\rho = \sigma_i$. For simplicity of the analysis and for modeling consistency, we want to have the inflexion points of all the 1-Lax curves[2] in a neighborhood of $(\sigma_i, 0)$. The concavity of the 1-Lax curves is given by the sign of:

$$\nabla\lambda_1.r_1 = 2\,\rho\,(3\,a\,\rho + b - a\,R) + q\,(12\,a\,\rho^2 + 6\,(b - a\,R)\,\rho + 2\,(c - b\,R))$$

which gives when substituting a, b and c for their respective expression:

$$\begin{aligned}&\nabla\lambda_1.r_1 = \tfrac{6\,\rho\,b}{R-3\,\sigma_i}\,(\rho - \sigma_i) + \\ &2\,b\,q\left(\tfrac{6\,\rho^2}{R-3\,\sigma_i} - \tfrac{9\,\sigma_i}{R-3\,\sigma_i}\,\rho + \tfrac{V\,\sigma}{b\,(\sigma-R)} - (R + \sigma + \tfrac{\sigma^2}{R-3\,\sigma_i})\right)\end{aligned} \tag{2.21}$$

where the first term which corresponds to a zero value of the perturbation q vanishes at $\rho = \sigma_i$, which is equivalent for the equilibrium flux to having an inflexion point at $\rho = \sigma_i$.

---

[2] The 1-field would be called GNL if no 1-Lax curve had any inflexion point, which is clearly not the case since the equilibrium flux which corresponds to the 1-Lax curve for $q = 0$ has an inflexion point.

For admissible values of b it is not possible to have expression (2.21) vanishing at (σ_i, q) for all $q \in [q_-, q_+]$, thus it is not possible to have all the 1-Lax curves having an inflexion point at $\rho = \sigma_i$. If we note $(\overline{\rho}, \overline{q})$ an inflexion point of a 1-Lax curve, a less restrictive condition would be to have its density coordinate $\overline{\rho}$ 'close' to the density coordinate σ_i of the inflexion point at equilibrium. In order to do so we set b such that the term which does not depend on ρ in 2.21 equals zero, i.e. $b = \frac{c}{R}$ which reads:

$$b = \frac{V\,\sigma}{\sigma - R}\,\frac{R - 3\,\sigma_i}{(R - 3\,\sigma_i)\,(R + \sigma) + \sigma^2}$$

which has a sense since the denominator of the right term satisfies $(R - 3\,\sigma_i)\,(R + \sigma) + \sigma^2 < (-2\,\sigma)\,(R + \sigma) + \sigma^2 < 0$ because we assumed $2\,\sigma + R - 3\,\sigma_i < 0$. We also proved that $b < 0$. We must also verify that the value chosen for b is not too small, i.e. that the flux is still decreasing at $\rho = \sigma$. This condition which reads:

$$\frac{V\,\sigma}{\sigma - R}\,\frac{R - 3\,\sigma_i}{(R - 3\,\sigma_i)\,(R + \sigma) + \sigma^2} \geq -\frac{\sigma\,V}{(R - \sigma)^2}\,\frac{R - 3\,\sigma_i}{2\,\sigma + R - 3\,\sigma_i}$$

is equivalent to $\sigma - 2\,\sigma_i \leq 0$ which is true according to remark 2.16. Then an inflexion point (ρ, q) for a 1-Lax curve satisfies:

$$\rho = \sigma_i\,\left(1 + \frac{q}{1 + 2\,q}\right) \tag{2.22}$$

where we assumed that $1 + 2\,q \neq 0$ (i.e. is positive given the restriction expressed by the positivity of the speed (2.6)). In order to have the projection on the density axis of the set of inflexion points (i.e. the points (ρ, q) satisfying (2.22)) included in a neighborhood $[\sigma_i\,(1 - \alpha_-), \sigma_i\,(1 + \alpha_+)]$) of σ_i, for α_-, α_+ positive and small (meaning that $\sigma_i\,(1 - \alpha_-) \approx \sigma_i \approx \sigma_i\,(1 + \alpha_+)$), we additionally require:

$$q_+ \leq \frac{R}{\sigma_i\,(1 + \alpha_+)}\,\frac{\alpha_+}{1 - 2\,\alpha_+} \quad \text{and} \quad q_- \geq -\frac{R}{\sigma_i\,(1 - \alpha_-)}\,\frac{\alpha_-}{1 + 2\,\alpha_-}$$

where we assumed that $\alpha_+ < 1/2$ and $\alpha_- < 1/2$. When we add to this the conditions from 2.2.2, assuming that $2\,R < 3\,\sigma_i$ it summarizes as:

$$q_- \geq \max\left(-\frac{R}{\sigma_i\,(1 - \alpha_-)}\,\frac{\alpha_-}{1 + 2\,\alpha_-}, \max_{[\sigma,R]}\left(-\frac{\rho\,\frac{d^2 Q_c^{eq}(\rho)}{d\rho^2}}{2\,\frac{dQ_c^{eq}(\rho)}{d\rho} + \rho\,\frac{d^2 Q_c^{eq}(\rho)}{d\rho^2}}\right)\right)$$

and:

$$q_+ \leq \frac{R}{\sigma_i\,(1 + \alpha_+)}\,\frac{\alpha_+}{1 - 2\,\alpha_+}.$$

2.5.2 Solution of the Riemann problem

We consider the Riemann problem for system (2.3) with the velocity function defined by (2.20) and the initial datum:

$$(\rho, q)(0,x) = \begin{cases} (\rho_l, q_l) & \text{if } x < 0 \\ (\rho_r, q_r) & \text{if } x > 0 \end{cases}$$

and we follow the method used in [63] to construct the solution. We define u_m by the solution in Ω_c of system:

$$\begin{cases} \frac{q_m}{\rho_m} = \frac{q_l}{\rho_l} \\ v_c(u_m) = v_c(u_r) \end{cases}$$

and we define u_p by the solution in Ω_c of the system:

$$\begin{cases} \lambda_1(u_p) = \Lambda(u_l, u_p) \\ \frac{q_p}{\rho_p} = \frac{q_l}{\rho_l}. \end{cases}$$

We also note $u_{i,l}$ the inflexion point of the 1-Lax curve going through u_l.

1. **Case 1:** $u_l \in \Omega_f$ and $u_r \in \Omega_f$

   For all values of (ρ_l, ρ_r) the solution consists of a contact discontinuity from u_l to u_r.

2. **Case 2:** $u_l \in \Omega_c$ and $u_r \in \Omega_c$

   (a) If $v_c(u_l) > v_c(u_r) \geq v_c(u_{i,l})$ the solution consists of a shock wave from u_l to u_m and a 2-contact discontinuity from u_m to u_r.

   (b) If $v_c(u_r) \geq v_c(u_l) \geq v_c(u_{i,l})$ the solution consists of a 1-rarefaction wave from u_l to u_m and a 2-contact discontinuity from u_m to u_r.

   (c) If $v_c(u_l) > v_c(u_{i,l}) > v_c(u_r)$

      i. If $\Lambda(u_l, u_m) \geq \lambda_1(u_m)$ the solution consists of a shock wave from u_l to u_m and a 2-contact discontinuity from u_m to u_r.

      ii. If $\lambda_1(u_m) > \Lambda(u_l, u_m)$ the solution consists of a shock wave from u_l to u_p, a 1-rarefaction wave from u_p to u_m and a 2-contact discontinuity from u_m to u_r.

   (d) If $v_c(u_{i,l}) \geq v_c(u_r) > v_c(u_l)$ the solution consists of a shock wave from u_l to u_m and a 2-contact discontinuity from u_m to u_r.

   (e) If $v_c(u_{i,l}) \geq v_c(u_l) \geq v_c(u_r)$ the solution consists of a 1-rarefaction wave from u_l to u_m and a 2-contact discontinuity from u_m to u_r.

   (f) If $v_c(u_r) > v_c(u_{i,l}) > v_c(u_l)$

        i. If $\Lambda(u_l, u_m) \geq \lambda_1(u_m)$ the solution consists of a shock wave from u_l to u_m and a 2-contact discontinuity from u_m to u_r.
        ii. If $\lambda_1(u_m) > \Lambda(u_l, u_m)$ the solution consists of a shock wave from u_l to u_p, a 1-rarefaction wave from u_p to u_m and a 2-contact discontinuity from u_m to u_r.

3. **Case 3:** $u_l \in \Omega_c$ and $u_r \in \Omega_f$
    (a) If $v_c(u_l) \geq v_c(u_{i,l})$ The solution consists of a 1-rarefaction wave from u_l to u_m and of a contact-discontinuity from u_m to u_r.
    (b) If $v_c(u_{i,l}) > v_c(u_l)$
        i. If $\Lambda(u_l, u_m) \geq \lambda_1(u_m)$ the solution consists of a shock wave from u_l to u_m and a contact discontinuity from u_m to u_r.
        ii. If $\lambda_1(u_m) > \Lambda(u_l, u_m)$ the solution consists of a shock wave from u_l to u_p, a 1-rarefaction wave from u_p to u_m and a contact discontinuity from u_m to u_r.

4. **Case 4:** $u_l \in \Omega_f$ and $u_r \in \Omega_c$

    Let u_m be defined by the solution in Ω_c of the system:

$$\begin{cases} \frac{q_m}{\rho_m} = \frac{q_-}{R} \\ v_c(u_m) = v_c(u_r) \end{cases}$$

    and let $\Lambda(u_l, u_m)$ be the Rankine-Hugoniot phase transition speed defined in (2.9) between u_l and u_m.

    (a) If $\Lambda(u_l, u_m) \geq \lambda_1(u_m)$ the solution consists of a phase transition from u_l to u_m and of a 2-contact discontinuity from u_m to u_r.
    (b) If $\lambda_1(u_m) > \Lambda(u_l, u_m)$ let $u_p := (\rho_p, q_p)$ be defined by the solution in Ω_c of the system:

$$\begin{cases} \frac{q_p}{\rho_p} = \frac{q_-}{R} \\ \lambda_1(u_p) = \Lambda(u_l, u_p). \end{cases}$$

    The solution consists of a phase transition from u_l to u_p, of a 1-rarefaction wave from u_p to u_m, and of a 2-contact discontinuity from u_m to u_r.

2.5.3 Benchmark tests

In this section we compare the numerical results given by the modified Godunov scheme on benchmark tests in which the exact solution can be approximated almost exactly using wavefront tracking [39]. We use the phase transition model (2.3) with an equilibrium described by the Li velocity (2.20) with the following choice of parameters: $V = 45$, $R = 1000$, $\sigma_- = 211$, $\sigma = 220$, $\sigma_+ = 236$ $\sigma_i = 750$. We use three benchmark tests, one phase transition from free-flow to congestion (FF-C), one phase transition from congestion to free-flow (C-FF), and a more complex benchmark test involving more than one discontinuity (FF-C-FF).

Phase transition from free-flow to congestion

We use the following parameters:

1. $u_l = (120, -0.48)$ which corresponds to a free-flow situation with $v = 45$.
2. $u_r = (800, 0.01)$ which corresponds to a congested situation under equilibrium with $\rho = 500$ and $v = 3.5$.

This configuration gives rise to a phase transition between u_l and a congested state u_m on the lower bound of the congestion region, followed by a 2-contact discontinuity from u_m to u_r (Riemann case 4, first subcase), as illustrated in figure 2.10.

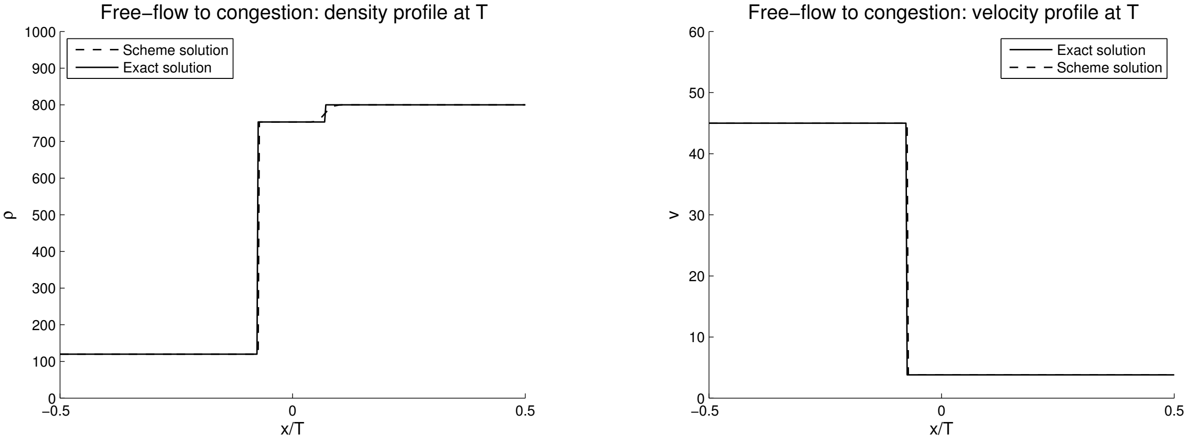

Figure 2.10: Free-flow to congestion benchmark Riemann problem.
Exact solution (continuous line) and computed solution (dashed line) for density (left) and speed (right). In this graph $T =$ and $\Delta x = 0.0025$.

Phase transition from congestion to free-flow

We use the following parameters:

1. $u_l = (800, 0.2)$ which corresponds to a congested state over equilibrium with $v = 4.1$.
2. $u_r = (120, -0.48)$ which corresponds to a free-flow state.

This configuration gives rise to a rarefaction from u_l to a metastable state u_m, followed by a contact discontinuity from u_m to u_r (Riemann case 3, first subcase), which is depicted in figure 2.11.

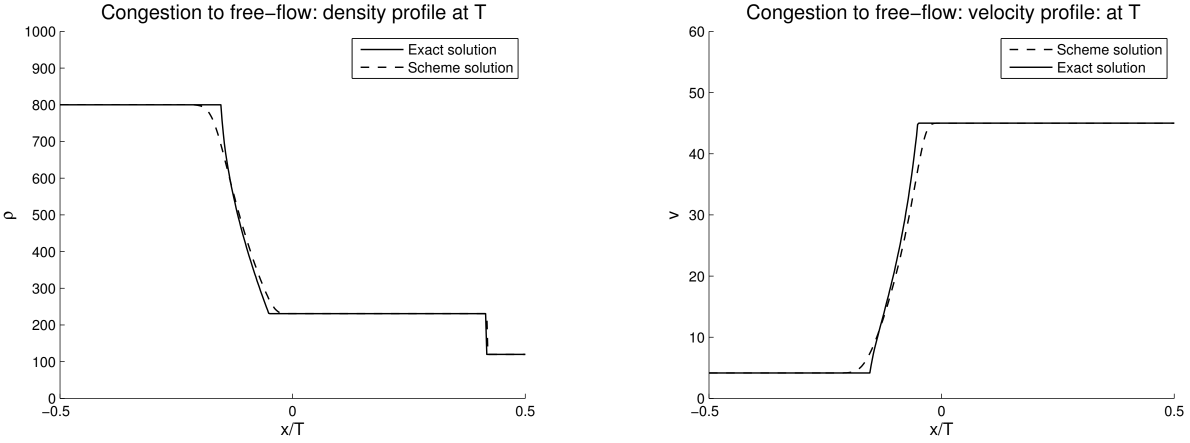

Figure 2.11: Congestion to free-flow benchmark Riemann problem.
Exact solution (continuous line) and computed solution (dashed line) for density (left) and speed (right). In this graph $T = 0.46$ and $\Delta x = 0.0025$.

Free-flow to congestion to free-flow

In this section we use the following more realistic benchmark test:

$$u_0(x) = \begin{cases} (180, -0.20) & \text{when } -0.5 \leq x \leq -0.3. \\ (700, -0.1) & \text{when } -0.3 \leq x \leq -0.1. \\ (900, 0) & \text{when } -0.1 \leq x \leq 0.1. \\ (300, 0.1) & \text{when } 0.1 \leq x \leq 0.3. \\ (50, -0.79) & \text{when } -0.3 \leq x \leq 0.5. \end{cases}$$

The evolution of these initial conditions yields at time T the profiles from figure 2.12.

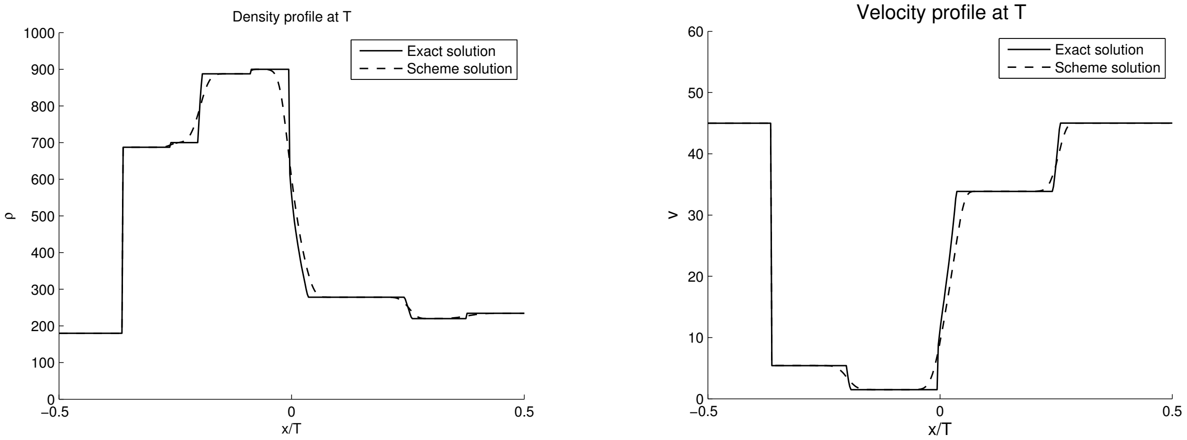

Figure 2.12: Experimental benchmark conditions.
Exact solution (continuous line) and computed solution (dashed line) for density (left) and speed (right). In this graph $T = 0.37$ and $\Delta x = 0.0025$.

Error computation

The values of the error $E(T)$ and of the formal order of convergence γ are outlined in table 2.4 for $T = 4$, (a typical time when interactions have moved out of the computational domain).

	FF-C		C-FF		FF-C-FF	
Cell ♯	$E(T)$	$\gamma(T)$	$E(T)$	$\gamma(T)$	$E(T)$	$\gamma(T)$
50	$5.3\,10^{-02}$	6.6	$5.0\,10^{-02}$	4.4	$8.9\,10^{-02}$	$8.7\,10^{-01}$
100	$2.7\,10^{-02}$	3.6	$3.0\,10^{-02}$	-4.7 10^{-01}	$6.1\,10^{-02}$	$8.5\,10^{-01}$
200	$1.3\,10^{-02}$	-9.6 10^{-02}	$1.8\,10^{-02}$	2.2 10^{-02}	$4.5\,10^{-02}$	$8.0\,10^{-01}$
400	$6.5\,10^{-03}$		$1.0\,10^{-02}$		$3.4\,10^{-02}$	

Table 2.4: L^1 relative error.
Exact solution and the modified Godunov scheme solution for three test cases explicitly described above, and for different numbers of space cells. We note FF-C the case of a phase transition from free-flow to congestion, C-FF the case of a phase transition from congestion to free-flow, and FF-C-FF the last case.

Chapter 3

Phase transition model analysis: properties and performance

In this chapter, we analyze the modeling performances of the phase transition model introduced in the previous chapter. After a perspective on the different scales at which traffic can be modeled, we briefly remind the reader of the seminal scalar macroscopic traffic flow model described in details in Chapter 1, motivate the historical introduction of non-scalar traffic flow models, and describe how the model proposed in the previous chapter answers the concerns and issues raised by the transportation community on so-called *higher-order models*.

3.1 Modeling traffic at a macroscopic scale

The theory of traffic modeling incorporates the design and analysis of mathematical tools for accurate representation of traffic dynamics. Road networks can be studied at different scales [155]. At a fine scale, the representation of traffic is closer to the true nature of the phenomena on the road. However, a detailed traffic model requires a large volume of accurate measurements for calibration and validation, and correspondingly large computation power. Consequently, different scales have been historically associated with different applications, depending on data availability and computational requirements.

At a *nanoscopic scale*, vehicles are considered to behave independently under the control of a driver who reacts to stimuli from neighboring vehicles according to a specific behavioral model. Traffic dynamics can be modeled as a set of coupled *ordinary differential equations* (ODE) with decision variables resulting from a demand model (see for instance [1]). At a *microscopic scale*, vehicles are considered to behave independently by reacting to stimuli from neighboring vehicles according to a dynamical model. Traffic dynamics can be modeled as a set of coupled ordinary differential equations [37]. Nanoscopic and microscopic models have been used mostly for off-line non-real-time simulation and planning (Quadstone Paramics [45], VISSIM [94]).

At a *mesoscopic scale*, vehicles are considered as a large set of atomic elements with individual behavior according to macroscopic laws or relations. Traffic dynamics can be modeled as cellular automata [57] or using gas-kinetic models [188]. Mesoscopic models have been widely applied to real-time on-line and off-line network-wide control and dynamic traffic assignment, with significant prior data collection for calibration (DynaMIT [21], DyNASMART [166]).

At a *macroscopic* scale, vehicles are considered to behave as a continuum medium. Traffic dynamics is modeled as a distributed system, using *partial differential equations* (PDE) inspired from hydrodynamics theory [159, 97, 189]. Consequently, in this framework, the effect of network-wide route choices is not conveniently accounted for. One of the strengths of macroscopic models resides in the level of complexity they capture at a relatively low analytical and computational cost, and with limited data requirements for calibration. This has motivated the use of macroscopic models in particular for real-time on-line estimation and corridor management (METANET [168], Mobile Millennium [19], TOPL [56]). Furthermore, the mathematical theory of hydrodynamics modeling brings a solid mathematical structure to macroscopic models. This theoretical strength can be leveraged for the development of mathematically sound lower-scale models, by equivalence (see [99, 113, 118, 155]), and serve as an anchor for the development of consistent multi-scale modeling frameworks (e.g. the AIMSUN simulation software [14]).

These properties of macroscopic models have motivated sustained research on extension of seminal models such as the *Lighthill-Whitham-Richards* (LWR) model, presented in the following section, with the goal of capturing complex observed phenomena missing from the LWR theory. Challenges in the design of so-called *higher-order models* relate to the development of sound physical understanding, well-defined analytical structure, and preserved computational tractability of the solution algorithm. In this chapter, we show that allowing the speed function to take values around the classical stationary bivariate relation enables the simulation of higher-order traffic phenomena at the same computational cost as classical solution methods for the LWR model, and with a preserved physical interpretation.

In the following section, we present the historical context for the introduction of scalar macroscopic models, presented in details in Section 1.2.3.

3.1.1 First order scalar macroscopic models

The basis for the theory of macroscopic traffic modeling was set by the seminal articles from Lighthill and Whitham [159], and Richards [189], that introduced a PDE model describing the evolution of the density $\rho(t, x)$ of vehicles at time t and location x

$$\frac{\partial \rho(t,x)}{\partial t} + \frac{\partial Q(\rho(t,x))}{\partial x} = 0, \tag{3.1}$$

where the flow is expressed as a function of the density $Q(\rho(t, x))$. This so-called LWR model expresses the conservation of vehicles on the road. Different traffic models were later shown to be equivalent to the LWR formulation, in particular the Newell *car-following model* [178] and the *cell-transmission model* (CTM) [71], in the case of a triangular flux function $Q(\cdot)$ [177], also called triangular *fundamental diagram*:

$$Q(\rho) \doteq \begin{cases} \rho\, v_{\max} & \text{if} \quad \rho \leq \rho_c \\ (\rho - \rho_{\max})\; w & \text{if} \quad \rho \geq \rho_c \end{cases} \tag{3.2}$$

where $v_{\max}$, ρ_c, $\rho_{\max}$ and w denote the *free-flow speed*, the *critical density*, the *jam density* and the *backward moving wave speed*, respectively, which are required to satisfy

$$\rho_c\, v_{\max} = (\rho_c - \rho_{\max})\; w \tag{3.3}$$

for continuity of the flow at the critical density. Density values below the critical density correspond to *free-flow* states and density values above the critical density correspond to *congestion* states. For non-vanishing values of the flow q and the speed v, the definition of the flux function $Q(\cdot)$ is equivalent to the definition of a speed function $V(\cdot)$ through the equality $q = v\,\rho$. The use of a single-valued fundamental diagram mapping a density value to a unique flow value dates back to the observations by Greenshields in Ohio in 1934 [107], Greenberg in the Lincoln tunnel in 1959 [106], and Edie in the Holland tunnel in the early 1960's [85].

The LWR theory has been validated with experimental data for traffic modeling (see [175] for instance), and in particular the triangular fundamental diagram from equation (3.2) has been shown to accurately model the *stationary relation* between density and flow, under proper time-space aggregation of traffic measurements [46, 47, 76]. One of the most desirable properties of the LWR model lies in its ability to capture the formation and growth of queues at bottlenecks. However the LWR model is known to be unable to reproduce more complex observed traffic phenomena such as *stop-and-go waves*, *traffic hysteresis*, and *phantom jams* [118].

3.1.2 Non-stationary traffic flow

The introduction of more complex macroscopic models for traffic flow dates back to the *Payne-Whitham* model (PW) [183], which consists in a 2×2 system[1] of PDEs. The first equation is the LWR PDE (see equation (3.1)) and the second equation models the acceleration of vehicles as resulting from a reaction to local traffic conditions and a relaxation around the stationary relation. In a discrete form with a minor modification at on-ramps [182], this model was later used extensively for estimation and control [221, 222].

Several remarks were raised [73, 78] on the lack of physical consistency of so-called higher-order models, in which vehicles with negative speed, and *anisotropy* property, were shown to arise. Anisotropy characterizes the fact that modeled drivers react to stimuli from the front and from behind[2]. These considerations led to the development of improved non-

---

[1] A set of 2 equations for a 2-tuple of state variables.

[2] The justification for this terminology is the fact that in a so-called anisotropic model, we have $\lambda_1 \leq v \leq \lambda_2$, were v denotes the speed of vehicles, and $\lambda_{1,2}$ the characteristic speeds at which information propagate.

scalar models that did not exhibit these flaws; using a convective derivative in [13], and the so-called *non-equilibrium* model [233].

Independently, Kerner proposed the *three-phase theory* [134, 136, 137] postulating the existence of three phases of traffic; *free-flow*, *synchronized flow*, and *moving jam*, instead of the classical *free-flow* and *congestion.* So-called *third order* PDE models inspired from physical systems such as the model from Helbing [112], introducing the *speed variance* as a traffic state, have also been proposed.

The relative strengths and weaknesses of first and second-order models have been outlined in several articles [73, 78, 118, 151, 155, 181], including discussions on the expected modeling abilities of extensions to state-of-the-art macroscopic traffic models. This coincides with the emergence of sustained research focused on the understanding and modeling of specific phenomena missing from the LWR theory; *stop-and-go* waves, *hysteresis* patterns, *capacity drop*, and the understanding, validation, and modeling of their candidate causes; *lane changes*, *heterogeneous drivers*, *bounded acceleration*, *acceleration and deceleration curves.* Complementary efforts have investigated the nature of these phenomena and proposed models to reproduce them, with specific emphasis on:

- Development of parsimonious models able to reproduce stop-and-go waves [158], hysteresis patterns [233], the capacity drop [182].
- Validation of the causality hypothesis and development of models for lane changes [127, 143, 145], heterogeneous drivers [53, 146], bounded acceleration [148], acceleration and deceleration waves [229].

From the perspective of intelligent transportation systems, a critical feature of traffic models consists in their ability to handle streaming measurements for accurate estimation of traffic conditions [25, 170, 221, 227]. Observability of quantities required for on-line model calibration, ability to take advantage of measurements of various traffic quantities, computational tractability and model accuracy are essential properties for traffic monitoring.

The focus of the present chapter is on the assessment of accuracy and practicality of the *phase transition model* (PTM) introduced in the previous chapter, for traffic modeling and on-line traffic estimation. We show that, by allowing the classical state variable density ρ to be complemented in congestion by a perturbation variable p at the stationary state, the PTM is able to *propagate* the impact of non-stationary dynamics, rather than *predict* its emergence. It is observed that for time-space diagram reconstruction from initial and boundary conditions, significant accuracy is gained from the ability to account for joint observations of different traffic quantities. Specific attention is given to the physical mesoscopic interpretation of the model, and the practicality of implementation of the associated discrete solution algorithm. In particular the convexity of the state-space of the model, required for the use of finite volume schemes such as the Godunov scheme, is assessed. The performance of the proposed model and its ability to model complex traffic phenomena such as *hysteresis patterns*, *phantom jams*, forward-moving discontinuities in congestion, is assessed on benchmark cases and on experimental vehicle trajectories from the *Next Generation SIMulation* (NGSIM) datasets [179].

3.2 Phase transition model properties

In this section we present the properties of the phase transition model introduced in the previous chapter, on benchmark tests and on experimental vehicle trajectories described in section 3.3.1.

3.2.1 Mesoscopic interpretation

In this section we show that a meaningful mesoscopic interpretation, outlined in [30], can be associated with the discrete numerical method presented in the previous section and with the solution to the Riemann problem (see [74] for a related discussion on a *Markovian* perspective for modeling of complex traffic phenomena). In particular, we provide a physical interpretation for the numerical flux between two cells that depends on their corresponding phases.

First, we note that the perturbation variable p indicates how much the speed of the associated traffic state deviates from the stationary state. Hence from the mesoscopic perspective it can be viewed as an indication of the aggressiveness of the corresponding element of flow. It follows that the quantity p/ρ is the average aggressiveness per driver; it is positive if the observed speed is higher than the stationary speed, and negative otherwise.

Free-flow to free-flow: the flux between two cells in the free-flow phase T_f is the flow from the upstream cell (first case of equation (1.6)). This is in accordance with the definition of the free-flow phase as a phase in which the traffic demand is lower than the traffic supply, hence the demand from the upstream cell can be accommodated by the downstream cell, and the corresponding upstream flow can be realized between the two cells.

Congestion to congestion or free-flow: the flux between two cells in the congestion phase is the flow of the intermediary state u_{m} (second and third case of equation (1.6)). In this case, the middle state u_{m} has same value of p/ρ as the upstream state u_{up}, and same speed v as downstream state u_{down} (see second and third case of the Riemann problem in the previous chapter). The fact that the numerical flux between two cells is defined by the average aggressiveness of the upstream state u_{up} and the speed of the downstream state u_{down} can be understood as follows: drivers from the upstream cell adapt their speed to the speed of the drivers from the downstream cell. They adapt their speed and pick their spacing according to their natural driving behavior, represented here by the average aggressiveness of the element of flow to which they belong. Hence the numerical flux between the two cells is the flow that corresponds to a personalized modification, by the upstream drivers from the state u_{up}, of their speed, in order to match the speed of the downstream drivers.

Free-flow to congestion: the flux between two cells in the congestion phase is the flow of the intermediary state u_{m} (fourth case of equation (1.6)). In this case, the middle state

u_{m} has the lowest possible average aggressiveness p/ρ compatible with the speed v of the downstream state u_{down} (see fourth case of Riemann problem). This can be understood as follows; in the free-flow phase, the demand is not constrained by the supply and drivers are free to drive at the free-flow speed, hence the traffic state is entirely defined by its density. In particular, the aggressiveness of drivers is uniquely determined from the value of the density. When the drivers from the free-flow phase enter the congestion phase, they switch from a phase in which the demand is the defining constraint to a phase in which the supply is the defining constraint. This naturally yields a degree of aggressiveness that represents their driving speed compared to the stationary speed. Since the free-flow drivers emerge from a free-flow phase, the average aggressiveness of their corresponding element of flow is as low as possible. However, they have to adapt their speed according to the speed of the downstream traffic. They modify their speed to reach the speed of the downstream drivers, which is the second defining element for the intermediary state. In that sense, the aggressiveness of drivers is created by the interaction of a free-flow phase upstream and a congestion phase downstream. This is similar to the fact that congestion in the LWR model arises only from junctions.

3.2.2 Set-valued fundamental diagram

In this section, we quantify how the set-valued nature of the congestion phase of the PTM fundamental diagram increases the accuracy with which non-stationary traffic observations are accounted for by the admissible domain of the model. We propose a method for projecting state values falling outside of the state space back onto the state-space, and compare its performance with a similar method for the LWR model. In an estimation setting, the figures presented in this section indicate appropriate values for the error statistics associated with the boundary of the state-space.

PTM theory

The PTM state variables include the density ρ and an additional perturbation variable p in congestion that captures non-stationary traffic states observed in practice (see Figure 3.1). However, for measurements outside of the union $T_f \cup T_c$ of the free-flow phase and the congestion phase, a method has to be designed to project the observations onto the admissible domain.

For the LWR model, this can be accomplished by assuming that measurements of density outside of the range $[0, \rho_{\max}]$ are not valid or correspond to the endpoints $\{0, \rho_{\max}\}$, that measurements of speed outside of the range $[0, v_{\max}]$ are not valid or correspond to the endpoints $\{0, v_{\max}\}$, and that a measurement of a given quantity automatically yields another quantity using the stationary relation.

In the case of the PTM, for traffic observations falling outside of the domain $T_f \cup T_c$, we propose to project along the eigen-trajectories of the system, i.e. along the curves of

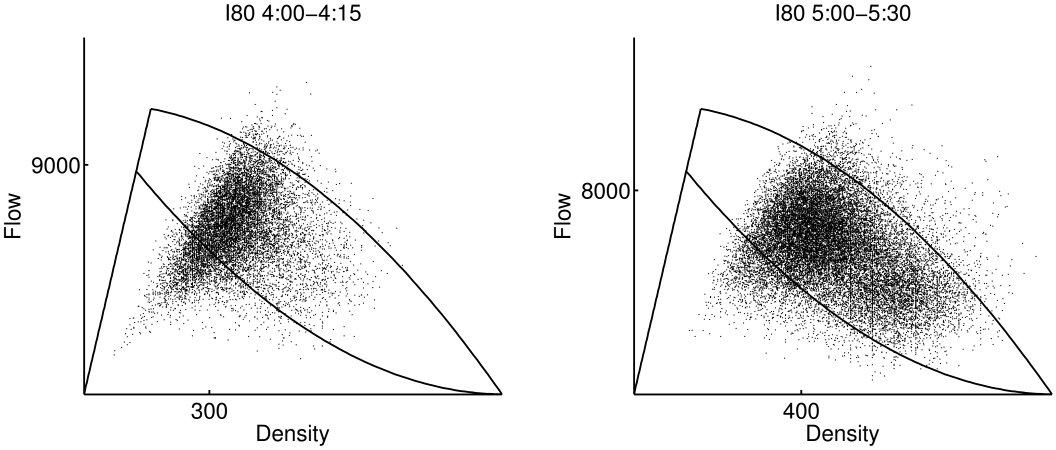

Figure 3.1: Set-valued congestion phase.
The PTM triangular fundamental diagram is able to capture to some extent the cloud of points observed in the congestion phase. The figures correspond to a visual fit of a triangular stationary relation with positive and negative perturbation, and a free-flow speed $v_{\max} = 70$ mph. Note that the visually linear edge on the left of the cloud of points, does not correspond to the free-flow speed $v_{\max}$, but to the maximal speed of vehicles in the conditions considered, approximatively 30 mph and 20 mph for the left, and right sub figure respectively.

constant average aggressiveness p/ρ or constant speed v. Here we address the case of perfect measurements. The projection method is illustrated in Figure 3.2.

The set-valued nature of the PTM fundamental diagram in congestion is of particular interest in the case of joint measurements from different traffic quantities, for instance loop counts and loop occupancies, or probe speeds and loop counts.

Empirical validation

In this section we illustrate the average absolute error associated with the process of projection onto the fundamental diagram for the CTM and the PTM. We consider the discretized values of flow, density, speed from the NGSIM datasets, as measurements of the ground-truth traffic state, and we assume that the associated measurement error (due to sensing and processing error) can be neglected in the analysis presented in this section.

For points falling outside of the fundamental diagram of the PTM, we compute the average absolute error between the measurement, and its projection onto the diagram using the method described in previous section. The associated density and speed errors are represented in the second and last columns of table 3.1, respectively.

We also represent the error associated with using the stationary relation in the CTM. Specifically, in the first column of table 3.1, we present the error on density when observing speed and computing the density from the stationary relation. In the third column of table 3.1, we present the error on speed when observing density and computing the speed

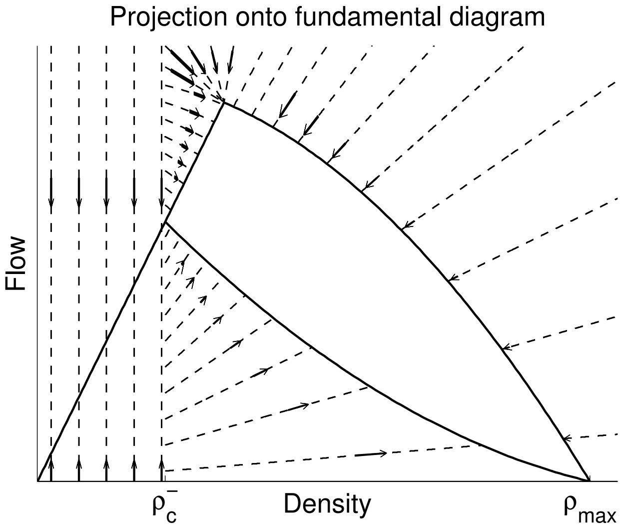

Figure 3.2: Projection onto PTM diagram.
Outliers with a density corresponding to the free-flow phase are projected along iso-density curves (vertical dashed lines left). Outliers with higher density than the maximal free-flow density and higher speed than the free-flow speed are projected along iso-average aggressiveness curves, or trajectories of the first type, iso-p/ρ (dashed curves at the center for both axis). Outliers with higher speed than the free-flow speed and higher average aggressiveness than its maximum allowed value are projected onto the capacity point of the diagram (dashed curves center top). Outliers with higher density than the maximal free-flow density and lower speed than the free-flow speed are projected along iso-speed curves, or trajectories of the second type, iso-v (dashed lines emanating from the origin).

from the stationary relation.

	Density CTM error (vpm)	Density PTM error (vpm)	Speed CTM error (mph)	Speed PTM error (mph)
I-80 4-4:15	58.9	8.5	5.4	0.1
I-80 5-5:30	61.0	5.2	3.4	0.0

Table 3.1: Average projection error.
Average absolute error associated with the stationary state hypothesis for the CTM and with the projection on the set-valued fundamental diagram for the PTM. The first column corresponds to the computation of density from speed observation using the stationary relation, and the converse for the third column. The second column corresponds to the error in density due to projection, and similarly for the speed in the fourth column. For each dataset, the error is averaged for all values of density, speed, and flow represented in figure 3.1, obtained from vehicle trajectories according to the method described in section 3.3.1 to handle NGSIM data.

It is clear from table 3.1 that inferring the density from speed measurements and the stationary relation yields a very high error (first column). One may also note that for the PTM, since the projection is often realized along iso-speed trajectories, there is a very low resulting error on speed.

The respective accuracy of the dynamics of the two models is presented in section 3.3.3.

3.2.3 Forward-moving discontinuity in congestion phase

One of the specific features of the stationary bivariate relation for traffic is that information propagates downstream in free-flow, and upstream in congestion. The PTM has a two-dimensional state in congestion that allows two speeds of propagation of information. The PTM is usually calibrated to have the first speed of propagation negative (see section 3.3.2) according to the stationary state theory. The second speed of propagation is always positive, and corresponds to the speed of vehicles at the upstream state. In this section we study the increased modeling capabilities brought by this feature.

PTM theory

In the congestion phase, two types of waves can arise in the PTM solution. Waves of the second type are contact-discontinuities; they connect two states $u_{\text{up}} = (\rho_{\text{up}}, p_{\text{up}})$ and $u_{\text{down}} = (\rho_{\text{down}}, p_{\text{down}})$ with identical traffic speed $v = V_{PTM}(u_{\text{up}}) = V_{PTM}(u_{\text{down}})$, and move at the speed v of traffic. This phenomenon is illustrated in Figure 3.3.

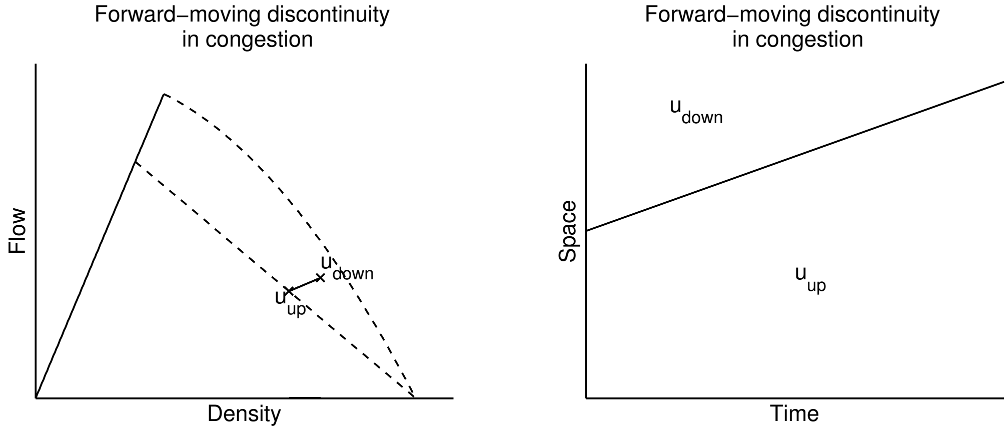

Figure 3.3: Forward-moving discontinuity in congestion.
The interaction between states u_{up} and u_{down} with the same speed, yields a forward-moving contact discontinuity in the congestion phase. Inverting the location of u_{up} and u_{down} also yields a forward-moving contact discontinuity.

This type of waves models the propagation without dispersion of traffic phases with different density and flow, but identical speed. Since the discontinuity propagates at the speed of traffic, this phenomenon does not depend on the sign of the flow difference between the upstream and the downstream phase, and, unlike for a shockwave, no mixing is introduced between the two states on each side of the discontinuity. The interface between two groups of vehicles with different densities and flow but identical speed is preserved with time.

Empirical validation

The aggregate time-space diagrams for density and speed in the I80 5-5:30 dataset are presented in Figure 3.4.

In addition to several backward moving shock waves spanning the entire domain, we observe a clear forward-moving discontinuity emanating from the upstream of the section around time 750 seconds. A number of forward-moving discontinuities are observed during the episodes of light congestion (blue in figure 3.4). One may note that the forward-moving discontinuities for the episodes of light congestion travel faster than the forward moving discontinuity corresponding to heavy congestion (red in figure 3.4), as the PTM would predict. Finally the comparison of the top and bottom plots of Figure 3.4 illustrates that discontinuities in density can propagate forward or backward, whereas discontinuities in speed only propagate backward, which corresponds to the constitutive properties of the PTM. The ability of the model to reproduce this phenomenon is illustrated in section 3.3.3.

3.2.4 Hysteresis phenomenon

The phenomenon of hysteresis has been studied with much attention by the transportation community [176, 214, 232], with different candidate explanations; acceleration and deceleration waves, heterogeneous drivers, lane changes. Recent results [144] seem to discard the hypothesis of acceleration and deceleration waves in favor of the hypothesis of heterogeneous drivers. The model proposed is consistent with this theory in the sense that loops can form in both directions, irrespective of the speed gradient.

The existence of hysteresis loops in density-flow coordinates can be traced back to the solution to the Riemann problem (second case of u_{up}, u_{down}, in the congestion phase T_c). An intermediary state u_{m} arises between the initial upstream state u_{up} and the initial downstream state u_{down}. The upstream state u_{up} and the intermediary state u_{m} have the same value of the average aggressiveness per driver p/ρ. The downstream state u_{down} and the intermediary state u_{m} have the same value of speed v. The relative value of these two quantities for the upstream and downstream states u_{up} and u_{down} impacts the orientation of the loop (see Figure 3.5).

Only two configurations are possible in congestion for which no hysteresis loop arises.

- In the case of an upstream state u_{up} and a downstream state u_{down} with the same value of the average aggressiveness p/ρ, no hysteresis occurs, and the only difference introduced by switching the two states is the change of nature of the connecting wave (shock or rarefaction).

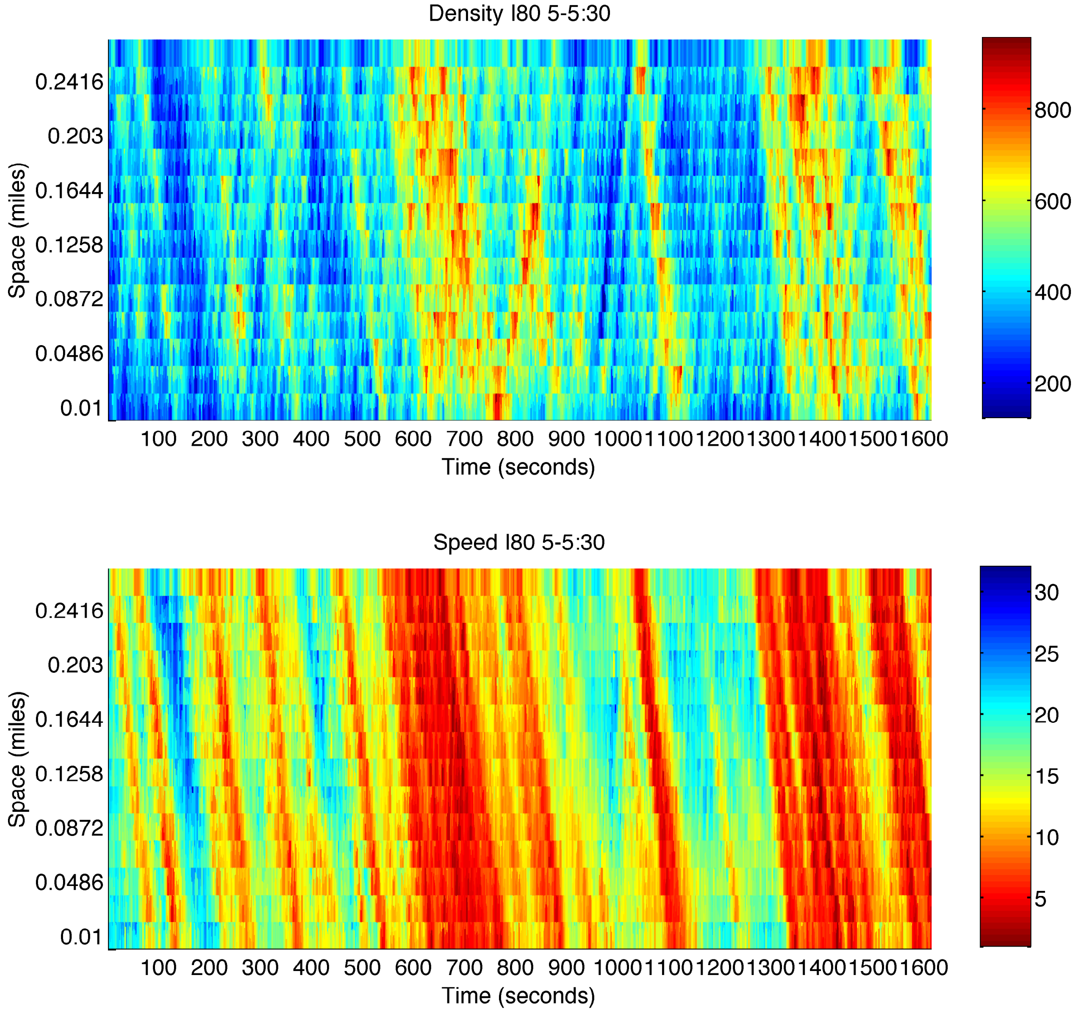

Figure 3.4: I80 5-5:30 time-space diagrams for NGSIM dataset.
Density is expressed in vehicles per mile, speed is expressed in miles per hour. A forward-moving discontinuity corresponding to heavy congestion (in red) arises from the upstream boundary around time 750 seconds. No forward-moving discontinuity in speed is observed. The top subplot corresponds to density and the bottom subplot corresponds to speed.

- In the case of an upstream state u_{up} and a downstream state u_{down} with same value of speed v, the connecting wave is a contact discontinuity for the two permutations of the initial setting, and corresponds to the forward-moving discontinuity described in section 3.2.3.

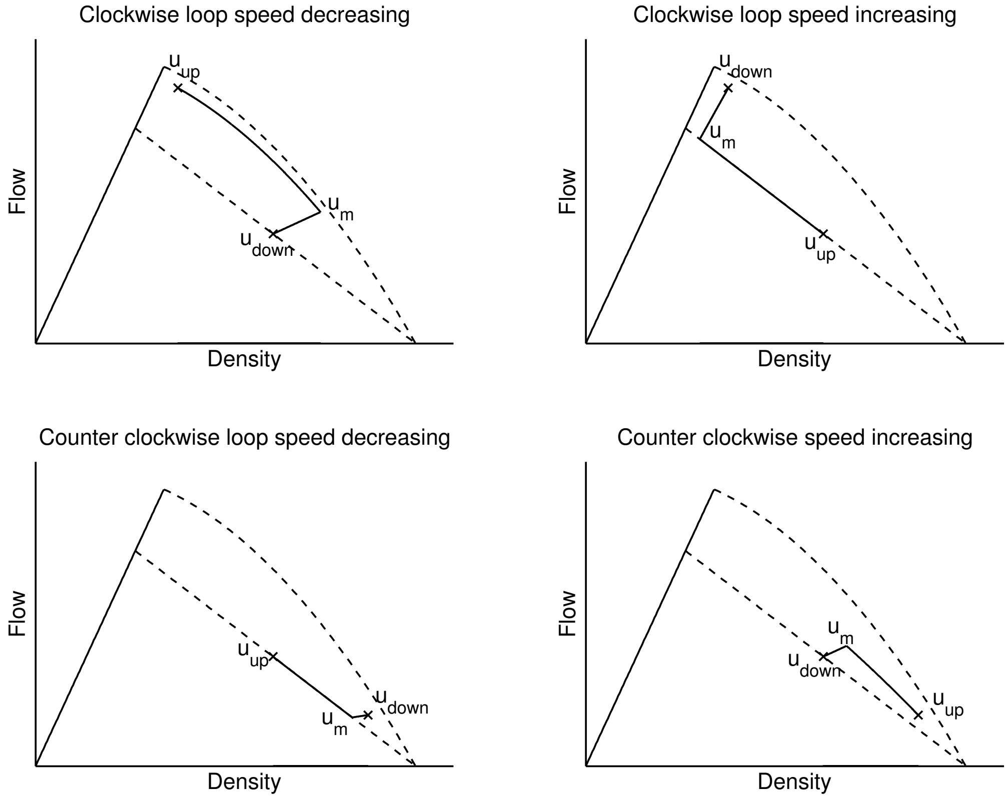

Figure 3.5: Hysteresis patterns.
Between upstream and downstream states, u_{up} and u_{down}, respectively. Clockwise loops (top row) introduce values of the density outside of the interval defined by the initial densities of the upstream and downstream states. Counterclockwise loops (bottom row) introduce values of the flow outside of the interval defined by the flows of the initial upstream and downstream states.

The type of hysteresis phenomena modeled by the PTM is similar to the hysteresis described in [233], and can be physically explained using the mesoscopic interpretation presented in section 3.2.1. The NGSIM dataset used in this study unfortunately did not enable us to observe any of these phenomena directly (the dataset is very limited in time and space). Note that these hysteresis phenomena are for macroscopic quantities, not for trajectories (see [144] for instance).

3.2.5 Phantom jam

The emergence and propagation of traffic disturbances causing drivers to decrease their speed for no clear reason in congestion, or so-called phantom jams, is well-known to most commuters and the topic of active research, with recent explanations tracing its cause back to the heterogeneity of driving behaviors [146]. It is clear from the solution to the Riemann problem that the PTM is not able to model the emergence of extreme[3] values of speed. However, in this section we show that the PTM is able to model the emergence of extreme values of density and flow.

We motivate the subsequent macroscopic description by the mesoscopic model described in section 3.2.1, in which drivers from an upstream phase adjust their speed to the speed of the drivers from the downstream phase, according to their own driving behavior. One might note that this mesoscopic model can be obtained similarly by expressing the fact that upstream drivers maximize their speed under the constraint of their driving behavior, and the speed of the downstream drivers, that they cannot exceed without creating an accident.

In the congestion phase, the solution to the Riemann problem associated with the PTM exhibits different types of hysteresis loops (see previous section). It is clear that the intermediary state arising always has a speed in the interval defined by the speeds of the upstream and downstream states. However, different loop behaviors can arise (see Figure 3.5):

1. Clockwise loops are the cause of the emergence of intermediary states with extreme values of density (top row). In the case of a transition from a high speed to a low speed, a higher value of density arises (top left case) whereas in the case of a transition from a low speed to a high speed a lower value of density arises (top right case).

2. Counter-clockwise loops are the cause of the emergence of intermediary states with extreme values of flow (bottom row). In the case of a transition from a high speed to a low speed, a lower value of flow arises (bottom left case) whereas in the case of a transition from a low speed to a high speed a higher value of flow arises (top right case).

In the four cases described above, from a mesoscopic perspective, the difference in flow and density between the downstream state u_{down} and the middle emerging state u_{m} is explained by the fact that the upstream and downstream drivers have different levels of aggressiveness, translating into different preferred spacing for the same speed.

This feature of the PTM seems appropriate for modeling the propagation of disturbances in traffic. In Figure 3.5, one can note that if u_{down} is viewed as a disturbance of u_{up}, then the intermediary state u_{m} arising is always an amplified disturbance, in density or flow, and this amplified disturbance travels upstream (negative wave speed connecting u_{up} and u_{m}). Note that this phenomenon is a locally convected phenomenon, i.e. it results from the emergence of u_{m} from u_{up} and u_{down}. It is very different from convective instabilities commonly observed in fluids, characterized by a dispersion relation [190], that amplify over time.

---

[3] In the context of a Riemann problem, by extreme value of speed we mean a value of speed outside of the interval defined by the speeds of the upstream and downstream states.

3.3 Phase transition model validation

In this section we present the datasets and the numerical methods used in the following model calibration and model comparison.

3.3.1 Vehicle trajectories datasets

Datasets specifications

We consider the following NGSIM datasets [179] from highway I-80:

1. **I-80 4:00-4:15**: vehicles trajectories are recorded at a 0.1 second resolution for a 0.34 miles stretch of freeway I-80 Northbound at Powell Street, Emeryville, CA, with 6 lanes including a HOV lane, during 15 minutes from 4 pm to 4:15 pm (2052 vehicles). We consider the middle stretch from relative mile 0.03 to relative mile 0.3, which is a straight line. We remove the first and last 100 seconds to avoid boundary effects. We discretize the dataset into 14 cells and 749 time-steps.

2. **I-80 5:00-5:30**: vehicles trajectories are recorded at a 0.1 second resolution for a 0.34 miles stretch of freeway I-80 Northbound at Powell Street, Emeryville, CA, with 6 lanes including a HOV lane, during 30 minutes from 5 pm to 5:30 pm (3626 vehicles). We consider the middle stretch from relative mile 0.03 to relative mile 0.3, which is a straight line. We remove the first 100 and last 250 seconds to avoid boundary effect. We discretize the dataset into 14 cells and 1104 time-steps.

The choice of the number of cells for discretization of the dataset is driven by the sampling frequency of the collected data for accurate computation of flow, density and speed according to Edie's generalized definition [84]. We want to have a time-step "large" compared to the sampling period and a cell size "large" compared to the distance traveled by the vehicles during a sampling period (see [155] for a detailed discussion on the notion of scale in traffic modeling). Here we consider a time-step of 10 times the sampling period, and a cell-size of 10 times the distance traveled at the free-flow speed (taken as 70 mph) between two consecutive reports. The average point speed of the vehicles is 17 mph and 12 mph for I-80 4:00-4:15 and I-80 5:00-5:30, respectively. The discretization parameters for each dataset are given in table 3.2.

	Sampling period	Time-step	Cell size	Average ♯ points per cell
I-80 4-4:15	0.1 sec	1 sec	102 feet	71 points
I-80 5-5:30	0.1 sec	1 sec	102 feet	96 points

Table 3.2: Discretization parameters for NGSIM dataset.
The time-step and cell-size are chosen as a function of the sampling period.

In the following analysis, we consider the computed values of density, flow and speed according to Edie's generalized definition, for the discretization grid associated with the parameters from table 3.2, as *ground-truth* traffic state for benchmarking the performances of the PTM and the CTM.

Dataset properties

The density time-space diagrams of the NGSIM datasets used for model testing and validation are reproduced in Figure 3.6. In this figure, the 5 leftmost mainline lanes are considered for computation of the density, flow, and speed according to Edie's generalized definition, with discretization parameters described in previous sub section.

The dataset consists of 5 mainline lanes including an HOV lane, with an on-ramp upstream of the stretch considered and an off-ramp downstream. Several heavy congestion patterns can be observed propagating upstream at similar speeds. Heavy congestion can also be observed propagating downstream in the I80 5-5:30 dataset, starting from the upstream boundary at around 800 seconds in relative time. Several light congestion waves can also be observed propagating downstream, starting from downstream of heavy congestion, in the last quarter of the I80 4-4:15 dataset.

One may note that the datasets considered exhibit only congestion phenomena, hence only allow the validation of the PTM in the congestion phase. This is a clear limitation of the experimental results presented here, that should be complemented in the future by an analysis of the performance of the PTM on datasets more representative of general traffic properties.

In the following section, we present a method for calibrating the parameters of the PTM, and the results obtained on the datasets described in this section.

3.3.2 Model calibration

The parameters of the PTM consist of the free-flow speed, the parameters of the stationary relation used in the congestion phase, and the parameters $p_{\min}$ and $p_{\max}$, specifying the maximal admissible range around the stationary relation for the fundamental diagram in congestion.

Several algorithms can be found in the literature for calibration of a single model parameter, in particular in the case of the CTM. The jam density $\rho_{\max}$ and the free-flow speed $v_{\max}$ are usually assumed to be known, and the congestion wave speed w can be estimated using different methods. An algorithm for the estimation of the congestion wave speed based on vehicle trajectories can be found in [164]. This parameter can similarly be estimated considering a Lagrangian approach as described in [52].

In this section, we consider a methodology similar to the methodology described in [67], for joint estimation of all parameters of the model from macroscopic quantities.

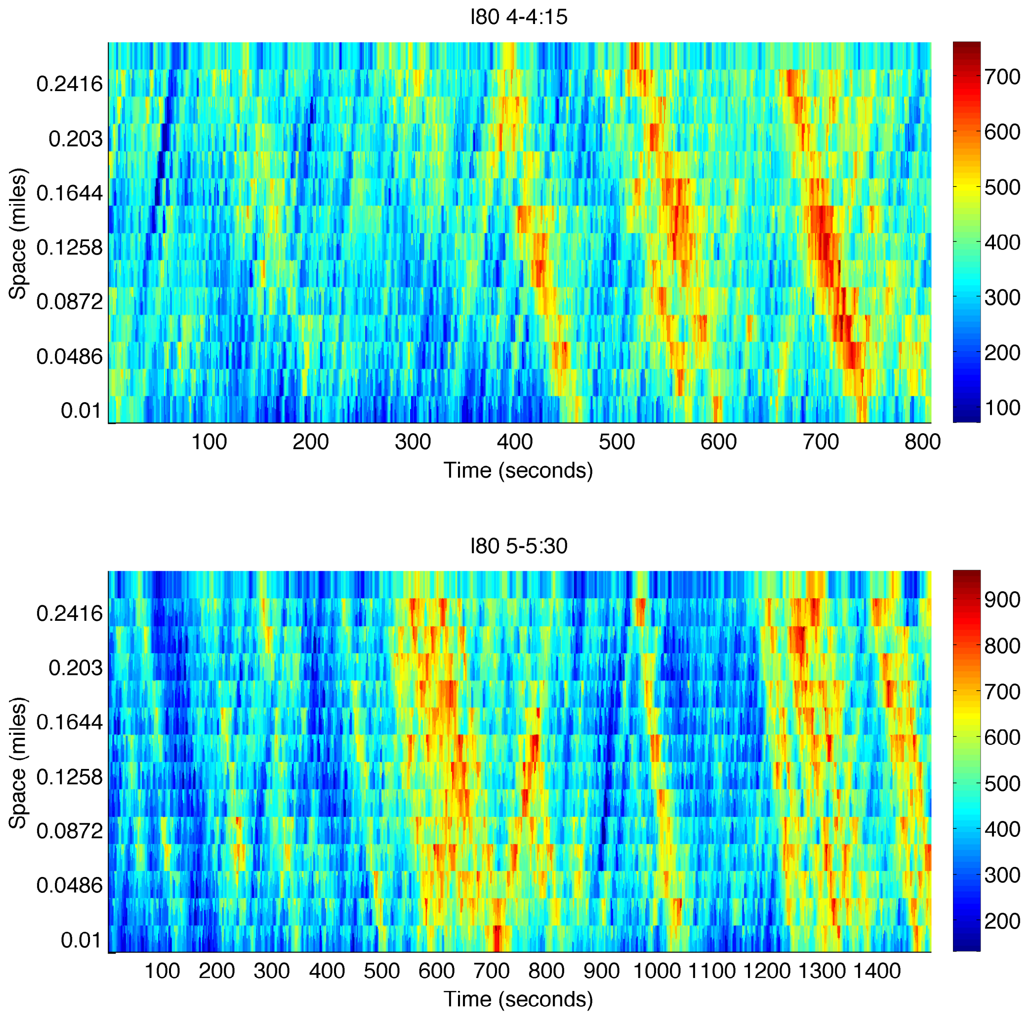

Figure 3.6: Density time-space diagrams.
I80 4-4:15 (top), I80 5-5:30 (bottom).

Methodology and results

We propose to compare the time space diagrams reconstructed by the PTM and the CTM from the knowledge of initial and boundary conditions. Given a training data set of macroscopic measurements, the method consists of the definition of a cost function, the direct computation of the initial and boundary condition, and of the identification of the set of parameters at which the minimum of the cost function is attained for the reconstructed time space diagrams. We consider the L^1 metric:

$$L^1(u_{PTM}) = \frac{\sum_n \sum_j |u_{PTM}(n\,\Delta t, j\,\Delta x) - u_{NGSIM}(n\,\Delta t, j\,\Delta x)|}{\sum_n \sum_j |u_{NGSIM}(n\,\Delta t, j\,\Delta x)|}, \tag{3.4}$$

in which we note $u_{PTM}(n\,\Delta t, j\,\Delta x)$ the value of the quantity u, at the cell indexed by n, at the time-step indexed by j, computed using the discrete PTM on a grid with discretization parameters Δt and Δx. We use a similar notation for the ground-truth u_{NGSIM} obtained by discretizing the NGSIM vehicle trajectories.

The quantities u_{NGSIM} and u_{PTM} must be defined on the same discretization grid. The reference u_{NGSIM} is defined on the physical grid described in section 3.3.1, chosen according to data availability. The discrete solution u_{PTM} to the PTM can be computed on an arbitrarily refined numerical grid. The discrete solution converges toward the analytical solution when the refinement of the numerical grid increases. The level of refinement of the grid is guided by the numerical benchmarks from [31] and [49], which provide empirical results on the distance to the analytical solution of the PDE as a function of the refinement level. The values of the reference u_{NGSIM} on the refined grid can be obtained from its values on the coarse physical grid in a straightforward manner.

In order to assess the importance of the error variable used for calibration, we propose to compute the error metric (3.4) where u is successively defined as ρ, q and v. Due to the nonlinearity of the models investigated, and the consequent non-convexity of the optimization problem considered, the cost function is optimized by exhaustive enumeration on a a grid with parameters $\Delta\rho = 10$ vpm, $\Delta v = 5$ mph, $\Delta w = 0.5$ mph, $\Delta p_{\min} = 0.1$, $\Delta p_{\max} = 0.1$. The optimal parameters for I80 4:00-4:15 and I80 5:00-5:30 are presented in tables 3.3 and 3.4 respectively. In the interest of space, we only consider the instantiation of the PTM for a triangular stationary relation, with potentially positive and negative perturbation.

The optimal parameters obtained fall into the range of plausible values from a physical perspective. There is significant dependency of the optimal parameters to the error variable (which arises for the CTM as well, but is not represented here, in the interest of space). One might note that the optimal value of the congestion wave speed obtained for the 5 aggregated lanes is greater than the typical value for a single lane (around 11.5 mph), which might be due to tentative lane changes. The optimal value of the congestion wave speed is fairly stable across error variables, however the jam density exhibits large relative variations, in particular for the I80 datasets in which the congestion level is more important.

The optimal parameters obtained for different error variables can vary significantly for a given dataset, in particular for the perturbation parameters. In the case of the density error

Error variable	Optimal parameters					Optimal L^1 error for error variable
	$\rho^*_{\max}$	$v^*_{\max}$	w^*	$p^*_{\min}$	$p^*_{\max}$	
Density (k)	160	50	14	-0.01	0.94	0.152
Flow (q)	150	40	15.5	-0.21	0.77	0.176
Speed (v)	120	40	13.5	-0.99	0.99	0.137

Table 3.3: Optimal parameters for I80, 4:00-4:15.
PTM parameters minimizing the L^1 error metric, obtained from the ground truth field for density (ρ), flow (q) and speed (v).

Error variable	Optimal parameters					Optimal L^1 error for error variable
	$\rho^*_{\max}$	$v^*_{\max}$	w^*	$p^*_{\min}$	$p^*_{\max}$	
Density (k)	190	55	13	-0.25	0.95	0.130
Flow (q)	180	55	13.5	-0.75	0.45	0.164
Speed (v)	150	55	13	-0.05	0.35	0.161

Table 3.4: Optimal parameters for I80, 5:00-5:30.
PTM parameters that minimize the L^1 error metric, obtained from the ground truth field for density (ρ), flow (q) and speed (v).

variable, one might note that the parameter $p_{\max}$ often takes larger values than the parameter $p_{\min}$ in absolute value. This corresponds to a fundamental diagram with a wider domain in congestion above the stationary relation than below, and using the mesoscopic interpretation from section 3.2.1, to a greater number of aggressive drivers than non-aggressive drivers.

One might note that a natural calibration of the PTM, which would consist in using the parameters of a calibrated CTM for the stationary relation of the PTM, and second in maximizing the spread between $p_{\min}$ and $p_{\max}$ in order to minimize the projection error described in section 3.2.2, is not obtained as a result of the optimization procedure. The optimal values of the classical parameters $\rho_{\max}$, $v_{\max}$, w of the PTM, are very similar to the optimal values of the parameters of the CTM (presented in the following section), however the parameters $p_{\min}$ and $p_{\max}$ are not often set to their extremal values. We recall that the parameter $p_{\min}$ is lower bounded by -1 to guarantee positivity of speed, and that large values of the parameter $p_{\max}$ correspond to positive first characteristic speed in congestion, which is not desirable for physical reasons. This result illustrates that the set-valued diagram of the PTM is valuable for accurate forward propagation of traffic state, but that there is a trade-off between a wide congestion phase and congestion dynamics close to the dynamics associated with the stationary relation.

Model sensitivity

The sensitivity of the error metric (3.4) to the parameters around the optimum indicates the order of magnitude of the error likely to occur in a practical setting, where uncertainties arise in the calibration procedure. These uncertainties can be due to inherent measurement noise, to numerical error in the optimization routine, or to the fact that the parameters are calibrated from a visual fit. Thus the ability of the model to guarantee good performances for parameters in a neighborhood of the optimum of the error metric is an important factor contributing to the model choice.

We propose to assess the sensitivity of the error metric to the parameters in two different ways. We compute the *partial variation* of the error metric around the optimum, i.e. the variation of the error metric when a single parameter varies around the optimum. We also compute the *total variation* of the error, i.e. the variation of the error metric when a single parameter varies around the optimum, and consequently the other parameters are re-calibrated according to this change.

Since no specific joint dependency of the error metric on tuples of parameters is observed in the numerical results, we focus our analysis on dependency along a line. In the interest of space, we do not present detailed results for the free-flow speed and the jam density. They are briefly discussed in the following sub section. Figure 3.7 presents the results for the congestion wave speed w. One may note that for both models, the *total variation* of the error metric is relatively low for variations of the congestion wave speed around its optimal value, i.e. re-calibration of the other parameters of the model is able to account for a lack of optimality of the congestion wave speed.

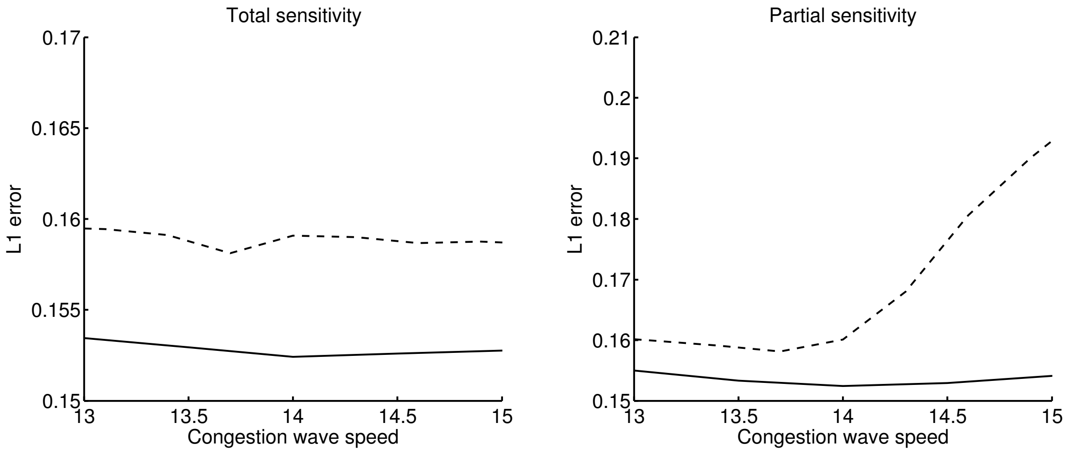

Figure 3.7: Sensitivity to congestion wave speed.
For the PTM (solid line) and the CTM (dashed line), for the I80 4:00-4:15 dataset. The left sub figure denotes the sensitivity of the *global optimum* to the value of the congestion wave speed. The right sub figure denotes the sensitivity of the error metric *along the dimension* corresponding to the congestion wave speed.

The results for the *partial variation* differ significantly for both models. It is clear that lower values of the congestion wave speed have a relatively low impact on the error metric, for both models. However, the CTM error is highly sensitive to higher values of the congestion wave speed, which can be explained by noting that the optimal free-flow speed is low, and that subsequently, modifying the value of the congestion wave speed toward higher values impacts the phase to which observations around the optimal critical density belong to. This is not the case when modifying the value of the congestion wave speed toward lower values. This high sensitivity, in the case of higher values than the optimal congestion wave speed, does not occur with the PTM, which may be due to the two-dimensional nature of the congestion phase, and the corresponding choice of the perturbation bounds $p_{\min}$ and $p_{\max}$, which illustrates the higher robustness of the PTM to calibration error for this parameter.

3.3.3 Model comparison

In this section we propose a comparative quantitative analysis of the ability of each model to reconstruct the time-space diagram from the knowledge of initial and boundary conditions.

Methodology and quantitative results

In order to assess the performance of the PTM, we propose to compare the model with a classical well-known discrete model from the literature, for which implementation details and calibration procedure are well documented: the CTM.

We assume that boundary conditions are known upstream and downstream, as well as an initial condition. These terms are computed explicitly from the spatio-temporal discretization of vehicle trajectories (see section 3.3.1). This corresponds to the computation of the solution to the IBVP defined in equation (6.2) and in practical terms to the case of measurements from sensors (loops, radars, probes, etc) available at given locations on the freeway as boundary conditions, and a spatial profile assumed to be known at some instant (cameras, satellite, empty road, etc) as initial condition. The traffic profile on the stretch of road between the sensors, from the time at which the spatial profile is known, is computed by running the models forward in time. For initial or boundary conditions falling outside of the fundamental diagram, we use the projection methods described in section 3.2.2 for both the CTM and the PTM[4].

We compare the solution to the initial-boundary value problem for the CTM and the PTM as follows:

- **Training procedure:** we calibrate the model parameters on the I80 4:00-4:15 dataset, for the error variable density.

---

[4] For completeness, different projections have been tested for the PTM, in particular iso-density in the congestion phase. The results obtained are not significantly different from the ones presented in this section and are omitted in the interest of space.

- **Testing procedure:** we compare the models on the I80 5:00-5:30 dataset on the reconstructed density, flow, speed fields. We use the set of parameters obtained from the training procedure.

The optimal parameters for the PTM are the following: $\rho^*_{\max} = 160$ vpm, $v^*_{\max} = 50$ mph, $w^* = 14$ mph, $p^*_{\min} = -0.01$, $p^*_{\max} = 0.94$, with an error of 0.152 on the training set. The CTM is calibrated using the procedure described in previous section and the obtained optimal parameters are the following $\rho^*_{\max} = 160$ vpm, $v^*_{\max} = 25$ mph, $w^* = 13.7$ mph, with an associated error of 0.158 on the training set.

Remark 3.1. *The values of the free-flow speed* $v_{\max}$ *obtained after calibration can be significantly lower than classical values for both models (e.g. for the CTM in the case of the I80 4:00-4:15 dataset, with values of* 25 *mph). It is clear that the cost function does not depend on the free-flow speed for sufficiently high values of the free-flow speed. Since the NGSIM datasets exhibit heavy to moderate congestion with maximal speeds between* 20 *mph and* 30 *mph (see figure 3.1), it is expected that optimal values of the free-flow speed fall above this range. Further analysis show that for all datasets, the cost function increases by about* 1 *percent per mph for free-flow speed values under the optimal free-flow speed, however the variations of the cost function stay within a* 0.5 *percent range for values of the free-flow speed higher than its optimal value. Since the I80 5:00-5:30 dataset exhibits heavier congestion than the I80 4:00-4:15 dataset, this remark legitimates the use of the free-flow speed calibrated on the I80 4:00-4:15 dataset for testing on the I80 5:00-5:30 dataset.*

We compute the L^1 error (3.4) for the three error variables density, flow and speed, for the single set of optimal parameters based on the error variable density. The results for the CTM and the PTM are presented in table 3.5.

	Density	Flow	Speed
PTM	0.139	0.167	0.165
CTM	0.146	0.242	0.227

Table 3.5: Model accuracy.
L^1 error for parameters obtained for the error variable density, between the reconstructed profile and the ground-truth profile for density, flow, and speed, for the CTM and the PTM.

The results from the left column of table 3.5 illustrate that the CTM and PTM have similar performances for the error variable for which they are calibrated (density in table 3.5), which is consistent with the fact that the PTM is a direct extension of the LWR model in congestion, and specifically of the CTM for the numerical results presented in this section. In particular, the results on the test set are better than the results on the training set, which is satisfying with regard to over-fitting. The results illustrate that even though the PTM has a larger state-space, the corresponding dynamics do not necessarily provide significant added value compared to the CTM, for the error variable used for calibration.

However, the PTM shows a clear superiority for other relevant traffic variables (flow and speed in that case), for which the model was not calibrated. For both the variable flow and speed, the error is reduced by at least 25 percent by the PTM compared to the CTM. This illustrates that the PTM calibration is more robust in the sense that optimal parameters for a given error variable yield a low error for other error variables as well. In the following section, we study the difference in the reconstructed time-space profiles from a qualitative perspective.

Qualitative analysis

The time-space diagrams for the dataset I80 5:00-5:30 with the discretization parameters detailed in section 3.3.1 are represented in figure 3.8 for the CTM, the PTM and the ground-truth profile obtained directly by discretization of the vehicles trajectories. One may note that flow and speed are computed a posteriori from the density field in the case of the CTM, whereas in the case of the PTM, speed is obtained from the density ρ and perturbation p fields, and the flow is obtained classically as a product of density and speed.

The comparison of the reconstructed density fields for the CTM and the PTM shows that the PTM is able to some extent to propagate forward observations gathered at the upstream boundary. The capability of the PTM for hysteresis modeling is illustrated for the density variable in the second part of the time domain for the upstream part of the section, where interactions between forward moving discontinuities and backward moving shock waves yield curved propagation of congestion waves. However, one might note that the impact of these more complex phenomena is not clear overall since the L^1 error for density is similar for the two models (table 3.5, left column).

The comparison of the reconstructed flow fields for the CTM and the PTM shows that the PTM allows the propagation of forward moving discontinuities in flow, and density, within the backward moving congestion phase around the center of the time period. The comparison of the reconstructed speed fields for the CTM and the PTM shows that the PTM captures more extensively the high speed waves at the beginning of the time period. Similarly, high speed values around the center of the time period, and the downstream end of the section, are more accurately captured by the PTM.

The numerical performances of the phase transition model illustrated in this chapter on the NGSIM dataset in a forward-simulation context are promising for real-time data assimilation applications. Specific interest of the PTM for traffic monitoring lies in its ability to model both the evolution of the density and the velocity field, using a system of conservation laws. In the current context of traffic information systems in which both probe data measuring individual speeds and classical fixed infrastructure measuring quantities related to the density and the flow, the need for such complex models is more and more important.

In the following chapter, we present relevant related concepts from the estimation theory perspective.

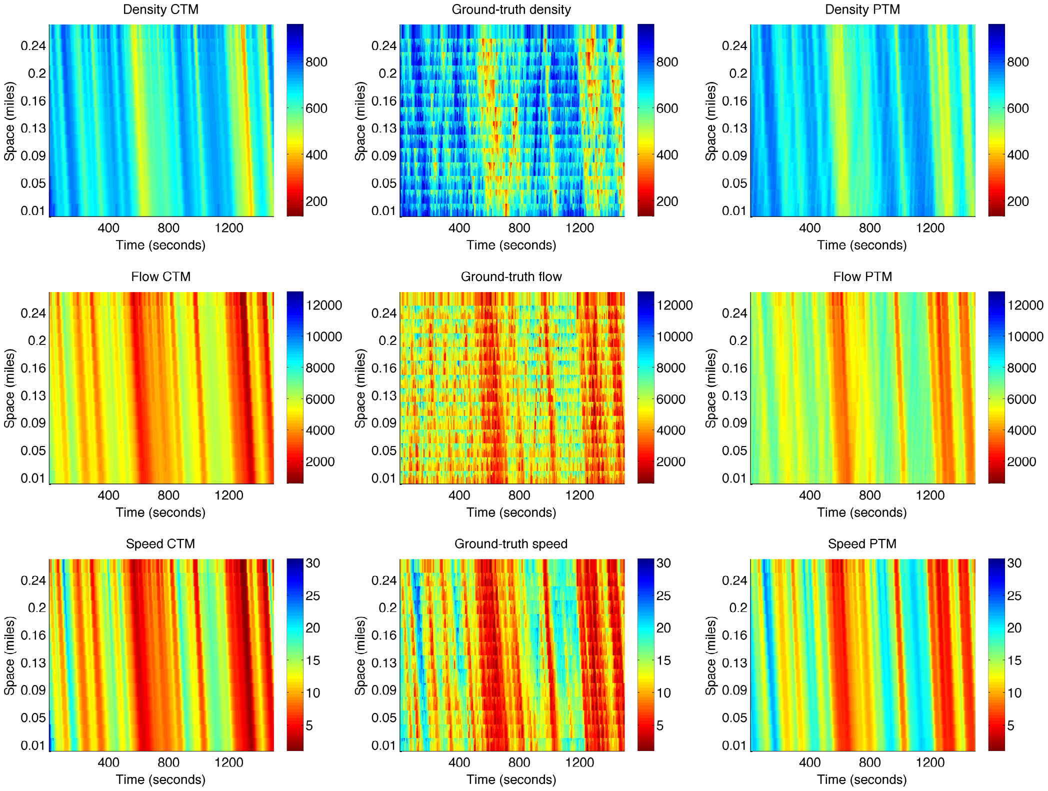

Figure 3.8: Time-space diagrams.
For I80 5-5:30, for density (top row), flow (center row), speed (bottom row), for the CTM (left column), the PTM (right column) and the ground-truth profile (center column).

Chapter 4

Advanced estimation methods for distributed systems

In this chapter, we consider the estimation problem, which consists in the computation of the best estimate of a statistical process, given available measurements and a statistical or physical underlying model. We present two frameworks in which the estimation problem for distributed systems can be posed; *Bayesian networks* articulated around the efficient representation of joint distributions by conditional probabilities, and *Kernel methods*, which allow the formulation of the best state-space representation of a given system as a convex optimization problem.

4.1 Bayesian networks

Most physical principles assumed by classical traffic models can be seen as defining information propagation rules. For scalar macroscopic models, the mass conservation principle yields a *partial differential equation* (PDE) which can be directly solved by a *wavefront tracking* method [39], or numerically by the *Godunov* scheme [103]. Both of these methods provide an encoding of the spatio-temporal dependencies of the physical system. Unlike in the estimation problem, in which the model errors can be corrected via observations, the forecast problem relies heavily on an accurate model as the forecast error grows with the length of the forecast horizon [131]. Thus, knowing the exact dependency structure of the network is crucial for traffic forecasting applications.

Bayesian networks [125, 128, 184] provide an efficient framework to represent and work with dependencies in distributed systems, in particular to address fundamental problems such as learning and inference. This statistical framework allows us to learn the conditional dependencies that best fit the data and avoid the need for detailed assumptions regarding the physical system, which are often unknown or inaccurate. Thus, Bayesian models are more flexible and capture a variety of traffic phenomena, unlike classical models. Once the dependency structure of the network is identified, it can be used to forecast the evolution of traffic conditions.

4.1.1 Mathematical formulation

A Bayesian network is a directed acyclic graph in which each vertex represents a random variable and an edge between two vertices implies a dependence between the two random variables, where the strength of the influences is represented by conditional probabilities [184]. We consider a directed acyclic graph $\mathcal{G}(\mathcal{V}, \mathcal{E})$ where $\mathcal{V} = \{\mathcal{V}_{n,t} | (n, t) \in \{1, \ldots, N\} \times \{1, \ldots, T\}\}$ is a set of vertices and $\mathcal{E}$ is a set of directed edges [128]. Each vertex $\mathcal{V}_{n,t}$ in the graph is naturally associated with a random variable representing the traffic velocity at a spatio-temporal location indexed by n for the spatial dimension and by t for the temporal dimension. A typical Bayesian network is outlined in Figure 4.1. The graph structure encodes the *Markov conditions* [184] which state that each vertex $\mathcal{V}_{n,t}$ is independent of its non-descendants given its parents. The probability of a set of values $\mathcal{D} = (\nu_{1,1}, \ldots, \nu_{N,T})$ for a graph $\mathcal{G}$ with a parameter set Θ reads:

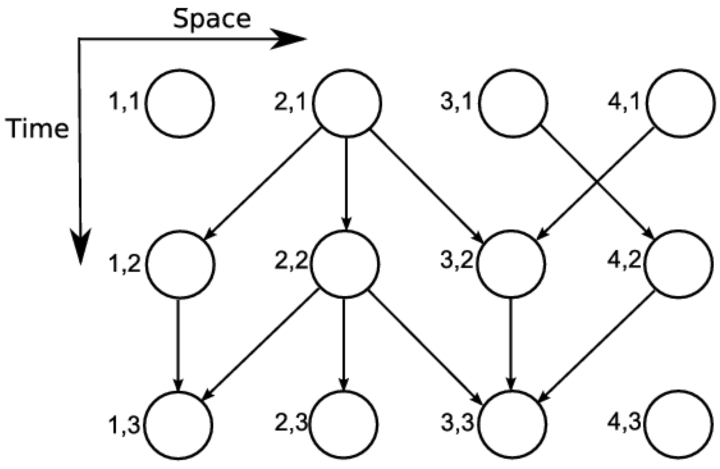

Figure 4.1: Bayesian network for vehicular traffic.
Traffic dependencies are modeled by a Bayesian network in which each vertex represents the distribution of traffic velocity at a given spatio-temporal location. The horizontal dimension corresponds to space and the vertical dimension corresponds to time.

$$p(\mathcal{D}|\Theta, \mathcal{G}) = \prod_{n=1}^{N} \prod_{t=1}^{T} p(\nu_{n,t} | \pi_{n,t}, \Theta),$$

where $\pi_{n,t}$ denotes the set of parents of the vertex $\mathcal{V}_{n,t}$, and $\mathcal{D}$ the data (observations). Realizations of random variables are denoted by lower-case letters. The term Θ denotes the parameters of the joint distribution of the graph. The *log-likelihood* for a dataset $\mathcal{D}$ on the graph $\mathcal{G}$ is given by:

$$l(\mathcal{D};\Theta,\mathcal{G}) = \sum_{n=1}^{N}\sum_{t=1}^{T}\log p(\nu_{n,t}|\pi_{n,t},\Theta). \tag{4.1}$$

In a typical learning framework, in which the conditional distributions are more often available, equation (4.1) conveniently expresses the likelihood of the data in terms of local conditional probabilities. In the case in which joint distributions are available, this expression can be transformed to:

$$l(\mathcal{D};\Theta,\mathcal{G}) = \sum_{n=1}^{N}\sum_{t=1}^{T}\log p(\nu_{n,t},\pi_{n,t}|\Theta) - \log p(\pi_{n,t}|\Theta),$$

where the first term is assumed to be known as the joint distribution of a vertex and its parents. The second term can be computed by marginalizing out the vertex $\mathcal{V}_{n,t}$ [128]. As illustrated in Figure 4.1, Bayesian networks are an efficient tool to represent complex dependency relations between random variables. However, Bayesian network theory depends on strong assumptions regarding the generative distributions being modeled, such as symmetry, decomposition and intersection properties described in [184]. For example, the generative distribution of $\mathcal{G}$ is required to satisfy the *decomposition* axiom, which states that if $\forall\, Y \in \mathcal{Y}$, X is independent of Y, then X is independent of $\mathcal{Y}$ (with X, Y being two nodes of the network and $\mathcal{Y}$ a set of nodes). This property is satisfied by the Gaussian distribution. However, it is not satisfied by most probability distributions (see [184] for an example and [133] for the general case). This is a strong motivation for the choice of the Gaussian distribution as the generative distribution for our problem in the following section.

4.1.2 Bayesian network for traffic modeling

In the case of traffic, space and time are discretized into intervals of respective size Δx and Δt. Each vertex of the Bayesian network has a spatio-temporal index $(n,t) \in \{1,\ldots,N\}\times\{1,\ldots,T\}$, and thus the Bayesian network has a grid form (Figure 4.1). In particular, the discretization grid used for the Godunov scheme could be used for Bayesian network definition. The horizontal dimension represents space and the vertical dimension represents time. Each vertex $\mathcal{V}_{n,t}$ is associated with a probability distribution which represents the traffic velocity at the corresponding spatio-temporal location. A directed edge between two vertices implies a dependence between the corresponding velocity distributions. In order to use Bayesian representation of traffic, the following assumptions can be made.

Assumption 4.1. *Traffic state evolution can be represented by a Markov process.*

In particular the dependency structure learned only depends on the dynamics of the traffic state. The parameters of the dependency structure are the parameters of the state transition matrix of a Markov process. This assumption ignores the recurrence of traffic conditions based on the time of day and day of week.

Assumption 4.2. *Traffic state evolution can be modeled as a linear function of past observations.*

For tractability, it is common practice to assume that the traffic state distributions belong to the Gaussian family. In particular the Gaussian family is closed under the conditional operator, and conditional Gaussian distributions have expressions analytical in the parameters of the original distributions [83]. Using Gaussian distributions to model spatio-temporal traffic state dependencies corresponds to the assumption that locally, traffic state evolution can be considered to be linear in the observations. According to the triangular model of traffic [71, 177], this assumption is true within a single traffic phase (free flow or congestion).

Specific traffic properties can be summarized by the following set of constraints $\mathcal{C}$ on the structure of a graphical representation of a traffic model.

$$\mathcal{C} = \begin{cases} \forall(\nu_{n,t}, \nu_{n',t}) \in \mathcal{V}^2, \ (\nu_{n,t}, \nu_{n',t}) \notin \mathcal{E} \\ \forall(\nu_{n,t}, \nu_{n',t'}) \in \mathcal{V}^2 \text{ s.t. } t < t', (\nu_{n',t'}, \nu_{n,t}) \notin \mathcal{E} \end{cases} \tag{4.2}$$

The first line in equation (4.2) states that there is no direct dependency relationship between the velocity on the highway at two different locations at the same time step. The second line in equation (4.2) states that the traffic state at a given time period can only impact the traffic state at a future time period, i.e. information does not propagate backwards in time.

Remark 4.1. *Any graph $\mathcal{G}$ generated under the structure constraint $\mathcal{C}$ expressed by* (4.2) *is acyclic.*

This feature is of crucial importance for the tractability of a structure learning algorithm.

4.1.3 Bayesian structure learning

Problem formulation

Structure learning is a natural problem in Bayesian network theory [125, 128]. Given a set of vertices $\mathcal{V}$ and a set of constraints $\mathcal{C}$ on the Bayesian network, the structure learning problem consists of finding an optimal set of edges $\mathcal{E}$ and an optimal set of distribution parameters Θ for the application of interest. A standard approach to this problem is the maximization of a *score function*. In general, for correctness and tractability of use, a score function should satisfy the following properties:

- The *decomposability* property states that the score can be decomposed in a sum of local scores. This allows efficient comparison of structures by local comparisons.

- The *asymptotic consistency* property states that in the limit of a large number of samples, the score function prefers the model with the fewest number of parameters. A more formal definition can be found in [54].

- The *local consistency* of the score guarantees that a locally greedy structure search nudges the model in an optimal direction. It states that if two vertices $\mathcal{V}_j$ and $\mathcal{V}_i$ are not independent from each other given the parents of $\mathcal{V}_i$ in the generative distribution, then adding the edge $\mathcal{V}_j \rightarrow \mathcal{V}_i$ increases the value of the score function. Similarly, if they are independent given the parents of $\mathcal{V}_i$, adding the edge $\mathcal{V}_j \rightarrow \mathcal{V}_i$ decreases the score function.

The *Bayesian Information Criterion* (BIC) score [110, 197], satisfies all of the conditions listed above and is one of the most commonly used score functions. The BIC score is given by:

$$S_{BIC}(D, \mathcal{G}, \Theta) = \log P(D|\Theta, \mathcal{G}) - \frac{d}{2} \log m + \mathcal{O}(1) \tag{4.3}$$

where D is the data, Θ is the maximum likelihood distribution parameters for D, d is the number of edges, and m is the sample size per vertex. The BIC score is an approximation of the *Bayes-Dirichlet* score [197], which expresses the posterior probability of the network parameters Θ given the data D.

The structure learning problem can then be formulated as an optimization problem. Given a set of vertices $\mathcal{V}$, a set of constraints $\mathcal{C}(4.2)$ on a network structure, a score function $\mathcal{S}_{BIC}$ (4.3), and a dataset $\mathcal{D}$, we consider the following problem:

$$\begin{aligned} \max_{\Theta, \mathcal{E}} \quad & \mathcal{S}_{BIC}(\mathcal{D}, \mathcal{G}(\mathcal{V}, \mathcal{E}), \Theta) \\ \text{subject to:} \quad & \mathcal{G}(\mathcal{V}, \mathcal{E}) \text{ satisfies } \mathcal{C} \end{aligned} \tag{4.4}$$

Solving this problem produces the structure of the Bayesian network most likely to explain the observed data given the modeling constraints [192]. The solution of this optimization problem consists of the set of edges and the distribution parameters which are the closest to the generative distribution in the *BIC* score sense.

The structure learning step corresponds to a classical model identification and model calibration steps. A calibrated model can also be used for state estimation in a state-space formulation.

Structure learning algorithm

In general, finding the optimal Bayesian network structure given a dataset $\mathcal{D}$ requires searching through the entire *directed acyclic graph* (DAG) space and selecting the graph $\mathcal{G}$ with the highest score function value $S(D, \mathcal{G}, \Theta)$. This is clearly intractable given that the size of the DAG space is super-exponential in the number of vertices.

Definition 4.1. *We define a valid topological ordering to be an ordering where the vertices are sorted by ascending time index.*

Given the constraint set $\mathcal{C}(4.2)$ and the resulting property stated in Remark 4.1, we can reduce the DAG space to a set of topological orderings of the vertices that satisfy the constraints.

Lemma 4.1. *All topological orderings are equivalent. As stated in the constraint set $\mathcal{C}$, there are no dependencies between vertices with the same time index, thus all topological orderings allow for the same set of dependencies.*

As a result, the DAG space can be limited to a single topological ordering of the vertices. The restricted DAG space given the constraint set $\mathcal{C}$ is however exponential in the number of vertices in the network. While the general structure learning problem is this setting is hard, more tractable solutions exist for finding an *inclusion-optimal* model. An inclusion-optimal model is a Bayesian network that contains the generative distribution and has no subgraph with the same set of independence relations[1]. In general, the inclusion-optimal structure must be found by searching over all topological orderings. However, as explained above, given the constraints of our problem it is sufficient to consider one arbitrary valid topological ordering.

Algorithm 1 *Greedy equivalence search algorithm for traffic modeling.* Forward phase: edge additions which maximize the increase of the score function. Backward phase: Edge removals which do not decrease the score function.

```
Define the edges $\mathcal{E} = \emptyset$
Define topological ordering satisfying the constraints $\mathcal{C}$
Forward phase
for each vertex $\mathcal{V}_{n,t}$ do
    for each candidate parent $\tilde{\pi}_{n,t}$ do
        Compute the score of the graph with the additional edge $(\mathcal{V}_{n,t}, \tilde{\pi}_{n,t})$
        Keep the local structure maximizing the score
    end for
end for
Backward phase
for each vertex $\mathcal{V}_{n,t}$ do
    for each parent $\pi_{n,t}$ do
        Compute the score of the graph with the edge $(\mathcal{V}_{n,t}, \pi_{n,t})$ removed
        Keep the local structure maximizing the score
    end for
end for
```

We adapt the *greedy equivalence search* (GES) algorithm[2] from [54] that finds an inclusion-optimal Bayesian network to solve our structure learning problem. The pseudocode for the modified version of this greedy search algorithm is given in Algorithm 1. The

---

[1] This is not necessarily optimal in the general sense as there might be a graph with fewer edges that also contains the generative distribution.

[2] In addition to the properties listed in the previous subsection, this algorithm also requires that $\mathcal{G}$ satisfies the path property [54] which expresses that a dependency in $\mathcal{G}$ can be characterized by the existence of a path between vertices.

algorithm consists of two phases, a *forward phase* with edge additions and a *backward phase* of edge removals. Edge additions and removals are performed only when they increase the score function. The set of *candidate parents* of a vertex is a parameter of the algorithm which denotes the set of possible parents considered for each vertex in the forward phase of the algorithm. In Section 6.3 (Figure 4.3) we analyze the sensitivity of the algorithm to this parameter.

The simplified version of the greedy equivalent search algorithm from [54] is used to solve the optimization problem (4.4). The search algorithm given in Algorithm 1 has a manageable complexity that is linear in its inputs. The complexity is equal to the product of the sample size $|\mathcal{D}|$, the number of vertices in the Bayesian network $|\mathcal{V}|$, and the size of the candidate parents set. It should be noted that this structure learning procedure easily lends itself to be distributed over a parallel computing framework, due to the *local consistency* property of the score function.

Numerical results

In this section we present results on sensitivity and robustness to noise with a benchmark dataset. Results on the velocity forecast accuracy and its impact on route choice with experimental traffic data from the *Mobile Millennium* traffic estimation system can be found in [192].

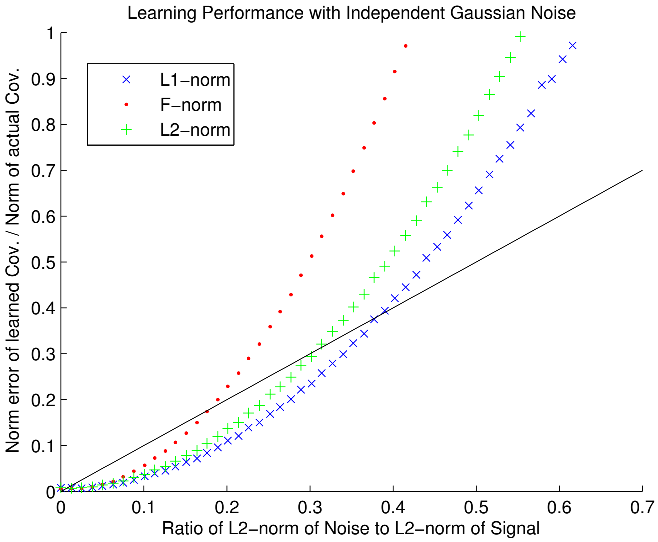

Figure 4.2: Stability of the structure learning algorithm.
The relative error in the covariance matrix increases with respect to the relative L^2 norm of the noise with respect to the data. The algorithm is able to reconstruct the covariance structure reasonably well for relative L^2 norm of the noise lower than 0.2.

We study the performance of the structure learning algorithm for two criteria; first the robustness to noise in the training set, second the impact of the optimal number of parents on the forecast accuracy with synthetic data.

In order to study the robustness of our structure learning algorithm, we consider a dataset generated from a probability distribution corresponding to the Bayesian network detailed in Figure 4.1. We then add independent and identically distributed Gaussian noise to each observation in the network. This is assumed to model a real life situation, where the data does not correspond exactly to a given generative distribution, but is subject to sensing, processing and modeling errors. The results from Figure 4.2 show that the structure learning algorithm is stable (error in the structure of the joint covariance matrix learned is lower than the error in the signal) up to reasonably high relative values of noise to signal ratio.

We also analyze the sensitivity of the forecast accuracy to the number of parents using synthetic data from the graph from Figure 4.1. The complexity of the algorithm increases linearly with the size of the candidate parents. Therefore, it is important to understand the trade-off between accuracy and computation time.

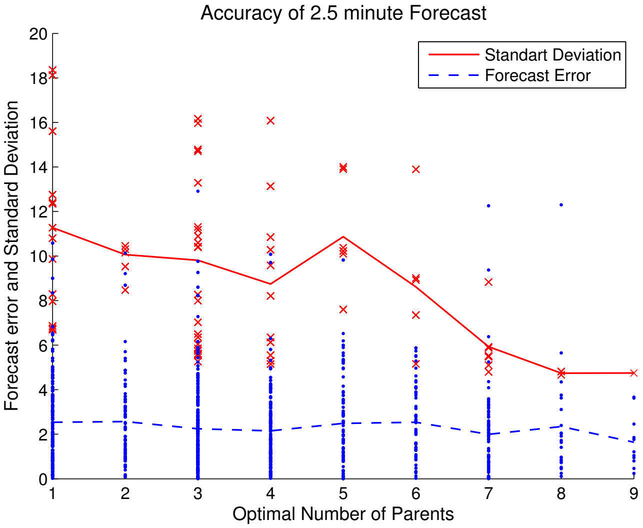

Figure 4.3: Dependency to optimal number of parents
Traffic state forecast at locations which depend on a high number of parents have the same forecast mean error in average (dashed blue line) but a smaller standard deviation (continuous red line).

The results from Figure 4.3 show that the accuracy of the forecast mean is not significantly impacted by the optimal number of parents. However, the forecast standard deviation error decreases with the number of parents. More information leads to a tighter estimate, which is what would be expected from a statistical estimate that is unbiased and consistent. This is of particular importance for applications which focus on distributed quantities such as travel time.

Bayesian networks are particularly appropriate for the formulation of estimation and forecast problems for distributed systems. However, in the case of unobserved variables, the computational cost associated with Bayesian networks can be become significant. In the following section, we present a framework based on convex programming, which allows the identification of the optimal model parameters in a very efficient manner.

4.2 Kernel method for state-space identification

Kernel regression methods can be considered as an extension of regression techniques, for which the underlying relation between covariates and responses is not pre-defined in advance.

4.2.1 Regression methods

We consider the following problem of model identification between a set of covariates x_i, e.g. entry times on a road section, and responses y_i, e.g. travel-times on the road section.

Given the knowledge of a dataset of size N noted $\mathcal{S} = \{(x_i, y_i) \in \mathbb{R}^+ \times \mathbb{R}^+ | i = 1, \cdots, N\}$, the objective consists of learning a function $h : \mathbb{R}^+ \to \mathbb{R}^+$ which given $\mathcal{S}$, would provide an estimate of the travel time y for any $x \in \mathbb{R}^+$. In the linear case for the L^2 norm, the well-known unconstrained least-squares method reads:

$$\min_\theta \quad \|y - x^T \theta\|_2^2 \tag{4.5}$$

where $y \in \mathbb{R}^{N\times 1}$ is the vector of realized travel time or output, $x^T \in \mathbb{R}^{N\times 1}$ is the vector of entry time or input. One must note that here x is a row vector and y is a column vector so θ is a scalar. The well-known solution of this problem can be computed as:

$$\theta_{\text{opt}} = (x\, x^T)^\dagger\, x\, y \tag{4.6}$$

where the notation $(x\, x^T)^\dagger$ denotes the pseudo-inverse of $(x\, x^T)$ and the optimal estimate is given by $\hat{y} = (x\, x^T)^\dagger\, x^T\, x\, y$. This estimate does not have bias, i.e. the mean of the output y equals the mean of the estimate $\hat{y}$.

The regression problem defined in (4.5) is often ill-posed in the sense that the solution does not depend continuously on the data (the case of multiple solutions falls into that denomination). Formulation (4.5) could also lead to over-fitting in the case of non-linear regression since there is no penalization for high values of the solution θ_{opt}. In order to prevent these two possible flaws, it is a common practice to add to the objective function a quadratic term called *Tikhonov regularization* [211] which has the form $\rho^2\, |\theta|^2$ in the scalar case, where the scalar ρ acts as a regulation variable on the penalty. Then the optimal estimate becomes:

$$\hat{y} = (x\, x^T + \rho^2\, \mathrm{I})^{-1}\, x^T\, x\, y. \tag{4.7}$$

For ρ large enough, the problem is well-posed and over-fitting with respect to θ is prevented [88].

4.2.2 Kernel methods

The linear regression method described in section 4.2.1 can be extended to non-linear regression methods through the use of a kernel. One can consider a mapping function $\phi(\cdot)$ from the covariates space to a higher-dimensional space, and consider the linear regression problem between the mapped covariates $\phi(x_i)$ and the responses y_i. This is the main principle of kernel methods, which consist in using a feature space, in which the dataset is represented, and to consider linear relations between objects in this feature space, and between these features and the outputs. Given a positive semi-definite matrix $K = (k_{ij})$, we define the kernel function by $K_{\text{f}} : \mathcal{X} \times \mathcal{X} \to \mathbb{R}$, where $\mathcal{X}$ denotes the covariates space, such that $K_{\text{f}}(x_i, x_j) = k_{ij}$. This implicitly defines a feature mapping $\phi(\cdot)$ between $\mathcal{X}$ and a Hilbert space $\mathcal{H}$ by $\phi(\cdot) : \mathcal{X} \to \mathcal{H}$ such that $\langle \phi(x_i), \phi(x_j) \rangle_{\mathcal{H}} = K_{\text{f}}(x_i, x_j)$. In the following we note X_{map} a matrix representation of the mapping $\phi(\cdot)$ (thus the i-th column of X_{map} is $\phi(x_i)$). When $\phi(\cdot)$ has scalar values, X_{map} is a row vector.

Remark 4.2. *One does not have to define a mapping function $\phi(\cdot)$ to define a kernel matrix, but can simply consider a positive semi-definite matrix and use it as a kernel. It is also possible to define a kernel matrix from a mapping $\phi(\cdot)$ and one of its matrix representation X_{map} as $K = X_{map}^T X_{map}$.*

The inner product in $\mathcal{H}$ naturally appears to be given by the Gram matrix K, called the kernel. Kernel techniques [68, 194] have several benefits:

- They enable to work with any types of features of the initial data-set, which has *a priori* no particular structure, in a Hilbert space.
- They guarantee a reasonable computational cost for the algorithm by allowing a complexity related to the number of points represented and not the number of features used (this is known as the kernel trick and is described in Remark 4.5).

Thus, kernel methods provide several extensions to usual regression methods, and can be easily written in a machine learning framework.

4.2.3 Kernel learning

Given the knowledge of a training set $\mathcal{S}_{\text{tr}} = \{(x_i, y_i) | i = 1, \cdots, n_{\text{tr}}\}$, the kernel learning problem consists of identifying the best mapping for the elements of the test set, $\mathcal{S}_{\text{t}} = \{x_i | i = n_{\text{tr}} + 1, \cdots, n_{\text{tr}} + n_{\text{t}}\}$. In order to match the structure of this problem, we define the kernel matrix in block form as:

$$K = \begin{pmatrix} K_{\text{tr}} & K_{\text{trt}} \\ K_{\text{trt}}^T & K_{\text{t}} \end{pmatrix} \tag{4.8}$$

where $k_{ij} = \langle \phi(x_i), \phi(x_j) \rangle_{\mathcal{H}}$ for $i, j = 1, \cdots, n_{\text{tr}}, n_{\text{tr}} + 1 \ldots n_{\text{tr}} + n_{\text{t}}$. K_{t} denotes the inner products between the elements of the test set. The Gram matrix K_{tr} is the result of an optimization problem over the training set, and we learn the cross-term K_{trt}, which expresses the inner-product in the feature space between the elements of the test-set and the elements of the training set.

Convex formulation of the kernel learning problem

In this section we formulate the kernel learning problem as a convex problem. Expressing the linear least-squares (4.5) for the mapped input X_{map} with the regularization term described in section 4.2.1 yields:

$$p^* = \min_\theta \quad \|y - X_{\text{map}}^T \theta\|_2^2 + \rho^2 \|\theta\|_2^2 \tag{4.9}$$

where we note p^* the optimal value of this problem. Using the change of variable $z = X_{\text{map}}^T \theta - y$ yields the equivalent formulation:

$$\begin{aligned} p^* = \quad & \min_{\theta, z} \quad \|z\|_2^2 + \rho^2 \|\theta\|_2^2 && (4.10) \\ & \text{subject to} \quad z = y - X_{\text{map}}^T \theta && (4.11) \end{aligned}$$

The Lagrangian dual of this problem reads:

$$d^* = \max_\alpha \quad \left(-2\,\alpha^T y - \alpha^T \left(I + \frac{X_{\text{map}}^T X_{\text{map}}}{\rho^2} \right) \alpha \right). \tag{4.12}$$

In this equation, we see the expression of the kernel matrix:

$$K = X_{\text{map}}^T X_{\text{map}}. \tag{4.13}$$

If we denote $K_\rho = I + \frac{X_{\text{map}}^T X_{\text{map}}}{\rho^2}$ the regularized kernel, the dual optimal point and dual optimal value of problem (4.12) can be expressed as:

$$\alpha^* = K_\rho^{-1} y \quad \text{and} \quad d^* = y^T K_\rho^{-1} y. \tag{4.14}$$

Remark 4.3. *Since the primal* (4.10)-(4.11) *and dual* (4.12) *are convex and strictly feasible, strong duality holds and primal optimal value p^* and dual optimal value d^* are equal. We note that expression* (4.12) *shows that the dual optimal value is a maximum over a set of linear functions of K_ρ, so the optimal value is a convex function of the regularized kernel matrix K_ρ. Since the choice of the kernel is crucial for the optimal value, it is interesting to minimize the optimal value d^* with respect to the kernel.*

Remark 4.4. *Optimizing the kernel matrix physically means looking for the best mapping function $\phi(\cdot)$ such that there is a linear relation between the features of the inputs $\phi(x_i)$ and* *the outputs y_i. If one takes $\phi(\cdot)$ as the identity mapping, then the optimal value of* (4.12) *becomes:*

$$y^T\, K_\rho^{-1}\, y = y^T \left(I + \frac{x^T\, x}{\rho^2} \right)^{-1} y \tag{4.15}$$

which may not be optimal for non-linear systems.

Remark 4.5. *One must note that the kernel matrix* (4.13) *is a square matrix which has the dimension of $x^T\, x$, and thus its size does not depend on the number of features represented in X_{map} but only on the number of covariates x_i. The dimension of the image space of $\phi(\cdot)$, which is the dimension of the feature space, does not appear in the kernel matrix. This is the kernel trick mentioned in section 4.2.2.*

Cross-validation

The optimal value of (4.9) as expressed in (4.14) depends on the kernel matrix (4.13) and on the regularization parameter ρ. The parameter ρ is tuned through a re-sampling procedure [86], the *k-fold cross-validation* (here k does not denote the kernel matrix but the number of folds used in the cross-validation method). This technique consists in dividing the dataset into k parts of approximately equal size, and using a subset for training while the remainder is used for testing [215]. For instance if the different parts are $\{P_i | i = 1, \cdots, k\}$ then given $n \in \{1, \cdots, k\}$ one would use P_n as a training set and $\bigcup_{i=1,\cdots,k,\, i \neq n} P_i$ as a test set. This is useful to make extensive use of the dataset while avoiding bias on the training set. Here we use this method on the training set to pick the optimal value of the regularization parameter ρ and on the whole set to have a meaningful estimation error.

Kernel regression

As stated in Remark 4.3, the optimal value of the regularized regression problem (4.9) is a convex function of the regularized kernel matrix K_ρ and can be optimized over the kernel. The kernel optimization problem, which consists in minimizing the value d^* defined in (4.14) with respect to the regularized kernel K_ρ reads:

$$\min_{K_\rho} \quad y^T\, K_\rho^{-1}\, y \tag{4.16}$$

$$\text{subject to} \quad K_\rho \succeq 0 \tag{4.17}$$

where the constraint on the kernel matrix enforces that the regularized kernel K_ρ must be a Gram matrix. This problem is convex according to Remark 4.3. In order to prevent overfitting with respect to K_ρ, we follow [142] and constrain K_ρ to be a convex combination of given kernels, i.e. we define a set of kernels $\{K_1, \cdots, K_k\}$ and consider the problem:

$$\min_\lambda \quad y^T K_\rho^{-1} y \tag{4.18}$$

$$\text{subject to} \quad \lambda_i \geq 0 \quad \sum_{i=1}^{k} \lambda_i = 1 \tag{4.19}$$

$$K_\rho = \sum_{i=1}^{k} \lambda_i K_i. \tag{4.20}$$

In a learning setting, the optimization problem (4.18) is defined only on the training set but the expression of the kernel matrix as a linear combination of known kernels must be satisfied on the entire set. Using the notation introduced in (4.8) we write $K_\rho = \begin{pmatrix} K_{\text{tr}} & K_{\text{trt}} \\ K_{\text{trt}}^T & K_{\text{t}} \end{pmatrix}$ and under this form the problem reads:

$$\min_\lambda \quad y^T K_{\text{tr}}^{-1} y \tag{4.21}$$

$$\text{subject to} \quad \lambda_i \geq 0 \quad \sum_{i=1}^{k} \lambda_i = 1 \tag{4.22}$$

$$K_\rho = \sum_{i=1}^{k} \lambda_i K_i \tag{4.23}$$

which can be written in a semi-definite program form using an epigraphical property and the Schur complement:

$$\min_{\lambda,t} \quad t \tag{4.24}$$

$$\text{subject to} \quad \lambda_i \geq 0 \quad \sum_{i=1}^{k} \lambda_i = 1 \tag{4.25}$$

$$K_\rho = \sum_{i=1}^{k} \lambda_i K_i \ \text{ and } \ \begin{pmatrix} t & y^T \\ y & I + \frac{K_{\text{tr}}}{\rho^2} \end{pmatrix} \geq 0. \tag{4.26}$$

The solution of this optimization problem is the parameter λ^* giving the optimal convex combination of the set of kernels $\{K_1 \cdots K_k\}$ which minimizes d^* from (4.14).

Rank-one kernel optimization

The kernel optimization problem in the form of (4.24)-(4.25)-(4.26) is not tractable and cannot be efficiently solved by standard optimization software. A rank-one decomposition of kernels can be used in order to find an equivalent formulation in a linear program form. This is done through the introduction of several intermediate problems. Assuming we can write the regularized kernel as a convex combination of dyads: $K_\rho = \sum_{i=1}^{p} \nu_i \, l_i \, l_i^T$ where l_i are row vectors and ν_i are positive scalars such that $\sum_{i=1}^{p} \nu_i = 1$. Since by definition $K_\rho = I + \frac{K}{\rho^2}$, the decomposition of K_ρ into a sum of dyads is possible whenever the kernel K itself can be written as a sum of dyads. In practice, the kernel is a positive semi-definite matrix, so it can be diagonalized in an orthonormal basis and this property is satisfied. Thus, we can write an equivalent formulation of problem (4.18)-(4.19)-(4.20) as:

$$\Psi = \quad \min_\nu \quad y^T K_\rho^{-1}(\nu)\, y \tag{4.27}$$

$$\text{subject to} \quad \nu_i \geq 0 \quad \sum_{i=1}^{p} \nu_i = 1 \tag{4.28}$$

$$K_\rho = \sum_{i=1}^{p} \nu_i\, l_i\, l_i^T \tag{4.29}$$

where the vectors l_i are the eigenvectors of the matrices K_j from equation (4.20). Introducing the change of variable $\kappa = K_\rho^{-1}(\nu)$ and doing some computations enables one to rewrite problem (4.27)-(4.28)-(4.29) as:

$$\Psi = \max_\kappa \quad \left(2\, y^T \kappa - \max_{1 \leq i \leq p} (l_i^T\, \kappa)^2\right) \tag{4.30}$$

and the optimal κ is related to the optimal ν by the following relation

$$\kappa^* = K_\rho^{-1}(\nu^*). \tag{4.31}$$

One can note that solving problem (4.30) for the vector variable κ is the same as solving the problem:

$$\Psi = \max_{\gamma,\beta} \quad \left(2\, y^T \gamma\, \beta - \max_{1 \leq i \leq p} (l_i^T\, \gamma\, \beta)^2\right) \tag{4.32}$$

for the variables γ and β. This is simply obtained by writing $\kappa = \gamma\, \beta$ in problem (4.30), with γ scalar and β vector. The optimal point (γ^*, β^*) of problem (4.32) satisfies:

$$\Psi^{1/2}\, \beta^* = \gamma^*\, \beta^* = \kappa^*. \tag{4.33}$$

If we minimize over γ in (4.32) we obtain the following optimization problem:

$$\Psi^{1/2} = \quad \max_\beta \quad y^T\, \beta \tag{4.34}$$

$$\text{subject to} \quad |l_i^T\, \beta| \leq 1 \quad i = 1, ..., p. \tag{4.35}$$

The Lagrangian of this problem can be written as:

$$\mathcal{L}(\beta, u) = y^T\, \beta + \sum_{i=1}^{p} \left(|u_i| - u_i\, \left(l_i^T\, \beta\right)\right) \tag{4.36}$$

and taking the Lagrangian dual of problem (4.34)-(4.35) yields:

$$\Psi^{1/2} = \quad \min_u \quad \|u\|_1 \tag{4.37}$$

$$\text{subject to} \quad y = \sum_{i=1}^{p} u_i \, l_i \tag{4.38}$$

using the strict feasibility of the primal and convexity of the primal and the dual. Problem (4.38) is a linear program. The optimal ν^* can be retrieved from the optimal u^* from the relation:

$$\nu_i^* = \frac{|u_i|^*}{\Psi^{1/2}}. \tag{4.39}$$

Indeed one can check that with this value of the vector ν equations (4.31)-(4.33) yields $\Psi^{1/2} \, K_\rho(\nu^*) \, \beta^* = y$ and on the other hand we can write $\Psi^{1/2} \, K_\rho(\nu^*) \, \beta^* = \sum_{i=1}^{p} |u_i^*| \, (l_i^T \, \beta) \, l_i$ which is equal to $\sum_{i=1}^{p} u_i \, l_i$ using the optimality condition in the Lagrangian (4.36). This proves that if u^* is optimal for (4.37)-(4.38) then ν^* given by (4.39) is optimal for (4.27)-(4.28)-(4.29) and vice-versa.

Kernel learning and kernel regression methods have been mostly applied to static machine learning problems. A corresponding theory for dynamical and distributed systems is still the topic of active research.

In the following chapter, we present how a control-theoretical formulation of Bayesian networks, namely nonlinear filtering techniques, can be applied to scalar hyperbolic conservation laws, and the extent to which discontinuity and non-differentiability of the solution to the partial differential equations impact the optimality of the resulting estimates.

Chapter 5

Sequential data assimilation for scalar macroscopic traffic flow models

In this chapter we consider the problem of sequential data assimilation for the nonlinear partial differential equations traffic models presented in the previous chapters. As mentioned before, the estimation for nonlinear systems requires the use of suboptimal techniques for which there is no analytical or numerical access to the optimum. The focus of this chapter is on the analysis of the impact of the specific properties of the solutions to partial differential equations based traffic models, onto the optimality of the estimates provided by classical advanced filtering techniques.

The estimation problem for nonlinear systems has been heavily studied in particular within the meteorology community, with subsequent development of sophisticated data assimilation techniques [36, 152], which fall into two major categories: *variational methods* and *optimal interpolation* methods. Variational methods [152] consist of finding the solution of a model (with or without stochastic forcing) which minimizes a certain distance to observations. Estimates provided by optimal interpolation methods are not in general solutions to a model, but minimize a weighted distance to the model solution and to the observations. In meteorology, a common example of a variational method is the 3D-Var algorithm [65] for the static problem and 4D-Var algorithm in the time-varying case [66].

The theory of inverse problems [131] is concerned with the estimation of model parameters. A specific type of *inverse methods* consists in iteratively updating the estimates as data becomes available [91], instead of solving an inverse problem once using all measurements in batch. These so-called *sequential estimation algorithms*, particularly appropriate for on-line estimation, often rely on *Bayes rule* and a computationally explicit optimality criterion (e.g. *Gauss-Markov* theorem for *minimum mean squared error* estimation). In the case of additive noise, one of the most well-known sequential estimation algorithms is the seminal *Kalman filter* [132].

5.1 Data assimilation

5.1.1 Application to transportation networks

In the transportation field, applications of sequential state estimation date back to the 1970's and the work of Gazis [100, 208], who independently used the *Kalman Filter* (KF) and the *Extended Kalman Filter* (EKF) to estimate traffic density in the Lincoln tunnel, New-York, for the purpose of traffic control. More recent work from Papageorgiou [221, 222] involves the application of the EKF to a non-scalar traffic model [182]. The EKF has also been applied [196] to the LWR equation with a Smulders [201] flux function.

The *Mixture Kalman Filter* (MKF) [51] is an extension of the KF to conditionally linear dynamical systems. The MKF has been applied in the transportation community [114, 206, 209] to the *cell-transmission model* (CTM) [71, 72], which exhibits piecewise linear dynamics, conditioned on the phases of traffic (free-flow, congestion) upstream and downstream.

In the recent years, *sequential Monte Carlo* methods, or *Particle Filters* (PF), and so-called *ensemble methods* such as the EnKF have been applied to traffic estimation [171, 227, 228]. Ensemble methods [93] consist of representing the first moment of the state estimate distribution by a set of samples and using a linear measurement update, whereas particle methods [105] consist in propagating a sample representation of the full distribution of the estimate and using a nonlinear measurement update.

Another notable filter is the *Unscented Kalman Filter* (UKF) [129] which introduces an *unscented transformation* providing an exact representation of the first two moments of a distribution by a set of deterministically determined samples (see [170] for a traffic application).

A variety of traffic models and filters have been shown to perform well for practical applications. However, the problem of the structural limits of data assimilation algorithms for traffic estimation has not received much attention. It is well-known that, in practice, high accuracy can be achieved with sufficiently accurate measurements in sufficiently large volumes. But with massive datasets coming from increasingly diverse sources, traceability and high quality of traffic data are not necessarily guaranteed. Being able to identify the estimation errors inherent to the structure of traffic phenomena is required for the design of more robust, transparent data assimilation algorithms, and scalable, appropriate data collection methodologies.

In this chapter, we analyze the structural properties of one of the most classical macroscopic traffic flow models, the *Lighthill-Whitham-Richards* (LWR) *partial differential equation* (PDE) [159, 189], in the context of estimation. We present the difficulties resulting from these properties, which create significant challenges for the design of an optimal filtering algorithm for this model.

5.1.2 Optimal filtering for LWR PDE

Structural properties of the LWR PDE and its discretized forms impact the optimality of estimates produced by classical sequential estimation techniques. The focus of this chapter is on the analysis and quantification of the lack of estimate optimality resulting from the following properties of the LWR PDE, and its numerical discretization using the Godunov scheme.

Nonlinearity of the fundamental diagram

One of the main properties of the LWR PDE is the nonlinearity of its flux function (fundamental diagram), which allows the modeling of traffic phases of different nature: *free-flow* and *congestion*. Nonlinearities of the model are the cause of the appearance of discontinuities in the solution of the partial differential equation. Consequently, the distribution of the uncertainty on the true state is a mixture distributions at shock waves even for unimodal noise distributions on the initial condition. In this chapter, we analytically show the emergence of mixture distributions in the solution of the PDE and numerically illustrate their importance on benchmark tests.

The mixture nature of the distribution of the uncertainty on the true state resulting from initial condition uncertainty propagating through an uncertain model raises the question of the relevance of minimal variance estimate for traffic applications. The estimate mean produced by classical filters may indeed correspond to a state with zero true probability, and the estimate covariance may exhibit large values corresponding to a variability due to the coexistence of different modes in the distribution of the uncertainty on the true state, each with significantly smaller covariance.

Non-differentiability of the discretized model

The most common numerical scheme used to compute the solution of the LWR PDE is the *Godunov scheme* [103], a finite volume scheme which consists of iteratively solving *Riemann problems* [89] between neighboring discretization cells and averaging their solution at each time-step on each spatial cell, as described in Chapter 1. In this chapter we prove that this scheme is non-differentiable and we derive the expression of its non-differentiability domain.

The lack of differentiability of the Godunov scheme, a common discretization of the LWR PDE, is relevant for data assimilation algorithms whose optimality guarantees are based on Taylor series analysis, which assumes exact computation of the derivative up to a certain order. This is the case in particular for the EKF, which considers propagation of the estimate covariance using the tangent (linearized) model. Numerical results quantify estimate errors induced by this property of the discretized model. The result also affects known order of accuracy of the estimate moments of the UKF, since in this case the Taylor series does not exist up to the required order.

This chapter can thus be viewed as a theoretical and numerical study of the implications of the structural properties of the Godunov scheme and CTM on filtering algorithms. It sheds some new light on the proper use of these schemes for traffic estimation purposes, and provides conclusions which are illustrated by detailed numerical studies.

While the results presented here are derived for the Godunov scheme, because historically is was one of the first numerical schemes proposed to solve scalar hyperbolic conservation laws (and the LWR PDE in particular), other proposed schemes such as the CTM exhibit the same features as the Godunov scheme, and thus our analysis applies to them as well.

The remainder of the chapter is organized as follows. Section 5.2 introduces the general theory of sequential data assimilation and optimal filtering. Section 5.3 focuses on the *Riemann problem* which is the keystone of numerical solutions of continuous and discrete scalar conservation models and the focus of our subsequent analysis. Section 5.4 and 5.5 point at the structural properties of macroscopic traffic models derived from the LWR PDE, in particular model nonlinearity in Section 5.4 and model non-differentiability in Section 5.5.

5.2 Nonlinear estimation

5.2.1 Deterministic filters

In this section we present the EKF and the UKF for nonlinear systems. The EKF forecast step is based on model linearization. The UKF consists in representing exactly the first two moments of the prior distribution by a set of deterministic samples. In particular, no sampling term is required for the application of these algorithms.

Extended Kalman filter

The EKF is an extension of the KF for nonlinear state-space models. The EKF consists in using a Taylor series truncation of the model at the current state to propagate the state statistics. We present the case of a nonlinear state model combined with a linear observation model, although nonlinear observation equation can also be considered through a similar linearization of the observation operator at the analysis step. The forecast mean is given by a zero-th order truncation of the model, whereas the forecast covariance is given by a first order truncation of the model. If we note A_{t+1} the linearization of the nonlinear model dynamics $\mathcal{A}(p,t)$ at the state estimate p, the forecast and analysis steps for the EKF read:

$$\text{Forecast:} \begin{cases} x_{t+1|t} = \mathcal{A}(x_{t|t}, t) \\ \Sigma_{t+1|t} = A_{t+1}\,\Sigma_{t|t}\,A_{t+1}^T + W_{t+1} \end{cases} \tag{5.1}$$

$$\text{Analysis:} \begin{cases} x_{t+1|t+1} = x_{t+1|t} + K_{t+1}\left(y_{t+1} - C_{t+1}\,x_{t+1|t}\right) \\ \Sigma_{t+1|t+1} = \Sigma_{t+1|t} - K_{t+1}\,C_{t+1}\,\Sigma_{t+1|t} \\ \text{where} \quad K_{t+1} = \Sigma_{t+1|t}\,C_{t+1}^T\,\left(C_{t+1}\,\Sigma_{t+1|t}\,C_{t+1}^T + V_{t+1}\right)^{-1} \end{cases} \tag{5.2}$$

where the only difference with the Kalman filter resides in the propagation of the state mean at the forecast step, using the nonlinear state model. Different sources of sub-optimality arise in the derivation of the EKF:

1. **Accuracy of the Taylor truncation**:
    - a The model approximation used at the forecast step (5.1) for the covariance propagation requires that the model Jacobian be accurately computed.
    - b The mean given by the EKF is a second order Taylor series approximation of the MMSE, whereas the covariance is a fourth order approximation of the MMSE error covariance.
2. **Closure assumption**: it is assumed that there is no significant interaction between higher order statistics and the first two moments of the state estimate.

Cases in which the closure assumption breaks, due to the importance of higher order terms in the model Taylor series have been documented, with illustrations of estimates biased and inconsistent [129], and with diverging error statistics [90]. Cases in which this assumption breaks, due to the importance of higher-order statistics can be found in [172, 173] in the case of bimodal distributions.

Remark 5.1. *An approximation made in the EKF equations lies in the propagation of the state covariance* $\Sigma_{t+1|t}$. *This covariance is then used at the analysis step* (5.2) *at which observations are combined with the model forecast. The study of the resulting error structure of the state covariance after propagation in the context of traffic is to the best of our knowledge an open problem, and is a focus of the research presented in this chapter.*

Unscented Kalman filter

The UKF [129] is built on the unscented transformation, which consists in representing a distribution with mean μ and variance Σ by a set of weighted samples, or *sigma points*, chosen deterministically such that the weighted sample mean is μ and the weighted sample covariance is Σ [130]. For for a state-space of dimension n, the $2\,n+1$ sigma points produced by the unscented transformation are defined as

$$\begin{cases} x^0 & = \mu \\ x^k & = \mu + ((n+k)\,\Sigma)_k^{\frac{1}{2}} \quad k = 1, \dots, n \\ x^{k+n} & = \mu - ((n+k)\,\Sigma)_k^{\frac{1}{2}} \quad k = 1, \dots, n \end{cases} \tag{5.3}$$

where $((n+k)\,\Sigma)_k^{1/2}$ denotes the k^{th} column of the square root of $(n+k)\,\Sigma$. The corresponding weights w^k are parameterized by κ, which controls the spread of the sigma points:

$$\begin{cases} w^0 & = \frac{\kappa}{\kappa+n} \\ w^k & = \frac{1}{2(\kappa+n)} \quad k = 1, \dots, n \\ w^{k+n} & = \frac{1}{2(\kappa+n)} \quad k = 1, \dots, n. \end{cases} \tag{5.4}$$

Choosing the samples according to (5.3) and the weights according to (5.4) yields that the weighted sample mean and weighted sample covariance are equal to the distribution mean and covariance for any choice of κ. The forecast and analysis step of the UKF can be written as follows:

$$\text{Forecast:} \begin{cases} \text{Propagate sigma-points} \\ \quad x^k_{t+1|t} = \mathcal{A}(x^k_{t|t}, t) \quad k = 1, \dots, 2\,n+1 \\ \text{Compute forecast mean and covariance} \\ \quad x_{t+1|t} = \sum_{k=0}^{2\,n+1} w_k\, x^k_{t+1|t} \\ \quad \Sigma_{t+1|t} = \sum_{k=0}^{2\,n+1} w_k \left(x^k_{t+1|t} - x_{t+1|t}\right) \left(x^k_{t+1|t} - x_{t+1|t}\right)^T \end{cases} \tag{5.5}$$

$$\text{Analysis:} \begin{cases} \text{Compute sigma-points observations} \\ \quad z^k_{t+1|t} = \mathcal{C}_{t+1}\, x^k_{t+1|t} \quad k = 1, \dots, 2\,n+1 \\ \text{Compute observation mean and covariance} \\ \quad z_{t+1|t} = \sum_{k=0}^{2\,n+1} w_k\, z^k_{t+1|t} \\ \quad Z_{t+1|t} = \sum_{k=0}^{2\,n+1} w_k \left(z^k_{t+1|t} - z_{t+1|t}\right) \left(z^k_{t+1|t} - z_{t+1|t}\right)^T \\ \text{Compute covariance between forecast and observation} \\ \quad Y_{t+1|t} = \sum_{k=0}^{2\,n+1} w_k \left(x^k_{t+1|t} - x_{t+1|t}\right) \left(z^k_{t+1|t} - z_{t+1|t}\right)^T \\ \text{Compute posterior mean and covariance} \\ \quad x_{t+1|t+1} = x_{t+1|t} + K_{t+1} \left(y_{t+1} - z_{t+1|t}\right) \\ \quad \Sigma_{t+1|t+1} = \Sigma_{t+1|t} - K_{t+1}\, Z_{t+1|t}\, K^T_{t+1} \\ \quad \text{where} \quad K_{t+1} = Y_{t+1|t}\, Z^{-1}_{t+1|t} \end{cases} \tag{5.6}$$

where the unscented transformation is first used to compute the sigma points for the current estimates, which are then propagated through the model and whose mean and covariance is computed (5.5). At the analysis step, the forecast observation associated with each sigma point through the (potentially) nonlinear observation model $\mathcal{C}_{t+1}$, is computed as $z^k_{t+1|t}$, which allows the computation of the observation mean $z_{t+1|t}$, observation covariance $Z_{t+1|t}$, and the covariance between forecast state and observation as $Y_{t+1|t}$. The analysis mean and covariance are then computed exactly using Kalman equations (5.6).

Different sources of sub-optimality arise in the UKF:

1. **Limited number of samples**: the mean and the covariance propagated by the UKF are fourth order approximations of the MMSE and MMSE error covariance.

2. **Closure assumption**: it is assumed that there is no significant interaction between higher order statistics and the first two moments of the state estimate.

The UKF has been applied to traffic estimation [170] and was compared with the EKF for the Papageorgiou model (1.10). The two filters were empirically shown to have similar performances for joint state and parameter estimation [111] for this model (1.10). The results of this comparison are completed by the analysis presented in Section 5.4 and Section 5.5, in which we study the state distribution features due to model nonlinearities and non-differentiability analytically and numerically in the case of the LWR model, and in which we show how they affect the EKF and the UKF. In particular we analyze the true distribution structure at shock waves of the LWR model, in the continuous and discrete domain. The Papageorgiou model is defined in the discrete domain, and exhibits an anticipation term which reduces the sharpness and amplitude of spatial variations. Consequently, the impact of the existence of shock waves on the performance of the filters is stronger in the case of the LWR model in the continuous domain.

5.2.2 Stochastic filters

A wide variety of filters extend the Kalman filter for nonlinear state models by representing the state by a set of random samples (*particles*, *ensemble members*). The rules for sample propagation, update, and for resampling, are of different types. The need for pseudo-random generator at every step of these algorithms justifies the appellation *stochastic filters*.

Ensemble Kalman filter

The EnKF [92, 93] consists in representing the state statistics by a set of ensemble members which are evolved in time and whose mean is an estimator of the true state. The state error covariance is represented by the ensemble covariance. Formally, with N ensemble members, the EnKF equations read:

$$\text{Forecast:}\begin{cases} x^k_{t+1|t} = \mathcal{A}(x^k_{t|t}, t) + w^k_{t+1} \quad k = 1, \ldots, N \\ x_{t+1|t} = \frac{1}{N}\sum_{k=1}^{N} x^k_{t+1|t} \\ \Sigma_{t+1|t} = \frac{1}{N-1}\sum_{k=1}^{N}\left(x^k_{t+1|t} - x_{t+1|t}\right)\left(x^k_{t+1|t} - x_{t+1|t}\right)^T \end{cases} \tag{5.7}$$

$$\text{Analysis:}\begin{cases} x^k_{t+1|t+1} = x^k_{t+1|t} + K_{t+1}\left(y_{t+1} + v^k_{t+1} - C_{t+1}\, x_{t+1|t} - \overline{v_{t+1}}\right) \quad k = 1, \ldots, N \\ \Sigma_{t+1|t+1} = \Sigma_{t+1|t} - K_{t+1}\, C_{t+1}\, \Sigma_{t+1|t} \\ \text{where} \quad K_{t+1} = \Sigma_{t+1|t}\, C^T_{t+1}\left(C_{t+1}\, \Sigma_{t+1|t}\, C^T_{t+1} + V_{t+1}\right)^{-1} \end{cases} \tag{5.8}$$

where we noted $\overline{v}$ the mean of v. In the limit of large number of samples, the EnKF converges toward the KF for linear systems. Due to the independent ensemble forecasts (5.7), it is *embarrassingly parallel* and particularly appropriate for efficient distributed computations. At the analysis step (5.8), the modeled observation noise is explicitly added to the measured observation, to capture the full observation noise in the analysis equation [42]. In the context of traffic estimation, the EnKF has been applied to the Bay Area highway networks with a traffic model equivalent to the LWR PDE, formulated in the velocity variable [227]. The principal source of sub-optimality arising in the EnKF is sampling error:

1. **Sampling error**: the use of a finite number of ensemble members introduces a sampling error in the estimate distribution.

Remark 5.2. *The covariance given by the EnKF is the state error covariance and not the state covariance. In the KF, the state mean and state error covariance are propagated analytically. The state error covariance coincides with the state covariance. On the other hand, the EnKF analytically propagates ensemble members whose mean is an unbiased estimator of the state mean, and covariance coincides by definition of the update equations with the state error covariance, but not with the state covariance, except in the limit of an infinite number of ensemble members.*

Extensions of the EnKF giving access to higher order moments of the state distribution have also been considered [10] by integrating a modified analysis step.

Particle filter

The PF, also known as *bootstrap filter*, or sequential Monte Carlo method [11, 105, 163] can be traced back to the seminal articles of Metropolis and Ulam [169], later generalized by Hastings [109]. These methods represent the full statistics of the state by a set of samples which are propagated through the state model. When observations are received, sample weights are scaled by the relative likelihood of the new observation, and the updated representation of the probability distribution is re-sampled. Formally, the PF steps in the case of N particles are as follows:

$$\text{Forecast:} \quad x^k_{t+1|t} = \mathcal{A}(x^k_{t|t}, t) + w^k_{t+1} \quad k = 1, \dots, N$$

$$\text{Analysis:} \begin{cases} \text{Re-weighting:} \\ \quad \alpha^k_{t+1} = \alpha^k_t \, \frac{p(y_{t+1}|x^k_{t+1|t})}{\sum_{k=1}^N \alpha^k_t \, p(y_{t+1}|x^k_{t+1|t})} \quad k = 1, \dots, N \\ \text{Re-sampling:} \\ \quad \text{Generate } N \text{ samples } x^k_{t+1|t+1} \text{ from the distribution defined by} \\ \quad P(X = x^k_{t+1|t+1}) = \alpha^k_{t+1}, k = 1, \dots, N \end{cases}$$

The PF has been applied to the case of transportation systems [171] on the stochastic model described in [34]. The particle filter is the only filtering method able to capture the complete state distribution, in the limit of infinite number of samples, without restrictive assumption on the dynamics or on the statistics. Well-known weaknesses of the PF relate to the problem of sample degeneracy for high dimensional [202] systems. The use of an appropriate *proposal distribution* at the re-weighting step is key to reducing the sample weight variance given the system history, but more sophisticated *importance sampling* or *rejection sampling* techniques are often considered [11, 218]. The sources of sub-optimality in the PF relate to:

1. **Sampling error:** the use of a finite number of particles introduces a sampling error in the estimate distribution.

The *implicit particle filter* is a notable extension [55] of the PF which allows a-priori the definition of the desired weights of the particles after analysis and thus alleviation of the problem of sample degeneracy in the case of the *exponential family*. Another research track has explored the use of the EKF, EnKF or UKF to compute the proposal distribution in the particle filter [218].

Sustained improvements of the filters presented above have been in large part driven by specific improvements for systems exhibiting strong nonlinearity or non-normality, identified as the causes of inaccurate estimates and forecast. In the following section, we present the seminal macroscopic traffic models which have been considered for real-time data assimilation on transportation networks. The subsequent sections will then focus on the analysis of the performance of the respective filtering schemes on the models.

5.3 Discontinuities and uncertainty

At the macroscopic level, traffic flow exhibits nonlinearities which can be modeled using nonlinear conservation laws such as the LWR PDE. Nonlinearities are the cause for discontinuities which may arise in finite time in the solution to the Cauchy problem associated with the PDE even with smooth initial and boundary data. According to the definition of the solution to the Riemann problem (5.10), shock waves persist when, at a spatial discontinuity, the upstream density is lower than the downstream density. Thus they cannot be neglected by any traffic application. Physically, these discontinuities model the existence of queues, which are one of the main focus of traffic flow research.

5.3.1 Estimation and control

Queues extremities are phenomena with very limited spatial extent, which characterize the interface between significantly different phases of traffic flow. This property makes them relatively hard to directly measure and monitor using classical fixed sensing infrastructure. This is especially true when the upstream end of the queue is stationary, and can only be directly measured if it lies on a fixed sensor or by probe vehicles reporting measurements exactly at the corresponding location.

Large traffic variations occurring on a short spatial extent, typical of queues extremities, make them particularly hazardous, and being able to alert drivers of sudden changes in speed is one of the focal points of traffic safety applications [119].

For control applications, accurately locating the location and propagation speed of queues is critical. Their location typically impacts ramp metering algorithms directly, since they are often designed around the values of the upstream and downstream flow at the upstream end of the queue. In the absence of sensors, the algorithm depends on the estimated flows upstream and downstream of the ramp.

Furthermore, accurate estimation of the propagation speed of queues is one of the most essential components of traffic forecast and dynamic travel-time estimation. Estimating their propagation speed requires the estimation of the left and right density at the queue extremities, as well as accurate knowledge of the fundamental diagram.

In the context of model-based estimation, the influence of model nonlinearity and non-differentiability on the quality of the estimates for traffic phenomena has not received much attention in the traffic community with a few notable exceptions [111, 207] (see [33] for a related problem for atmospheric models, and [50] for a study of non-differentiability in a general context). In the following section, we consider the Riemann problem, which is a benchmark problem for studying the solution to the LWR PDE, and the evolution of shock waves. We then consider in Section 5.3.3 the Riemann problem with stochastic datum, which is used in the following sections as a framework for the study of the propagation of discontinuities in presence of uncertainties.

5.3.2 Riemann problem

The Riemann problem is a Cauchy problem with a self-similar initial condition, of the form:

$$\rho(t=0,x) = \begin{cases} \rho_l & \text{if} \quad x < 0 \\ \rho_r & \text{if} \quad x > 0 \end{cases} \tag{5.9}$$

The solution to the Riemann problem is the solution to the Cauchy problem associated with the PDE with initial condition the Riemann datum (5.9). The Riemann problem is a key building block for proofs of existence of solutions to the Cauchy problem for general initial conditions in the space of *bounded variations* (BV), via Helly's theorem [39]. It is also critical to the design of numerical schemes such as the wavefront tracking method [39] and the Godunov scheme, which proceeds by iteratively solving the Riemann problem between discretization cells, before averaging its solution on each cell (see equations (1.7) and (1.8)).

For a flux function $Q(\cdot)$ with constant concavity sign, the unique entropy solution to the Riemann problem is defined for $(t,x) \in \mathbb{R}^+ \backslash \{0\} \times \mathbb{R}$ as follows

1. If $Q'(\rho_l) > Q'(\rho_r)$ the solution is a shock wave

$$\rho_R\left(\frac{x}{t}, \rho_l, \rho_r\right) = \begin{cases} \rho_l & \text{for} \quad \frac{x}{t} < \sigma \\ \rho_r & \text{for} \quad \frac{x}{t} > \sigma \end{cases} \tag{5.10}$$

   where the location of the discontinuity is $x = \sigma t$, with σ given by the Rankine-Hugoniot relation:

$$\sigma = \frac{Q(\rho_l) - Q(\rho_r)}{\rho_l - \rho_r} \tag{5.11}$$

   which expresses the conservation of ρ at the discontinuity.

2. If $Q'(\rho_l) < Q'(\rho_r)$ the solution is a rarefaction wave

$$\rho_R\left(\frac{x}{t}, \rho_l, \rho_r\right) = \begin{cases} \rho_l & \text{for} \quad \frac{x}{t} \le Q'(\rho_l) \\ (Q')^{-1}(\frac{x}{t}) & \text{for} \quad \frac{x}{t} \in (Q'(\rho_l), Q'(\rho_r)) \\ \rho_r & \text{for} \quad \frac{x}{t} \ge Q'(\rho_r) \end{cases}$$

The interested reader is referred to Evans [89] and Leveque [156] for more details, and Piccoli [97] in the context of traffic. Shock waves and rarefactions waves respectively model the upstream and downstream ends of a queue. One may note that depending on the flow difference at the discontinuity, the propagation speed may be positive or negative.

Remark 5.3. *This brief description of the Riemann problem for the scalar conservation law is also of interest for continuous non-scalar traffic models in which discontinuities arise (see [31, 231]).*

For estimation purposes, it is appropriate to consider uncertain Riemann datum, which requires the definition of the Riemann problem with stochastic datum.

5.3.3 Riemann problem with stochastic datum

We consider a Riemann problem for a scalar conservation law with concave flux, with stochastic datum [69] defined by:

$$\rho(t=0,x) = \begin{cases} \varrho_l & \text{if} \quad x<0 \\ \varrho_r & \text{if} \quad x>0 \end{cases} \tag{5.12}$$

where ϱ_l, ϱ_r are random variables. We further note ς the random variable defining the resulting shock speed, whose distribution is given by the distribution of the Rankine-Hugoniot speed (5.11) for the realizations of the stochastic datum (ϱ_l, ϱ_r). We focus our analysis on the case in which each realization of the solution to the Riemann problem with stochastic datum is a shock wave. In the following proposition, we derive the analytical expression of the random field solution of the Riemann problem with stochastic datum in this case.

Proposition 5.1. *The solution of the Riemann problem with stochastic datum* (ϱ_l, ϱ_r) (5.12) *with bounded support, respectively* $\mathcal{D}_l, \mathcal{D}_r$ *such that* $\sup(\mathcal{D}_l) < \inf(\mathcal{D}_r)$, *is a random field* $\varrho_{t,x}$, *defined by:*

$$P\left(\varrho_{t,x}=\rho\right) = P\left(\varrho_l=\rho|\varsigma>\frac{x}{t}\right) P\left(\varsigma>\frac{x}{t}\right) + P\left(\varrho_r=\rho|\varsigma<\frac{x}{t}\right) P\left(\varsigma<\frac{x}{t}\right). \tag{5.13}$$

Proof. By assumption on the Riemann datum, $\sup(\mathcal{D}_l) < \inf(\mathcal{D}_r)$, the solution of a realization of the Riemann problem is a shock wave between a realization ρ_l of ϱ_l and a realization ρ_r of ϱ_r, with shock wave speed given by the Rankine-Hugoniot relation (5.11) which defines the realizations of the stochastic shock wave speed ς. If we note $\mathbf{1}_I$ the characteristic function of interval I, the solution to a realization of the Riemann problem at $(t,x) \in \mathbb{R}^+\backslash\{0\} \times \mathbb{R}$ is given by:

$$\rho = \rho_l \mathbf{1}_{\sigma>\frac{x}{t}} + \rho_r \mathbf{1}_{\sigma<\frac{x}{t}}.$$

which is the solution of the deterministic Riemann problem in the case of a shock wave (5.10). For $(t, x) \in \mathbb{R}^+ \backslash \{0\} \times \mathbb{R}$, a realization σ of the shock wave speed such that $\sigma > x/t$, the solution is drawn from the left datum, which reads:

$$P\left(\varrho_{t,x} = \rho | \varsigma > \frac{x}{t}\right) = P\left(\varrho_l = \rho | \varsigma > \frac{x}{t}\right).$$

Writing the similar equation for the case $\sigma < \frac{x}{t}$ and using the law of total probability, we obtain equality (5.13), and the proof. □

The case in which the support of the left and right datum do not intersect and are such that all realizations of the Riemann problem are rarefaction waves can be treated similarly. For simplicity, we do not address here the case where the support of the left and right datum have a non-empty intersection and consequently the realization of the solution to the Riemann problem can be a shock wave or a rarefaction wave.

Remark 5.4. *For numerical simulations, correlated initial noise in the Godunov scheme accurately models the Riemann problem. Specifically, the Riemann problem with stochastic datum can be modeled numerically by using the same realization of left initial noise for all cells on the left of the discontinuity in the discrete initial condition, and the same realization of the right initial noise for all cells on the right of the discontinuity in the discrete initial condition.*

In the two following sections, we consider a Riemann problem with stochastic datum modeling initial condition error. We show specific consequences of the nonlinearity of the PDE on the statistics of the distribution of the uncertainty on the true state and compare the true solution of the so-called *stochastic Riemann problem* with forecast state estimates given by the EKF, UKF and EnKF. We also consider the solution to the discrete Godunov scheme and assess how diffusion and modeling errors impact the applicability of the conclusions drawn for the continuous solution to the discrete solution.

5.4 Model nonlinearity

In this section, we present the consequences of model nonlinearities on the estimate statistics propagated by different schemes. We show that propagating only the first two moments of the distribution can lead to significant estimation error at shock waves where mixture distributions between the left and right state arise and propagate. We show that despite modeling error and numerical diffusion, this phenomenon is also present in the solution to the Godunov scheme. We focus our analysis on the EKF, EnKF and UKF, which offer distinct properties; the EKF consists in a linearization of the model, the EnKF exhibits stochastic error and converges toward the classical Kalman filter in the limit of infinite number of samples, and the UKF consists in deterministic sampling toward accurate propagation of the first two moments of the estimate distribution.

5.4.1 Mixture solution to the Riemann problem

In this section we show that the existence of discontinuities in the solution to the PDE combined with the existence of stochastic terms in the state-space model may introduce mixture distributions that travel with shock waves and propagate around it.

We note $\mathcal{D}$ the set of points (t, x) for which there is a non-zero probability that, in the (x, t) plane, a realization of the solution to the Riemann problem with stochastic datum (5.12) exhibits a discontinuity on the left of (t, x) and a non-zero probability that a realization exhibits a discontinuity on the right of (t, x):

$$\mathcal{D} = \left\{(t, x) \in \mathbb{R}^+ \backslash \{0\} \times \mathbb{R} | \min \left\{P(\varsigma < x/t), P(\varsigma > x/t)\right\} > 0\right\}.$$

Proposition 5.2. *In the domain $\mathcal{D}$, the solution to the Riemann problem with stochastic datum* (5.12) *is a mixture distribution.*

Proof. Outside of $\mathcal{D}$, we have by definition $P(\varsigma < x/t) = 0$ or $P(\varsigma > x/t) = 0$. According to equation (5.13), in the first case the solution of the Riemann problem is given by $P(\varrho_{t,x} = \rho) = P(\varrho_l = \rho | \varsigma > x/t)$, and in the second case, the solution of the Riemann problem is given by $P(\varrho_r = \rho | \varsigma < x/t)$, hence in both cases the solution is a conditional of the left or right initial datum. In $\mathcal{D}$, the solution is given by equation (5.13), where the two weighting terms are non-zero by definition. The random field $\varrho_{t,x}$ is a mixture of the left datum conditioned on the positivity of $\varsigma - x/t$, and the right datum conditioned on the negativity of $\varsigma - x/t$, as expressed by equation (5.13). ☐

The mixture nature of the solution of the Riemann problem with stochastic datum is illustrated in Figure 5.1, obtained by Monte Carlo simulation with 10^5 samples, for a Greenshields flux with parameters $V = 80$ mph and $\rho_{\max} = 120$ vpm (where *mph* and *vpm* respectively stand for *miles per hour* and *vehicles per mile*), and a Riemann problem with independent uniform left and right datum centered at $\rho_l = 30$ vpm, $\rho_r = 90$ vpm. Variances 100 and 400 are considered in Figure 5.1 left and right respectively. The domain where the minimum of the weighting terms ($P(\varsigma > \frac{x}{t})$ and $P(\varsigma < \frac{x}{t})$) is non-zero characterizes the domain $\mathcal{D}$, and the locus of the mixture distribution.

The mixture nature of the random field is due to the stochastic nature of the shock wave speed. Propagating a moment-based representation of the datum, as in the case of the EKF, through the deterministic model does not capture the mixture nature of the random field. The random field $\tilde{\varrho}_{t,x}$ defined by the stochastic initial datum and a deterministic Rankine-Hugoniot speed associated with the mean of the datum reads:

$$P\left(\tilde{\varrho}_{t,x} = \rho\right) = P\left(\varrho_l = \rho\right) \mathbf{1}\left(\sigma > \frac{x}{t}\right) + P\left(\varrho_r = \rho\right) \mathbf{1}\left(\sigma < \frac{x}{t}\right) \tag{5.14}$$

where the stochastic nature of the shock wave speed and non-independence between the datum and the shock wave speed are neglected. The difference between the state distribution propagated in this method and the true mixture distribution is illustrated in Figure 5.2, for the same model parameters and initial condition as in Figure 5.1, with a variance

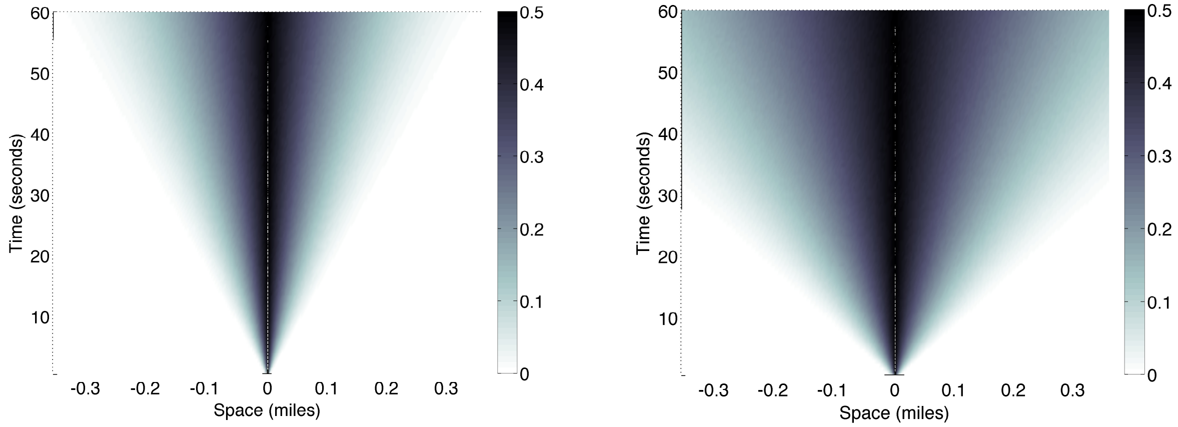

Figure 5.1: Mixture random field.
The minimum $\min\left\{P(\varsigma > \frac{x}{t}), P(\varsigma < \frac{x}{t})\right\}$ is represented over space and time for additive uniform noise with zero mean and variance 100 (left) and 400 (right). The mean of the left (resp. right) datum is 30 vpm (resp. 90 vpm). As can be seen, the higher the variance on initial data, the less it is acceptable to neglect the mixture nature of the random field.

100 and 10^7 particles. Figure 5.2 displays distributions corresponding to positive locations $(0.01, 0.11, 0.21$ miles), which corresponds to the right side of the left subfigure in Figure 5.1. This is a situation in which $P(\varsigma > \frac{x}{t}) < P(\varsigma < \frac{x}{t})$ (more chance for the shock to be on the left than on the right of location x at time t). This explains that the dominating mode corresponds to the right initial data. The dominating mode is the only mode represented by the random field $\tilde{\varrho}_{t,x}$, which is accurate far from the shock wave only. The correlation represented by the non-uniform distribution of the dominating mode is not captured by the random field $\tilde{\varrho}_{t,x}$. Additionally, we represent a distribution[1] with same mean and variance as the true distribution $\varrho_{t,x}$ (which is the underlying principle of the UKF). This distribution (in dotted line) exhibits a large variance which captures the variability due to the mixture nature of the true distribution. One may note that this distribution includes negative values with non-zero probabilities, and positive values outside of the admissible range according to the model, with non-zero probabilities.

Remark 5.5. *The solution to the stochastic Riemann problem given by equation* (5.14) *may be accurate if the mixture from equation* (5.13) *is degenerate and only one mode arises on each side of the shock wave. This is the case if the Rankine-Hugoniot speed is deterministic, which may arise in the case of specific correlated statistics or if the solution to the Riemann problem is a contact discontinuity (e.g. in case of piecewise linear fundamental diagrams, see Proposition 5.4).*

---

[1] For graphical comparison, we use the same family as the initial condition, i.e. a uniform distribution (represented in dotted line in Figure 5.2).

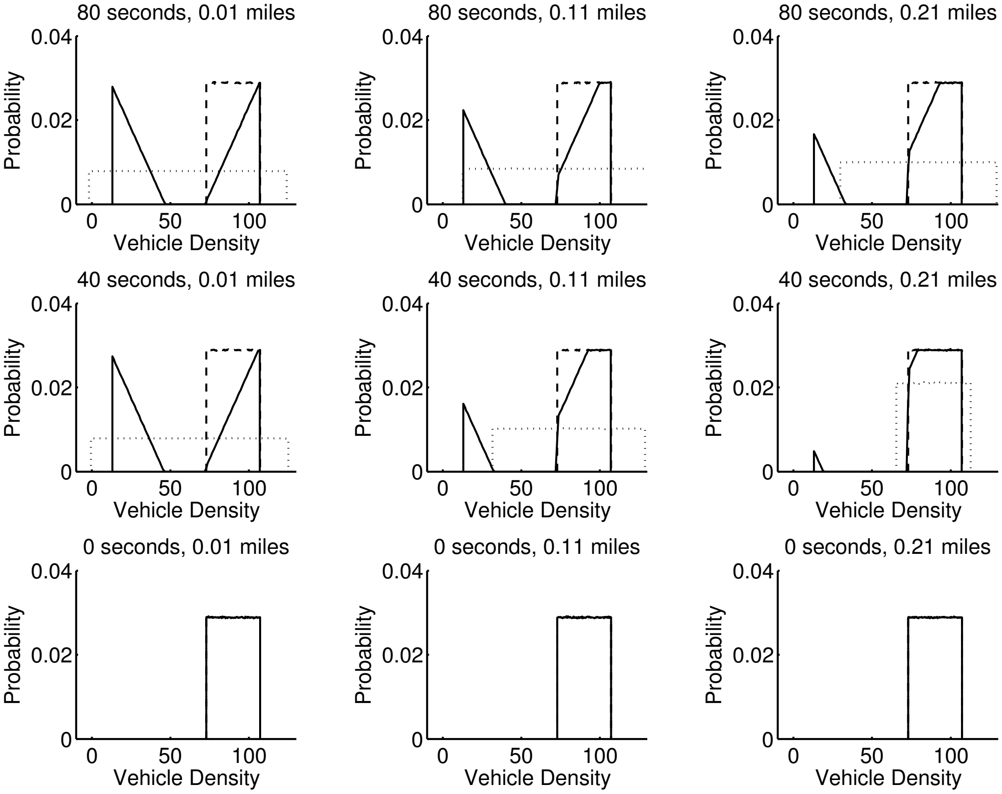

Figure 5.2: Distribution of vehicle density at different space-time locations.
Probability density function of the uncertainty $\varrho_{t,x}$ on the true state (solid line), uniform probability density function with identical mean and variance (dotted line), probability density function $\tilde{\varrho}_{t,x}$ given by a deterministic shock wave speed between the left and right stochastic initial datum (dashed line). This computation corresponds to a Greenshields fundamental diagram with uniform initial noise of variance 100. The true shock wave is initially located at location 0 and does not move.

Proposition 5.3. *For a Greenshields fundamental diagram, if the left initial noise and the right initial noise are such that the sum* $\rho_l + \rho_r$ *is constant across all realizations* ρ_l, ρ_r*, then the random field* $\varrho_{t,x}$ *is not a mixture distribution.*

Proof. The shock wave speed associated with a realizations ρ_l, ρ_r of the Riemann datum reads:

$$\sigma_G = \frac{V\,\rho_l\left(1 - \frac{\rho_l}{\rho_{\max}}\right) - V\,\rho_r\left(1 - \frac{\rho_r}{\rho_{\max}}\right)}{\rho_l - \rho_r}$$

which can be rewritten as:

$$\sigma_G = V - \frac{V}{\rho_{\max}}\,(\rho_l + \rho_r)$$

which according to the assumption on the statistics is the same for all realizations ρ_l, ρ_r. The domain $\mathcal{D}$ is thus empty, and the random field $\varrho_{t,x}$ is equal to the left or right datum. $\square$

Proposition 5.4. *For a triangular fundamental diagram, if* $\mathcal{D}_l, \mathcal{D}_r \subseteq [0, \rho_c]$ *or* $\mathcal{D}_l, \mathcal{D}_r \subseteq [\rho_c, \rho_{\max}]$*, the random field* $\varrho_{t,x}$ *is not a mixture, for almost all* $(t, x) \in \mathbb{R}^+\backslash\{0\} \times \mathbb{R}$*.*

Proof. By assumption, we have $\rho_l < \rho_r$ for all realizations of the two distributions. If $\mathcal{D}_l \subseteq [0, \rho_c]$ and $\mathcal{D}_r \subseteq [0, \rho_c]$, a realization σ_T of the shock wave speed ς_T for the triangular diagram reads:

$$\sigma_T = \frac{Q(\rho_r) - Q(\rho_l)}{\rho_r - \rho_l},$$

which can be rewritten using expression (1.3) and the fact that $\rho_l \in \mathcal{D}_l$, $\rho_r \in \mathcal{D}_r$, as:

$$\sigma_T = \frac{\rho_l\,V - \rho_r\,V}{\rho_l - \rho_r} = V$$

which yields a shock wave speed equal to the free-flow speed for all realizations. Therefore the shock wave speed is deterministic, and the random field solution of the Riemann problem is unimodal for almost all $(t, x) \in \mathbb{R}^+\backslash\{0\} \times \mathbb{R}$. Similarly if $\mathcal{D}_l, \mathcal{D}_r \subseteq [\rho_c, \rho_{\max}]$, the shock wave speed is the speed of backward moving waves w. The domain $\mathcal{D}$ is thus empty, and the random field $\varrho_{t,x}$ is equal to the left or right datum. $\square$

Consequently, for estimation using the CTM, when the traffic state is completely in free-flow ($\mathcal{D}_l, \mathcal{D}_r \subseteq [0, \rho_c]$) or completely in congestion ($\mathcal{D}_l, \mathcal{D}_r \subseteq [\rho_c, \rho_{\max}]$), the estimate distributions on the left and on the right do not mix and the normality assumption of the initial condition estimates propagates (this conditional linearity of the dynamics is used by the MKF).

5.4.2 Mixture solutions to the Godunov scheme

In this section, we analyze numerically how the emergence of mixture distributions in the solution of the Riemann problem for stochastic datum relates to the emergence of mixture distributions in the solution to the Godunov scheme. The Godunov scheme computes a numerical solution to the Cauchy problem on a discretization grid, by iteratively solving Riemann problems between neighboring cells and averaging their solutions within each cells. Numerical estimates produced in this manner differ from the estimates obtained by solving the Riemann problem on a continuous domain, due to numerical diffusion introduced in the averaging step and the discrete setting. Additionally, in the intent of modeling numerical diffusion, discretization error and inherent modeling error, it is common practice [131] to introduce an additive random source term to the discretized PDE (1.5). In order to study the emergence of mixture distributions in this context, we propose the following numerical experiments.

We consider the Greenshields fundamental diagram with parameters $V = 80$ mph, $\rho_{\max} = 120$ vpm, and the stochastic Riemann datum ($\varrho_l = \mathcal{N}(30, 100)$, $\varrho_r = \mathcal{N}(90, 100)$) (we truncate the normal distribution to force its support into the admissible domain $[0, \rho_{\max}]$ of the model). Using Monte Carlo simulations with 10^5 samples, we compute the (continuous) solution of the Riemann problem and the (discrete) solution of the Godunov scheme with *Courant-Friedrichs-Lewy* (CFL) [156] condition equal to one, spatially uniform left and right realizations of initial noise, and for various discretization grid sizes and values of the model noise.

Numerical diffusion: The influence of numerical diffusion on continuous and discrete numerical estimates (see Figure 5.3) is assessed by comparing the solution to the Riemann problem (solid line) with the solution to the Godunov scheme on a coarse grid (6 space cells, 18 time-steps, dashed line) and on a fine grid (12 space cells, 36 time-steps, dotted line). The Monte Carlo simulation is run with 10^5 samples. As illustrated in Figure 5.3, comparison of the numerical solutions on different grids illustrates that diffusion in the Godunov scheme smoothens the mixture nature of the solution to the Riemann problem. The numerical solution exhibits two modes but due to diffusion, a non-zero probability arises between the two modes. This illustrates that by discretization of the constitutive model, the true nature of the distribution of uncertainty is blurred. This is not necessarily a problem if the discrete numerical model (Godunov scheme in this case) is considered to be the physical model, i.e. is considered to represent the dynamics of the true state, as commonly done in transportation. However, it show the limitation of discrete approaches for estimation with continuous physical models, such as the LWR PDE.

Model noise: We propose to compare (see Figure 5.4) the continuous solution to the Riemann problem (solid line), the discrete solution to the Godunov scheme with no model noise (dotted line), and model noise represented by a random variable $\mathcal{N}(0, 50)$ (dashed line), on a grid with 6 space cells, 18 time-steps. The addition of a model noise term to the Godunov scheme to account for model errors leads to a reduction of the mixture nature of the distribution solution to the stochastic Riemann problem. It induces a diffusion of the

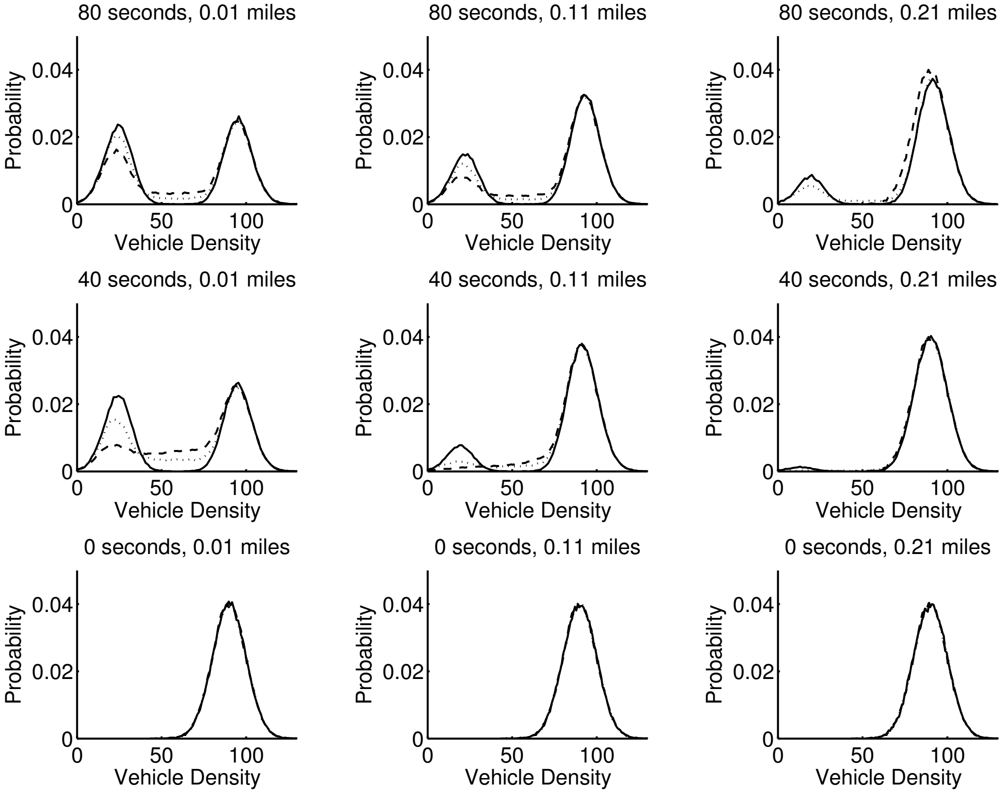

Figure 5.3: Numerical diffusion.
The mixture nature of the solution of the Riemann problem (solid line) is more accurately captured by the numerical solution with low numerical diffusion (dotted line) computed on the fine grid than by the numerical solution with high numerical diffusion (dashed line) computed on the coarse grid.

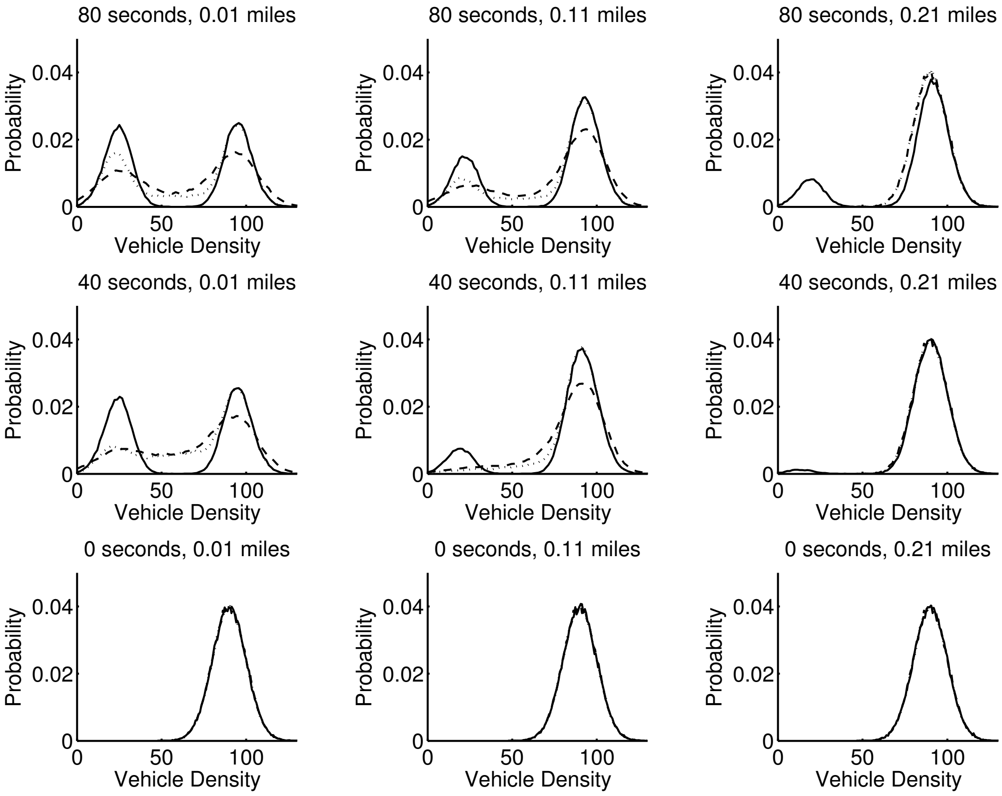

Figure 5.4: Model noise.

The probability density function of the solution of the Riemann problem is represented in solid line, the probability density function of the solution of the Godunov scheme with no noise is represented in dotted line, the solution of the Godunov scheme with Gaussian centered model noise with variance 50 is represented in dashed line.

true distribution, which contributes to further smoothen the two components of the mixture (see Figure 5.4). This diffusion is more structured that pure numerical diffusion (see Figure 5.3), but this example clearly advocates for noise modeling in order to account specifically for discretization error as a function of the state and the corresponding distribution of uncertainty [121, 120, 213].

Lack of correlation: The existence of mixture distributions around the discontinuity creates a correlation between the two sides of the shock wave (see Figure 5.5). By propagating a single component of the mixture on each side of the shock wave, the covariance structure is misrepresented by the linearized model. This is illustrated in Figure 5.5 representing the covariance structure of the estimate at time-step 20, for a Monte Carlo simulation with 10^4 particles in the left sub figure, and for the linearized model in the right sub figure. The fundamental diagram is a Greenshields fundamental diagram with parameters $V = 80$ mph, $\rho_{\max} = 120$ vpm, and the stochastic Riemann datum corresponds to $(\varrho_l = \mathcal{N}(15, 100), \varrho_r = \mathcal{N}(75, 100))$, in vehicles per mile. This corresponds to a shock-wave moving forward, starting at time 0 from cell 0. One may note that due to the CFL condition, at time 20, no physical correlation can exist farther than 20 cells around the diagonal. The block diagonal structure of the linearized model estimate at the shock wave appears clearly, whereas for the Monte Carlo simulation with 10^4 particles, the state error covariance matrix is band diagonal, which illustrates the correlation between the two sides of the shock wave due to the mixture components. The comparison between the two figures displays the lack of correlation, across the shock, of the covariance given by the linearized model. In the absence of correlation, measurements realized on one side of the shock do not influence the estimate on the other side of the shock. The fact that the linearized model overestimates the variance around cells neighboring the discontinuity location is visible from the color scale.

5.4.3 Discussion

In this section, we discuss how the properties of the distribution of the uncertainty on the true state solution of the Riemann problem with stochastic datum relate to the accuracy of the estimate given by classical filters at the analysis step.

Forecast mean: The estimate given by the mean of the distribution obtained by deterministic propagation of the mean of the left and right datum (case of EKF), with additive model noise, seems biased since it only captures one component of the mixture (see Figure 5.2 as well for instance). Close to the shock wave, the diffusivity of the Godunov scheme numerically alleviates this drawback by smoothing the mixture through diffusion. The bias at the shock wave due to mixture uncertainty is less likely to occur with sample-based filters which implicitly consider a stochastic model through the propagation of samples by a deterministic model (see experiments below). We reemphasize here that the true shock wave speed for Figure 5.2 and Figure 5.3 is zero, hence the true shock wave does not move from location 0.

Forecast variance: As illustrated in Figure 5.2, close to the shock wave, even when

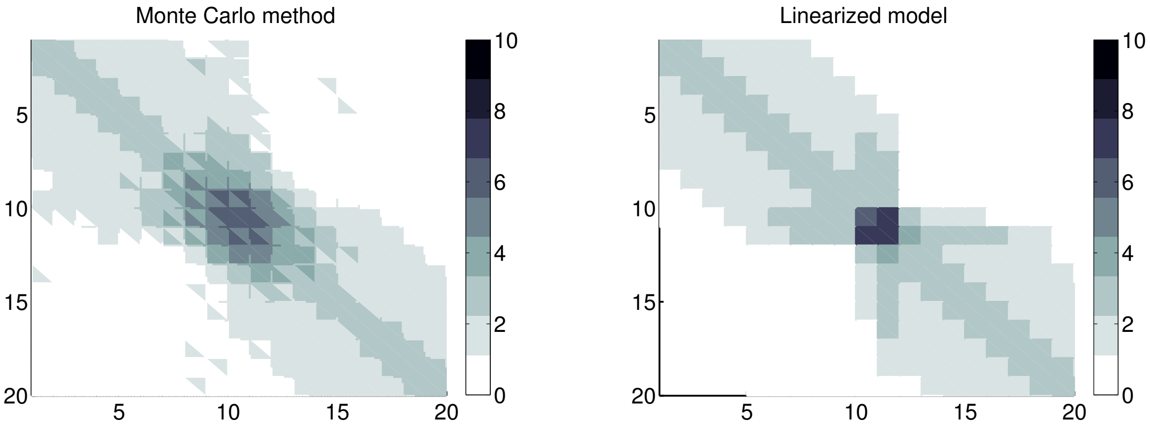

Figure 5.5: State error log-covariance matrix.
The shock wave is located at cell 10. The logarithm of the absolute value of the state error covariance matrix given by a Monte Carlo simulation with 10^4 particles (left) illustrates significant correlation between the two sides of the discontinuity, due to the existence of mixture distributions. The state error covariance given by a linearized model (right) is block-diagonal at the shock wave, due to the lack of correlation between the two sides of the shock wave in the linearized model. This lack of correlation might be problematic for estimation, because measurements might not give information across shocks.

the mean and the variance of the uncertainty on the true state are propagated accurately, representing the mixture distribution of the uncertainty by a unimodal distribution leads to considering a variance corresponding to the two modes, hence a greater dependency on the observations at the analysis step, through an increased gain, which is due to a poor representation of the uncertainty related to the prior distribution. On the other hand, if only a single mode of the uncertainty is accurately captured (case of EKF), the estimate exhibits a lower variance than the uncertainty, which is a classical cause of divergence of the filter.

Analysis step with mixture uncertainty: We consider the case of a stationary shock wave with left and right initial data ($\varrho_l = \mathcal{N}(30, 100), \varrho_r = \mathcal{N}(90, 100)$), for a Greenshields fundamental diagram with parameters $V = 80$ mph, $\rho_{\max} = 120$ vpm. The true stationary shock wave is located at location 20.5 throughout each simulation. Figure 5.6 and Figure 5.7 display the prior and posterior true uncertainty, and respectively the normal distributions corresponding to the EKF estimate and the EnKF ensemble estimates[2], as well as the observations. The prior distribution of the uncertainty on the true state is computed by Monte Carlo simulation with 10^5 particles, and its posterior obtained by full Bayesian update. We study the characteristics of the analysis step of the EKF and the EnKF, at different times,

---

[2] Even though the EnKF propagates and updates ensemble, for visual consistency in a context of minimum variance estimation, and due to the low number of ensemble members used, we present the normal distribution corresponding to the ensemble members distribution.

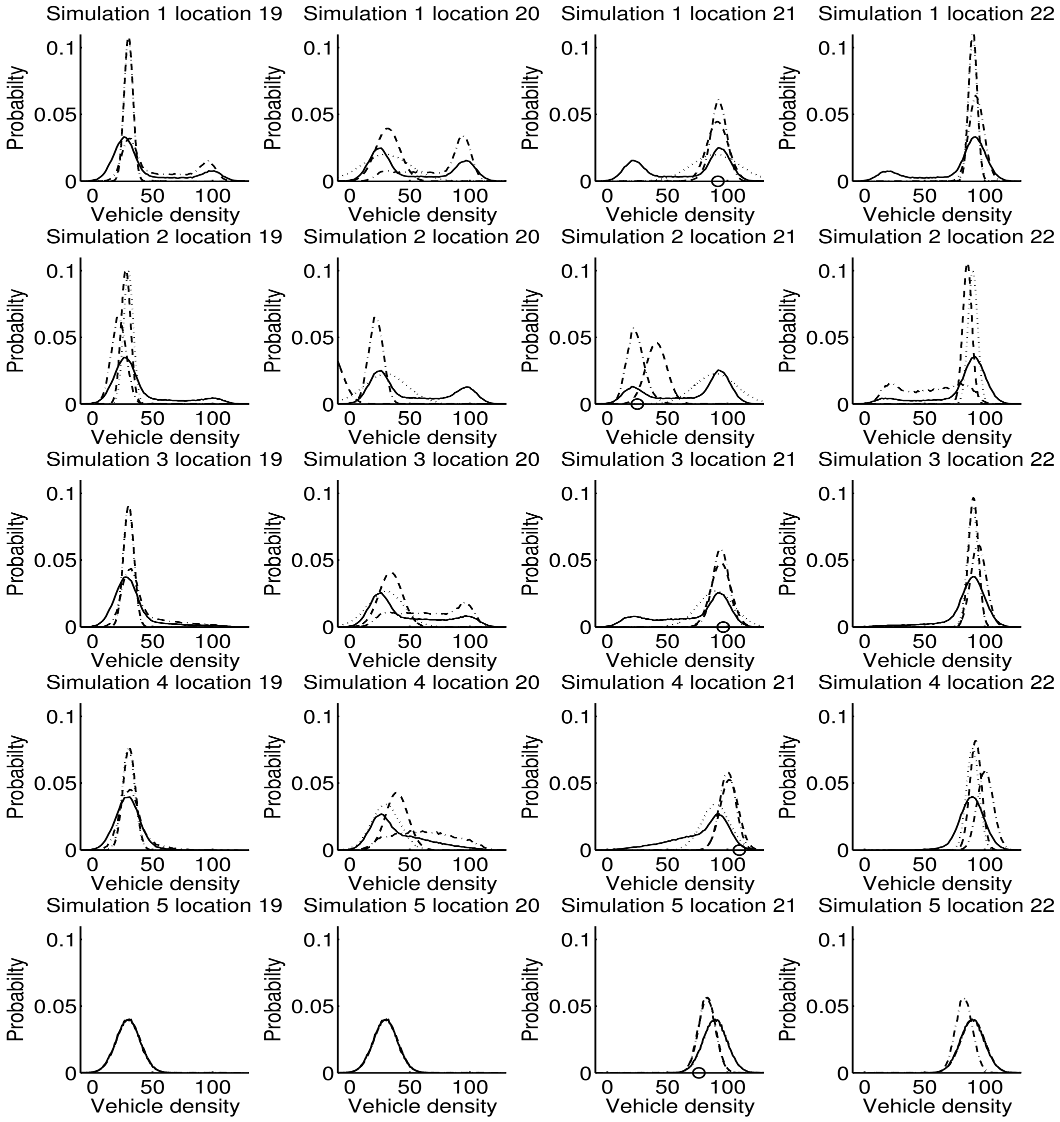

Figure 5.6: EKF analysis step.
The analysis step at different times is represented for a stationary shock-wave at location 20.5, between 30 vpm and 90 vpm, initial condition noise variance 100, and observation noise variance 100. The observation is represented by a circular marker. The prior distribution of the uncertainty on the true state obtained by Monte Carlo simulation with 10^5 samples is represented in solid line, the posterior distribution obtained by Bayesian update is represented in dash-dotted line. The prior distribution given by propagation through the linearized model is represented in dotted line, and the posterior distribution given by the analysis step of the EKF is represented in dashed line.

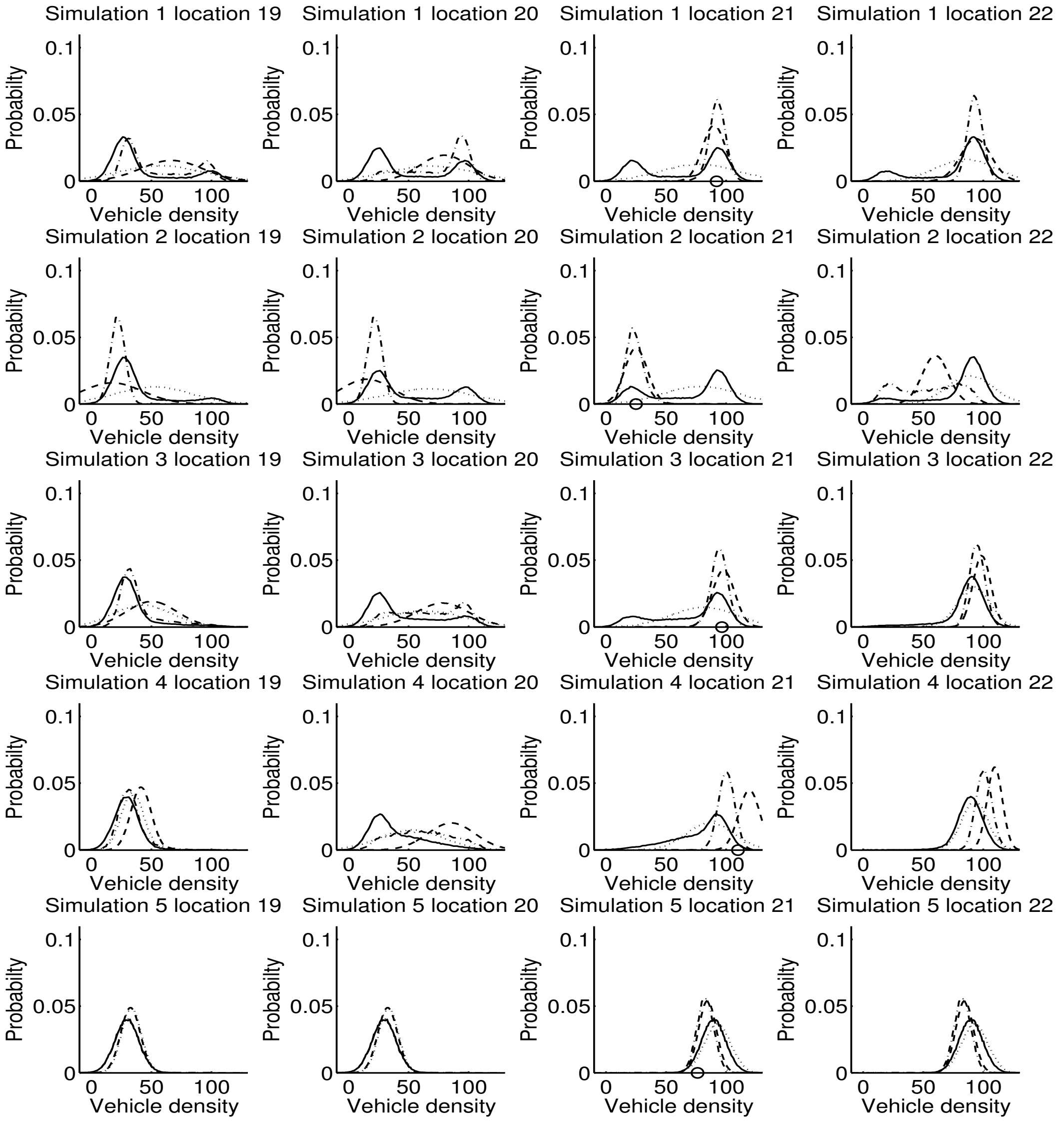

Figure 5.7: EnKF analysis step.

The analysis step at different times is represented for a stationary shock-wave at location 20.5, between 30 vpm and 90 vpm, initial condition noise variance 100, and observation noise variance 100. The observation represented by a circular marker. The prior distribution of the uncertainty on the true state obtained by Monte Carlo simulation with 10^5 samples is represented in solid line, the posterior distribution obtained by Bayesian update is represented in dash-dotted line. The estimate distributions given by the EnFK are represented as normal distributions with corresponding mean and variance. The prior given by propagation of 40 ensemble members is represented as a normal distribution in dotted line, and the posterior given by the analysis step of the EnKF is represented as a normal distribution in dashed line.

with a single observation with observation noise variance 100. The posterior computed by the analysis is not propagated further but simply displayed. This means that each row in Figure 5.6 and Figure 5.7 corresponds to a a different value of the true state, a different realization of the observation noise, and a single analysis step. For the sake of comparison we always sample an observation at location 21.

The sensitivity of the filters to the observation is illustrated by the significant difference between the prior and the posterior (respectively dotted and dashed lines), around the shock-wave, for both the EKF and the EnKF. At the location of the observation (location 21), the prior provided by the EKF, which only captures a single mode, is more inaccurate than the prior given by the EnKF, which can account partially for mixture distributions representation with ensemble members. However, after analysis, the posteriors for the two filters are very similar at the location of the observation. Away from the shock wave (location 1 and 4), it is clear that the EKF estimate exhibits a non-consistent error variance (simulations $1, 2, 3$ in particular).

The correlation across the shock wave clearly discriminates the two filters. Across the shock wave, at location 20, the posterior given by the EKF (dashed line) is often centered on the wrong mode of the posterior uncertainty (dash-dotted line). This is not the case for the EnKF which captures the two modes of the mixture in most cases. When the observation corresponds to a mode of the mixture uncertainty not well-represented by the estimate (for instance run 2, location 21 of Figure 5.6), it can be noted that the posterior distribution can provide more inaccurate estimate than the prior; for instance the posterior given by the EKF (dashed line) for run 2, location 20, is outside the range of values represented. This illustrates the difficulty to capture true correlation induced by mixture uncertainty across the shock wave.

The mixture nature of the uncertainty is clearly reduced by the observation, however, the two modes are still present and propagate in the posterior uncertainty (dash-dotted line at location 19 and 20 for simulation 1, location 22 for simulation 2, location 20 for simulation 3).

These numerical examples illustrate the limitations of the suboptimal MMSE estimates provided by the EKF and EnKF, in the case of mixture distributions arising in traffic flow around shock-waves. Stochastic filters such as the EnKF are more robust to the mixture nature of the uncertainty, since their sample representation allows them to better capture the full variance of the two modes of the distribution of the uncertainty on the true state. However, this leads to higher sensitivity of the filter and may lead to instabilities at shock waves. On the other hand, deterministic filters able to capture only a single mode of the distribution of the uncertainty on the true state exhibit a lower variance than the uncertainty, which may cause divergence of the estimate if the models have low error terms.

5.5 Model non-differentiability

In this section, we show that the numerical Godunov flux defined in (1.5)- (1.6) is non-differentiable. We prove that consequently, the discrete-time dynamics of the Godunov scheme is non-differentiable, which prevents straightforward application of filtering algorithms requiring differentiability to discrete transportation models based on the Godunov scheme.

5.5.1 Characterization of non-differentiability domain

The Godunov scheme consists of a dynamical system (1.5) resulting from the discretization of the transport equation where the numerical flux $q_G(\cdot,\cdot)$ can be defined in a piecewise manner on regular sub-domains in the case of a concave flux with a single maximum (1.6). The following proposition states the lack of continuous differentiability at a specific boundary between two of these sub-domains.

Proposition 5.5. *On the domain $\mathcal{S}$ defined as:*

$$\mathcal{S} = \left\{(\rho_l, \rho_r) \in [0, \rho_{\max}]^2 \mid \quad \rho_l < \rho_r \quad \textit{and} \quad Q(\rho_l) = Q(\rho_r)\right\}, \tag{5.15}$$

the numerical Godunov flux (1.6) *is not differentiable.*

Proof. The expression of the numerical Godunov flux is given by equation (1.6). In each sub-domain of definition corresponding to each line of (1.6), if the flux function $Q(\cdot)$ is differentiable, the numerical flux $q_G(\cdot,\cdot)$ is also left and right differentiable. It is straightforward to compute its left and right derivative on each sub-domain:

$$\frac{\partial q_G}{\partial \rho_l}(\rho_l, \rho_r) = \begin{cases} Q'(\rho_l) & \text{if} \quad \rho_r \le \rho_l < \rho_c \\ 0 & \text{if} \quad \rho_r \le \rho_c \le \rho_l \\ 0 & \text{if} \quad \rho_c < \rho_r \le \rho_l \\ \begin{cases} Q'(\rho_l) & \text{if} \quad Q(\rho_l) < Q(\rho_r) \\ 0 & \text{if} \quad Q(\rho_l) > Q(\rho_r) \end{cases} & \text{if} \quad \rho_l < \rho_r \end{cases} \tag{5.16}$$

$$\frac{\partial q_G}{\partial \rho_r}(\rho_l, \rho_r) = \begin{cases} 0 & \text{if} \quad \rho_r \le \rho_l < \rho_c \\ 0 & \text{if} \quad \rho_r \le \rho_c \le \rho_l \\ Q'(\rho_r) & \text{if} \quad \rho_c < \rho_r \le \rho_l \\ \begin{cases} 0 & \text{if} \quad Q(\rho_l) < Q(\rho_r) \\ Q'(\rho_r) & \text{if} \quad Q(\rho_l) > Q(\rho_r) \end{cases} & \text{if} \quad \rho_l < \rho_r. \end{cases} \tag{5.17}$$

As indicated by the fourth case of equation (5.16) (or equivalently for the right derivative with the fourth case of equation (5.17)), the left derivative of the numerical flux is only defined on the left and on the right of the domain $\mathcal{S}$ defined by (5.15), with the left value being $Q'(\rho_l)$ and the right value being 0. The left and right values are equal only at the capacity point (point of maximal flux), in the case of a flux differentiable at capacity. Since the left derivative is not differentiable on $\mathcal{S}$, the numerical flux is not differentiable on its domain of definition. $\square$

The domain of non-differentiability of the numerical Godunov scheme corresponds to the locus of stationary shock waves. In particular, the numerical Godunov flux and the discrete dynamics associated with the Godunov scheme are differentiable at moving shock waves. In the case of discretization schemes with higher numerical viscosity, for instance the *Lax-Friedrichs* numerical scheme [156], differentiability is obtained everywhere but numerical approximation of discontinuities is less accurate.

Proposition 5.6. *The discrete time dynamics of the Godunov scheme is non-differentiable, and in the case of a differentiable flux function $Q(\cdot)$, the non-differentiability domain consists of the locus $\mathcal{S}$ of stationary shock-waves.*

Proof. The numerical flux is non-differentiable in the domain $\mathcal{S}$ defined by (5.15). Since it is impossible to have at the same time $(\rho_{i-1}^n, \rho_i^n) \in \mathcal{S}$ and $(\rho_i^n, \rho_{i+1}^n) \in \mathcal{S}$, the discrete time dynamics defined by equation (1.5) is non-differentiable. In the case of a differentiable flux function $Q(\cdot)$, the numerical flux is also differentiable in all its sub-domains of definition, and it can be checked in Figure 5.8 that it is also continuously differentiable at their boundaries, thus $\mathcal{S}$ is the non-differentiability domain of the discrete time dynamics associated with the Godunov scheme. $\square$

The non-differentiability of the discrete dynamics associated with the Godunov scheme does not result from a numerical issue but results from the structure of the solution of the continuous partial differential equation considered. This can be verified by considering the solution to the Riemann problem in the case of a stationary shock wave. The solution that consists of upstream and downstream densities with equal fluxes is stationary. However, it is clear that a slight perturbation of the upstream or downstream density causes the shock wave to propagate and the domain corresponding to the left or right initial condition to eventually prevail, depending on the flux balance at the discontinuity.

Remark 5.6. *In the case of non-differentiable flux functions $Q(\cdot)$ such as the triangular flux function or the Smulders flux function, it is clear that the dynamics of the numerical solution is not differentiable. However, since the flux function results from an empirical fit, the flux function can be approximated by a smooth function with relatively small consequences. The non-differentiability described in Proposition 5.5 results from the intrinsic properties of the conservation law, which can only by fixed by modifying the constitutive physical principles of the model.*

Remark 5.7. *For junction problems modeled as the maximization of a linear objective function of the traffic state under linear inequality constraints (see Remark 1.1), the optimum is always attained at a vertex of the constraint polytopes, hence the flow through the junction*

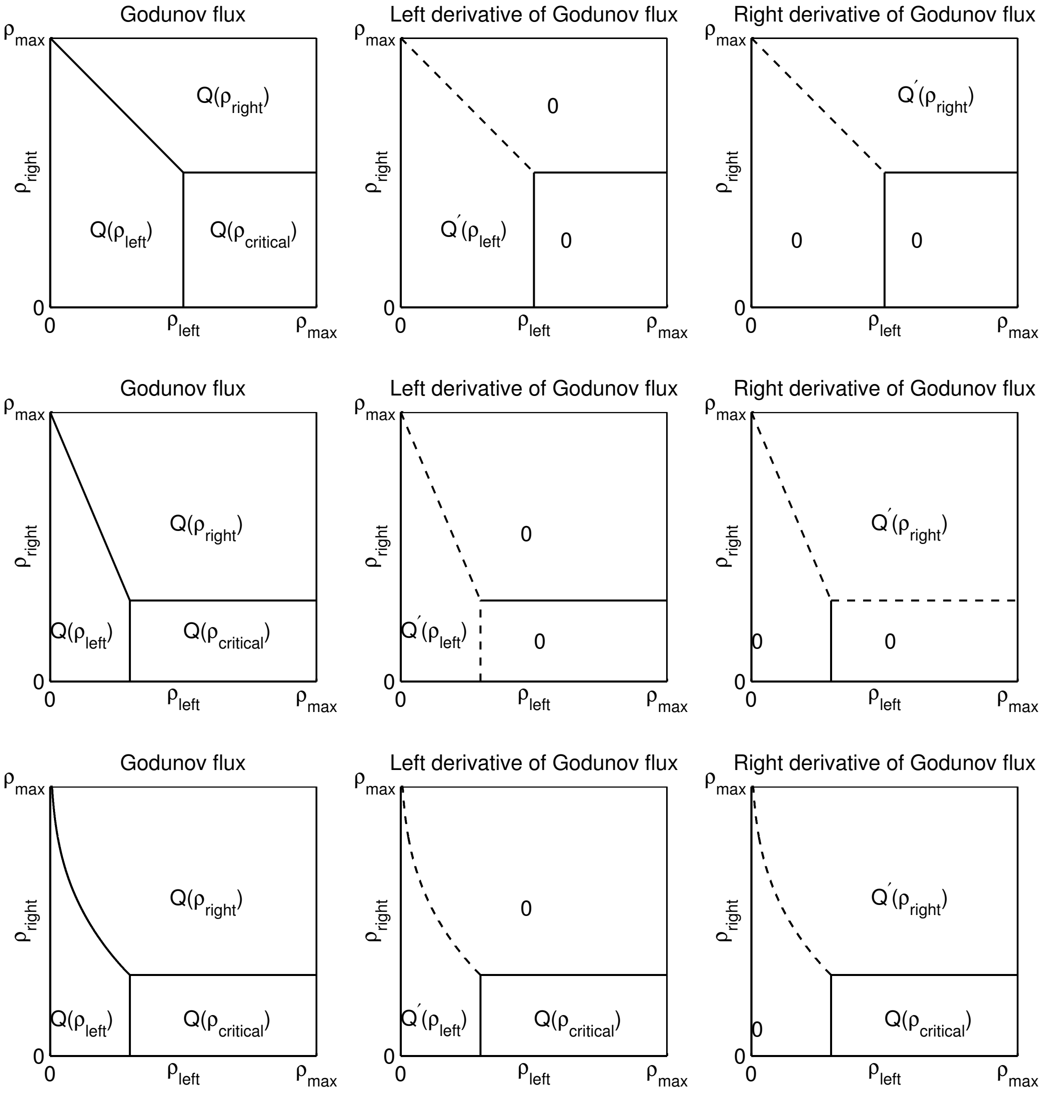

Figure 5.8: Locus of non-differentiability of the numerical Godunov flux.
The top, middle and bottom row respectively correspond to the Greenshields, triangular, and exponential fundamental diagram. The Godunov flux is defined in a piecewise manner on the three sub-domains delimited by solid or dashed line. A dashed line indicates discontinuity across the boundary of the domain, whereas a solid line indicates continuity at the boundary. The three diagrams exhibit non-differentiability of the locus of stationary shock-waves (center and right column, oblique curve). Additionally, the triangular diagram (middle row) exhibits non-differentiability at the critical density.

is not a differentiable function of the traffic state and the same difficulties happen there as well.

5.5.2 Numerical experiments

In this section, we analyze the estimation error induced by the lack of differentiability of the numerical Godunov flux at the locus of stationary shock waves.

For clarity we present results for the case of the Greenshields flux function (1.2) (with parameters $V = 80$ mph and $\rho_{\max} = 120$ vpm, as in the previous section), which is differentiable on its domain of definition. Similarly, in order to simplify the analysis, we consider only initial condition noise, drawn from i.i.d. normal distribution $\mathcal{N}(0, 100)$. The model noise is considered to be 0. We use the Godunov scheme (1.5), with CFL condition [156] equal to 1, and 80 cells in space. The distribution of the uncertainty on the true state is computed using a Monte Carlo simulation with 10^4 particles, and the forecast moments using different propagation models are compared against the true moments. In order to assess the accuracy of the estimate covariance, we compute two error metrics. The error metric for the mean, in Figure 5.9, is the relative L^2 error:

$$\frac{\|\mu_e - \mu\|_2}{\|\mu\|_2}$$

where μ_e denotes the estimated mean using the forecast step of a model, and μ is the true forecast. The error metric for the covariance, in Figure 5.10, is the relative absolute error on the error covariance trace, defined by:

$$\frac{\mathrm{trace}(|\tilde{\Sigma} - \Sigma|)}{\mathrm{trace}(\Sigma)}$$

where $\tilde{\Sigma}$ denotes the estimated error covariance given by the forecast model and Σ denotes the true error covariance.

Estimate error: The error induced by the use of a linearization method at the locus of the stationary shock wave is illustrated in solid line in Figure 5.9 for the mean and in Figure 5.10 for the covariance, for the use of the derivative of the numerical Godunov flux on the left at its point of non-differentiability. For state propagation using a Monte Carlo method with 50 particles (right sub figure) or the linearized model (right sub figure), the shock waves leads to the highest error, which is due to the fact that only entropic shock waves are propagated by the scheme; the uncertainty associated with the initial condition propagates toward the shock wave location. In the case of a rarefaction, the uncertainty associated with the initial datum propagates outward, and the centered fan is deterministic.

The state error covariance given by forward simulation using the linearized dynamics diverges in time from the covariance of the uncertainty on the true state (see Figure 5.10 left). In the case of a stationary shock wave (solid line), the divergence is slightly faster than in the case of a moving shock wave. In particular, noting that the oscillations in the curve associated with a moving shock wave (dashed line) in Figure 5.9 and Figure 5.10 correspond to a change of cells and that the meaningful error for this phenomenon corresponds to the lower envelope of this curve, the divergence associated with the stationary shock wave is noticeably greater. However, one may note that Figure 5.9, left, and Figure 5.10, left, only correspond to considering the derivative on the left at the non-differentiability locus. Different weightings of the left and right derivative at the non-differentiability domain might lead to better results.

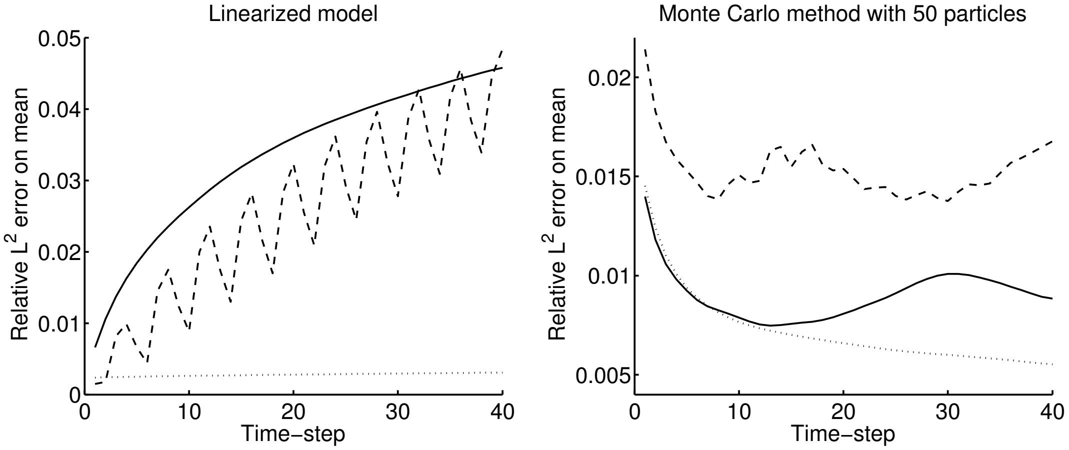

Figure 5.9: Mean error growth.
The growth with time of the relative L^2 error on the mean is represented for a linearized model (left) and a Monte Carlo simulation with 50 particles (right). The solid line corresponds to the case of a stationary shock wave with $\rho_l = 30$ vpm, $\rho_r = 90$ vpm, the dashed line corresponds to the case of a moving shock wave, with $\rho_l = 15$ vpm, $\rho_r = 75$ vpm, the doted lined corresponds to the case of a rarefaction wave, with $\rho_l = 90$ vpm, $\rho_r = 30$ vpm.

5.5.3 Discussion

In this section we analyze the consequences of non-differentiability of the dynamics of the Godunov scheme for state estimation.

As illustrated in Figure 5.9 left, the trend of the estimation error due to model nonlinearity is comparable for the stationary shock wave (solid line) and for the moving shock wave (dashed line). This is consistent with the fact that the propagation of the estimate mean in the linearized model does not involve differentiability. The error introduced is simply due to the nonlinearity of shock waves with the Greenshields flux function. In the case of the rarefaction wave (dotted line), the estimation error is much smaller due to the entropy condition and the fact that information propagates outward from the initial discontinuity.

For a moving shock wave (dashed line), the error exhibits a typical oscillation feature due to error of location of the shock wave. The increasing part of the oscillation corresponds

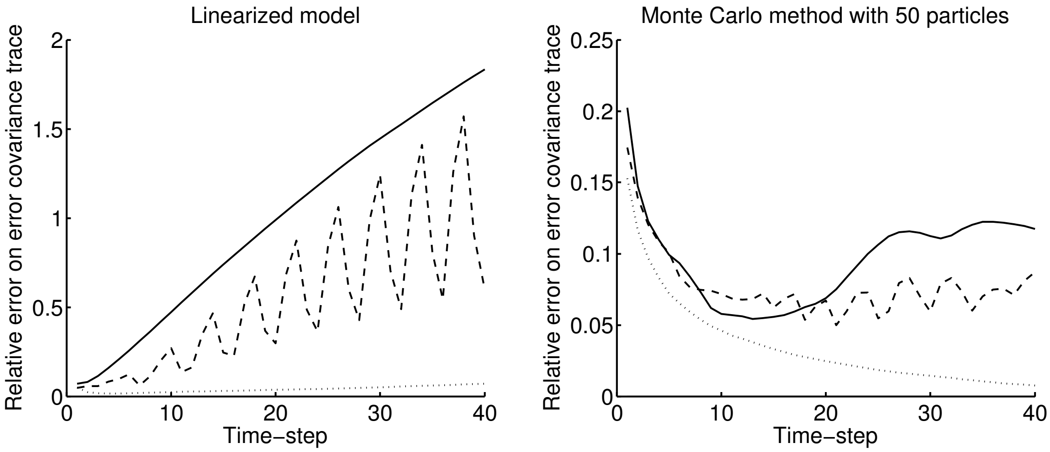

Figure 5.10: Covariance error growth.
The growth with time of the relative error on the error covariance trace is represented for a linearized model (left) and a Monte Carlo simulation with 50 particles (right). The solid line corresponds to the case of a stationary shock wave with $\rho_l = 30$ vpm, $\rho_r = 90$ vpm, the dashed line corresponds to the case of a moving shock wave, with $\rho_l = 15$ vpm, $\rho_r = 75$ vpm, the dotted lined corresponds to the case of a rarefaction wave, with $\rho_l = 90$ vpm, $\rho_r = 30$ vpm.

to the mixture nature of the distribution of the uncertainty arising in the cell where the shock wave will move, hence increasing the error with the linearized model. The decreasing part of the oscillation corresponds to the shock wave actually propagating to the cell, and reducing the error. The finite slope on the decreasing part corresponds to the effect of diffusion.

The non-differentiability of the numerical flux introduces an error in the error covariance which increases with time at a rate noticeably greater than the error growth rate in the error covariance for a moving shock wave (see Figure 5.10 left in which the trend of the solid line is comparable to the trend of the top of the peaks of the dashed line).

Inaccurate estimation of the state covariance at the forecast step, depicted in Figure 5.10, impacts the use of measurements at the analysis step. This is illustrated in Figure 5.11, in which we consider an analysis done at time 40, for the case of the stationary shock wave, with the same parameters used in Figure 5.10. We compare the posterior error covariance computed by the analysis step defined by the Kalman filter (1.15), with on one hand a covariance computed by propagation of the initial condition covariance through the linearized state model, and on the other hand a covariance computed by a Monte Carlo simulation with 10^4 samples. The prior means and the observations are identical for both cases, hence the discrepancy in the posteriors is solely due to the discrepancy in the prior covariances and result from the inaccuracy of the covariance propagated by the linearized non-differentiable model. A Monte Carlo simulation with 10^4 samples is considered to provide the distribution of the uncertainty on the true state.

As illustrated in Figure 5.11, the error associated with the prior covariance induces an

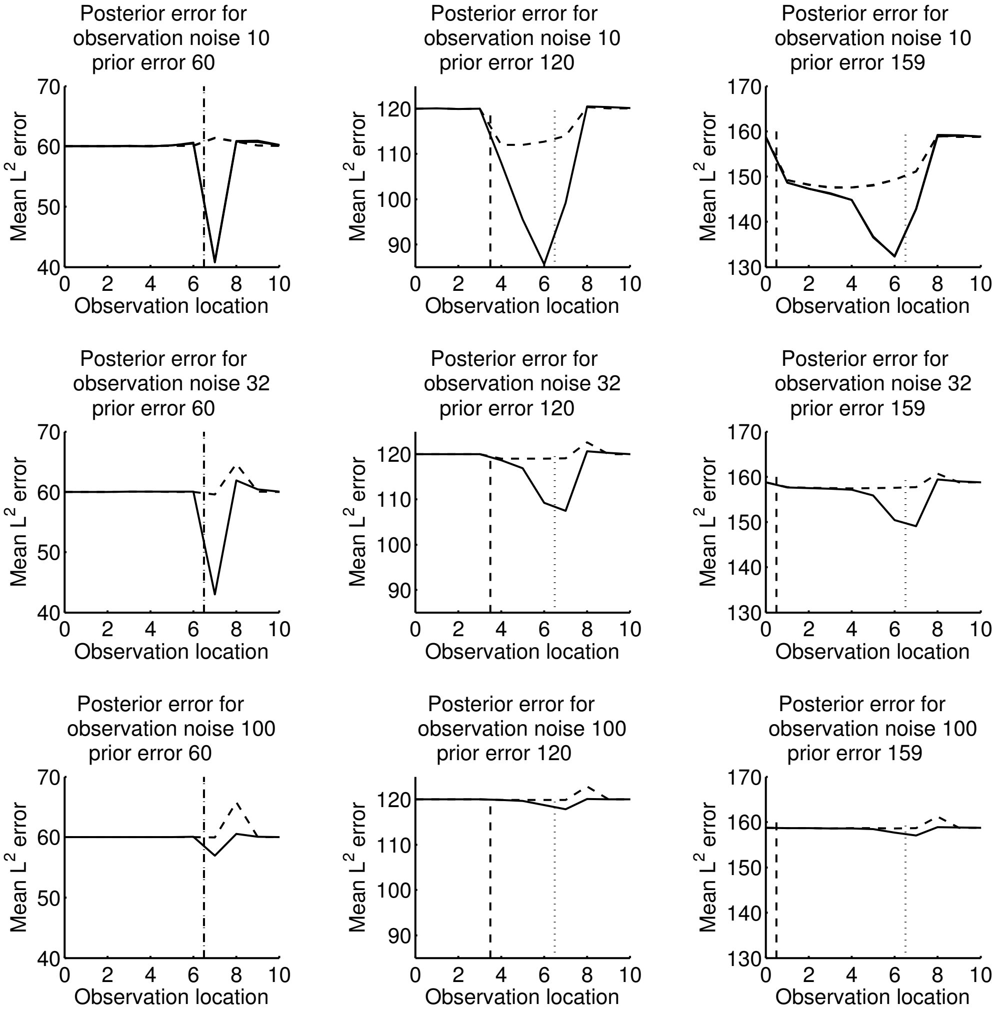

Figure 5.11: Posterior mean error.

The mean L^2 error of the posterior for 10^3 draws of the observation at each location, is represented as a function of the observation location for an analysis with prior covariance obtained by Monte Carlo simulation with 10^4 samples (solid line), and for an analysis with prior covariance propagated by the linearized model (dashed line). Top, middle, and bottom row respectively correspond to observation noise standard deviation 10, 32, 100. The prior shock wave, represented as a vertical dotted line, is located between cells 6 and 7 for all simulations. For the left, middle, right columns, the true shock wave, represented as a vertical dashed line, is respectively located between cells 6 and 7, 3 and 4, 0 and 1.

error in the posterior mean. In particular, for observations close to the discontinuity, one can note that the error in the posterior can be higher than the prior error, which corresponds to the horizontal line. The inability to capture the covariance structure at the shock wave, presented in the previous section, is also visible on the case of an accurate prior (left column) with a different posterior error for observations located on the left or on the right of the shock wave, although the problem is symmetric, as illustrated by the posterior error for the true covariance error in that case.

The fact that the filter may diverge due to the wrong covariance structure propagation by the linearized non-differentiable model is illustrated in Figure 5.12 in which we present the posterior covariance for the two different analysis described above, on one hand with the covariance propagated by the linearized model, and on the other hand with the covariance associated with the true distribution of uncertainty, computed using a Monte-Carlo simulation with 10^5 samples and the parameters of Figure 5.11 left column.

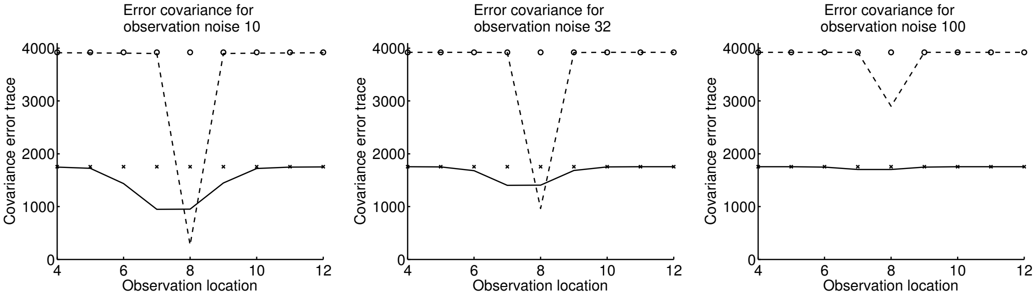

Figure 5.12: Posterior covariance error.
The posterior covariance for the linearized model (dashed) and for the Monte-Carlo simulation with 10^5 samples (solid) with respective prior covariance in circle and cross, are represented as a function of the observation location.

For observation with low error located close to the shock wave location, the analysis can cause the linearized filter to diverge by introducing a covariance lower than the covariance on the uncertainty. This echoes the analysis on the nonlinearity and the difficulty to model correctly the correlation structure at shock waves. In particular it is clear that observations away from shock waves do not particularly improve the estimates, and observations close to shock waves can potentially decrease the accuracy of the estimates and performance of the filter at the next time step.

The analysis presented in this chapter is focused on scalar macroscopic traffic flow models. These results are illustrative of the applicability of these filters to the phase transition models presented in the previous chapters. In particular, the robustness of stochastic filters such as the ensemble Kalman filter to modeling errors, described in this chapter, makes it a good candidate for real-time data assimilation with non-scalar traffic flow models.

Chapter 6

Boundary stabilization of weak solutions to scalar conservation laws

In this chapter, we consider the problem of stabilization of systems modeled by scalar hyperbolic conservation laws. This applies directly to traffic modeling with the LWR model, and to fluid-dynamic models with the Burgers equation. We assume that the actuators of the system are located at the boundaries. In particular, for transportation networks, this problem setting can be understood as the problem of the design of variable speed limits or ramp metering.

The problem of boundary control of partial differential equations has been the focus of sustained research. A large volume of literature is concerned with the problem of boundary control of the viscous Burgers equation. Control results can be found in [43, 44, 138, 139, 165, 200]. A Lyapunov approach, from which the method presented in this chapter was inspired, has been proposed in [139], for classical solutions to the PDE.

Lyapunov methods for classical solutions of networks of scalar conservation laws have also been proposed in [18], and for classical solutions of 2×2 systems with characteristics speeds of constant opposite sign in [64, 81]. Similar work on boundary damping techniques with applications to the Saint-Venant equations has been proposed in [75, 187]. Switching techniques for linear hyperbolic systems are investigated in [6, 7]. A frequency domain framework [161] has been used to design a boundary control for the linearized Saint-Venant equations in [162] (see also [108] for boundary control of the Saint-Venant equations). A specific method for *flat* systems has been introduced in [95] (see also [186] in the context of the Burgers equation).

Methods developed specifically for well-posedness results of conservation laws have also been applied to the problem of boundary control. In [8], a wavefront tracking method was used to compute the fixed horizon attainable set of initial-boundary value problem solutions of Temple systems of conservation laws.

Frameworks arising from the field of optimal control have also been applied to this problem [123, 122]. In [12], the authors proposed a viability framework for a Hamilton-Jacobi equation corresponding to an integral form of the Burgers equation, which leads to lower semi-continuous solutions. A linear relaxation method for the nonlinear discrete dynamics of the asymmetric cell-transmission model, a specific instantiation of the Godunov scheme for the LWR equation, has also been proposed in [104], with subsequent global optimization of the obtained equivalent convex problem. In the context of network traffic and dynamic traffic assignment, we refer the reader to [185] and the references therein. The problem of air traffic flow control has been notably addressed using adjoint methods in [20] and in [226] using a convex formulation.

One of the challenging features of conservation laws is the apparition of discontinuities in finite time in the solution to the Cauchy problem, even for smooth initial condition. This yields difficulties for most control approaches since classical control methods are not well-suited to handle discontinuities. In the case of parametric initial conditions, the problem of differentiating the solution to the scalar conservation law with respect to the initial condition parameter has been specifically addressed in [16] from a mathematical perspective. One must also note the more general shift differentiability method for functionals on $L^1 \cap BV$ introduced in [22, 41] (see section 6.2.1 for a definition of the class of BV functions).

A second specific challenge of boundary control of the solution to a conservation law also due to the non-linearity of the PDE is the fact that weak boundary conditions have to be considered. In this work, we specifically account for these two issues and show the stability of the weak entropy solution to the scalar conservation law (6.1).

6.1 Problem statement

Consider the scalar conservation law in one dimension of space

$$\partial_t u + \partial_x f(u) = 0 \tag{6.1}$$

in the domain $\Omega \doteq \{ (t,x) | \, t \geq 0 \text{ and } a \leq x \leq b \}$. The flux function $f(\cdot)$ is assumed to be smooth and strictly convex. The *initial-boundary value problem* (IBVP) for (6.1) in Ω with initial condition $u_0 : (a,b) \mapsto \mathbb{R}$, and boundary conditions $u_a, u_b : \mathbb{R}^+ \mapsto \mathbb{R}$, reads

$$\partial_t u + \partial_x f(u) = 0 \tag{6.2}$$
$$u(0,x) = u_0(x) \tag{6.3}$$
$$u(t,a) = u_a(t), \; u(t,b) = u_b(t). \tag{6.4}$$

The Lyapunov boundary stabilization problem can be formulated as follows.

Definition 6.1. *Given a stationary solution u^* to the PDE* (6.1)*, and an initial condition u_0 with bounded variations (see section 6.2.1), the Lyapunov (resp. asymptotic) boundary stabilization problem consists in the existence of boundary conditions u_a, u_b such that the IBVP* (6.2)-(6.3)-(6.4) *is well-posed and its solution is (resp. asymptotically) stable in the sense of Lyapunov at u^*.*

Stationary solutions to the PDE include uniform solutions and solutions with a single stationary jump discontinuity. We address the case of uniform solutions in Section 6.4.

The well-posedness of the IBVP (6.2)-(6.3)-(6.4) is critical to the definition of the problem, since the design of arbitrary boundary conditions can make the problem ill-posed (see [205] for an illustration on the LWR equation in the case of traffic). This would lead to a discrepancy between the control implemented and its realized value in the system, and a divergence between the desired trajectory of the system and its real trajectory. In the case of traffic, it corresponds for instance to installing a green traffic light at the location of a traffic jam with the intended goal that cars in the jam adopt the corresponding free-flow speed. For well-posedness of the IBVP (6.2)-(6.3)-(6.4), the PDE (6.1) and the boundary conditions (6.4) must be understood in the weak sense. The weak formulation is presented in Section 6.2.2.

6.2 Preliminaries

In this section, we introduce the notations and classical results subsequently used throughout this chapter.

6.2.1 BV functions

Consider an interval $J \subset \mathbb{R}$, and a map $u : J \mapsto \mathbb{R}$. The *total variation* of u is defined as

$$\text{Tot. Var.}\{u\} \doteq \sup \left\{ \sum_{i=1}^{N} |u(x_j) - u(x_{j-1})| \right\} \tag{6.5}$$

where the supremum is taken over all $N \geq 1$ and all $(N+1)$-tuples of points $x_j \in J$ such that $x_0 < x_1 < \ldots < x_N$. If the total variation of u is finite, $u \in BV$. Specific properties of BV functions leveraged in the following sections are presented below[1].

Lemma 6.1. *[39] Let $u : (a,b) \mapsto \mathbb{R}^n$ have bounded variations. Then for every $x \in (a,b)$, the left and right limits*

$$u(x-) \doteq \lim_{y \mapsto x-} u(y), \quad u(x+) \doteq \lim_{y \mapsto x+} u(y)$$

are well defined. Moreover, u has at most countably many points of discontinuity.

The following lemma concerns piecewise constant approximability of BV functions.

Lemma 6.2. *[39] Let $u : \mathbb{R} \mapsto \mathbb{R}^n$ be right continuous with bounded variations. Then, for every $\epsilon > 0$, there exists a piecewise constant function v such that:*

$$\textit{Tot. Var.}\{v\} \leq \textit{Tot. Var.}\{u\}, \quad \|v - u\|_{L^\infty} \leq \epsilon.$$

---

[1] Proofs of these properties can be found in section 2.4 of [39].

If, in addition,

$$\int_{-\infty}^{0} |u(x) - u(-\infty)|\, dx + \int_{0}^{+\infty} |u(x) - u(\infty)|\, dx < \infty,$$

then one can find v with the additional property

$$\|u - v\|_{L^1} \leq \epsilon.$$

The space of BV functions and its closure in L^1 are at the center of well-posedness results for conservation laws using wavefront-tracking methods.

6.2.2 Weak solutions to the initial-boundary value problem

It is well-known that approximate jump discontinuities can arise in finite time in solutions to conservation laws [89]. Thus classical solutions do not exist in general, and it is necessary to consider a more general formulation of the conservation law.

Weak entropy solution to the Cauchy problem

The *weak formulation* of the conservation law is obtained by considered derivatives in the sense of distribution.

Definition 6.2. *A function $u : [0, T] \times \mathbb{R} \mapsto \mathbb{R}$ is a weak solution to the Cauchy problem* (6.2)-(6.3) *if the initial condition* (6.3) *is satisfied, and if additionally, for any continuously differentiable function ϕ with compact support contained in $(-\infty, T) \times \mathbb{R}$,*

$$\int_{0}^{T} \int_{-\infty}^{\infty} (u\, \phi_t + f(u)\, \phi_x)\, dx\, dt + \int_{-\infty}^{\infty} u_0(x)\, \phi(0, x) dx = 0, \tag{6.6}$$

and $t \mapsto u(t, \cdot)$ is continuous from $[0, T]$ into L^1_{loc}.

When integrated in a domain in which u is smooth around an approximate jump discontinuity, the weak formulation (6.6) yields the *Rankine-Hugoniot* relation [89] defining the speed σ of propagation of approximate jump discontinuities

$$\sigma\, \Delta u = \Delta f(u), \tag{6.7}$$

where $\Delta u = u_r - u_l$ is the jump in u, with u_r, u_l the right and left values of u, respectively, at the approximate jump discontinuity.

For uniqueness of the solution to the weak solution of the Cauchy problem associated with the conservation law, an additional *admissibility condition* (see Section 4.5 of [70]) is required. Different conditions have been proposed in literature. In the scalar case, one of the first admissibility conditions is due to Oleinik [180]. Kruzkhov [141] showed that it was sufficient to satisfy the entropy inequality condition for a specific family of entropy-entropy flux pairs in the scalar case, yielding the Kruzkhov entropy condition. The Lax admissibility condition [147], which exhibits a convenient geometric interpretation, states that for a i-shock joining a left state u_l and a right state u_r, the following inequality must be satisfied:

$$\lambda_i(u_l) \geq \sigma \geq \lambda_i(u_r) \tag{6.8}$$

where $\lambda_i(u)$ is the i^{th} characteristic speed of u, and σ is the Rankine-Hugoniot speed (6.7). In the scalar case, for a convex flux, these formulations have been proven to be equivalent (see Section 2.1 of [154]). The Lax admissibility condition allows the selection of a particular weak solution.

Definition 6.3. *A function* $u : [0, T] \times \mathbb{R} \mapsto \mathbb{R}$ *is the weak entropy solution to the Cauchy problem* (6.2)-(6.3) *if it is a weak solution (definition 6.2), that satisfies the Lax admissibility condition* (6.8)*.*

The definition of weak conditions to the IBVP requires a corresponding statement of *weak boundary conditions*, presented in the following section.

Weak boundary conditions

The first statement of weak boundary conditions was introduced in [15] in the scalar case in multiple dimensions of space, with C^2 flux and C^2 initial and boundary datum, using a vanishing viscosity method. In one dimension, this formulation reads:

$$\max_{k\in[\alpha,\beta]} \operatorname{sgn}\left(u(t,a) - u_a(t)\right)\,\left(f(u(t,a)) - f(k)\right) = 0 \tag{6.9}$$

$$\min_{k\in[\gamma,\delta]} \operatorname{sgn}\left(u(t,b) - u_b(t)\right)\,\left(f(u(t,b)) - f(k)\right) = 0 \tag{6.10}$$

for almost all $t > 0$, and where $\alpha = \min(u(t,a), u_a(t))$, $\beta = \max(u(t,a), u_a(t))$, $\gamma = \min(u(t,b), u_b(t))$, $\delta = \max(u(t,b), u_b(t))$, and sgn denotes the sign function. This formulation was shown to hold for systems of conservation laws in one dimension of space in [82], and proven equivalent to a formulation derived from the solution to the Riemann problem at the boundary, later extended to account for continuous boundary not necessarily static in [3]. In the scalar case, at a left boundary a, the statement of weak boundary conditions derived from the structure of the solution to the Riemann problem is the following.

Definition 6.4. *A function* $u : \Omega \mapsto \mathbb{R}$ *satisfies the boundary condition* u_a *at* a *if for all except countably many times* t*, the waves composing the solution to the Riemann problem centered at* a *with initial data*

$$\begin{cases} u_a(t) & \text{if} \quad x < a \\ u(t,a) & \text{if} \quad x > a \end{cases} \tag{6.11}$$

have negative speeds.

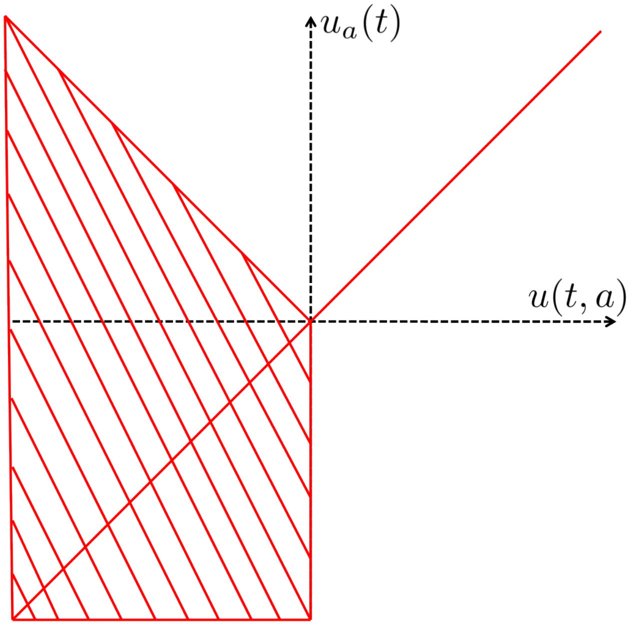

Figure 6.1: Weak boundary conditions.
In the case of a quadratic convex flux centered at 0. The solution to the Riemann problem with initial datum in the striped domain exhibits a wave with negative speed. For initial datum on the first bisector, no wave arises. The white zone exists only for a zero time duration.

The domain for which the couples boundary condition-boundary trace prevail for a non-zero duration, (definition 6.4) is represented in figure 6.1 for a Burgers flux.

In [153], a simplified formulation is proposed for the scalar case with strictly convex continuously differentiable flux functions (see also [96]). Similar formulations were derived for a scalar traffic model in [205] and scalar traffic models on networks with application to estimation in [227], following [97]. In the case of a strictly convex continuously differentiable flux, this statement states that for almost all times t, one of the following mutually exclusive conditions must be satisfied:

$$\begin{cases} u(t,a) = u_a(t) \\ f'(u(t,a)) \leq 0 \text{ and } f'(u_a(t)) \leq 0 \text{ and } u(t,a) \neq u_a(t) \\ f'(u(t,a)) \leq 0 \text{ and } f'(u_a(t)) > 0 \text{ and } f(u(t,a)) \geq f(u_a(t)). \end{cases} \tag{6.12}$$

The same can be done at the downstream boundary $x = b$:

$$\begin{cases} u(t,b) = u_b(t) \\ f'(u(t,b)) \geq 0 \text{ and } f'(u_b(t)) \geq 0 \text{ and } u(t,b) \neq u_b(t) \\ f'(u(t,b)) \geq 0 \text{ and } f'(u_b(t)) < 0 \text{ and } f(u(t,b)) \geq f(u_b(t)). \end{cases} \tag{6.13}$$

A well-posedness result for the IBVP associated with a scalar conservation law (6.1) with the boundary statement from definition 6.4 is presented in the following section.

6.2.3 Well-posedness of the initial-boundary value problem

In [15], a solution satisfying (6.6) in the scalar case is contructed using a vanishing viscosity method for the weak boundary conditions statement (6.9)-(6.10) and is shown to be the admissible solution according to Kruzkhov entropy condition [141].

More recently, an existence result for $n \times n$ systems using wavefront tracking was proposed in [3]. The *standard Riemann semigroup* (SRS) method, introduced in [38] for the Cauchy problem associated with a Temple system [210] of conservation laws, was extended to the IBVP in [4, 5], with the boundary conditions statement from definition 6.4. In [5], it is shown for a $n \times n$ system that if the SRS exist, its trajectories coincide with wavefront tracking solutions. Uniqueness and continuous dependence is obtained for the case of non-characteristic conditions, and uniqueness for the characteristic case. The SRS is constructed for 2×2 system in [4]. We state in the scalar case for a static boundary the main result of [4] for characteristic boundary conditions, obtained for 2×2 systems with continuous boundary (see theorem C of [4]).

Theorem 6.1. *[4] Let f be a smooth map such that the system* (6.1) *is strictly hyperbolic with characteristic field linearly degenerate or genuinely nonlinear. There exists positive constants L and δ, and a continuous semigroup S defined for data in $L^1 \cap BV$ with total variation bounded by δ, such that*

- *The map* $t \mapsto u(t,\cdot)$ *yields a solution to the IBVP* (6.6)-(6.3)-(6.11).
- *For piecewise constant initial and boundary data, the trajectories of the semigroup coincide with the solution to the IBVP obtained by piecing together the standard solutions to the Riemann problems at the points of discontinuity of the initial condition and at the boundary.*
- *For initial data* u_0', u_0''*, boundary data* $u_a' = u_a''$ *in* $L^1 \cap BV$ *with total variation bounded by* δ*, let* u', u'' *denote the corresponding trajectories of the semigroup* S*, and* $t', t'' > 0$*, then*
$$\|u'(t',\cdot) - u''(t'',\cdot)\|_1 \leq L\left(\|u_0' - u_0''\|_1\right). \tag{6.14}$$

In the following section we use this result in the case of a left and a right boundary to show that we can restrict our Lyapunov analysis to the case of piecewise smooth data.

6.3 Approximation of solution

In this section, we present results on the approximability of the solution to an *initial-boundary value problem* (IBVP) with initial condition in BV by the solution to an IBVP with piecewise smooth solution at all times. We show that the solution to the IBVP with BV data can be approximated arbitrarily closely in the L^1 norm by the solution to an IBVP with piecewise smooth data. We define the required regularity class used throughout the chapter.

Definition 6.5. *We note* PWS^+ *the class of piecewise smooth functions* $f : \mathbb{R} \mapsto \mathbb{R}$ *such that the gradient* g *of* f *satisfies the following properties:*

- g *is positive almost everywhere.*
- *there is a finite number of locations at which* g *is a negative Dirac mass.*

We now state the approximability result.

Theorem 6.2. *Let* $T, \delta > 0$*,* $a < b$*, and let* $u_0 : (a,b) \mapsto \mathbb{R}$*,* $u_a, u_b : (0,T) \mapsto \mathbb{R}$ *be functions with total variation bounded by* δ*. For every* $\epsilon > 0$*, there exists* $u_0^\epsilon : (a,b) \mapsto \mathbb{R}$ *in* PWS^+ *such that the solution* u *to the IBVP for equation* (6.1) *and data* (u_0, u_a, u_b) *and the solution* u^ϵ *to the IBVP for equation* (6.1) *and data* (u_0^ϵ, u_a, u_b) *satisfy:*

$$\forall\, 0 \leq t \leq T, \quad \|u(t,\cdot) - u^\epsilon(t,\cdot)\|_1 \leq \epsilon.$$

Proof. Using lemma 6.2 in the compact domain $[a,b]$, we can approximate the initial condition condition u_0 approximated arbitrarily closely in the L^1 sense by a piecewise constant function u_0^ϵ with a finite number of discontinuities and lower total variation.

Using the continuous dependence result of theorem 6.1, the resulting trajectories u, u_ϵ of the semigroup for the identical boundary conditions u_a, u_b, can be made arbitrarily close in the L^1 norm by controlling the distance between the initial conditions. □

Remark 6.1. *It is clear that approximating the problem data by piecewise constant data satisfies the requirements of theorem 6.2. However, the class of piecewise constant data is not close for the semigroup. In the case of wavefront tracking, the propagation of piecewise constant conditions is achieved by introduction of non-entropic shock waves. As shown in section 6.4, the entropy condition is a critical component of the stability of the solution to the IBVP. Hence we work in the class of piecewise smooth functions, that allows approximations of BV function, as proven in theorem 6.2, and is close for the semigroup as proven in theorem 6.3.*

We show that under suitable boundary conditions, the solution to the IBVP with piecewise smooth data is piecewise smooth.

Theorem 6.3. *Let $T, \delta > 0$, $a < b$, and let $u_0 : (a, b) \mapsto \mathbb{R}$, $u_a, u_b : (0, T) \mapsto \mathbb{R}$ be in PWS^+. Let u denote the solution to the IBVP* (6.6)-(6.3)-(6.11)*. At all times $0 \leq t \leq T$, $u(t, \cdot)$ is piecewise smooth.*

Proof. Let $x_1, \ldots, x_N$ denote the locations of the discontinuities in the initial condition, including a, b. We construct the solution to the IBVP by piecing together the shock waves or rarefaction waves created at x_i, and the classical solution constructed by the method of characteristics between the waves. By definition, the solution created is a solution in the sense of (6.6) since equation (6.1) is satisfied in the classical sense between the waves, and the shock waves propagate according to the Rankine-Hugoniot relation (6.7). It is also the admissible solution according to the Lax condition (6.8) by enforcing the existence of entropic shock waves only. Finally the constructed solution coincides with the trajectory of the semigroup from theorem 6.2 (see [40]).

We now show that at all time, the number of discontinuities is finite. Since there is a finite number of discontinuities in the initial and boundary conditions, a finite number of discontinuities enters the space-time domain. In the scalar case the interaction of two discontinuities creates no more than one discontinuity, so the interaction of discontinuities contributes to decreasing their number. Finally as mentioned above, since the initial and boundary conditions are piecewise smooth increasing, all discontinuities are created at time 0 or at the boundary. □

In the next section, we present the Lyapunov stability analysis for functions in PWS^+.

6.4 Lyapunov analysis

In this section, we propose a Lyapunov function and compute its derivative. In the following we call $\tilde{u} = u - u^*$ where u^* is a uniform, hence stationary, solution around which we want to stabilize the system, and u is the solution to the IBVP associated with the scalar conservation law (6.1). Following the results from section 6.3, we assume that u is in PWS^+.

6.4.1 Lyapunov function candidate

We consider the classical Lyapunov function candidate [139, 140]:

$$V(t) = \int_a^b \tilde{u}^2(x,t)\,dx. \tag{6.15}$$

where u is a weak solution to the scalar conservation law. From definition 6.3, we have $t \mapsto u(t,\cdot)$ continuous from $[0,T]$ to L^1, and the function $V(\cdot)$ is well-defined and continuous. We index the jump discontinuities of $u(t,\cdot)$ in increasing order of their location at time t by $i = 0,\ldots,N(t)$, including for notational purposes the boundaries a, b, with $x_0(t) = a$ and $x_N(t) = b$. The Lyapunov function candidate can be rewritten as:

$$V(t) = \frac{1}{2}\sum_{i=0}^{N(t)-1} \int_{x_i(t)}^{x_{i+1}(t)} \tilde{u}^2(t,x)\,dx. \tag{6.16}$$

From theorem 6.3, we know that for all integer $i \in [0, N(t))$, the function $u(t,\cdot)$ is smooth in the domain $(x_i(t), x_{i+1}(t))$, thus $\partial_t u(t,\cdot)$ exists and is continuous for t such that $x_i(t) < x_{i+1}(t)$. Since discontinuity trajectories are differentiable with speed given by the Rankine-Hugoniot relation (6.7), it follows that at any time t such that $N(t)$ is constant in a neighborhood of t and the boundary trace is continuous, the function $V(\cdot)$ is differentiable.

6.4.2 Differentiation of the Lyapunov function candidate

In this section, we compute the derivative of the Lyapunov function candidate (6.15), at any time t such that $N(t)$ is constant in a neighborhood and the boundary trace is continuous. Differentiating expression (6.16) yields:

$$\frac{dV}{dt}(t) = \frac{1}{2}\sum_{i=0}^{N(t)-1} \int_{x_i(t)}^{x_{i+1}(t)} \partial_t \tilde{u}^2\,dx + \frac{1}{2}\sum_{i=0}^{N(t)-1} \left[\tilde{u}^2(t, x_{i+1}(t)-)\,\frac{dx_{i+1}}{dt}(t) - \tilde{u}^2(t, x_i(t)+)\,\frac{dx_i}{dt}(t)\right]. \tag{6.17}$$

As detailed at the end of section 6.4.1, the term under the sum is smooth, and we can write $\partial_t \tilde{u}^2 = 2\,\tilde{u}\,\partial_t \tilde{u}$. Since u satisfies the conservation law (6.1), we have $\partial_t \tilde{u} = -\partial_x f(\tilde{u} + u^*)$. The derivative of the Lyapunov function can be written as:

$$\begin{aligned}\frac{dV}{dt}(t) = &-\sum_{i=0}^{N(t)-1} \int_{x_i(t)}^{x_{i+1}(t)} \tilde{u}\,\partial_x f(\tilde{u} + u^*)\,dx \\ &+ \frac{1}{2}\sum_{i=0}^{N(t)-1} \left[\tilde{u}^2(t, x_{i+1}(t)-)\,\frac{dx_{i+1}}{dt}(t) - \tilde{u}^2(t, x_i(t)+)\,\frac{dx_i}{dt}(t)\right].\end{aligned}$$

By integrating by parts the sum terms, we obtain:

$$\begin{aligned}\frac{dV}{dt}(t) = &- \sum_{i=0}^{N(t)-1} \left[\tilde{u}\, f(\tilde{u}+u^*)\right]_{x_i(t)}^{x_{i+1}(t)} + \sum_{i=0}^{N(t)-1} \int_{x_i(t)}^{x_{i+1}(t)} f(\tilde{u}+u^*)\, \partial_x \tilde{u}\, dx \\ &+ \frac{1}{2} \sum_{i=0}^{N(t)-1} \left[\tilde{u}^2(t, x_{i+1}(t)-)\, \frac{dx_{i+1}}{dt}(t) - \tilde{u}^2(t, x_i(t)+)\, \frac{dx_i}{dt}(t)\right].\end{aligned}$$

and if we note $F(\cdot)$ a primitive function of the flux function $f(\cdot)$ we have:

$$\begin{aligned}\frac{dV}{dt}(t) = &\, \tilde{u}(t,a)\, f(\tilde{u}(t,a)+u^*) - \tilde{u}(t,b)\, f(\tilde{u}(t,b)+u^*) - F(\tilde{u}(t,a)+u^*) + F(\tilde{u}(t,b)+u^*) \\ &+ \sum_{i=1}^{N(t)-1} \left[\Delta_i\left(\tilde{u} f(\tilde{u}+u^*) - F(\tilde{u}+u^*)\right) - \frac{1}{2}\frac{dx_i}{dt}(t)\, \Delta_i\, \tilde{u}^2\right],\end{aligned}$$

where Δ_i is defined around the discontinuity $x_i(t)$ as in equation (6.7). Using the Rankine-Hugoniot relation, defined in equation (6.7), to write the speed of the approximate jump discontinuity $dx_i(t)/dt$ as a function of the left and right jump values we obtain:

$$\begin{aligned}\frac{dV}{dt}(t) = &\, \tilde{u}(t,a)\, f(\tilde{u}(t,a)+u^*) - \tilde{u}(t,b)\, f(\tilde{u}(t,b)+u^*) - F(\tilde{u}(t,a)+u^*) + F(\tilde{u}(t,b)+u^*) \\ &+ \sum_{i=1}^{N(t)-1} \Delta_i\left(\tilde{u} f(\tilde{u}+u^*) - F(\tilde{u}+u^*)\right) - \sum_{i=1}^{N(t)-1} \frac{\tilde{u}(t,x_i-)+\tilde{u}(t,x_i+)}{2}\, \Delta_i f(\tilde{u}+u^*).\end{aligned} \tag{6.18}$$

In equation (6.18) we identify the first four terms that depend on the boundary trace of the solution, and the last two terms that depend on the shock dynamics inside the domain. In the following section, we analyze the stability properties of the internal terms.

6.4.3 Internal stability

The last two terms of equation (6.18) correspond to approximate jump discontinuity in the solution and are neither observable nor controllable from the boundaries. We now show that these terms have a stabilizing effect on the Lyapunov function candidate (6.15).

Proposition 6.1. *Given a uniform stationary solution u^* to the scalar conservation law* (6.1)*, the approximate jump discontinuity dynamics*

$$\sum_{i=1}^{N(t)-1} \left[\Delta_i\left(\tilde{u} f(\tilde{u}+u^*) - F(\tilde{u}+u^*)\right) - \frac{\tilde{u}(t,x_i-)+\tilde{u}(t,x_i+)}{2}\, \Delta_i f(\tilde{u}+u^*)\right] \tag{6.19}$$

of the solution u to the IBVP, contributes to the decrease of the Lyapunov function candidate (6.15)*.*

Proof. In order to show that the term (6.19) is negative, we show that each term in the sum is negative. If we note u_l, u_r the value of u on the left and on the right of the approximate jump discontinuity, respectively, and $\tilde{u}_l, \tilde{u}_r$ the corresponding reduced variables, we want to show that

$$\begin{aligned}[(\tilde{u}_r f(\tilde{u}_r + u^*) - F(\tilde{u}_r + u^*)) - (\tilde{u}_l f(\tilde{u}_l + u^*) - F(\tilde{u}_l + u^*))]\\ - \frac{\tilde{u}_l + \tilde{u}_r}{2}\left(f(\tilde{u}_r + u^*) - f(\tilde{u}_l + u^*)\right) \leq 0.\end{aligned}$$

Equivalently, in the original state variable $u = \tilde{u} + u^*$, we have:

$$\begin{aligned}[((u_r - u^*)\, f(u_r) - F(u_r)) - ((u_l - u^*)\, f(u_l) - F(u_l))]\\ - \frac{u_l + u_r - 2\,u^*}{2}\left(f(u_r) - f(u_l)\right) \leq 0.\end{aligned}$$

This can be rewritten as:

$$F(u_l) - F(u_r) + \frac{1}{2}(u_r - u_l)\,(f(u_r) + f(u_l)) \leq 0, \tag{6.20}$$

in which we recognize Oleinik entropy condition [180]. Thus we have equivalence between stability of the approximate jump discontinuity dynamics and Oleinik entropy condition. □

Remark 6.2. *From the equivalence with the Oleinik entropy condition, since the flux function is strictly convex, we see that the internal dynamics is strictly stabilizing (no contact discontinuity).*

Remark 6.3. *When the number of shocks is constant inside the domain and the trace of the solution is continuous, the internal dynamics is stabilizing in the sense that it contributes to the decay of the Lyapunov function candidate* (6.15)*. Since the Lyapunov function candidate is continuous, the internal dynamics is always stabilizing. This is critical for boundary stabilization where the control action cannot apply directly inside the domain (unlike the case of distributed control [79, 87, 157]). From equation* (6.20)*, one can note that the magnitude of the internal stability does not depend on the equilibrium u^*.*

Remark 6.4. *At a time t at which the number of discontinuities is not constant or the boundary trace is not continuous, the Lyapunov function is not differentiable, however the difference between the right and left derivative at t^+ and t^-, respectively, can be computed. This is addressed in section 6.6.*

If the trace of the solution to the IBVP always takes the value of the boundary condition, it is clear that the solution is stabilizable using boundary control since it amounts to finding boundary controls u_a, u_b such that $g(u_a) < g(u_b)$, where $g : x \mapsto (x - u_*)\, f(x) - F(x)$ is not constant (strict convexity of f).

However, as described in section 6.2.2, this assumption may render the IBVP ill-posed and thus the control inapplicable. In the following section, we show that the Lyapunov function is stabilizable under the proper statement of weak boundary conditions from definition 6.4.

6.5 Well-posed boundary stability

In this section, we motivate and define the *control space* and propose a stabilizing controller.

6.5.1 Control space

Due to the emergence of approximate jump discontinuities in the solution to the conservation law (6.1), weak solutions have to be considered, and boundary conditions have to be considered in the weak sense. It means that it is not always possible to enforce a specific value of the boundary condition. This leads to considering the domain where the boundary controls apply to the solution of the IBVP (introduced in [27] for the specific case of a Burgers flux).

Definition 6.6. *Let us denote $s_{\min}$, $s_{\max}$ the minimal and maximal speed of the waves composing the solution to the Riemann problem at the boundary. The control space at the left boundary is the set of pairs (u_l, u_r) such that $s_{\min} \geq 0$ and $s_{\max} > 0$. The control space at the right boundary is the set of pairs (u_l, u_r) such that $s_{\min} < 0$ and $s_{\max} \leq 0$.*

Definition 6.4 from section 6.2.2 and definition 6.6 are compatible. Definition 6.4 is a weak formulation that characterizes the couples boundary condition-boundary trace prevailing for non-zero time durations. Definition 6.6 categorizes the couples boundary conditions-boundary trace, potentially existing for zero time durations, leading to the boundary trace instantaneously taking the value of the boundary condition (see figure 6.1 and figure 6.2).

Proposition 6.2. *Let m denote the minimum of the strictly convex flux function f. The control spaces $\mathcal{C}_a, \mathcal{C}_b$ at the left and right boundaries, respectively, are characterized as the set of pairs (u_l, u_r) such that one of the following properties is satisfied*

$$\mathcal{C}_a \doteq (u_l, u_r) \quad s.t. \quad \begin{cases} u_l = u_r \\ u_l \geq m \quad and \quad u_r \geq m \\ u_l \geq m \quad and \quad u_r \leq m \quad and \quad f(u_l) > f(u_r), \end{cases} \tag{6.21}$$

$$\mathcal{C}_b \doteq (u_l, u_r) \quad s.t. \quad \begin{cases} u_l = u_r \\ u_l \leq m \quad and \quad u_r \leq m \\ u_l \geq m \quad and \quad u_r \leq m \quad and \quad f(u_l) < f(u_r). \end{cases} \tag{6.22}$$

Proof. Following definition 6.6, we characterize the cases in which the solution to the Riemann problem with initial datum (u_l, u_r) exhibits no wave (first line of equations (6.21)-(6.22)), or waves entering the domain, with at least one non-characteristic wave speed. The second line of equations (6.21)-(6.22) corresponds to entering shock waves or rarefaction waves arising between left and right states with characteristic speed of the same sign, and the third line corresponds to the case of shock waves entering the domain arising between left and right states with characteristic speed of opposite sign. □

One may note that in proposition 6.2, the term u_l corresponds to the boundary condition at boundary a and to the boundary trace at boundary b. Similarly the term u_r corresponds to the boundary trace at boundary a and to the boundary condition at boundary b.

A graphical representation of the control space for the left boundary a is presented in figure 6.2, in the case of the Burgers flux, i.e. a quadratic convex flux with minimum at 0. Cases for which the minimum is not zero can be retrieved by translation. For a general smooth strictly convex flux, a similar representation is obtained by local horizontal and vertical dilatations of the figure.

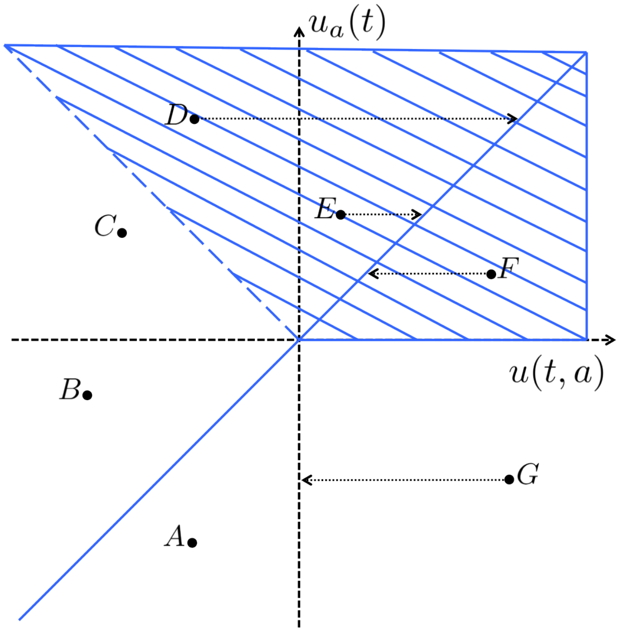

Figure 6.2: Control space.
In the case of a convex quadratic flux with minimum at 0. Top-right quadrant, first bisector, and upper part of top left quadrant (points D, E, F): the control applies, i.e. the boundary trace takes the value of the boundary condition, as represented by the horizontal arrow. Left zone except first bisector (points A, B, C): the control does not apply, the couple boundary condition-boundary trace prevails for a non-zero time duration. Bottom right quadrant (point F): any control yields a zero boundary trace, represented by a horizontal projection onto the vertical axis.

Figure 6.2 illustrates the following distinct interactions between the boundary condition, or control, and the boundary trace, or observed value.

- In the domain of weak boundary conditions with negative wave speed arising at the boundary (white zone on the left of vertical axis), the control does not apply. If the upstream value $u(t,a)$ is observed, and a control is applied such that the couple $u(t,a)$, $u_a(t)$ is represented by the point A, no actuation happens. The trace $u(t,a)$ does not change, it is not impacted by the control chosen. Similarly, no actuation is possible at points B and C, and in general in the left white zone.

- In the top right quadrant and upper part of top left quadrant of the control space (striped zone), corresponding to line 2 and 3 of equation (6.21) respectively, a control action applies; the trace $u(t,a)$ of the solution takes the control value. If a control is applied to a boundary trace value such that the pair is represented by the point D, the trace instantaneously takes the value of the control and the resulting configuration is the projection of D onto the first bisector. Similar behavior occurs with the points E and F, which belong to the control space. The part of the bottom left quadrant such that the control and the trace of the solution are equal is also part of the strong boundary conditions domain according to definition 6.6 and its characterization in proposition 6.2.

- In the bottom right quadrant, any control action yields a vanishing boundary trace, which is illustrated in the case of the application of a control $u_a(t)$ such that the couple $(u(t,a),u_a(t))$ is represented by the point G. The trace of the solution $u(t,a)$ takes the value 0, as illustrated by a horizontal projection onto the axis $x=0$. The control has an action, but not the one intended (i.e. applied), thus the bottom right quadrant is not part of the control space (see definition 6.6).

Using the characterization of the control space introduced in this section, we show in the following section that the system is stabilizable.

6.5.2 Lyapunov stabilization

In this section, we prove that there exists boundary conditions in the control space (6.21)-(6.22) such that the candidate Lyapunov function (6.15) is strictly decreasing.

Lemma 6.3. *Let $g : u \mapsto (u-u^*)\,f(u) - F(u)$, with f a smooth strictly convex function, and F a primitive of f. Let m denote the minimum of f. The function g is smooth on the real line, and satisfies the following properties:*

- *g is strictly increasing in $(-\infty, \min(m,u^*))$, strictly decreasing in $(\min(m,u^*), \max(m,u^*))$, and strictly increasing in $(\max(m,u^*), +\infty)$.*

- *For $u > v$ such that $f(u) = f(v)$, we have $g(u) > g(v)$.*

Proof. The fact that g is smooth results from the smoothness of f. The first property is obtained by computing the derivative $g'(u) = (u-u^*)\,f'(u)$ of g, and noting that f is strictly convex with minimum at m. To prove the second property, let us consider $u > v$ such that $f(u) = f(v)$. The difference $g(v) - g(u)$ reads $g(v) - g(u) = F(u) - F(v) + (v-u)\,f(u)$ that is strictly negative by strict convexity of f. □

The function g is represented for the case of the Burgers flux function in figure 6.3 with the arbitrary choice of $g(m) = 0$.

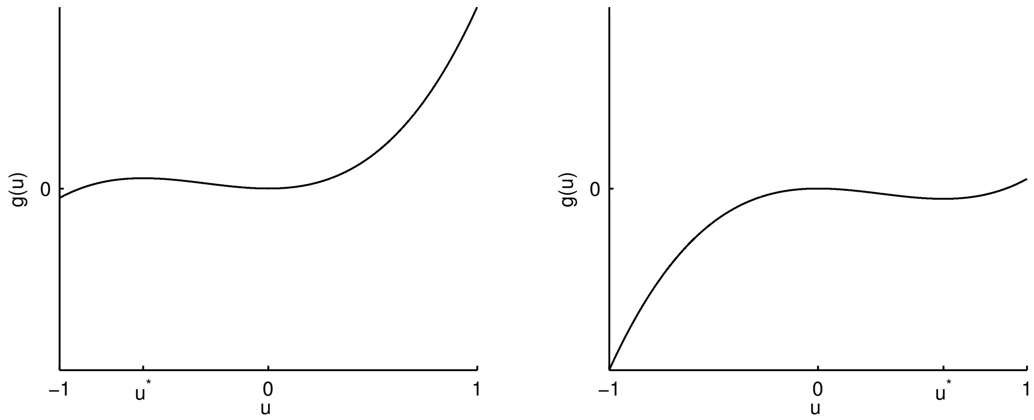

Figure 6.3: Representation of the variations of g.
For a Burgers flux function f in the case $u^* < 0$ (left) and in the case $u^* > 0$ (right). The points $u = m$ ($m = 0$ in this case) and $u = u^*$ ($u^* = \pm 0.5$ in this case) are local extrema of g.

Theorem 6.4. *Let* $V(\cdot)$ *denote the Lyapunov function candidate* (6.15) *for the PDE* (6.1)*. There exists boundary conditions* $u_a(\cdot), u_b(\cdot)$ *in the control space* (6.21) (6.22)*, respectively, such that the function* $V(\cdot)$ *is strictly decreasing. Hence if there exists a solution to the PDE* (6.1) *with such controls, it is asymptotically stabilizable in the sense of Lyapunov.*

Proof. We show that it is always possible to choose $u_a(t), u_b(t)$ in the control space such that $g(u_a(t)) < g(u_b(t))$. We consider the case of $u^* < m$.

- If $u(t,a) \geq m$ and $u(t,b) > m$ then any boundary condition $u_a(t) \geq m$ is in the upstream control space. Since g is strictly increasing in $[m;\infty)$, with $u_b(t) = u(t,b)$, it is possible to obtain the strict decrease of the Lyapunov function.

- If $u(t,a) > m$ and $u(t,b) \leq m$ then any boundary conditions $u_a(t) \geq m$, $u_b(t) \leq m$ are in the control space. Since g is decreasing in $[u^*, m]$ it is possible to choose boundary controls in the control space that guarantees $g(u_a(t)) < g(u_b(t))$.

- If $u(t,a) \leq m$ and $u(t,a) \neq u^*$ and $u(t,b) \leq m$ any boundary condition $u_b(t) \leq m$ is in the downstream control space. Since u^* is a local maximum of g, it is possible to obtain the strict decrease of the Lyapunov function.

- If $u(t,a) = u^*$ and $u(t,b) \leq m$ the choice $u(t,b) = u^*$ gives a neutral effect of the boundary terms on the Lyapunov function. By assumption we know that the solution u is in PWS$^+$, hence in this case either the solution is identically equal to u^* or contains shock waves which yields a strictly decreasing Lyapunov function.

- If $u(t,a) < m$ and $u(t,b) > m$,

- If $g(u(t,a)) < g(u(t,b))$ the choice $u_a(t) = u(t,a)$ and $u_b(t) = u(t,b)$ in the control space leads to the strict decrease of the Lyapunov function.
- If $g(u(t,a)) \geq g(u(t,b))$ and $u(t,a) \neq u^*$, since u^* is a local maximum of g and according to second result of lemma 6.3, it is possible to pick $u_b(t) \leq m$ such that $f(u_b) > f(u(t,b))$ and $g(u_b) > g(u(t,a))$.
- If $g(u(t,a)) \geq g(u(t,b))$ and $u(t,a) = u^*$, the choice $u_b(t) = u^*$ is in the downstream control space and yields a neutral effect of the boundary terms. Similarly to above, by assumption on the regularity of the solution, we have either the solution identically equal to u^* or the Lyapunov function strictly decreasing.

The case $u^* > m$ can be treated similarly. The case $u^* = m$ can be treated similarly, however involves greater reliance on the internal dynamics. Specifically internal dynamics are the sole contributor to the decrease of the Lyapunov function in the case 2 and 4 above, and the controller is passive (equal to the boundary trace) in the case 5 above. ☐

Remark 6.5. *From the proof of theorem 6.4 it is clear that the stabilizing control is a piecewise continuous function of the boundary trace. Since the solution is piecewise smooth with a finite number of discontinuities, the boundary condition exhibits no more than a finite number of discontinuities. These discontinuities induce rarefaction waves or shock waves, which preserve the piecewise smooth nature of the solution.*

In the following section we propose a control design which maximizes the instantaneous decrease rate of the Lyapunov function.

6.6 Maximizing Lyapunov function decrease rate

In this section, we characterize the values of the control, in the control space, that minimize the Lyapunov function derivative. Since boundary controls introducing a shock wave contribute with a negative term to the internal dynamics, we propose to first characterize the type of wave introduced in specific regions of the control space.

6.6.1 Nature of the waves created by boundary control

The type of wave created at the boundary impacts the value of the derivative of the Lyapunov function. In the scalar case, the type of wave arising is defined by the Lax entropy condition (6.8). This allows us to partition the control space according to the type of wave introduced by the control. Table 6.1 summarizes for the upstream boundary the cases in which the boundary control belongs to the control space, with mention of the type of wave introduced.

	$u(t,a) < m$	$u(t,a) \geq m$
$u_a \geq m$	$f(u_a) > f(u(t,a))$: Shock	$u_a > u(t,a)$: Shock $u_a = u(t,a)$: No wave $u_a < u(t,a)$: Rarefaction wave
$u_a < m$	$u_a = u(t,a)$: No wave	$u_a \in \emptyset$ Rarefaction with vanishing boundary trace

Table 6.1: Upstream boundary.
Admissible boundary controls and corresponding wave created at the upstream boundary based on the value of the trace of the solution at this boundary.

From proposition 6.1, we have that the internal dynamics resulting from the existence of entropic shock waves contributes to the decrease of the Lyapunov function. Here we characterize the benefits of the change in the number of shock waves in the solution, resulting from internal interaction, and entrance or exit of a discontinuity at the boundary.

Proposition 6.3. *At a time t at which the number of approximate jump discontinuities $N(t)$ changes:*

- *If two shock waves interact, the derivative of the Laypunov function decreases.*
- *If a discontinuity crosses the boundary, let us note u^- the value of the boundary trace at time t^- and u^+ the value of the boundary trace at time t^+. The jump in the derivative of the Lyapunov function for the upstream case reads*

$$S(u^-, u^+) \doteq \frac{dV}{dt}(t^+) - \frac{dV}{dt}(t^-) = \big(f(u^+) - f(u^-)\big)\, \frac{\tilde{u}^- + \tilde{u}^+}{2}, \tag{6.23}$$

  and the opposite for the downstream case.

Proof. We show each part of proposition 6.3 separately.

- We show that in the case of $|N(t+)| = |N(t-)| - 1$ due to the interaction of two shocks inside the domain, there is a decrease in the slope of the derivative of the Lyapunov function if and only if the Rankine-Hugoniot speed of the left shock is greater than the Rankine-Hugoniot speed of the right shock, which is a necessary condition for the interaction.

  We compute the difference in the right and left derivative, at time t, of the Lyapunov function, by taking the difference of equation (6.18) at time t^+ and t^-. It is clear that the boundary terms cancel out, and that in the sum terms, only the terms corresponding to the interacting shocks and the created shock do not cancel out. We note

(u_l^+, u_r^+) the left and right values at the created shock at time t^+. We use similar notations for the interacting shocks at time t^-. The left and right states of the left shock at time t^- are denoted (u_{1l}^-, u_{1r}^-), and the left and right states of the right shock at time t^- are denoted (u_{2l}^-, u_{2r}^-). We note that by continuity outside of the approximate jump locations, we have $u_{1r}^- = u_{2l}^-$, and $u_{1l}^- = u_l^+$ and $u_{2r}^- = u_r^+$. After some long but straightforward algebra, this allows us to simplify the difference to:

$$\frac{dV}{dt}(t^+) - \frac{dV}{dt}(t^-) = \frac{1}{2}\left[\left(f(u_{1r}^-) - f(u_{1l}^-)\right)\left(u_{2l}^- - u_{2r}^-\right) + \left(f(u_{2r}^-) - f(u_{2l}^-)\right)\left(u_{1r}^- - u_{1l}^-\right)\right],$$

and the right side is negative if and only if the two shocks intersect, which is satisfied by assumption.

- In the case of a shock entering or exiting from the boundary, we show that the sign of the difference in the right and left derivative, at time t, of the Lyapunov function, depends on the sign of $u^* - (u^- + u^+)/2$. We compute the difference between the Lyapunov function derivative at time t^+ and at time t^-. It is clear that only the boundary term at time t^+ and t^-, and the term corresponding to the entered or exited shock do not cancel out. If we note u^- the boundary trace at t^- and u^+ the boundary trace at t^+, we obtain after simplification:

$$\frac{dV}{dt}(t^+) - \frac{dV}{dt}(t^-) = \left(f(u^+) - f(u^-)\right)\frac{\tilde{u}^- + \tilde{u}^+}{2},$$

for both entering and exiting shocks. We treat the case of a shock entering the domain from upstream boundary for a convex flux. We have $u^+ > u^-$ from the entropy condition, hence from the Rankine-Hugoniot relation we obtain $f(u^+) > f(u^-)$ since the shock speed is positive. So the jump in the Lyapunov derivative is negative if and only if $\tilde{u}^- + \tilde{u}^+ < 0$, which is equivalent to $(u^- + u^+)/2 < u^*$.

□

In the following section, we leverage these results to design a stabilizing boundary controller that maximizes the instantaneous decrease rate of the Lyapunov function.

6.6.2 Greedy boundary control

The boundary control that maximizes the decrease rate of the Lyapunov function is the boundary control in the control space, that either introduces a rarefaction wave and minimizes the jump in the Lyapunov function derivative (6.18), or introduces a shock wave at the boundary and minimizes the jump in the Lyapunov function derivative resulting from the change in the boundary trace and in the number of shock waves (6.23). The corresponding optimization problem can be formulated as follows.

Proposition 6.4. *Let u denote the solution to the IBVP associated with the scalar conservation law (6.1). The upstream boundary control* u_a^r *and downstream boundary control* u_b^r *that minimize the decrease of the Lyapunov function by introducing rarefaction waves or no waves at the boundary can be obtained by solving*

$$\begin{aligned} u_a^r &\doteq \arg \min_{\{u|(u,u(t,a))\in\mathcal{C}_a \text{ and } u\leq u(t,a)\}} g(u)-g(u(t,a)) \\ u_b^r &\doteq \arg \max_{\{u|(u(t,b),u)\in\mathcal{C}_b \text{ and } u\geq u(t,b)\}} g(u)-g(u(t,b)). \end{aligned}$$

The upstream boundary control u_a^s *and downstream boundary control* u_b^s *that minimize the decrease of the Lyapunov function by introducing discontinuities at the boundary, can be obtained by solving*

$$\begin{aligned} u_a^s &\doteq \arg \min_{\{u|(u,u(t,a))\in\mathcal{C}_a \text{ and } u> u(t,a)\}} S(u(t,a),u) \\ u_b^s &\doteq \arg \max_{\{u|(u(t,b),u)\in\mathcal{C}_b \text{ and } u< u(t,b)\}} S(u(t,b),u). \end{aligned}$$

Proof. This results from the characterization of the cases when the boundary control introduces a rarefaction wave or a shock wave, and the previous analysis on the resulting evolution of the Lyapunov function derivative. ☐

In the following section we present numerical results of the implementation of the boundary control proposed.

6.7 Numerical examples

In this section, we present numerical results obtained for a benchmark scenario. The numerical scheme used is the standard Godunov scheme [103] with 600 cells in space and a time discretization satisfying the tight *Courant-Friedrich-Levy* (CFL) condition [156]. We consider the flux function $u \mapsto u^2/2$, the equilibrium state $u^* = -0.2$, and the space domain $[0,1]$ with the initial condition:

$$u_0(x) = \begin{cases} 0.5 & \text{if} \quad 0\leq x\leq 1 \\ -0.5 & \text{if} \quad 1\leq x\leq 2 \\ 0.4 & \text{if} \quad 2\leq x\leq 3 \end{cases} \tag{6.24}$$

which corresponds to a stationary shock wave at location $x = 1$. The characteristic speeds associated with the boundary traces are positive. In figure 6.4 we present the evolution of the system under the greedy boundary control solution to the optimization problem defined in proposition 6.4. As a benchmark, we also present the evolution of the system under the

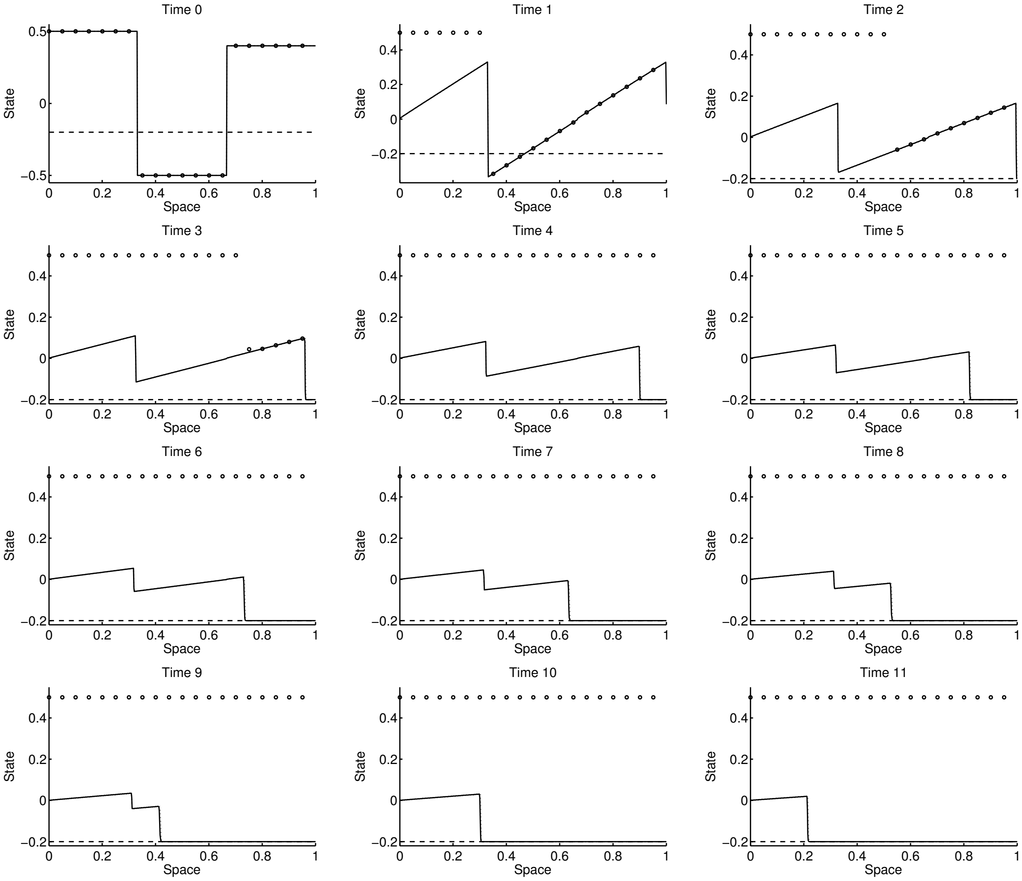

Figure 6.4: Numerical solution of Burgers equation.
For the greedy boundary control defined in proposition 6.4 (solid line) and for the brute force boundary conditions $u_a = u_b = u^*$ (dotted line), the solution is stabilized at the point u^* (dashed line) in the domain $[0, 1]$. In the case of no control (circle markers), the solution is not stabilized at u^*.

brute force boundary control $u_a = u_b = u^*$, and in the case of no control, i.e. when the control is defined as equal to the boundary trace at all times.

The evolution of the solution under the action of the greedy boundary control and the brute force boundary control are very similar. The decrease of the corresponding Lyapunov functions is represented in figure 6.5, center sub figure. One can note that the main difference in the Lyapunov functions arises close to time 0. Later in time, the control has been achieved at the boundary, and the evolution of the system is purely due to internal dynamics. Due to the specific benchmark test used, the brute force controller slowly catches up with the advantage taken initially by the greedy controller before time 10. The slight increase in the difference between the Lyapunov function around time 10 is due to the fact that the solution controlled by the greedy method reaches a discontinuity (see figure 6.4, between time 9 and 10).

This evolution of the Lyapunov functions and their difference is explained by the values of the boundary control and the corresponding values taken by the boundary trace, presented in figure 6.5, left and right sub figures.

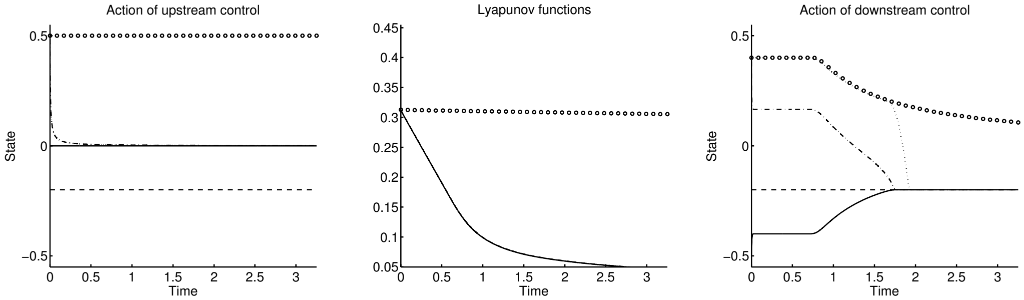

Figure 6.5: Boundary controls and Lyapunov functions.
The Lyapunov functions for different controls are represented in the center sub figure, for the greedy boundary control defined in proposition 6.4 (solid line), for the brute force boundary control $u_a = u_b = u^*$ (dashed line), and in the case of no control (circular markers). The upstream and downstream boundary are represented in the left and right sub figure respectively. The greedy boundary condition is represented in solid line, and the corresponding boundary trace in dash-dot line. The brute force control is represented by the horizontal dashed line, and the corresponding boundary trace is represented in dotted line. The case of no control is represented in circular markers.

The upstream control represented in the left sub figure is constantly set to 0, corresponding to a characteristic boundary condition, which introduces a rarefaction wave. In this case, the action of the greedy control and the brute force control yield similar system reaction, but the value of the greedy control, which is in the control space, is taken, as indicated by the convergence of the dash-dot line to the solid line (with a non-instantaneous convergence due to diffusion).

The downstream greedy control introduces a shock wave from the initial time. Since the distance, in the right sub figure, around time 0, between the solid and dashed line (objective) is smaller than the distance between the circular marker (boundary trace with no action) and the dashed line, this clearly contributes to the decrease of the Lyapunov function. However, it is observed that the dash-dot line decreases instantaneously toward the solid line but then stays stationary at a value different from the solid line. This discrepancy is a consequence of discretization, and of the fact that the discrepancy prevails in time, which is due the fact that the boundary condition cannot propagate further into the domain, due to the current value of the solution, before time 1.7. Indeed the stationary boundary trace is close to 0.2, and the boundary condition is around -0.4, hence the trace should take the value -0.4. However the value of the solution inside the domain toward the downstream boundary is 0.4, hence the action of the control is exactly compensated by the internal dynamics, which is not observable from the boundary. Hence the control does not have significant action. This is an inherent limitation to boundary control for conservation laws.

Note that while it might seem disappointing that the greedy Lyapunov approach performs as well as the brute force approach, its superiority is twofold:

- It is proven to stabilize the system, whereas the brute force approach can only be checked post-facto, assuming it works.
- The controller does effectively apply. Conversely the brute force approach is ineffective in the sense that the prescribed value of the controller does not necessarily apply.

Chapter 7

Contributions and open problems

This dissertation work has been pursued in the context of the *Mobile Millennium* project and the revolution in traffic monitoring systems owing to the explosion of mobile devices in the world. The resulting paradigm changes in the field of traffic engineering motivated a significant proportion of the research endeavors considered in this work.

The emergence of mobile sensing and the mass of associated streaming velocity measurements motivated research efforts on novel traffic models and estimation algorithms. Investigations on the equivalence of velocity-based conservation laws and density-based conservation laws, as well as the theoretical research on higher-order PDE models, led to successful implementations at a large scale (Northern California road network) in the real-time *Mobile Millennium* system.

However, the issues of data quality and model error, considerably emphasized by crowdsourcing in an online real-time environment, called for the development of advanced data assimilation techniques and the proper understanding of their underlying uncertainty structure given the properties of the mathematical models used. Precise knowledge of the accuracy of the estimates provided in real-time is a critical factor to the applicability of a traffic monitoring system, especially in a large-scale system in which so-called ground-truth is not directly available.

The control problems investigated during this dissertation, at a macroscopic level for flow control in the previous chapter, as well as the stochastic on-time arrival routing problem [191, 35], which was implemented and applied in an operational setting to traffic estimates based on the modeling and estimation work described in this dissertation and in [227] in particular, delineate the state of the art in the mathematics of traffic monitoring, and the emerging directions for the future science of intelligent large-scale infrastructure.

The contribution of this thesis and the natural extensions to this work are as follows.

2×2 **phase transition model of traffic flow.** Chapter 2 presented an extension to the original phase transition model presented by Colombo. The model proposed accounts for the variability of traffic state due to heterogeneous driving behaviors, and different traffic patterns at different locations. The Cauchy problem associated with the system of hyperbolic conservation laws was shown to be well-posed in $L^1 \cap BV$. A Riemann solver was constructed, and a numerical discretization scheme derived from the classical Godunov scheme implemented.

Extensions to this work include the proper formulation of the junction problem for modeling traffic flow at road crossings using a 2×2 traffic model. It is known that congestion is created at junctions and at the location of sudden driving maneuvers. The contribution of this work has been to provide mathematical tools to model non standard individual traffic behaviors. The problem of junction modeling has been solved for scalar traffic models but few results exist for non-scalar network models of traffic flow.

A theoretical problem of significant practical importance is the problem of mixed distributed and boundary control from eulerian and lagrangian actuators in the presence of limited information. Mathematical resolution of this problem would allow identifying a set of optimal ramp metering and probe-enforced variable speed limits for congestion mitigation. Unfortunately, standard approaches lead to ill-posed problems and non-realistic results. The use of a non-scalar model that properly accounts for macroscopic and microscopic traffic phenomena would allow great progress in this direction.

Estimation methods for non-scalar traffic models. Chapter 3 presented an assessment of the performance of the 2×2 phase transition model for time space diagram reconstruction, based on initial and boundary data extracted from high resolution camera-based experimental vehicle trajectories. The results were shown in a forward-simulation setting, in which perfect joint measurements from coincidental loop detectors and probe vehicles are collected. This ideal scenario allowed the identification of the propagation of forward-moving discontinuity in congested traffic flow, which had not been surely observed previously in the literature, and the assessment of the greater robustness of the 2×2 model to calibration error.

Extensions to this work include the use of a proper estimation framework in order to assess the impact of observation error and model error on the accuracy of the estimates. The problem of data fusion from loop detectors and probe vehicles is also a very important practical question.

Finally, the use of such macroscopic models able to account for heterogeneous driving behavior would be of great interest for the design of stochastic routing algorithms [35, 191], which require the knowledge of the cause of the traffic state estimate distribution variance; from a routing perspective, a large link travel-time variance caused by driver heterogeneity is very different from a large link travel-time variance due to algorithmic and data limitations corresponding to numerical uncertainty.

Adaptive estimation algorithms. In Chapter 5, a model-based analysis of the consequence of nonlinearity and non-differentiability on estimation error, and specifically on the structure of the uncertainty propagated by suboptimal filtering algorithms was presented. It was shown that the emergence of discontinuities in the solution to scalar hyperbolic conservation laws causes the emergence of mixture uncertainty distribution on the traffic state, and the robustness of stochastic filters to this uncertainty structure was assessed numerically.

This work paves the ground for smart adaptive estimation methods and filtering algorithms. Advanced estimation methods currently applied to traffic monitoring are derived from the theory of linear dynamical systems. The design of real-time online provably optimal sequential estimation algorithms for specific non-linear conservation law models is still an open problem.

A second extension to this work relates to the notion of data quality. With the increased volume of crowd-sourced data used for large scale civil infrastructure monitoring, the ability to track down the nature of errors and the location of uncertainty is a critical feature of estimation algorithms, in particular for safety-sensitive cyber-physical systems. State-of-the art estimation methods provide online estimates which are derived from prior knowledge of model and observation errors. However, estimation algorithms are currently not bound to online quality criteria, which could be designed using the methods introduced in this work.

Boundary stabilization of weak entropy solutions. Chapter 6 proposed a boundary control design that guarantees the greedy decrease of a Lyapunov function candidate. This result solves a problem that has been approached in the literature with many different tools. In particular, our method accounts for the proper treatment of weak boundary conditions, the correct structure of emerging entropic shock waves in the solution to the partial differential equation, and allows the consideration of physical constraints on the control, in particular its total variation.

The approach chosen in this work is based on the assumption of the piecewise regularity of the solution, which is a standard assumption in the conservation laws community. A different approach can be based on general wave-front tracking approximations, which exhibit by nature a piecewise-constant property and approximate arbitrarily closely a BV solution. Another approach can be considered from the perspective of Hamilton-Jacobi equation, for which the gradient of the Barron-Jensen-Frankowska solutions has recently been shown to coincide with the classical weak entropy solutions of the associated conservation law.

Extensions to this work include the development of similar techniques for non-scalar models of traffic, in which the more complex structure of the Riemann invariants allows more complex controls. A problem of great interest for practical applications is the problem of well-posed distributed stabilization of traffic flow on corridors.

Bibliography

[1] K. Ahmed, M. Ben-Akiva, H. Koutsopoulos, and R. Mishalani. Models of freeway lane changing and gap acceptance behavior. In *Proceedings of the 13th International Symposium on Transportation and Traffic Theory, Lyon, France*, pages 501–515, 1996. 47

[2] A. Allstrom, J. Archer, A. Bayen, S. Blandin, J. Butler, D. Gundlegard, H. Koutsopoulos, J. Lundgren, M. Rahmani, and O.-P. Tossavainen. Mobile Millennium Stockholm. In *2nd International Conference on Models and Technologies for Intelligent Transportation Systems*, Leuven, Belgium June 2011. 2, 14

[3] D. Amadori. Initial-boundary value problems for nonlinear systems of conservation laws. *NoDEA: Nonlinear Differential Equations and Applications*, 4(1):1–42, 1997. 121, 123

[4] D. Amadori and R. Colombo. Continuous dependence for 2 × 2 conservation laws with boundary. *Journal of Differential Equations*, 138(2):229–266, 1997. 123

[5] D. Amadori and R. Colombo. Viscosity solutions and standard Riemann semigroup for conservation laws with boundary. *Rendiconti del Seminario Matematico della Universita di Padova*, 99:219–245, 1998. 123

[6] S. Amin, F. Hante, and A. Bayen. On stability of switched linear hyperbolic conservation laws with reflecting boundaries. *Hybrid System: Computation and Control, Lecture Notes in Computer Science*, 4981:602–605, 2008, doi:10.1007/978-3-540-78929-$1_4$4. 117

[7] S. Amin, F. Hante, and A. Bayen. Exponential stability of switched linear hyperbolic initial-boundary value problems. *IEEE Transactions on Automatic Control*, 57(2):291–301, 2012, doi:10.1109/TAC.2011.2158171. 117

[8] F. Ancona and P. Goatin. Uniqueness and stability of L^∞ solutions for Temple class systems with boundary and properties of the attainable sets. *SIAM Journal on Mathematical Analysis*, 34(1):28–63, 2002. 117

[9] B. Anderson and J. Moore. *Optimal filtering.* Prentice Hall, Upper Saddle River, NJ, 1979. 12

[10] J. Anderson. An ensemble adjustment Kalman filter for data assimilation. *Monthly weather review*, 129(12):2884–2903, 2001. 92

[11] C. Andrieu, N. De Freitas, A. Doucet, and M. Jordan. An introduction to MCMC for machine learning. *Journal of Machine learning*, 50(1):5–43, 2003. 92

[12] J.-P. Aubin, A. Bayen, and P. Saint-Pierre. Dirichlet problems for some Hamilton-Jacobi equations with inequality constraints. *SIAM Journal on Control and Optimization*, 47(5):2348–2380, 2008, doi:10.1137/060659569. 117

[13] A. Aw and M. Rascle. Resurrection of “second order” models of traffic flow. *SIAM Journal on Applied Mathematics*, 60(3):916–938, 2000. 5, 9, 50

[14] J. Barcelo, J. Casas, J. Ferrer, and D. Garcia. Modelling advanced transport telematic applications with microscopic simulators: The case with AIMSUN2. In *Proceedings of the 10th European Simulation Symposium, Nottingham, UK*, pages 362–367, 1998. 48

[15] C. Bardos, A.-Y. Leroux, and J.-C. Nedelec. First order quasilinear equations with boundary conditions. *Communications in partial differential equations*, 4(9):1017–1034, 1979. 4, 121, 123

[16] C. Bardos and O. Pironneau. Derivatives and control in the presence of shocks. *Computational Fluid Dynamics Journal*, 11(4):383–391, 2003. 118

[17] Y. Bar-Shalom, X. Li, T. Kirubarajan, and J. Wiley. *Estimation with applications to tracking and navigation.* John Wiley and Sons, New York, NY, 2001. 10

[18] G. Bastin, B. Haut, J.-M. Coron, and B. d Andrea-Novel. Lyapunov stability analysis of networks of scalar conservation laws. *Networks and Heterogeneous Media*, 2(4):751–759, 2007. 117

[19] A. Bayen, J. Butler, and A. Patire. Mobile Millennium final report. Technical report, California Center for Innovative Transportation, Institute of Transportation Studies, University of California, Berkeley, Research Report, UCB-ITS-CWP-2011-6, 2011. 2, 48

[20] A. Bayen, R. Raffard, and C. Tomlin. Adjoint-based control of a new eulerian network model of air traffic flow. *IEEE Transactions on Control Systems Technology*, 14(5):804–818, 2006. 118

[21] M. Ben-Akiva, M. Bierlaire, H. Koutsopoulos, and R. Mishalani. Real-time simulation of traffic demand-supply interactions within DynaMIT. *Transportation and network analysis: current trends: miscellanea in honor of Michael Florian*, 63:19–36, 2002. 48

[22] S. Bianchini. On the shift differentiability of the flow generated by a hyperbolic system of conservation laws. *Discrete and Continuous Dynamical Systems*, 6(2):329–350, 2000. 118

[23] S. Blandin, J. Argote, D. Work, and A. Bayen. A phase transition model of non stationary traffic flow: definition, properties and solution method. Submitted to Transportation Research Part B. 13

[24] S. Blandin, G. Bretti, A. Cutolo, and B. Piccoli. Numerical simulations of traffic data via fluid dynamic approach. *Applied Mathematics and Computation*, 210(2):441–454, 2009, doi:10.1016/j.amc.2009.01.057. 14, 19

[25] S. Blandin, A. Couque, A. Bayen, and D. Work. On sequential data assimilation for scalar macroscopic traffic flow models. In Review for *Physica D: Nonlinear Phenomena*, 2011., 2012. 13, 50

[26] S. Blandin, L. El Ghaoui, and A. Bayen. Kernel regression for travel-time estimation via convex optimization. In *IEEE Conference on Decision and Control*, Shanghai, China, December 2009. 14

[27] S. Blandin, X. Litrico, and A. Bayen. Boundary stabilization of the unviscid Burgers equation using a Lyapunov method. In *Proceedings of the 49th IEEE Conference on Decision and Controls, 2010 Atlanta, Georgia*, pages 1705–1712, 2010, doi:10.1109/CDC.2010.5717716. 13, 129

[28] S. Blandin, X. Litrico, B. Piccoli, and A. Bayen. Boundary stabilization of the transport equation using a Lyapunov method. In preparation for the *IEEE Transactions on Automatic Control*. 13

[29] S. Blandin, A. Salam, and A. Bayen. Individual speed variance in traffic flow: analysis of bay area radar measurements. In *Transportation Research Board 91st Annual Meeting, Washington, D.C., Jan. 22–26*, 2012. 14

[30] S. Blandin, D. Work, P. Goatin, B. Piccoli, and A. Bayen. A class of perturbed cell transmission models to account for traffic variability. In *89th Transportation Research Board Annual Meeting, Washington D.C., January 10-14*, 2010. 13, 51

[31] S. Blandin, D. Work, P. Goatin, B. Piccoli, and A. Bayen. A general phase transition model for vehicular traffic. *SIAM Journal on Applied Mathematics.*, 71(1):107–121, 2011. 9, 13, 63, 95

[32] S. Blandin, D. Work, P. Goatin, B. Piccoli, and A. Bayen. A general phase transition model for vehicular traffic. In *IFAC workshop on Control of Distributed Parameter Systems*, France, 2009. 13

[33] M. Bocquet, C. Pires, and L. Wu. Beyond Gaussian statistical modeling in geophysical data assimilation. *Monthly Weather Review*, 138:2997–3023, 2010. 94

[34] R. Boel and L. Mihaylova. A compositional stochastic model for real time freeway traffic simulation. *Transportation Research Part B*, 40(4):319–334, 2006. 92

[35] P. Borokhov, S. Blandin, S. Samaranayake, O. Goldschmidt, and A. Bayen. An adaptive routing system for location-aware mobile devices on the road network. In *IEEE Intelligent Transportation Systems Conference, Washington, D.C., October 2011*, 2011, doi:10.1109/ITSC.2011.6083021. 14, 140, 141

[36] F. Bouttier and P. Courtier. *Data assimilation concepts and methods.* Training course notes of the European Centre for Medium-Range Weather Forecasts, 1999, Reading, UK, 1999. 9, 85

[37] F. Brauer and J. Nohel. *The qualitative theory of ordinary differential equations: an introduction.* Dover, Mineola, NY, 1989. 47

[38] A. Bressan. The unique limit of the Glimm scheme. *Archive for Rational Mechanics and Analysis*, 130(3):205–230, 1995. 123

[39] A. Bressan. *Hyperbolic systems of conservation laws: the one-dimensional Cauchy problem.* Oxford University Press, Oxford, UK, 2000. 8, 16, 24, 25, 44, 70, 94, 119

[40] A. Bressan, G. Crasta, and B. Piccoli. *Well-posedness of the Cauchy problem for $n \times n$ systems of conservation laws.* American Mathematical Society, Providence, RI, 2000. 3, 4, 125

[41] A. Bressan and G. Guerra. Shift-differentiabilitiy of the flow generated by a conservation law. *Discrete and Continuous Dynamical Systems*, 3:35–58, 1997. 118

[42] G. Burgers, P. van Leeuwen, and G. Evensen. Analysis scheme in the ensemble Kalman filter. *Monthly Weather Review*, 126(6):1719–1724, 1998. 91

[43] J. Burns and S. Kang. A control problem for Burgers equation with bounded input/output. *Nonlinear Dynamics*, 2(4):235–262, 1991. 117

[44] C. Byrnes, D. Gilliam, and V. Shubov. On the global dynamics of a controlled viscous Burgers equation. *Journal of Dynamical and Control Systems*, 4(4):457–519, 1998. 117

[45] G. Cameron and G. Duncan. PARAMICS—Parallel microscopic simulation of road traffic. *The Journal of Supercomputing*, 10(1):25–53, 1996. 47

[46] M. Cassidy. Bivariate relations in nearly stationary highway traffic. *Transportation Research Part B*, 32(1):49–59, 1998. 49

[47] M. Cassidy and B. Coifman. Relation among average speed, flow, and density and analogous relation between density and occupancy. *Transportation Research Record: Journal of the Transportation Research Board*, 1591:1–6, 1997. 49

[48] M. Cassidy and J Windover. Methodology for assessing dynamics of freeway traffic flow. *Transportation Research Record*, 1484:73–79, 1995. 4

[49] C. Chalons and P. Goatin. Godunov scheme and sampling technique for computing phase transitions in traffic flow modeling. *Interfaces and Free Boundaries*, 10(2):195–219, 2008. 27, 28, 63

[50] J. Chandrasekar, A. Ridley, and D. Bernstein. A comparison of the extended and unscented Kalman filters for discrete-time systems with nondifferentiable dynamics. In *American Control Conference (ACC), 2007*, pages 4431–4436, 2007. 94

[51] R. Chen and J. Liu. Mixture Kalman filters. *Journal of the Royal Statistical Society: Series B (Statistical Methodology)*, 62(3):493–508, 2000. 12, 86

[52] N. Chiabaut, C. Buisson, and L. Leclercq. Fundamental diagram estimation through passing rate measurements in congestion. *IEEE Transactions on Intelligent Transportation Systems*, 10(2):355–359, 2009. 61

[53] N. Chiabaut, L. Leclercq, and C. Buisson. From heterogeneous drivers to macroscopic patterns in congestion. *Transportation Research Part B*, 44(2):299–308, 2010. 50

[54] D. Chickering and C. Meek. Finding optimal Bayesian networks. In *Proceedings of the Eighteenth Annual Conference on Uncertainty in Artificial Intelligence*, pages 94–102, San Francisco, CA, 2002. Morgan Kaufmann. 73, 75, 76

[55] A. Chorin and X. Tu. Implicit sampling for particle filters. *Proceedings of the National Academy of Sciences*, 106(41):17249–17254, 2009. 93

[56] A. Chow, V. Dadok, G. Dervisoglu, G. Gomes, R. Horowitz, A. Kurzhanski, J. Kwon, and X. Lu. Topl: Tools for operational planning of transportation networks. In *Proceedings of the 2008 Dynamic Systems and Control Conference, Ann Arbor, Michigan*, pages 20–22, 2008. 48

[57] D. Chowdhury, L. Santen, and A. Schadschneider. Statistical physics of ve-

hicular traffic and some related systems. *Physics Reports*, 329(4-6):199–329, 2000. 48

[58] C. Claudel and A. Bayen. Lax-Hopf Based Incorporation of Internal Boundary Conditions Into Hamilton–Jacobi Equation. Part I: Theory. *IEEE Transactions on Automatic Control*, 55(5):1142–1157, 2010, doi:10.1109/TAC.2010.2041976. 8

[59] C. Claudel and A. Bayen. Lax–Hopf Based Incorporation of Internal Boundary Conditions Into Hamilton-Jacobi Equation. Part II: Computational Methods. *IEEE Transactions on Automatic Control*, 55(5):1158–1174, 2010, doi:10.1109/TAC.2010.2045439. 8

[60] G. Coclite, M. Garavello, and B. Piccoli. Traffic flow on a road network. *SIAM Journal on Mathematical Analysis*, 36(6):1862–1886, 2005. 6

[61] R. Colombo. On a 2 × 2 hyperbolic traffic flow model. *Mathematical and Computer Modelling*, 35(5-6):683–688, 2002. 9, 16, 17, 18

[62] R. Colombo. Hyperbolic phase transitions in traffic flow. *SIAM Journal on Applied Mathematics*, 63(2):708–721, 2003. 16, 17, 19, 21, 24, 25, 29, 31, 35

[63] R. Colombo, P. Goatin, and F. Priuli. Global well-posedness of traffic flow models with phase transitions. *Nonlinear Analysis*, 66(11):2413–2426, 2007. 16, 25, 42

[64] J.-M. Coron, B. d'Andrea-Novel, and G. Bastin. A strict Lyapunov function for boundary control of hyperbolic systems of conservation laws. *IEEE Transactions on Automatic Control*, 52(1):2–11, 2007. 117

[65] P. Courtier, E. Andersson, W. Heckley, D. Vasiljevic, M. Hamrud, A. Hollingsworth, F. Rabier, M. Fisher, and J. Pailleux. The ECMWF implementation of three-dimensional variational assimilation (3D-Var). I: Formulation. *Quarterly Journal of the Royal Meteorological Society*, 124(550):1783–1807, 1998. 85

[66] P. Courtier, J. Thepaut, and A. Hollingsworth. A strategy for operational implementation of 4D-Var, using an incremental approach. *Quarterly Journal of the Royal Meteorological Society*, 120(519):1367–1387, 1994. 85

[67] M. Cremer and M. Papageorgiou. Parameter identification for a traffic flow model. *Automatica*, 17(6):837–843, 1981. 61

[68] N. Cristianini and J. Shawe-Taylor. *An Introduction to Support Vector Machines.* Cambridge University Press, Cambridge, UK, 2000. 79

[69] M. Cunha and F. Dorini. Statistical moments of the solution of the random Burgers-Riemann problem. *Mathematics and Computers in Simulation*, 79(5):1440–1451, 2009. 95

[70] C. Dafermos. *Hyperbolic conservation laws in continuum physics.* Springer-Verlag Berlin, Germany, 2010. 120

[71] C. Daganzo. The cell transmission model: a dynamic representation of highway traffic consistent with the hydrodynamic theory. *Transportation Research Part B*, 28(4):269–287, 1994. 4, 8, 49, 73, 86

[72] C. Daganzo. The cell transmission model, part II: Network traffic. *Transportation Research Part B: Methodological*, 29(2):79–93, 1995. 4, 5, 6, 8, 86

[73] C. Daganzo. Requiem for second-order fluid approximations of traffic flow. *Trans-*

portation Research Part B, 29(4):277–286, 1995. 5, 49, 50

[74] C. Daganzo, M. Cassidy, and R. Bertini. Possible explanations of phase transitions in highway traffic. *Transportation Research Part A*, 33(5):365–379, 1999. 4, 51

[75] J. De Halleux, C. Prieur, J.M. Coron, B. d'Andréa-Novel, and G. Bastin. Boundary feedback control in networks of open channels. *Automatica*, 39(8):1365–1376, 2003. 117

[76] J.M. Del Castillo and F.G. Benitez. On the functional form of the speed-density relationship Part II: empirical investigation. *Transportation Research Part B*, 29(5):391–406, 1995. 49

[77] J.M. Del Castillo and F.G. Benitez. On the functional form of the speed-density relationship I: General theory. *Transportation Research Part B*, 29(5):373–389, 1995. 20

[78] J.M. Del Castillo, P. Pintado, and F.G. Benitez. The reaction time of drivers and the stability of traffic flow. *Transportation Research Part B*, 28(1):35–60, 1994. 5, 49, 50

[79] M. Demetriou and I. Hussein. Estimation of spatially distributed processes using mobile spatially distributed sensor network. *SIAM Journal on Control and Optimization*, 48(1):266–291, 2009. 128

[80] R. Dobbs, S. Smit, J. Remes, J. Manyika, C. Roxburgh, and A. Restrepo. Urban world : Mapping the economic power of cities. Technical Report March, Mc Kinsey Global Institute, 2011. 1

[81] V. Dos Santos, G. Bastin, J.-M. Coron, and B. d'Andréa-Novel. Boundary control with integral action for hyperbolic systems of conservation laws: Stability and experiments. *Automatica*, 44(5):1310–1318, 2008. 117

[82] F. Dubois and P. LeFloch. Boundary conditions for nonlinear hyperbolic systems of conservation laws. *Journal of Differential Equations*, 71(1):93–122, 1988. 121

[83] R. Durrett. *Essentials of stochastic processes.* Springer, New York, NY, 1999. 73

[84] L. Edie. Discussion of traffic stream measurements and definitions. In *Proceedings of the 2nd International Symposium on the Theory of Traffic Flow, London, UK*, pages 139–154, 1963. 60

[85] L. Edie, R. Foote, R. Herman, and R. Rothery. Analysis of single lane traffic flow. *Traffic Engineering*, 33(4):21–27, 1963. 49

[86] B. Efron and G. Gong. A leisurely look at the bootstrap, the jackknife, and cross-validation. *American Statistician*, pages 36–48, 1983. 81

[87] N. El-Farra and P. Christofides. Coordinating feedback and switching for control of spatially distributed processes. *Computers and chemical engineering*, 28(1-2):111–128, 2004. 128

[88] H. Engl, K. Kunisch, and A. Neubauer. Convergence rates for Tikhonov regularization of nonlinear ill-posed problems. *Inverse Problems*, 5(4):523–540, 1989. 79

[89] L. Evans. *Partial differential equations.* American Mathematical Society, Providence, RI, 1998. 3, 87, 95, 120

[90] G. Evensen. Using the extended Kalman filter with a multilayer quasi-geostrophic

ocean model. *Journal of Geophysical Research*, 97(C11):17905–17924, 1992. 89

[91] G. Evensen. Inverse methods and data assimilation in nonlinear ocean models. *Physica D: Nonlinear Phenomena*, 77(1-3):108–129, 1994. 85

[92] G. Evensen. Sequential data assimilation with a nonlinear quasi-geostrophic model using Monte Carlo methods to forecast error statistics. *Journal of Geophysical Research*, 99:10143–10162, 1994. 91

[93] G. Evensen. The ensemble Kalman filter: Theoretical formulation and practical implementation. *Ocean dynamics*, 53(4):343–367, 2003. 12, 86, 91

[94] M. Fellendorf. VISSIM: A microscopic simulation tool to evaluate actuated signal control including bus priority. In *64th Institute of Transportation Engineers Annual Meeting, Dallas, TX*, 1994. 47

[95] M. Fliess, J. Lévine, P. Martin, and P. Rouchon. Flatness and defect of nonlinear systems: introductory theory and examples. *International journal of control*, 61(6):1327–1362, 1995. 117

[96] H. Frankowska. On LeFloch solutions to initial-boundary value problem for scalar conservation laws. *Journal of Hyperbolic Differential Equations*, 7(3):1–41, 2010. 123

[97] M. Garavello and B. Piccoli. *Traffic flow on networks.* American Institute of Mathematical Sciences, Springfield, MO, 2006. 6, 17, 48, 95, 123

[98] M. Garavello and B. Piccoli. On fluido-dynamic models for urban traffic. *Network and Heterogeneous Media*, 4(1):107–126, 2009. 16

[99] D. Gazis, R. Herman, and R. Potts. Car-following theory of steady-state traffic flow. *Operations Research*, 7(4):499–505, 1959. 48

[100] D. Gazis and C. Knapp. On-line estimation of traffic densities from time-series of flow and speed data. *Transportation Science*, 5(3):283–301, 1971. 86

[101] J. Glimm. Solutions in the large for nonlinear hyperbolic systems of equations. *Communication on pure and applied mathematics*, 18:697–715, 1965. 3, 4

[102] P. Goatin. The Aw-Rascle vehicular traffic flow model with phase transitions. *Mathematical and Computer Modelling*, 44(3-4):287–303, 2006. 16

[103] S. Godunov. A difference method for numerical calculation of discontinuous solutions of the equations of hydrodynamics. *Matematicheskii Sbornik*, 89(3):271–306, 1959. 4, 7, 70, 87, 136

[104] G. Gomes and R. Horowitz. Optimal freeway ramp metering using the asymmetric cell transmission model. *Transportation Research Part C: Emerging Technologies*, 14(4):244–262, 2006. 118

[105] N. Gordon, D. Salmond, and A. Smith. Novel approach to nonlinear/non-Gaussian Bayesian state estimation. In *Radar and Signal Processing, IEE Proceedings F*, volume 140, pages 107–113. IET, 1993. 86, 92

[106] H. Greenberg. An analysis of traffic flow. *Operations Research*, 7(1):79–85, 1959. 4, 6, 49

[107] B. Greenshields. A study of traffic capacity. *Proceedings of the Highway Research Board*, 14(1):448–477, 1935. 4, 5, 18, 49

[108] M. Gugat and G. Leugering. Global boundary controllability of the saint-venant

system for sloped canals with friction. In *Annales de l'Institut Henri Poincare*, volume 26, pages 257–270. Elsevier, 2009. 117

[109] W. Hastings. Monte-Carlo sampling methods using Markov chains and their applications. *Biometrika*, 57(1), 1970. 92

[110] D. Haughton. On the choice of a model to fit data from an exponential family. *The Annals of Statistics*, 16(1):342–355, 1988. 74

[111] A. Hegyi, D. Girimonte, R. Babuška, and B. De Schutter. A comparison of filter configurations for freeway traffic state estimation. In *Intelligent Transportation Systems Conference, 2006, ITSC 2006.*, pages 1029–1034, Toronto, CA, 2006. 90, 94

[112] D. Helbing. Improved fluid-dynamic model for vehicular traffic. *Physical Review E*, 51(4):3164–3169, 1995. 9, 50

[113] D. Helbing. Traffic and related self-driven many-particle systems. *Reviews of modern physics*, 73(4):1067–1141, 2001. 48

[114] J.-C. Herrera and A. Bayen. Incorporation of Lagrangian measurements in freeway traffic state estimation. *Transportation research Part B*, 44(4):460–481, 2010, doi:10.1016/j.trb.2009.10.005. 86

[115] T. Hey, S. Tansley, and K. Tolle, editors. *The Fourth Paradigm: Data-Intensive Scientific Discovery.* Microsoft Research, Redmond, WA, 2009. 2

[116] H. Holden and N. Risebro. A mathematical model of traffic flow on a network of unidirectional roads. *SIAM Journal on Mathematical Analysis*, 26(4):999–1017, 1995. 6

[117] H. Holden and N. Risebro. *Front tracking for hyperbolic conservation laws.* Springer-Verlag, New-York, NY, 2002. 16

[118] S. Hoogendorn and P. Bovy. State-of-the-art of vehicular traffic flow modelling. *Proceedings of the Institution of Mechanical Engineers, Part I: Journal of Systems and Control Engineering, Special Issue on Road Traffic Modelling and Control*, 215:283–303, 2001. 48, 49, 50

[119] C. Huang, Y. Fallah, R. Sengupta, and H. Krishnan. Adaptive intervehicle communication control for cooperative safety systems. *IEEE Network*, 24(1):6–13, 2010. 93

[120] J. Huttunen and J. Kaipio. Approximation error analysis in nonlinear state estimation with an application to state-space identification. *Inverse Problems*, 23:2141–2157, 2007. 104

[121] J. Huttunen and J. Kaipio. Approximation errors in nonstationary inverse problems. *Inverse problems and imaging*, 1(1):77–93, 2007. 104

[122] D. Jacquet. *Modelisation macroscopique du traffic et controle des lois de conservation non lineaires associees.* PhD thesis, Institut National Polytechnique de Grenoble, Grenoble, France, 2006. 117

[123] D. Jacquet, M. Krstic, and C. Canudas de Wit. Optimal control of scalar one-dimensional conservation laws. In *25th American Control Conference, 2006 Minneapolis, MN, USA*, pages 5213–5218, 2006. 117

[124] A. Jazwinski. *Stochastic processes and filtering theory.* Academic Press, New York,

NY, 1970. 10

[125] F. Jensen and T. Nielsen. *Bayesian networks and decision graphs.* Springer, New-York, NY, USA, 2007. 70, 73

[126] Z. Jia, C. Chen, B. Coifman, and P. Varaiya. The PeMS algorithms for accurate, real-time estimates of g-factors and speeds from single-loop detectors. In *IEEE Proceedings of Intelligent Transport Systems*, pages 536–541, 2001. 4

[127] W. Jin. A kinematic wave theory of lane-changing traffic flow. *Transportation Research Part B*, 44(8-9):1001–1021, 2010. 50

[128] M. Jordan. *Learning in graphical models.* MIT Press Cambridge, MA, USA, 1999. 70, 71, 72, 73

[129] S. Julier and J. Uhlmann. A new extension of the Kalman filter to nonlinear systems. In *Proceedings of AeroSense: SPIE 11th Annual International Symposium on Aerospace/Defense Sensing, Simulation and Controls.*, Orlando, FL, 1997. 12, 86, 89

[130] S. Julier, J. Uhlmann, and H. Durrant-Whyte. A new method for the nonlinear transformation of means and covariances in filters and estimators. *IEEE Transactions on Automatic Control*, 45(3):477–482, 2000. 89

[131] J. Kaipio and E. Somersalo. *Statistical and computational inverse problems.* Springer, New-York, NY, 2005. 9, 11, 70, 85, 101

[132] R. Kalman. A new approach to linear filtering and prediction problems. *Journal of basic Engineering*, 82(1):35–45, 1960. 10, 11, 85

[133] C. Kang and J. Tian. Markov properties for linear causal models with correlated errors. *The Journal of Machine Learning Research*, 10:41–70, 2009. 72

[134] B. Kerner. Experimental features of self-organization in traffic flow. *Physical Review Letters*, 81(17):3797–3800, 1998. 16, 50

[135] B. Kerner. Phase transitions in traffic flow. *Traffic and granular flow*, pages 253–283, 2000. 16, 20

[136] B. Kerner and H. Rehborn. Experimental properties of complexity in traffic flow. *Physical Review E*, 53(5):4275–4278, 1996. 50

[137] B. Kerner and H. Rehborn. Experimental properties of phase transitions in traffic flow. *Physical Review Letters*, 79(20):4030–4033, 1997. 50

[138] T. Kobayashi. Adaptive regulator design of a viscous Burgers system by boundary control. *IMA Journal of Mathematical Control and Information*, 18(3):427, 2001. 117

[139] M. Krstic. On global stabilization of Burgers equation by boundary control. *Systems and Control Letters*, 37(3):123–141, 1999. 117, 126

[140] M. Krstic and A. Smyshlyaev. *Boundary control of PDEs: A Course on Backstepping Designs.* Society for Industrial and Applied Mathematics Philadelphia, PA, 2008. 126

[141] S. Kruzhkov. First order quasilinear equations in several independent variables. *Mathematics of the USSR-Sbornik*, 10(2):217–243, 1970. 3, 4, 120, 123

[142] G. Lanckriet, N. Cristianini, P. Bartlett, L. El Ghaoui, and M. Jordan. Learning the kernel matrix with semidefinite programming. *Journal of Machine Learning Research*, 5:27–72, 2004. 81

[143] J. Laval. Linking synchronized flow and kinematic waves. In *Proceedings of Traffic and Granular Flow'05, Berlin, Germany*, pages 521–526, 2005. 50

[144] J. Laval. Hysteresis in traffic flow revisited: An improved measurement method. *Transportation Research Part B*, 45(2):385–391, 2011. 56, 58

[145] J. Laval and C. Daganzo. Lane-changing in traffic streams. *Transportation Research Part B*, 40(3):251–264, 2006. 50

[146] J. Laval and L. Leclercq. A mechanism to describe the formation and propagation of stop-and-go waves in congested freeway traffic. *Philosophical Transactions of the Royal Society A: Mathematical, Physical and Engineering Sciences*, 368(1928):4519–4541, 2010. 50, 59

[147] P. Lax. Hyperbolic systems of conservation laws II. *Communications on Pure and Applied Mathematics*, 10:537–566, 1957. 121

[148] J.-P. Lebacque. A finite acceleration scheme for first order macroscopic traffic flow models. In *Proceedings of the 8th IFAC symposium on transportation systems*, pages 815–820, 1997. 50

[149] J.-P. Lebacque. First-order macroscopic traffic flow models: Intersection modeling, network modeling. In *Proceedings of the 16th International Symposium on Transportation and Traffic Theory, College Park, MD*, 2005. 6

[150] J.-P. Lebacque. The Godunov scheme and what it means for first order macroscopic traffic flow models. In *Proceedings of the 13th International Symposium on Transportation and Traffic Theory*, pages 647–677, Lyon, France, 1996. 4, 8

[151] J.-P. Lebacque and J.-B. Lesort. Macroscopic traffic flow models: a question of order. In *Proceedings of the 14th International Symposium on Transportation and Traffic Theory, Jerusalem, Israel*, 1999. 50

[152] F.-X. Le Dimet and O. Talagrand. Variational algorithms for analysis and assimilation of meteorological observations: theoretical aspects. *Tellus A*, 38(2):97–110, 1986. 9, 85

[153] P. LeFloch. Explicit formula for scalar non-linear conservation laws with boundary conditions. *Mathematical methods in the applied sciences*, 10(3):265–287, 1988. 4, 123

[154] P. LeFloch. *Hyperbolic Systems of Conservation Laws: The theory of classical and nonclassical shock waves.* Lectures in Mathematics, ETH Zürich, Birkhäuser Basel, 2002. 121

[155] J.-B. Lesort, E. Bourrel, and V. Henn. Various scales for traffic flow representation: some reflections. In *Proceedings of Traffic and Granular Flow'03, Delft, the Netherlands*, pages 125–139, 2003. 47, 48, 50, 60

[156] R. Leveque. *Finite volume methods for hyperbolic problems.* Cambridge University Press, Cambridge, UK, 2002. 4, 7, 8, 27, 95, 101, 110, 112, 136

[157] P. Li, R. Horowitz, L. Alvarez, J. Frankel, and M. Robertson. An AHS link layer controller for traffic flow stabilization. *Transportation Research, Part C: Emerging Technologies*, 5(1):11–37, 1997. 128

[158] T. Li. Nonlinear dynamics of traffic jams. *Physica D: Nonlinear Phenomena*, 207(1-2):41–51, 2005. 6, 20, 38, 50

[159] M. Lighthill and G. Whitham. On kinematic waves, II: a theory of traffic flow on long crowded roads. *Proceedings of the Royal Society of London*, 229(1178):317–345, 1956. 4, 5, 48, 86

[160] W. Lin and D. Ahanotu. *Validating the Basic Cell Transmission Model on a Single Freeway Link*. Institute of Transportation Studies, University of California, Berkeley, California PATH technical report 95-3, 1995. 4

[161] X. Litrico and V. Fromion. Frequency modeling of open-channel flow. *Journal of Hydraulic Engineering*, 130(8):806–815, 2004. 117

[162] X. Litrico and V. Fromion. Boundary control of hyperbolic conservation laws using a frequency domain approach. *Automatica*, 45(3):647–656, 2009. 117

[163] J. Liu and R. Chen. Sequential Monte Carlo methods for dynamic systems. *Journal of the American statistical association*, 93(443):1032–1044, 1998. 12, 92

[164] X. Lu and A. Skabardonis. Freeway traffic shockwave analysis: Exploring NGSIM trajectory data. In *86th Transportation Research Board Annual Meeting, Washington D.C., January 21-25*, 2007. 61

[165] H. Ly, K. Mease, and E. Titi. Distributed and boundary control of the viscous Burgers equation. *Numerical Functional Analysis and Optimization*, 18(1):143–188, 1997. 117

[166] H. Mahmassani, T. Hu, S. Peeta, and A. Ziliaskopoulos. Development and testing of dynamic traffic assignment and simulation procedures for ATIS/ATMS applications. Technical report, Technical Report DTFH61-90-R-0074-FG, Center for Transportation Research, University of Texas at Austin, 1994. 48

[167] P.-E. Mazare, C. Claudel, and A. Bayen. Analytical and grid-free solutions to the Lighthill-Whitham-Richards traffic flow model. *Transportation Research Part B: Methodological*, 45(10):1727–1748, 2011, doi:10.1016/j.trb.2011.07.004. 8

[168] A. Messner and M. Papageorgiou. METANET: A macroscopic simulation program for motorway networks macroscopic simulation program for motorway networks. *Traffic Engineering and Control*, 31(8-9):466–470, 1990. 48

[169] N. Metropolis and S. Ulam. The Monte Carlo method. *Journal of the American Statistical Association*, 44(247):335–341, 1949. 92

[170] L. Mihaylova, R. Boel, and A. Hegyi. An unscented Kalman filter for freeway traffic estimation. In *Proceedings of the IFAC Symposium on Control in Transportation Systems, Delft, the Netherlands*, pages 29–31, 2006. 50, 86, 90

[171] L. Mihaylova, R. Boel, and A. Hegyi. Freeway traffic estimation within particle filtering framework. *Automatica*, 43(2):290–300, 2007. 86, 92

[172] R. Miller, E. Carter, and S. Blue. Data assimilation into nonlinear stochastic models. *Tellus A*, 51(2):167–194, 1999. 89

[173] R. Miller, M. Ghil, and F. Gauthiez. Advanced data assimilation in strongly nonlinear dynamical systems. *Journal of the Atmospheric Sciences*, 51(8):1037–1056, 1994. 89

[174] L. Munoz, X. Sun, R. Horowitz, and L. Alvarez. Traffic density estimation with the cell transmission model. In *American Control Conference, 2003. Proceedings of*

the 2003, volume 5, 2003. 4

[175] K. Nagel and P. Nelson. A critical comparison of the kinematic-wave model with observational data. In *Proceedings of the 16th International Symposium on Transportation and Traffic Theory, College Park, MD*, pages 145–164, 2005. 49

[176] G. Newell. Theories of instability in dense highway traffic. *Journal of the Operations Research Society of Japan*, 5:9–54, 1962. 56

[177] G. Newell. A simplified theory of kinematic waves in highway traffic, Part II: queueing at freeway bottlenecks. *Transportation Research Part B*, 27(4):289–303, 1993. 4, 5, 49, 73

[178] G. Newell. A simplified car-following theory: a lower order model. *Transportation Research Part B*, 36(3):195–205, 2002. 48

[179] NGSIM. Next Generation Simulation. http://ngsim-community.org/, 2006. 10, 51, 60

[180] O. Oleinik. Discontinuous solutions of non-linear differential equations. *Uspekhi Matematicheskikh Nauk*, 12(3):3–73, 1957. 3, 4, 120, 128

[181] M. Papageorgiou. Some remarks on macroscopic traffic flow modelling. *Transportation Research Part A*, 32(5):323–329, 1998. 4, 5, 50

[182] M. Papageorgiou, J.-M. Blosseville, and H. Hadj-Salem. Modelling and real-time control of traffic flow on the southern part of Boulevard Peripherique in Paris: Part I: Modelling. *Transportation Research Part A*, 24(5):345–359, 1990. 6, 49, 50, 86

[183] H. Payne. Models of freeway traffic and control. *Mathematical models of public systems*, 1(1):51–61, 1971. 5, 8, 49

[184] J. Pearl. *Probabilistic reasoning in intelligent systems: networks of plausible inference*. Morgan Kaufmann, 1988. 70, 71, 72

[185] S. Peeta and A. Ziliaskopoulos. Foundations of dynamic traffic assignment: The past, the present and the future. *Networks and Spatial Economics*, 1(3):233–265, 2001. 118

[186] N. Petit. *Delay Systems. Flatness in Process Control and Control of some Wave Equations*. PhD thesis, PhD thesis, Ecole des Mines de Paris, Paris, France, 2000. 117

[187] C. Prieur, J. Winkin, and G. Bastin. Robust boundary control of systems of conservation laws. *Mathematics of Control, Signals, and Systems*, 20(2):173–197, 2008. 117

[188] I. Prigogine and R. Herman. *Kinetic theory of vehicular traffic*. Elsevier, New-York, NY, 1971. 48

[189] P. Richards. Shock waves on the highway. *Operations Research*, 4(1):42–51, 1956. 4, 5, 48, 86

[190] P. Saffman. *Vortex dynamics*. Cambridge University Press, Cambridge, UK, 1992. 59

[191] S. Samaranayake, S. Blandin, and A. Bayen. A tractable class of algorithms for reliable routing in stochastic networks. In *Proceedings of the 19th International Symposium on Transportation and Traffic Theory, Berkeley, CA*, 2011, doi:10.1016/j.sbspro.2011.04.521. 14, 140, 141

[192] S. Samaranayake, S. Blandin, and A. Bayen. Learning the dependency structure

of highway networks for traffic forecast. In *IEEE Conference on Decision and Control*, Orlando, FL, December 2011. 14, 74, 76

[193] S. Schmidt. Kalman filter: Its recognition and development for aerospace applications. *Journal of Guidance and Control*, 4(1):4–7, 1981. 10

[194] B. Scholkopf and A. Smola. *Learning with kernels*. MIT press, Cambridge, MA, 2002. 79

[195] D. Schrank and T.Lomax. The 2009 urban mobility report. *Texas Transportation Institute*, College Station, TX, 2009. 1

[196] T. Schreiter, C. van Hinsbergen, F. Zuurbier, H. van Lint, and S. Hoogendoorn. Data-model synchronization in extended Kalman filters for accurate online traffic state estimation. In *2010 Proceedings of the Traffic Flow Theory Conference*, Annecy, France, 2010. 86

[197] G. Schwarz. Estimating the dimension of a model. *The annals of statistics*, pages 461–464, 1978. 74

[198] D. Serre. *Systems of conservation laws*. Diderot, Paris, France, 1996. 4, 18, 21

[199] S. Sherman. Non-mean-square error criteria. *IRE Transactions on Information Theory*, 4(3):125–126, 1958. 10

[200] N. Smaoui. Boundary and distributed control of the viscous Burgers equation. *Journal of Computational and Applied Mathematics*, 182(1):91–104, 2005. 117

[201] S. Smulders. Control of freeway traffic flow by variable speed signs. *Transportation Research Part B: Methodological*, 24(2):111–132, 1990. 86

[202] C. Snyder, T. Bengtsson, P. Bickel, and J. Anderson. Obstacles to high-dimensional particle filtering. *Monthly Weather Review*, 136(12):4629–4640, 2008. 92

[203] H. Sorenson. Least-squares estimation: from Gauss to Kalman. *Spectrum, IEEE*, 7(7):63–68, 1970. 10

[204] S. Stigler. Gauss and the invention of least squares. *The Annals of Statistics*, pages 465–474, 1981. 10

[205] I. Strub and A. Bayen. Weak formulation of boundary conditions for scalar conservation laws: an application to highway traffic modelling. *International Journal of Robust Nonlinear Control*, 16(16):733–748, 2006, doi: 10.1002/rnc.1099. 4, 119, 123

[206] X. Sun, L. Muñoz, and R. Horowitz. Mixture Kalman filter based highway congestion mode and vehicle density estimator and its application. In *American Control Conference (ACC), Boston, MA, 2004*, pages 2098–2103. IEEE, 2004. 86

[207] X. Sun, L. Muñoz, and R. Horowitz. Highway traffic state estimation using improved mixture Kalman filters for effective ramp metering control. In *Proceedings of the 42nd IEEE Conference on Decision and Control*, pages 6333–6338, Maui, HI, 2003. 94

[208] M. Szeto and D. Gazis. Application of Kalman filtering to the surveillance and control of traffic systems. *Transportation Science*, 6(4):419–439, 1972. 86

[209] C. Tampere and L. Immers. An extended Kalman filter application for traffic state estimation using CTM with implicit mode switching and dynamic parameters. In *Intelligent Transportation Systems Conference, 2007. ITSC 2007*, pages 209–216, Seattle,

WA, 2007. 86

[210] B. Temple. Systems of conversation laws with invariant submanifolds. *Transactions of the American Mathematical Society*, 280(2):781–795, 1983. 18, 123

[211] A. Tikhonov. Solution of incorrectly formulated problems and the regularization method. *Soviet Math. Dokl.*, 4(4):1035–1038, 1963. 78

[212] E. Toro. *Riemann solvers and numerical methods for fluid dynamics.* Springer, New-York, NY, 1997. 21

[213] O.-P. Tossavainen, J. Percelay, M. Stacey, J. Kaipio, and A. Bayen. State estimation and modeling error approach for 2D shallow water equations and Lagrangian measurements. *Water Resources Research*, 2011, doi: 10.1029/2010WR009401. 104

[214] J. Treiterer and J. Myers. The hysteresis phenomenon in traffic flow. In *Proceedings of the 6th International Symposium on Transportation and Traffic Theory, Sydney, Australia*, 1974. 56

[215] P. Turney. A theory of cross-validation error. *Journal of Experimental and Theoretical Artificial Intelligence*, 6:361–361, 1994. 81

[216] R. Underwood. Speed, volume, and density relationships: Quality and theory of traffic flow. *Yale Bureau of Highway Traffic*, pages 141–188, 1961. 4

[217] M. Van Aerde. Single regime speed-flow-density relationship for congested and uncongested highways. In *74th Annual Meeting of the Transportation Research Board*, Washington, DC, 1995. 6

[218] R. Van Der Merwe, A. Doucet, N. De Freitas, and E. Wan. The unscented particle filter. *Advances in Neural Information Processing Systems*, 13:584–590, 2001. 92, 93

[219] P. Varaiya. Reducing highway congestion: an empirical approach. *European journal of control*, 11(4-5):301–309, 2005. 5

[220] P. Varaiya. Congestion, ramp metering and tolls. *Philosophical Transactions of the Royal Society A: Mathematical, Physical and Engineering Sciences*, 366(1872):1921–1930, 2008. 4

[221] Y. Wang and M. Papageorgiou. Real-time freeway traffic state estimation based on extended Kalman filter: a general approach. *Transportation Research Part B*, 39(2):141–167, 2005. 4, 9, 49, 50, 86

[222] Y. Wang, M. Papageorgiou, and A. Messmer. Real-time freeway traffic state estimation based on extended Kalman filter: A case study. *Transportation Science*, 41(2):167–181, 2007. 9, 49, 86

[223] G. Whitham. *Linear and Nonlinear Waves.* John Wiley and Sons, New York, NY, 1974. 5, 8

[224] N. Wiener. *Extrapolation, interpolation, and smoothing of stationary time series with engineering applications.* The Technology Press of The Massachusetts Institute of Technology, Boston, MA, 1949. 10

[225] S. Wong and G. Wong. An analytical shock-fitting algorithm for LWR kinematic wave model embedded with linear speed-density relationship. *Transportation Research Part B: Methodological*, 36(8):683–706, 2002. 8

[226] D. Work and A. Bayen. Convex formulations of air traffic flow optimization problems. *Proceedings of the IEEE*, 96(12):2096–2112, 2008. 118

[227] D. Work, S. Blandin, O.-P. Tossavainen, B. Piccoli, and A. Bayen. A traffic model for velocity data assimilation. *Applied Mathematics Research eXpress*, 1(1):1–35, 2010. 14, 50, 86, 91, 123, 140

[228] D. Work, O-P. Tossavainen, S. Blandin, A. Bayen, T. Iwuchukwu, and K. Tracton. An ensemble Kalman filtering approach to highway traffic estimation using GPS enabled mobile devices. In *47th IEEE Conference on Decision and Controls, 2008 Cancun, Mexico*, pages 5062–5068, 2008, doi:10.1109/CDC.2008.4739016. 86

[229] H. Yeo and A. Skabardonis. Understanding stop-and-go traffic in view of asymmetric traffic theory. In *Proceedings of the 18th International Symposium on Transportation and Traffic Theory, Hong-Kong, China*, pages 99–115, 2009. 50

[230] H. Zhang. A theory of nonequilibrium traffic flow. *Transportation Research Part B: Methodological*, 32(7):485–498, 1998. 5, 19

[231] H. Zhang. Structural properties of solutions arising from a nonequilibrium traffic flow theory. *Transportation Research Part B: Methodological*, 34(7):583–603, 2000. 9, 95

[232] M Zhang. A mathematical theory of traffic hysteresis. *Transportation Research Part B*, 33(1):1–23, 1999. 56

[233] M. Zhang. A non-equilibrium traffic model devoid of gas-like behavior. *Transportation Research Part B*, 36(3):275–290, 2002. 9, 19, 50, 58